

INVESTIGATION OF THE EFFECTS OF PHONONS ON THE
CHARACTERISTICS OF SEMICONDUCTOR QUANTUM DOT BASED
STRUCTURES

DAVOUD GHODSI NAHRI

FACULTY OF SCIENCE
UNIVERSITY OF MALAYA
KUALA LUMPUR

2017

INVESTIGATION OF THE EFFECTS OF PHONONS ON
THE CHARACTERISTICS OF SEMICONDUCTOR
QUANTUM DOT BASED STRUCTURES

DAVOUD GHODSI NAHRI

THESIS SUBMITTED IN FULFILMENT
OF THE REQUIREMENTS
FOR THE DEGREE OF DOCTOR OF PHILOSOPHY

FACULTY OF SCIENCE
UNIVERSITY OF MALAYA
KUALA LUMPUR

2017

**UNIVERSITI MALAYA
ORIGINAL LITERARY WORK DECLARATION**

Name of Candidate: **Davoud Ghodsi Nahri**

Registration/Matric No: **SHC120051**

Name of Degree: **Doctor of Philosophy**

Title of Thesis ("this Work"): **INVESTIGATION OF THE EFFECTS OF
PHONONS ON THE CHARACTERISTICS OF SEMICONDUCTOR
QUANTUM DOT BASED STRUCTURES**

Field of Study: **Quantum nanophotonics**

I do solemnly and sincerely declare that:

- (1) I am the sole author / write of this Work;
- (2) This Work is original;
- (3) Any use of any work in which copyright exist was done by way of fair dealing and for permitted purposes and any excerpt or extract from, or reference to or reproduction of any copyright work has been disclosed expressly and sufficiently and the title of the Work and its authorship have been acknowledged in this Work;
- (4) I do not have any actual knowledge nor do I ought reasonably to know that the making of this work constitutes an infringement of any copyright work;
- (5) I hereby assign all and every rights in the copyright to this Work to the University of Malaya ("UM"), who henceforth shall be owner of all the copyright in this Work and that any reproduction or use in any form or by any means whatsoever is prohibited without the written consent of UM having been first had and obtained;
- (6) I am fully aware that if in the course of making this Work I have infringed any copyright whether intentionally or otherwise, I may be subject to legal action or any other action as may be determined by UM.

Candidate's Signature

Date

Subscribed and solemnly declared before,

Witness's signature

Date

Name:

Designation:

ABSTRACT

In the first part of this dissertation, a dissipative quantum dot (QD) -cavity system coupled to a longitudinal acoustic (LA) phonon reservoir is studied using a numerically exact real-time path-integral approach. Three distinct dynamical regimes of weak (WC), strong (SC), and coherent coupling (CC) are discussed and more accurate conditions identifying them are presented. Our results show that to have the CC regime, which is characterized by clear vacuum Rabi oscillation (VRO), vacuum Rabi splitting (VRS) should be larger than the sum of the widths of the corresponding peaks. In order to distinguish between contributions of population decay and impure dephasing, induced by LA phonons and the dissipations, on the quantum dynamics of the QD-cavity system, we propose a two-part phenomenological expression which fits the QD-cavity decay curves perfectly and is used to calculate the corresponding spectra. The emission rate increases from the carrier recombination rate to a maximum value, which is the mean of the QD and cavity dissipation rates, with QD-cavity coupling strength. We introduce a quantity that can be applied in determining the distinct coupling regimes; This quantity enables us to identify the onset of the SC regime as the point where the impure dephasing term begins to contribute to the central band of the spectrum significantly, as a result of the existence of VRO with a very small frequency (unclear VRO) at the corresponding decay curve. Its contribution to the width of the central band increases with the coupling strength up to the onset of the CC regime, then reduces as a result of the appearance of sidebands in the spectra. The effective population decay and impure dephasing rate contribute solely to the width—of the central and sideband peaks of the triplet spectra respectively—only beyond a very large coupling strength which is the same across the considered temperature range. In the second part, we demonstrate that all the available experimental data of temperature (T)-dependent shift of photoluminescence (PL) peak of In(Ga)As QD sam-

ples can be modeled successfully by using a two-oscillator model if and only if the whole temperature interval (0–300 K) is divided into a few parts (at most four parts), depending on dispersion degree of the PL peak from a monotonic behavior. Analysis of the numerical results show that excitons mostly interact (inelastically) with acoustic (AC) or optical (OP) phonons separately. Increasing QDs uniformity, by using some improved growth techniques, results in decreasing or removing the sigmoidal behavior, enhancing total AC phonon contribution to the redshift of the PL peak. Elevation of the zero bandgap (ZBG) energy up to a critical value about 1.4 eV, for In(Ga)As QDs grown using molecular-beam epitaxy, results in enhancement of QD symmetry and total OP phonon contribution and reduction of QDs uniformity and total AC phonon contribution, while a rollover happens for further increase of the ZBG. Therefore we find that the highest QD symmetry and the lowest exciton fine structure splitting correspond to this critical value of ZBG, in accordance with previous experimental results.

ABSTRAK

Dalam bahagian pertama disertasi ini, kuantum dot (QD) sistem -cavity lesap digandingkan kepada akustik membujur (LA) takungan fonon dikaji menggunakan masa nyata pendekatan jalan-penting yang berangka tepat. Tiga rejim berbeza dinamik lemah (WC), kuat (SC), dan gandingan koheren (CC) dibincangkan dan keadaan yang lebih tepat mengenal pasti mereka yang dibentangkan. Keputusan kami menunjukkan bahawa untuk mempunyai rejim CC, yang mempunyai ciri-ciri vakum jelas Rabi ayunan (V_{ro}), vakum Rabi membelah (V_{RS}) hendaklah lebih besar daripada jumlah lebar puncak yang sepadan. Dalam usaha untuk membezakan antara sumbangan pereputan penduduk dan dephasing suci, disebabkan oleh fonon LA dan dissipations, kepada dinamik kuantum sistem QD-rongga, kami mencadangkan ungkapan fenomenologi dua bahagian yang sesuai lengkung pereputan QD-rongga dengan sempurna dan digunakan untuk mengira spektrum yang sama. Kenaikan kadar pelepasan daripada kadar penggabungan semula pembawa kepada nilai maksimum, iaitu min QD dan rongga kadar pelepasan, dengan QD-rongga kekuatan gandingan. Kami memperkenalkan kuantiti yang boleh digunakan dalam menentukan rejim gandingan berbeza; Kuantiti ini membolehkan kami mengenal pasti bermulanya rejim SC sebagai titik di mana jangka dephasing suci mula menyumbang kepada band tengah spektrum dengan ketara, akibat daripada kewujudan V_{ro} dengan kekerapan yang sangat kecil (tidak jelas V_{ro}) di lengkung pereputan sepadan. Sumbangannya kepada lebar jalur bertambah pusat dengan kekuatan gandingan sehingga bermulanya rejim CC, kemudian mengurangkan akibat daripada kemunculan jalur sisi dalam spektrum. Pereputan penduduk berkesan dan kadar dephasing suci menyumbang semata-mata untuk lebar-puncak pusat dan jalur sisi spektrum triplet yang masing-masing sahaja di luar kekuatan gandingan yang sangat besar yang adalah sama di seluruh julat suhu dipertimbangkan. Dalam bahagian kedua, kita menunjukkan bahawa semua data uji kaji suhu (T) anjakan -dependent

daripada photoluminescence (PL) puncak In (Ga) Sebagai sampel QD boleh dimodelkan dengan jayanya dengan menggunakan model dua pengayun jika dan hanya jika selang suhu keseluruhan (0-300 K) dibahagikan kepada beberapa bahagian (paling empat bahagian), bergantung kepada tahap penyebaran puncak PL dari tingkah laku monotonic. Analisis keputusan berangka menunjukkan bahawa excitons kebanyakannya berinteraksi (inelastically) dengan akustik (AC) atau optik (OP) fonon secara berasingan. Meningkatkan QDs keseragaman, dengan menggunakan beberapa teknik pertumbuhan yang lebih baik, keputusan dalam mengurangkan atau menghapuskan tingkah laku sigmoidal, meningkatkan jumlah AC fonon sumbangan kepada anjakan merah puncak PL. Ketinggian sifar memberikan nilai jurang (ZBG) tenaga sehingga nilai kritikal kira-kira 1.4 eV, untuk Dalam (Ga) Sebagai QDs ditanam menggunakan epitaxy, keputusan dalam peningkatan simetri QD dan jumlah caruman OP fonon dan pengurangan QDs keseragaman dan jumlah molekul-beam sumbangan fonon AC, manakala peralihan yang berlaku untuk peningkatan selanjutnya ZBG. Oleh itu kita dapati bahawa QD simetri tertinggi dan yang paling rendah exciton struktur halus membelah sesuai dengan nilai ini kritikal ZBG, selaras dengan keputusan eksperimen sebelumnya.

ACKNOWLEDGEMENTS

I would like to thank my family especially my wife for their kindness, support, and co-operation. I thank my supervisor Prof. Dr. C. H. Raymond Ooi and friends who helped me in preparing and completing this work. Finally, I acknowledge the respectful referees especially Prof. Dr. Manfred Bayer and Prof. Dr. Mikhail Vasilevskiy for reviewing my thesis. This work was supported by High Impact Research MoE grant no. UM.C/625/1/HIR/MOHE/CHAN/04 from the Ministry of Education of Malaysia.

University of Malaysia

TABLE OF CONTENTS

ORIGINAL LITERARY WORK DECLARATION	ii
ABSTRACT	iii
ABSTRAK	v
ACKNOWLEDGEMENTS	vii
TABLE OF CONTENTS	viii
LIST OF FIGURES	x
LIST OF TABLES	xv
LIST OF ABBREVIATIONS	xvi
LIST OF APPENDICES	xviii
CHAPTER 1: INTRODUCTION	1
1.1 Introduction	2
1.1.1 Quantum Dots	1
1.1.2 Phonons	4
1.2 Motivations for Research	5
1.3 Accomplished Studies	7
CHAPTER 2: LITERATURE REVIEW	11
2.1 Quantum Confinement Effects, Density of States, and Electronic Structure	11
2.2 Phonons Dephasing in Quantum Dots	16
2.2.1 Types of Dephasing in Quantum Dots	16
2.2.2 Exact and Perturbative Approaches	18
2.2.3 Dephasing due to Optical-Phonon Interaction	27
2.2.4 Dephasing due to Acoustic-Phonon Interaction	31
2.2.5 Dephasing due to Both Optical- and Acoustic-Phonon Interactions	32
2.2.6 Comparison with the Perturbative Approach	33
2.2.7 Comparison with Experiment	37
2.3 Quantum Dot Cavity-Quantum Electrodynamical Systems	46
2.3.1 Theoretical Approaches to Investigate Quantum Dot-Cavity Quantum Electrodynamical Systems	50
2.4 General Formulation of Path-Integral Approach	53
2.4.1 Lagrangian Formulation of Quantum Mechanics	55
2.4.2 Definition of Influence Functional	58
2.5 Temperature-Dependent Bandgap Variation	60
2.5.1 Photoluminescence Spectrum	60
2.5.2 Semi-Empirical Models for Projecting Temperature-Dependent Bandgap Variation	61
2.5.3 Temperature-Dependent Bandgap Variation in Quantum Dot Samples	65

CHAPTER 3: MODELING AND SIMULATION METHODS	77
3.1 Introduction	77
3.2 Dissipative Quantum Dot-Cavity System Coupled to a Superohmic Environment	67
3.3 Real-Time Path-Integral Approach for the Open Quantum Dot-Cavity System	
3.4 Two-Oscillator Model	88
CHAPTER 4: RESULTS AND DISCUSSIONS	93
4.1 Introduction	93
4.2 Quantum Dot-Cavity Quantum Electrodynamics: Impure Dephasing-Induced Effects	93
4.3 Temperature-Dependent Shift of Photoluminescence Peak of In(Ga)As Quantum Dots: Role of Acoustic and Optical Phonons	108
CHAPTER 5: CONCLUSIONS	120
APPENDICES	123
REFERENCES	143

LIST OF FIGURES

- Figure 1.1 Characteristic size of a QD relative to a single atom and a photonic crystal. A single atom, shown in (a), measures a few angstrom while self-assembled InGaAs QDs, like the one shown in (b), typically have dimensions of tens of nanometer and consist of approximately 10^5 atoms. The micrograph in (b) shows an uncapped QD obtained by scanning tunneling microscopy. Single QDs can be embedded in photonic nanostructures for quantum-optics experiments, an example of which is (c) that shows a scanning electron micrograph image of a photonic-crystal waveguide, where the photonic lattice constant typically is around 250 nm (Lodahl, Mahmoodian, Stobbe, 2015). 2
- Figure 1.2 Atomic force microscope (AFM) scan of inhomogeneously broadened InAs QDs ensemble grown on (a) an unpatterned and (b) a patterned substrate with a period of 200 nm (Sergeev, Mitin, Strasser, 2010; Schramboeck, Andrews, Roch, Schrenk, Strasser, 2007). 4
- Figure 1.3 Two different mode types: acoustic (AC) and optical (OP) phonons. u is atom displacement. M is the mass of the larger atoms, which is represented by the larger open circles. m is the lower-mass atoms, represented by the small solid circles. 5
- Figure 2.1 Schematic representation of bulk and nanostructures and their density of states (DOS). 13
- Figure 2.2 Dispersion relations of electrons and holes for different dimensionalities. For all cases, the dispersions above the thick horizontal zero energy line are for electrons and the dispersions below are for holes. In the 2-D and 1-D cases, the dispersion shown is for the confined direction(s) only, while the 3-D dispersion can be used for the unconfined direction(s). 14
- Figure 2.3 (a) Discrete energy levels in a InAs QD grown on GaAs substrate. Wave functions are shown for the states shown. The listed InAs bandgap (0.354 eV) is the intrinsic bandgap value at room temperature (b) Energy levels in a perfect square well with infinitely high potential barriers. 16
- Figure 2.4 Dispersion relations of the LO, LA, and TA phonons taken in the calculations as well as normalized effective form factors [see Eq. 2.17] describing the coupling of QDs with three different sizes $r = 3, 6, \text{ and } 9 \text{ nm}$ to the various phonon modes (Krummheuer et al., 2002). 27
- Figure 2.5 The degeneracy has been lifted in acoustic and optical dispersion curves by an anisotropic lattice. a represents the lattice constant (Klingshirn, 1995). 28

- Figure 2.6 Optical polarizations induced by a δ -function-shaped optical pulse (left column) and absorption spectra (right column) for a QD interacting with optical phonons at a temperature of 300 K. The calculation results without phonon dispersion have been shown in the parts (a) and (b), in parts (c) and (d) [(e) and (f)] the results including dispersion are plotted for a 6-nm (3-nm) QD. The spectra of the n -phonon sidebands due to phonon emission ($n > 0$) or phonon absorption ($n < 0$) are shifted by $-n\hbar\omega_{LO}$ towards the ZPL. In part (d) they are multiplied by the factors 3×10^3 ($|n| = 1$) and 2×10^6 ($|n| = 2$); the corresponding factors in part (f) are 3×10^4 ($|n| = 1$) and 4×10^7 ($|n| = 2$) (Krummheuer et al., 2002). 30
- Figure 2.7 Optical polarizations induced by a δ -function-shaped optical pulse (left column) and absorption spectra (right column) for a 3-nm QD interacting with AC phonons at three different temperatures. Parts (a) and (b) refer to piezoelectric coupling, parts (c) and (d) to deformation potential coupling (Krummheuer et al., 2002). 32
- Figure 2.8 Optical polarizations induced by a δ -function-like optical pulse (left column) and absorption spectra (right column) for a 6-nm QD interacting with OP and AC phonons at three different temperatures $T = 4, 77,$ and 300 K (Krummheuer et al., 2002). 34
- Figure 2.9 Same as figure 2.8 but for a 3-nm QD (Krummheuer et al., 2002). 35
- Figure 2.10 Comparison of the exact absorption spectra (left column) with those obtained from a correlation expansion up to the second order in the coupling matrix elements (right column) for (a) and (b) polar optical, (c) and (d) piezoelectric, and (e) and (f) deformation potential, as well as for (g) and (h) the combination of all mechanisms at a temperature of 4 K (Krummheuer et al., 2002). 36
- Figure 2.11 Semilogarithmic plot of the EL intensity of a single QD. (a) With increasing temperature the line broadening increases due to stronger AC phonon interaction. (b) Comparison of the measured line shape with two calculated spectra, using alternatively a simple Gaussian (red dashed curve) and a realistic eight-band k-p wave function (green dotted curve) (Stock et al., 2011). 40
- Figure 2.12 Comparison of the spectral phonon density for two different wave functions. For AC phonons (energy < 10 meV) the Gaussian wave function (black curves) decreases too quickly, leading to an underestimation of the phonon scattering (Stock et al., 2011). 42
- Figure 2.13 OP phonon replica of a single QD. (a) The black dotted curve shows three ZPL lines, each one having a replica, separated by 36.5 meV (red spectra, top energy scale). (b) Comparison of the LO line shape between experimentally measured (black) and calculated spectra with (red dotted curve) or without (green dashed curve) taking into account a finite lifetime of the phonon of 10 ps. A finite lifetime of the phonon provides a better description of the broad line shape of the LO phonon replica (Stock et al., 2011). 43

- Figure 2.14 Overview of different QD-cQED systems including a nanophotonic cavity and single QD. Each panel displays a scanning electron micrograph of a real device along with a sketch illustrating the operational principle for a quantum emitter coupling to the structure. Furthermore, state-of-the-art experimental results are listed. (a) Micropillar cavity, the Bragg stack above and below the center of the pillar confines light to the central region as shown in the inset. (b) Modified photonic-crystal L3 cavity implemented in a membrane. The photonic band gap localizes light in the defect region and the schematic shows how a QD preferentially emits into the cavity mode. (c) A nanobeam cavity, the cavity mode is confined by 1D Bragg diffraction in the high-refractive-index material of the nanorod. (d) Microdisk cavity, the emitter couples to optical modes that travel circularly around the microdisk. The asterisk (*) indicates that in these cases γ was extracted from spectral rather than time-resolved data, i.e., it will be enlarged by dephasing processes. 49
- Figure 2.15 Space-time diagram showing possible paths for particle to proceed from Q_τ to Q_T . 56
- Figure 2.16 Temperature-dependent PL emission spectra of different QD samples (a) 5-layer and (b) 10-layer QD sample (Lu, Vaillancourt, Wen, 2010). 61
- Figure 2.17 Temperature-dependent bandgap energy variation in the 5-QD sample at various temperatures from 12 to 300 K. The data were measured from the PL emission. Dashed green and red traces show the energy gap shrinking projected by using the Varshni's formula and the PF ansatz, respectively. Blue and pink traces show calculated bandgap energies by using Lu model at the low ($T < 100$ K) and high temperature ($T > 100$ K) regions, which show a good agreement with the experimental data (Lu, Vaillancourt, Wen, 2010). 65
- Figure 2.18 The temperature-dependent PL peak evolutions are presented at various temperatures (15–300 K) for the InAs QD sample grown in conventional MBE (A0) and migration-enhanced MBE (MEMBE) (A1). The red cross is the experimental PL peak energy at different temperatures. The blue rectangle indicates the experimental PL linewidth (FWHM). The green dashed lines and the black solid lines represent the projected energy gap variations by using Varshni and Fan models, respectively (Yeo, Song, Lee, 2011). 66
- Figure 3.1 (a) A two-level QD, including a ground state $|G\rangle$ and an excited state $|X\rangle$, is coupled to a single mode cavity, with two photon levels $|0\rangle$ and $|1\rangle$, through the coupling strength g . The matrix elements γ_q describe interaction of the QD with the phonon reservoir which is represented by a continuum of LA phonon wave states. The radiative carrier recombination and the cavity loss rates are represented by γ_r and κ , respectively. (b) QD-cavity system represented in terms of the common basis states, with maximum one photon in the cavity or one exciton, interacting with the LA phonon bath and decaying with a g -dependent rate γ_1 . 69

- Figure 3.2 Time-dependence of normalized real (left panel) and imaginary (right panel) parts of the memory kernel $K(t)$ at different temperatures. It seems that the memory kernel with the length 4 ps, as $t_c = \epsilon n_c = 4$ ps, is appropriate for the spherical QD with radius 5 nm and the deformation potential coupling to LA phonons. 78
- Figure 3.3 Schematic representation of the configuration space including some trajectories (like the red path), started from an initial state, and the memory truncation. The ovals indicate the time points t_n ; Solid ovals correspond to the points within the memory length with the memory cutoff number $n_c = 3$ for the time point t_q , while hollow ovals correspond to the time steps p , with $q - p > n_c$, which are not taken into account at the time t_q . The solid lines indicate the path segments included in $\bar{T}_{j_q}^c$, while the dashed lines indicate non-included path segments at the time t_q . 85
- Figure 4.1 The decay dynamics of the QD-cavity system for different coupling strengths at $T = 0$ K with the recombination rate $\gamma_r (= 0.001 \text{ ps}^{-1}) = 0.0063 \text{ rad/ps} = 4.135 \text{ } \mu\text{eV}$ and the cavity decay rate $\kappa (= 0.0242 \text{ ps}^{-1}) = 0.1519 \text{ rad/ps} = 100 \text{ } \mu\text{eV}$. Three distinct dynamical regimes of weak, intermediate (strong), and coherent coupling can be determined in the figure. 95
- Figure 4.2 A comparison between the actual decay (pink), obtained using the numerical RTPI calculations, an exponential decay (red), obtained by fitting a single exponential to the actual decay, and a fit of the actual decay by using Eq. 4.1 (green) at $g = 15 \text{ } \mu\text{eV}$ and $T = 0$ K. 96
- Figure 4.3 Comparison between the decay curves, obtained by RTPI approach, and a fit of the phenomenological expression 4.1 for two cases. The phenomenological expression fits the numerically exact results of the QD-cavity decay curves perfectly. 99
- Figure 4.4 Two examples of fitting equation 4.1 to the exact state $|1\rangle$ population of the dissipation-less QD-cavity system, obtained from our microscopic RTPI calculation. The phenomenological expression projects the exact state population perfectly as well. 99
- Figure 4.5 The corresponding normalized spectra, $Re(\rho_{11}(\omega))$, of the decay curves shown in figure 4.1, calculated for different values of the QD-cavity coupling g at $T = 0$ K with $\gamma_r (= 0.001 \text{ ps}^{-1}) = 0.0063 \text{ rad/ps} = 4.135 \text{ } \mu\text{eV}$ and $\kappa (= 0.0242 \text{ ps}^{-1}) = 0.1519 \text{ rad/ps} = 100 \text{ } \mu\text{eV}$. The separated sideband peaks appear clearly at about $g = 60 \text{ } \mu\text{eV}$, indicating the onset of the CC regime. 100
- Figure 4.6 The normalized spectrum (black), Lorentzian part (red), and impure dephasing part (green), plotted for $g = 60 \text{ } \mu\text{eV}$ and $T = 0$ K. The spectrum is obtained as a result of combination of the Lorentzian and impure dephasing part. 101
- Figure 4.7 The central peak FWHM (CPFWM) extracted from the spectra for three different temperatures $T = 0, 20$ and 80 K as a function of g . $\gamma_r = 0.0063 \text{ rad/ps} = 4.135 \text{ } \mu\text{eV}$ and $\kappa = 0.1519 \text{ rad/ps} = 100 \text{ } \mu\text{eV}$. The cubic spline data interpolation has been used to connect the many points (not shown) calculated by numerically exact RTPI method. 102

- Figure 4.8 Γ_1 (FWHM of the effective population decay) and CPFWHM versus g at $T = 0 K$. The inset shows Γ_1 and CPFWHM at a short g interval. $\gamma_r = 0.0063 \text{ rad/ps} = 4.135 \mu\text{eV}$ and $\kappa = 0.1519 \text{ rad/ps} = 100 \mu\text{eV}$. The cubic spline data interpolation has been used to connect the many points (not shown) calculated by numerically exact RTPI method. 103
- Figure 4.9 The introduced quantity δ_{FWHM} , which is difference of CPFWHM and Γ_1 , for different QD-cavity coupling strengths at three diverse temperatures $T = 0, 20$ and $80 K$. The inset of figure 4.9 shows the introduced quantity as the main figure at small g . 104
- Figure 4.10 (a) The normalized impure dephasing spectra for different g at $T = 0 K$. As g increases within the CC regime, a rollover occurs and the contribution of (FWHM of) the impure dephasing spectra to (FWHM of) the central peak of the spectra, $Re(\rho_{11}(\omega))$, decreases to zero as a result of increasing clear VRO frequency which leads to growing separated sidebands. (b) The normalized impure dephasing spectra only for different small g at $T = 0 K$ for a better view. The parameters $\gamma_r = 0.001 \text{ ps}^{-1} = 0.0063 \text{ rad/ps}$ and $\kappa = 0.0242 \text{ ps}^{-1} = 0.1519 \text{ rad/ps}$ were used. 105
- Figure 4.11 FWHM of the effective population decay, Γ_1 , versus g at three various temperatures $T = 0, 20$, and $80 K$ with $\gamma_r = 0.0063 \text{ rad/ps} = 4.135 \mu\text{eV}$ and $\kappa = 0.1519 \text{ rad/ps} = 100 \mu\text{eV}$. The effective population decay rate is proportional to the inverse of temperature for the coupling strengths less than about $g = 500 \mu\text{eV}$. 107
- Figure 4.12 Fitted T-dependent shift of PL peak for SOQDs with different thicknesses (a) 1.8, (b) 2.4, and (c) 18 MLs. Dividing the whole T-interval to three shorter parts, shown by different colors, TOM projects the whole data successfully. 109
- Figure 4.13 Fitted T-dependent shift of PL peak for SOQDs with different thicknesses: (a) 1, (b) 1.5, (c) 2, and (d) 2.5 MLs. 111
- Figure 4.14 Fitted T-dependent shrinkage of bandgap peak for SOQDs grown by MBE, HDE, and MBE+MDH techniques with different thicknesses: (a) and (b) 1.6, (c) and (d) 2.4. 114
- Figure 4.15 Fitted PL peak shift of QDs grown using (a) MBE and (b) migration enhanced MBE [abbreviated as MEE] for the same number of 3 MLs. 114
- Figure 4.16 Fitted T-dependent shrinkage of bandgap energy peak for SOQDs with a different number of layers (a) 5 and (b) 10. 117

LIST OF TABLES

Table 2.1	Density of states (DOS) for electrons in the conduction band of a semiconductor. D stands for dimension. The 2 in the zero dimension case is just the spin degeneracy, since the volume part of the prefactor no longer exists. $\theta(E - E_n) = 0$ for $E < E_n$. and 1 for $E > E_n$.	12
Table 3.1	Phonon Energy Peaks for GaAs, InAs, and InGaAs Bulk	91
Table 4.1	Parameters Obtained Using Fit, Eqs. 3.53 and 3.54, the Final Column Shows the Obtained Transition Temperatures for SOQDs with 1.8, 2.4, and 18 MLs	108
Table 4.2	Parameters Obtained Using Fit, Eqs. 3.53 and 3.54, and the Obtained Transition Temperatures for SOQDs with 1, 1.5, 2, and 2.5 MLs	111
Table 4.3	Parameters Obtained Using Fit, Eqs. 3.53 and 3.54, and the Obtained Transition Temperatures for SOQDs Grown Using MBE, HDE, MBE+MDH, and MEE Methods with 1.6, 2.4, and 3 MLs	115
Table 4.4	Parameters Obtained Using Fit, Eqs. 3.53 and 3.54, and the Obtained Transition Temperatures for SOQDs with Different Number of Layers 5 and 10	118

LIST OF ABBREVIATIONS

1-D	One Dimension
2-D	Two Dimension
3-D	Three Dimension
AC	acoustic
AFM	Atomic Force Microscope
AlN	Aluminum Nitride
CB	Conduction Band
CC	Coherent Coupling
CPFWHM	Central Peak Full Width at Half Maximum
DOS	Density of States
EIT	Electromagnetically Induced Transparency
EL	Electroluminescence
ES	Excited State
FSS	Fine-Structure Splitting
FWHM	Full Width at Half Maximum
GS	Ground State
HDE	Heterogeneous Droplet Epitaxy
IBM	Independent Boson Model
IC	Intermediate Coupling
IHB	Inhomogeneous Broadening
In(Ga)As	Indium Gallium Arsenide
LA	Longitudinal Acoustic
LED	Light Emitting Diodes
LO	Longitudinal Optical
MBE	Molecular Beam Epitaxy
MDH	Modulation Doped Heterostructure
ME	Master Equation
MEE	Migration-Enhanced MBE
MLs	Monolayers
NZ	Nakajima-Zwanzig
OP	Optical
OQC	Open Quantum Dot-Cavity
PF	Power Function
PL	Photoluminescence
QD	Quantum Dot
QD-cQED	Quantum Dot-Cavity Quantum Electrodynamics
QUAPI	Quasi-Adiabatic Propagator Feynman Path Integral
RDM	Reduced Density Matrix
RQCDM	Reduced Open QD-Cavity Density Matrix
RTPI	Real-Time Path-Integral
SC	Strong Coupling
SK	Stranski-Krastanov
SNR	Squared 2-Norm of the Residual
SOQD	Self-Organized Quantum Dot
T	Temperature
TA	Transverse Acoustic
TC	Time-Convolutionless
TO	Transverse Optical
TOM	Two-Oscillator Model

VB	Valence Band
VRO	Vacuum Rabi Oscillation
VRS	Vacuum Rabi splitting
WC	Weak Coupling
ZB	Zero Bandgap
ZPL	Zero Phonon Line

University of Malaya

LIST OF APPENDICES

Appendix A Derivation of Discretized Real-Time Path-Integrals for
Dissipative Quantum Dot-Cavity System Coupled to Longitudinal
Acoustic Phonon Bath

124

University of Malaya

CHAPTER 1

INTRODUCTION AND MOTIVATIONS

1.1 Introduction

The existence of a discrete and anharmonic electronic spectrum is the prerequisite for many quantum-optics experiments since it enables generating single photon when an electron undergoes a transition between two levels. An obvious choice is a single atom, which represents a clean quantum system with discrete electronic states. The ability to create discrete electronic states in a solid-state system enables a range of new opportunities for integrated quantum-optics experiments, this can be achieved in a quantum dot (QD). As QDs are embedded in a solid (substrate), they are inherently coupled to the environment degrees of freedom (phonons). The interactions of the QD carriers with phonons lead to broadening of the discretized electronic states and play an important role in the electrical and optical properties of the QD structures. In this study, we focus on four important types of phonons called: transverse optical (TO), longitudinal optical (LO), transverse acoustic (TA), and longitudinal acoustic (LA) phonons. In the following, an introduction about QDs and phonons is presented.

1.1.1 Quantum Dots

QDs are electrically semiconducting nanostructured regions, composed of elements of groups II to VI the periodic table such as In(Ga)As/GaAs, GaAs/AlGaAs, InP/Zn(S, Se), GaN//AlN, GaSb/GaAs, Si, Ge/Si, CdSe/ZnS. A relatively new kind of QDs called perovskite have also been introduced (Park, Guo, Makarov, & Klimov, 2015). Generally, there are two types of colloidal and epitaxial QDs, our focus in this thesis is on epitaxial QDs which are grown by epitaxial methods and called self-assembled or self-

organized QDs as well. Although QDs consist of tens of thousands of atoms they have optical properties similar to single atoms due to the quantum confinement of electrons' and holes' wave-functions to a nanometer length scale. Therefore, they are also called "artificial atoms" or "macro atoms". Since QDs are solid-state emitters they can readily be implemented in photonic nanostructures such as nanowires, plasmonic nanoantennas, and photonic crystals. Figure 1.1 indicates the size of a QD relative to a single atom and a typical photonic nanostructure.

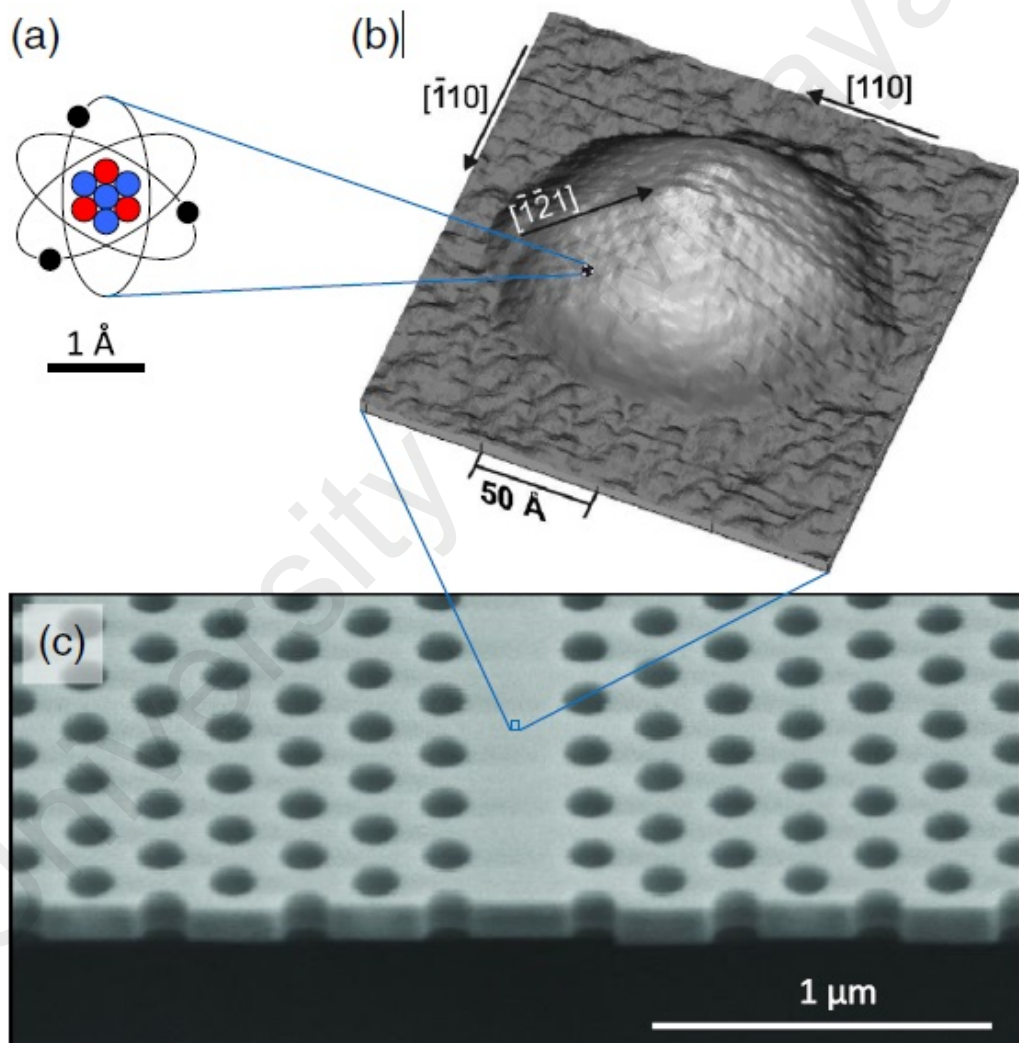


Figure 1.1: Characteristic size of a QD relative to a single atom and a photonic crystal. A single atom, shown in (a), measures a few angstrom while self-assembled InGaAs QDs, like the one shown in (b), typically have dimensions of tens of nanometer and consist of approximately 10^5 atoms. The micrograph in (b) shows an uncapped QD obtained by scanning tunneling microscopy. Single QDs can be embedded in photonic nanostructures for quantum-optics experiments, an example of which is (c) that shows a scanning electron micrograph image of a photonic-crystal waveguide, where the photonic lattice constant typically is around 250 nm (Lodahl, Mahmoodian, Stobbe, 2015).

As the size of a QD approaches the Bohr radius of the bulk exciton, quantum confinement effects become pronounced leading to quantized energy levels for charge carriers (electrons and holes) inside the QD. This leads to a discrete spectrum of quantum states like the energy levels of an atom and significant modification of the optical and electronic properties: Light emission from QDs has a higher quantum efficiency than emission from bulk materials. In addition, the nonlinear polarizability and transition oscillator strength are spectrally concentrated and increased in magnitude in the size regime of QDs.

One of the important experimental advantages of QDs is that they are made of semiconductor materials for which a wealth of growth and processing technology have been developed over the past decades. Sophisticated crystal-growth procedures combined with semiconductor processing methods such as electron-beam lithography, etching, and deposition constitute the generic nanofabrication platform on which the significant experimental progress within quantum nanophotonics during the past decades has been built. Since semiconductors are very sensitive to impurities and defects, QDs are fabricated by epitaxial methods such as molecular-beam epitaxy, where heterostructures are grown with monolayer precision under ultrahigh-vacuum conditions (Shchukin & Bimberg, 1999; Stangl, Holý, & Bauer, 2004; Biasiol & Heun, 2011). The most common approach to grow In(Ga)As QDs is the Stranski-Krastanov method that relies on the self-assembly of InAs or InGaAs QDs on a GaAs surface due to the 7% larger lattice constant of InAs compared to that of GaAs. As a consequence, only a thin wetting layer of InAs can be deposited on GaAs before the strain is relaxed by the nucleation of QDs in the form of randomly positioned islands. In order to protect the QDs from oxidation and to prevent interaction with surface states, a GaAs capping layer is grown atop the QDs. While Stranski-Krastanov QDs have a pyramidal shape before capping, they develop the shape of a truncated pyramid after capping (Eliseev et al., 2000) due to a significant material intermixing. This in turn leads to an inhomogeneous indium distribution and a strain that

varies throughout the QD. Typically, QDs are grown with heights in the range of 1–10 nm and in-plane sizes in the range of 2–70 nm (Lodahl, Mahmoodian, & Stobbe, 2015; Cheng, Lowe, Reece, & Gooding, 2014). Controlling the size and therefore the quantum confinement as well as the material composition enables tailoring the emission wavelength. Size variations between different ensemble's QDs within a single growth run are inevitable, i.e., a QD ensemble will be inhomogeneously broadened, implying that individual tuning of single QDs would generally be required in order to couple them mutually. Figure 1.2 represents atomic force microscope (AFM) scan of inhomogeneously broadened InAs QDs ensemble grown on (a) an unpatterned and (b) a patterned substrate with a period of 200 nm.

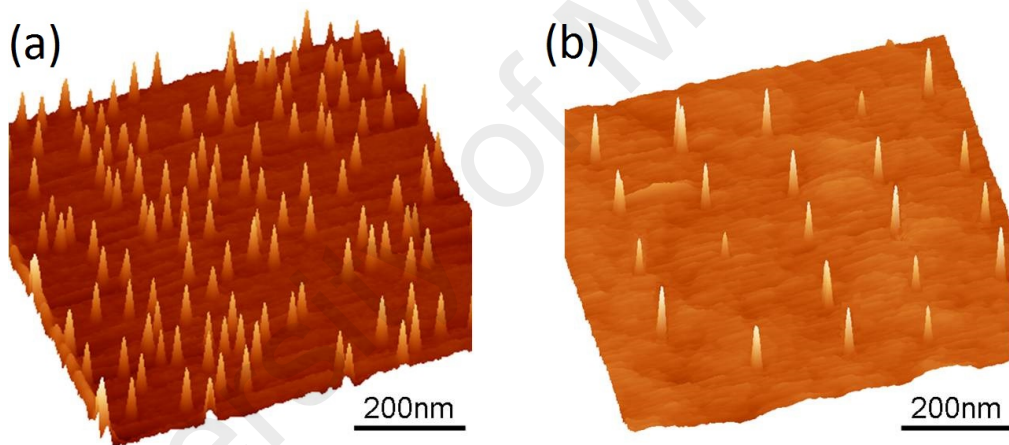


Figure 1.2: Atomic force microscope (AFM) scan of inhomogeneously broadened InAs QDs ensemble grown on (a) an unpatterned and (b) a patterned substrate with a period of 200 nm (Sergeev, Mitin, Strasser, 2010; Schramboeck, Andrews, Roch, Schrenk, Strasser, 2007).

1.1.2 Phonons

Lattice properties of the QDs do not differ significantly from the bulk. This is because the size of the QD is much larger than the lattice constant. Therefore, let us discuss the lattice of a bulk system. Independent normal modes of the lattice include two different mode types: acoustic (AC) and optical (OP) phonons. AC modes correspond to in-phase motion of two different types of atoms, in the case of a diatomic lattice such as InAs or

GaAs. That is, the entire unit cell moves cohesively. At the edge of the Brillouin zone only the more massive atoms oscillate. Optical modes, on the other hand, correspond to antiphase motion of the two types of atoms. For example, the In and As atom move with respect to each other within the unit cell. At the Brillouin zone edge the less massive atoms oscillate. Figure 1.3 illustrates these two types of modes (Klingshirn, 1995).

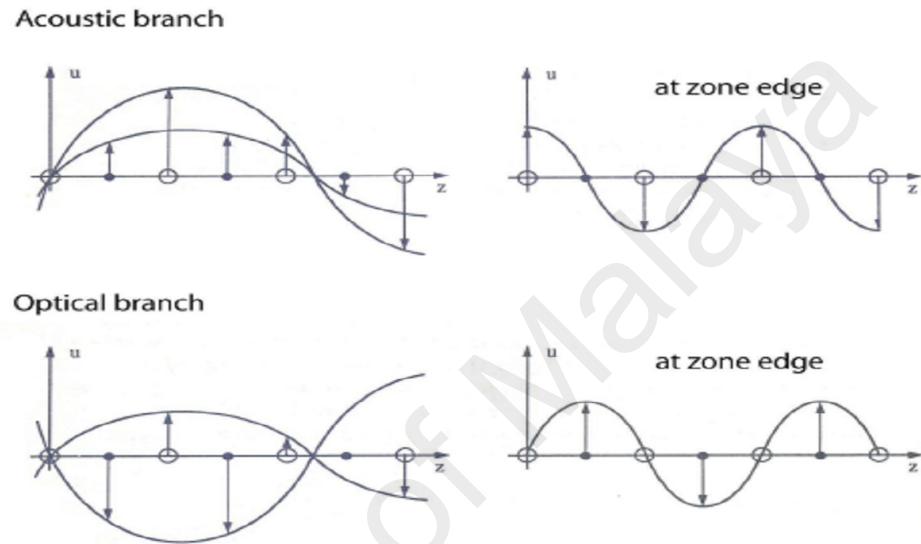


Figure 1.3: Two different mode types: acoustic (AC) and optical (OP) phonons. u is atom displacement. M is the mass of the larger atoms, which is represented by the larger open circles. m is the lower-mass atoms, represented by the small solid circles.

If the two atoms carry electric charge, that is, if the binding is at least partly ionic, then the oscillation of the atoms is connected with an oscillating electric dipole. These transverse eigenmodes can be generated by photons via resonant absorption. This is why the oscillations are called "optical" modes. The ability to couple to the light field is why the optical branches do not vanish at $k = 0$.

1.2 Motivations for Research

Semiconductor QD structures have been considered as promising systems for interesting applications such as high-performance optoelectronic devices, including lasers (Ghodsi Nahri, 2012c, 2012b, 2012a; Eliseev et al., 2000; Pelton & Yamamoto, 1999), optical amplifiers (Vasileiadis, Alexandropoulos, Adams, Simos, & Syvridis, 2008), pho-

photodetectors (Barve et al., 2010; Lu, Vaillancourt, & Meisner, 2007b, 2007a), and light emitting diodes (LEDs) (Basu, 1997), single and entangled photon sources (Somaschi et al., 2016; Park et al., 2015; Muller, Bounouar, Jons, Glassl, & Michler, 2014; Stevenson et al., 2012; Salter et al., 2010; Claudon et al., 2010; Michler et al., 2000; Benson, Santori, Pelton, & Yamamoto, 2000), cavity quantum electrodynamic effects (Hennessy et al., 2007; Reithmaier et al., 2004; Yoshie et al., 2004), quantum information and computation processing (Nilsson et al., 2013; Ladd et al., 2010; Chen, Piermarocchi, & Sham, 2001; Tanamoto, 2000; Burkard, Loss, & DiVincenzo, 1999), quantum cryptography, and teleportation (Nilsson et al., 2013). Other investigated applications of semiconductor nanostructures include photonic network components, such as optical switches and modulators (Kelly, 1995), among other nonlinear photonic devices. The potential of quantum information and computation processing has triggered many research since years ago and QDs have been investigated as integral parts of a variety of quantum information and computation processing schemes (Schrier & Whaley, 2005; Brown, Lidar, & Whaley, 2001; Brun & Wang, 2000). However, the key properties and suitability of QD structures to have a proper physical performance for improved applications strongly depend on understanding their basic characteristics such as phonon-induced effects on the performance of these structures.

We study the effects induced by LA phonons in a hybrid single QD-cavity system and by AC and OP phonons in samples of QD ensembles. A scalable QD-cavity platform, where the interaction between the single photon with the QD can be engineered and controlled to a high degree, can be obtained by understanding and controlling the effects induced by phonons on the QD-cavity dynamics. Such a scalable QD-cavity platform can realize a perfect single photon source (Somaschi et al., 2016; He et al., 2013; Gazzano et al., 2013; Michler et al., 2000) which is a main requirement for quantum computation and information processing (O'Brien, Furusawa, & Vuckovic, 2009; Knill, Laflamme, &

Milburn, 2001). It is also applicable for low-threshold and nano lasers (Strauf & Jahnke, 2011; Noda, 2006; Michler, 2003) as well as tests of fundamental aspects of quantum mechanics (Haroche & Raimond, 2006). Study of the effects induced by phonons on the bandgap width of self-organized quantum dots (SOQDs), on the other hand, offers a characteristic “fingerprint” of the material under investigation from which one can find optical and structural properties such as phonon statistics. It also is of considerable importance for improving QD-based structures including QDs’ samples applicable in optoelectronic devices.

1.3 Accomplished Studies

The thesis is organized as follows: In Chap. 2, the quantum confinement and its effects on the electronic structure and density of states of QDs are reviewed. AC and OP phonon-induced dephasing effects, separately and in combination, in QDs are discussed obtaining the relevant absorption spectra and optical polarization. The results of an exact and a perturbative approach are compared. The exact results of electroluminescence spectra accounting for AC and OP phonon are also compared with the experimental results. In section 2.3, QD-cavity quantum electrodynamics (QD-cQED) systems are introduced and the theoretical models to investigate them are briefly reviewed. General formulation of Feynman path-integral approach is presented in the next section. In section 2.5, temperature-dependent bandgap energy variation and three semi-empirical models for projecting it is presented. The models applied for performing the simulations of this work are presented in Chap. 3; Numerically exact real-time path-integral (RTPI) approach modified for the QD-cQED system and implementation of a suitable numerical algorithm to evaluate the derived density matrix elements are offered. In section 3.4, two-oscillator model applied to project temperature-dependent bandgap variation of self-assembled QD ensembles is given. Chap. 4 and 5 are devoted to simulation results and

conclusion. A detailed derivation of the QD-cavity density matrix elements by using the numerically exact RTPI approach is offered in the appendix.

To investigate the phonon-induced effects on the semiconductor QD structures, in this thesis, a solid-state cQED system, consisting of a single semiconductor QD (a solid-state emitter) coupled resonantly to single mode of an optical nanocavity, is investigated by using the numerically exact RTPI approach. Within this approach, we treat exciton-photon and exciton-phonon interactions on the same footing, exciton decay and cavity loss are included phenomenologically by adding the non-Hermitian terms to the Hamiltonian. In fact, we have applied the full non-Hermitian Hamiltonian within the path-integral formalism which is numerically exact. We identify three different regimes of QD-cQED in the simulated decay dynamics and provide more precise conditions for those regimes. We study the effects induced by impure dephasing of coherent coupling between the dressed states, originated from LA phonon bath and the dissipations, on the decay curves and the corresponding spectra by proposing a two-term phenomenological expression that perfectly reproduces the decay curves. We extract effective population decay and impure dephasing rates and obtain a maximum achievable value for the emission rate, which is the mean of the QD and cavity dissipation rates. Projecting the proposed phenomenological expression to the state population, obtained from our RTPI calculation for the dissipation-less QD-cavity system, we find an approximate expression for the effective impure dephasing rate. The effects of temperature and the QD-cavity coupling strength on the width of the central peak of the spectra is studied. To investigate the role of the effective impure dephasing rate on the width of central peak of the spectra we introduce a quantity which is applicable to determine the distinct regimes of the QD-cavity coupling as well. We demonstrate that the contribution of the impure dephasing part to the central band of the spectra starts at the onset of the strong coupling (SC) regime, which originates from the existence of vacuum Rabi Oscillation (VRO) with a very small fre-

quency (unclear VRO) at the corresponding decay curve. Its contribution to the central peak increases with the coupling strength within the SC regime as a result of enhancing frequency of the uncled VRO. At the onset of the CC regime, the contribution begins to reduce as a result of the appearance of sidebands in the spectra, which originates from clear VRO. The reduction continues down to zero as the effective population decay and impure dephasing rate contribute separately to the central and sideband peaks of the triplet spectra, respectively, only beyond a very large coupling strength which is the same across the considered temperature range. It is also shown that to obtain the maximum achievable emission rate, at a higher temperature, a larger coupling strength is required as a result of temperature-dependence of the effective population decay rate (Ghodsi Nahri, Mathkoo, & Ooi, 2016).

In the second part of this work, in order to study the role of AC and OP phonons at the temperature (T)-dependent shift of photoluminescence (PL) peak of self-assembled QD ensembles we apply the two-oscillator model (TOM) to 15 available experimental datasets of In(Ga)As/GaAs QD ensembles, with a different number of monolayers (MLs) and layers, taken from published papers [36-44]. We correspond the low energy oscillator to AC phonons and the high energy one to OP phonons. We find that the TOM can project all the samples with a good accuracy if the whole temperature interval 0-300 K is divided into, at most, four parts depending on the degree of the dispersion from a monotonic decrease of the bandgap energy peak. Our results suggest that, low QDs uniformity in an ensemble results in the dispersion (anomalous temperature behavior of PL peak), and the whole AC phonon contribution to the T-dependent shift of PL peak decreases for higher dispersions. Some growth techniques, which improve the QDs uniformity, lead to removal of the dispersion (sigmoidal behavior) and thus increase of AC phonon contribution to T-dependent shrinkage of the PL peak. We also propose a trade off between QDs uniformity (inhomogeneous broadening (IHB) of the QDs sample) and

QD symmetry. Enhancement of QDs uniformity increases total AC phonon contribution and enhancement of the symmetry increases total OP phonon contribution (Ghods Nahri & Ooi, 2014).

University of Malaya

CHAPTER 2

LITERATURE REVIEW

2.1 Quantum Confinement Effects, Density of States, and Electronic Structure

As the structure size is reduced, more confinement leads to an increase in the effective band gap of the material and causes excited states to move higher in energy just as energy levels move higher in an infinite potential square well. Reduction of the well width, with decrease of the QD size, deeply affects the QD energy levels and exciton fine structure through the strong size dependence of the exchange interaction and confinement energy. There are variety of advantages inherent in using low-dimensional system for devices compared to using bulk materials, they include, depending on the specifics of the system, improved efficiency, speed, and gain and noise reduction as well as a reduced threshold current density and insensitivity to operating temperature. The last item is due to energy spacing in the strong confinement regime being larger than $k_B T$ (Kelly, 1995). Additionally, oscillator strength becomes more concentrated as dimensions is reduced just as absorption becomes spectrally discrete. Gain, therefore, is also repartitioned into discrete states. The transition rate per electron-hole pair stays the same even as dimensions is reduced (Peaker & Grimmeiss, 1991), which leads to very strong lasing capability (Rafailov et al., 2006).

An appropriate way to approach the subject of low-dimensionality is to explore the properties of the density of states (DOS), a quantity that dictates the oscillator strength of certain transitions. The DOS is derived from the number of states per energy per volume. This calculation is explicitly worked out in many modern solid state physics text books like Ref. (Grahm, 1999).

Table 2.1: Density of states (DOS) for electrons in the conduction band of a semiconductor. D stands for dimension. The 2 in the zero dimension case is just the spin degeneracy, since the volume part of the prefactor no longer exists. $\theta(E - E_n) = 0$ for $E < E_n$, and 1 for $E > E_n$.

D	Prefactor	Energy Dependence
3	$(2m^*)^{2/3} / 2\pi\hbar^3$	$\sqrt{E - E_n}\theta(E - E_n)$
2	$m^* / \pi\hbar^2$	$\theta(E - E_n)$
1	$\sqrt{2m^*} / \pi\hbar^2$	$\theta(E - E_n) / \sqrt{E - E_n}$
0	2	$\delta(E - E_n)$

Table 2-1 shows the DOS for zero to three dimensions (Grahm, 1999). It must be noted that the energy across the gap to the bottom of the conduction band is E_n . The DOS for electrons substitutes $E - E_n$ for E (for holes in the valence band, E is replaced by $E_n - E$). The DOS is zero in the energy gap, so all results are only suitable in the proper region: $E > E_n$ (or $E < 0$). Figure 2.1 shows the schematic representation of bulk and nanostructures and their DOS.

The absorption coefficient is proportional to the DOS, which indicates that, as the dimensionality is reduced, both oscillator strength and absorption become more and more spectrally concentrated. In our case of interest, 0-D, absorption only occurs at very discrete energies. This contrasts sharply with the absorption of bulk materials where the oscillator strength density is uniform throughout K-space. In the bulk, absorption increases rapidly for energies above the band gap (Brus, 1984).

There are typical simplifying assumptions used to calculate the exciton energy structure in QDs. The first is to assume a cubic lattice in perfectly spherical nanocrystal. In addition, only transitions near the band edge, which is to say, near the Brillouin zone center are considered. Subsequent perturbations to the model based on the lattice structure and non-sphericity of the QDs, among other things, are then included in the calculations to take into account a more realistic representation of the actual QDs. These perturbations help account for experimentally observed exciton fine structure. Figure 2.2 presents dispersion relations of electrons and holes for different dimensionalities.

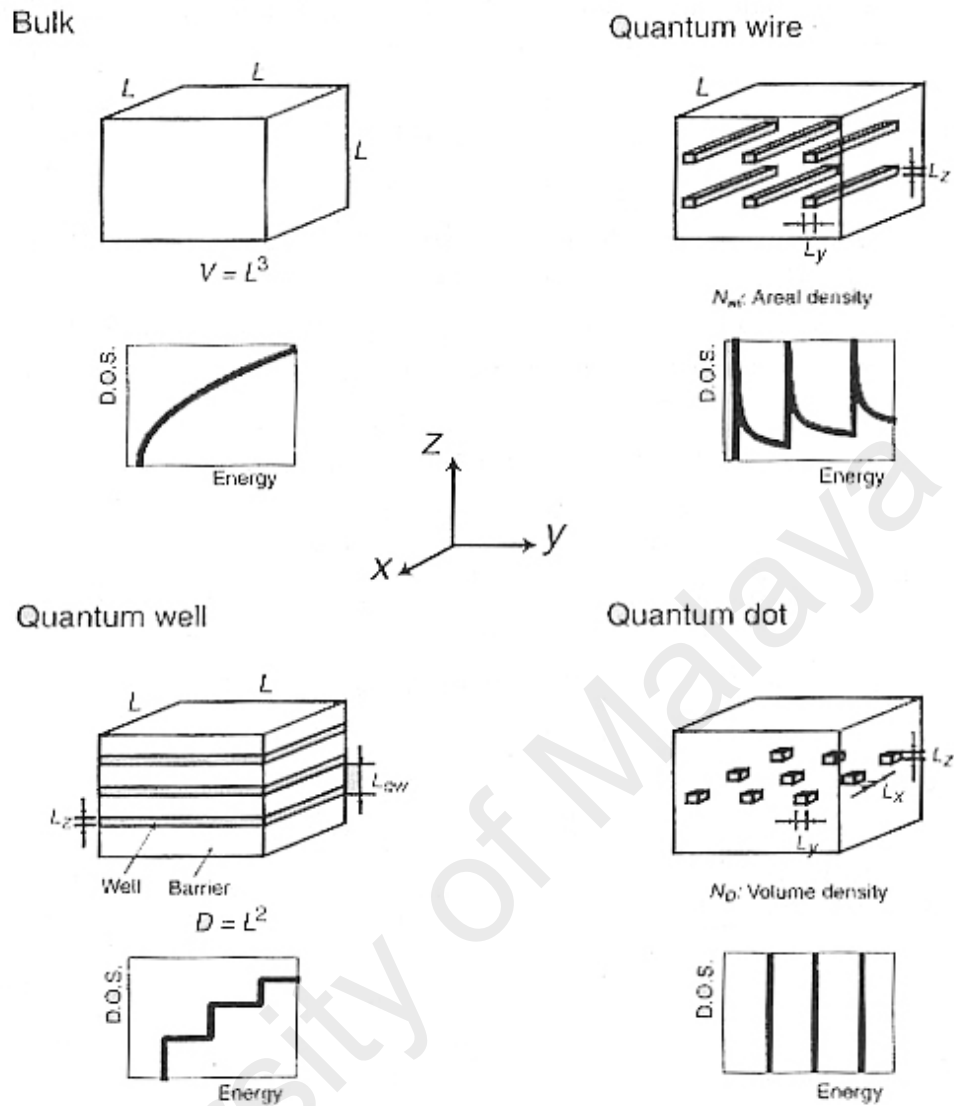


Figure 2.1: Schematic representation of bulk and nanostructures and their density of states (DOS).

Exciton confinement may be approached in a qualitative way. The exciton is confined by the band gap difference between the material making up the QD and the material surrounding the QD. The confinement increases the energy difference between the excited and ground states. The confinement strength for an exciton depends on the Bohr radius of the same exciton in the bulk semiconductor, α_B^{ex} , in conjunction with the size of the QD. The exciton Bohr radius is the hydrogen Bohr radius, α_B^H , modified by the exciton reduced mass m_r and the dielectric constant ϵ as $\alpha_B^{ex} = \alpha_B^H \epsilon / m_r$. Any externally applied forces cause the charge carrier, or carriers, to react with an effective mass.

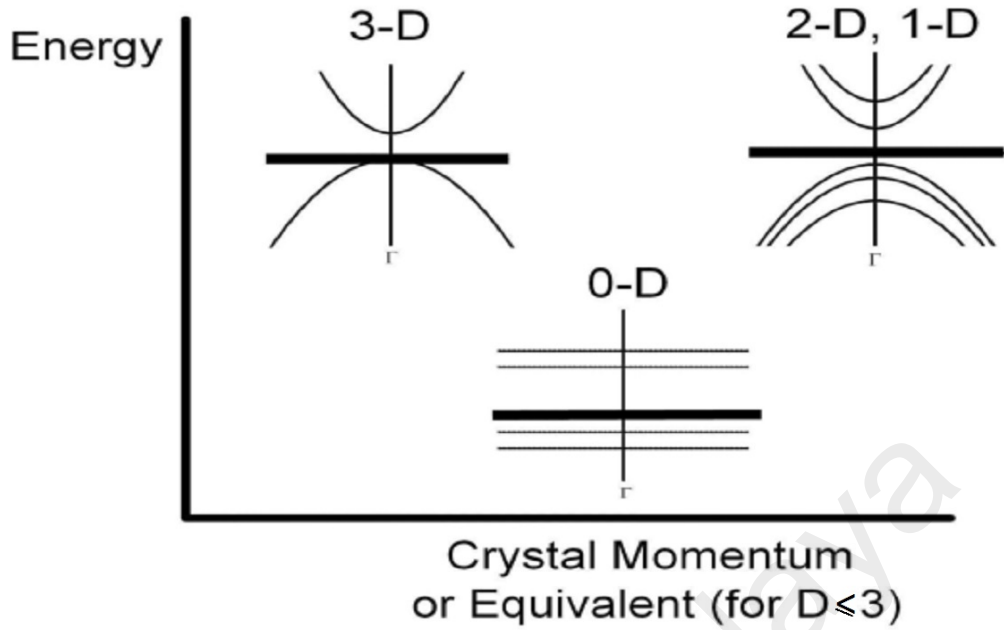


Figure 2.2: Dispersion relations of electrons and holes for different dimensionalities. For all cases, the dispersions above the thick horizontal zero energy line are for electrons and the dispersions below are for holes. In the 2-D and 1-D cases, the dispersion shown is for the confined direction(s) only, while the 3-D dispersion can be used for the unconfined direction(s).

Weak confinement occurs when the nanostructure diameter, $2R$, is much larger than α_B^{ex} . In this regime the confinement kinetic energy is smaller than the Coulomb interaction energy between the electron and hole.

When α_B^{ex} and $2R$ are comparable, the exciton exists in the intermediate confinement regime. This is the same as saying the confinement energy, arising from the exchange interaction (Chamarro, Gourdon, Lavallard, & Ekimov, 1995), is of the same order of magnitude as the Coulomb energy. The intermediate confinement regime is the cross over to the so-called molecular limit.

Strong confinement is the relevant case in this dissertation. The electron-hole pair is strongly confined when $2R$ is smaller than α_B^{ex} (α_B^{ex} is about 34 nm in bulk InAs). In this regime both carriers are independently confined. The exchange interaction is very strong since the electron and hole wave functions overlap dramatically, and, in fact, the confinement energy is much larger than the direct coulomb interaction. The Wannier exciton

(described by hydrogen Hamiltonian) can no longer reasonably be said to exist. Now an exchange interaction term must be included to the corresponding Hamiltonian and the direct coulomb term may be neglected. Therefore, when we use the term "excitons" in QDs, it is a misnomer and really refers to correlated electron-hole pairs in QDs. Confinement causes a larger band gap and atomic-like discrete states (see figure 2.3).

In QDs, the exciton experiences the potential of a 3-D quantum mechanical square well. Because QDs are usually overcoated with larger band gap semiconductor the excitons are in a finite potential well and can experience a small amount of wave function leakage outside the core of the QD, leading to a larger effective QD size. As indicated in Figure 2.3, energy bands for electrons in the conduction band (CB) and holes in the valence band (VB) break up into discrete, atomic-like levels.

In the 0-D case, in a 3-D square potential well with infinitely high barriers, the energy levels are obtained using (Harrison, 2005)

$$E_n = \frac{n^2 \hbar^2 \pi^2}{2m_{e,h}^* (2R)^2}, \quad n = 1, 2, 3, \dots \quad (2.1)$$

There are an infinite number of bound states. R is the half-width of the well (or the radius of the nanocrystal). In a real QD structure, there are finite number of bound states. As $R \rightarrow 0$, E_n diverges. In a real structure, the states converge to the Bloch states of the barrier material; in our case those of GaAs. Since the ground state energy is now larger than the intrinsic band gap, we can readily see that the confinement increases the energy of the exciton system. The exciton experiences an enhanced Coulomb (attractive, in this case) interaction. In particular, the exchange interaction plays a very larger role in the energy levels of strongly confined excitons. The exciton energy level structure consists of the transitions between discrete quantum levels of the electrons and holes. Among the various types of QDs, self-assembled QDs resemble most closely the ideal of

an artificial macroatom due to a strong carrier confinement and a resulting large energy level separation (Krügel, Vagov, Axt, & Kuhn, 2007).

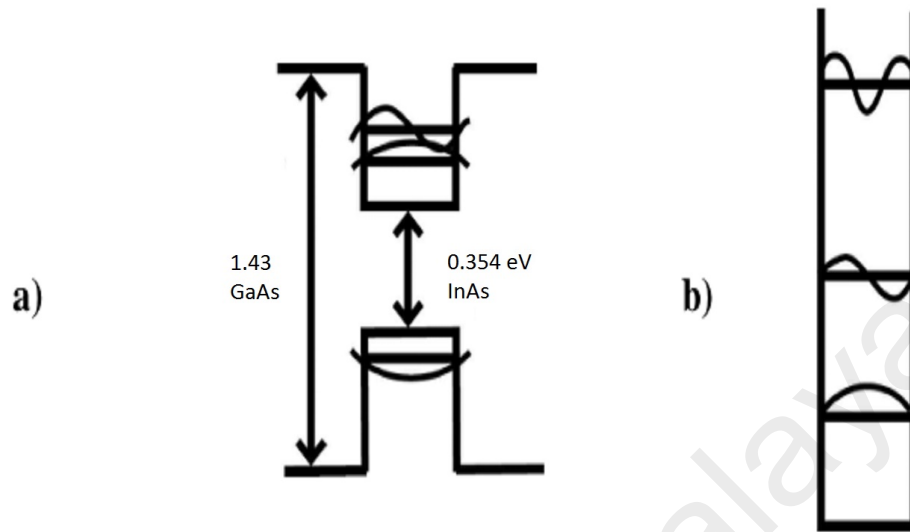


Figure 2.3: (a) Discrete energy levels in a InAs QD grown on GaAs substrate. Wave functions are shown for the states shown. The listed InAs bandgap (0.354 eV) is the intrinsic bandgap value at room temperature (b) Energy levels in a perfect square well with infinitely high potential barriers.

2.2 Phonons Dephasing in Quantum Dots

2.2.1 Types of Dephasing in Quantum Dots

Like any other semiconductor structure, the optical excitation of a semiconductor QD structure with a short coherent light pulse results in the creation of a coherent superposition between a generated pair of electron and hole at the CB and VB. Eventually, this phase coherence decays due to various interaction mechanisms of electrons and holes. A good knowledge of the dephasing is of utmost importance for many applications such as optoelectronic devices (Mukamel, 1995) or if semiconductor QDs are used as basic building blocks for quantum information and computation processing where the operation completely relies on the presence of coherence (Barenco, Deutsch, Ekert, & Jozsa, 1995; Zanardi & Rossi, 1998; Loss & DiVincenzo, 1998; Sherwin, Imamoglu, & Montroy, 1999; Tanamoto, 2000; Biolatti, Iotti, Zanardi, & Rossi, 2000). In general, exciton

coherence in QDs is too fragile to be used for these applications, although improvements in system design and QD fabrication may make QDs as viable components in the future. Other potential applications of particular interest include the storage of light, or of information transmitted by light. A slow exciton dephasing rate is required for these application. Slow light has also been demonstrated in GaAs quantum well system using the coherence of excitons (Ku et al., 2004). Another demonstrated phenomenon using exciton coherence is electromagnetically induced transparency (EIT) which based on exciton correlations was first observed in GaAs quantum wells (Phillips & Wang, 2002).

In higher dimensional systems, such as bulk semiconductors and quantum wells, the dephasing is mainly associated with a change of occupations due to transitions between different states, i.e., with reexcitation (thermalization), carrier relaxation, or recombination processes. This is called "impure dephasing". Impure dephasing, at least approximately, requires the conservation of energy between initial and final state which, in these cases of a continuous electronic spectrum, usually can be easily satisfied. In QDs, however, the electronic spectrum is discrete and it is much harder that this condition to be fulfilled. For the case of carrier-phonon interaction lack of this condition has resulted in the prediction of a so-called "phonon-bottleneck" in the relaxation (Bockelmann & Bastard, 1990; Benisty, 1995).

The dephasing of optical transitions, on the other hand, is not restricted to such real transitions; it is well known that virtual transitions which do not lead to a change of occupations also contribute to the dephasing of optical polarizations (Muljarov & Zimmermann, 2004; Muljarov, Takagahara, & Zimmermann, 2005; Muljarov & Zimmermann, 2007). This contribution leads to elastic scattering of AC phonons and is called "pure dephasing". Because of the large separation between the QD energy levels and the resulting strong reduction of real phonon-mediated transitions between these states, pure dephasing is of particular importance in small QDs at elevated temperatures where it dominates

the recombination process (Palinginis & Wang, 2001; Takagahara, 1999).

QDs behave in many aspects similar to atoms with a spectrum which can to a large extent be designed artificially. This fact together with their capability for integration make them very attractive for applications in quantum information and computation. However, the main difference compared to atoms is the coupling of their excitonic degrees of freedom to the lattice vibrations which typically results in much faster decoherence times. Typical dephasing times of single QDs have been found in experiments to be in the range from several hundreds of femtoseconds (Borri et al., 1999) at room temperature up to a few tens of picoseconds (Zrenner, 2000; Bonadeo et al., 1998; Gammon, Snow, Shanbrook, Katzer, & Park, 1996) at low temperatures. Using four-wave-mixing spectroscopy on an ensemble of QDs even dephasing times of more than 600 ps at 7 K have been observed (Borri et al., 2001).

2.2.2 Exact and Perturbative Approaches

In this part, we study the pure interactions of electrons and holes with AC and OP phonons by using exact (analytical) and perturbative approaches. To do so, we consider a strongly confined QD, i.e. a QD with well separated sublevels. We are interested in optical transitions from the uppermost level in the VB to the lowest CB state. The corresponding electronic degrees of freedom shall be represented by Fermi operators c^\dagger , c (d^\dagger , d) for the creation and annihilation of an electron (hole) in the lowest (uppermost) CB (VB) state. In addition to the dipole coupling to an external laser field the electron and hole interact with AC and OP phonons. The corresponding Hamiltonian is as:

$$\begin{aligned}
 H = & \hbar\Omega c^\dagger c - \mathbf{M}_0 \cdot \mathbf{E} \left(c^\dagger d^\dagger + dc \right) + \hbar \sum_{j,q} \omega_j(q) b_{j,q}^\dagger b_{j,q} \\
 & + \hbar \sum_{j,q} \left(\gamma_{j,q}^\ell b_{j,q} c^\dagger c - \gamma_{j,q}^h b_{j,q} d^\dagger d + H.C. \right), \quad (2.2)
 \end{aligned}$$

where $b_{j,q}$ and $b_{j,q}^\dagger$ denote Bose operators for the creation and destruction of a phonon in the phonon branch j with wave vector q and energy $\hbar\omega_j(q)$. The branch index j can represent either longitudinal-optical (LO) phonons, longitudinal-acoustic (LA) phonons, or transverse-acoustic (TA) phonons. It could also refer to interface or confined phonons. $\gamma_{j,q}^e$ and $\gamma_{j,q}^h$ are the QD-phonon coupling matrix elements for the electron and hole, respectively. Here, we restrict ourselves to the case of bulk phonon modes. $\hbar\Omega$ is the energy of the optical gap including the exciton binding energy but without polaronic renormalizations; note that we have taken the energy of the hole as the zero of energy. If the exciton binding energy is smaller than the separation of the single-particle energies the mixing of different states by the Coulomb interaction can be neglected and the excitonic effect reduces to a lowering of the gap by an amount given by the electron-hole Coulomb matrix element (Schmitt-Rink, Miller, & Chemla, 1987). Finally, \mathbf{M}_0 describes the dipole coupling to the laser field E . Without the dipole coupling the above Hamiltonian is known as the independent boson model (IBM) (G. Mahan, 1990). It has been well known for a long-time that the IBMs allow for exact results (Duke & Mahan, 1965; Wehner, Ulm, Chemla, & Wegener, 1998; V. Axt, Herbst, & Kuhn, 1999; Steinbach et al., 1999; Castella & Zimmermann, 1999).

We aim to analyze the dephasing properties of the optical polarization, induced by the coupling to phonons defined in Eq. 2.2. It should be noted that the carrier-phonon interaction in Eq. 2.2 does not lead to a change of the occupations of the electron or the hole level, because the interaction Hamiltonian commutes with the operators $c^\dagger c$ and $d^\dagger d$ for the respective occupations. Therefore, the model does not comprise an energy relaxation mechanism. Nevertheless, the phonon coupling may still cause to the pure dephasing (Mukamel, 1995). It has been found that pure dephasing may become the dominant dephasing mechanism at not too low temperatures for optically excited quantum wells (X. Fan, Takagahara, Cunningham, & Wang, 1998) and QDs (Palinginis & Wang, 2001).

Furthermore, the contribution of higher excited states to pure dephasing under realistic conditions is considerably smaller than the direct diagonal coupling even in QDs which are somewhat larger than those studied here. This finding also justifies our restriction to only two sublevels.

We still have to specify the QD-phonon coupling matrix elements $\gamma_{j,q}^{e(h)}$ for each interaction mechanism corresponding to the relevant phonon branches. Assuming that the QD and the surrounding barrier material do not differ significantly in their lattice and dielectric properties we can approximate the phonon modes with the corresponding three-dimensional bulk modes. Thus, the coupling matrix elements $\gamma_{j,q}^{e(h)}$ for the electron and hole can be separated into two factors, where the first depends on the specific coupling mechanism, whereas the second can be calculated from the wave functions $\psi^{e(h)}(\mathbf{r})$ of the electron and hole within the QD potential:

$$\gamma_{j,q}^{e(h)} = \phi_{j,q}^{e(h)} F_q^{e(h)}, \quad (2.3)$$

where $\phi_{j,q}^{e(h)}$ is the bulk coupling matrix element and with the form factors

$$F_q^{e(h)} = \int_V d^3r \left| \psi^{e(h)}(\mathbf{r}) \right|^2 e^{i\mathbf{q}\cdot\mathbf{r}}. \quad (2.4)$$

We consider the respective influences of three types of carrier-phonon coupling mechanisms: the polar optical coupling to LO phonons, the deformation potential coupling to LA phonons, and the piezoelectric coupling to LA and TA phonons. The polar optical interaction is accounted for by the usual Fröhlich-coupling (Krummheuer, Axt, & Kuhn, 2002):

$$\phi_{LO,q}^{e(h)} = i \left[\frac{e^2 \omega_{LO}(q)}{2\hbar \epsilon_0 V} \left(\frac{1}{\epsilon_\infty} - \frac{1}{\epsilon_s} \right) \right]^{\frac{1}{2}} \frac{1}{q}, \quad (2.5)$$

where ϵ_s and ϵ_∞ are the static and high-frequency dielectric constants, respectively, ϵ_0 de-

notes the vacuum susceptibility, e represents the elementary charge, V is a normalization volume, and $q = |\mathbf{q}|$ is the modulus of \mathbf{q} . Finally, $\omega_{LO}(q)$ is the angular frequency (the dispersion relation) of the LO phonons.

The coupling to AC phonons may be through the deformation potential or the piezoelectric coupling. While the deformation potential primarily couples the electronic system to LA phonons, the piezoelectric scattering couples it to both LA and TA phonons; usually the TA piezoelectric scattering is considerably larger due to the smaller sound velocity (G. D. Mahan, 1972). Accounting for both piezoelectric and deformation potential interactions the coupling $\varphi_{AC,q}^{e/h}$ to AC phonons is given by (G. D. Mahan, 1972; G. Mahan, 1990)

$$\varphi_{AC,j,q}^{e/h} = \frac{1}{\sqrt{2V\eta\hbar\omega_j(q)}} \left[qD_j^{e(h)} + iM_j(\hat{\mathbf{q}}) \right], \quad (2.6)$$

where η is the density of the semiconductor material, $D_j^{e(h)}$ denotes the deformation potential constant for electron (hole), and M_j is the piezoelectric coupling and $\hat{\mathbf{q}}$ is the unit vector in the direction of \mathbf{q} . The branch index j runs over the longitudinal and transverse modes and the constants $D_j^{e(h)}$ are nonzero only for the LA mode. The piezoelectric coupling would in principle result in an anisotropy (G. D. Mahan, 1972; G. Mahan, 1990) that is, usually neglected. Instead, an effective isotropic model is constructed that is obtained by averaging over the angles. More specifically, it is only the square of $M_j(\mathbf{q})$ that introduces the anisotropy in our final results as will become evident later. Therefore an angle average over this quantity is required. For a crystal with zinc blende structure the averaging yields (G. D. Mahan, 1972)

$$\frac{1}{4\pi} \int_0^{2\pi} d\phi \int_0^\pi d\theta \sin(\theta) M_j^2(\hat{\mathbf{q}}) = A_j \left(\frac{2ee_{14}}{\epsilon_s \epsilon_0} \right)^2, \quad (2.7)$$

where e_{14} is the piezoelectric coefficient and A_j are mode dependent geometrical factors that can be found, e.g., in Ref.(G. D. Mahan, 1972).

It should be noted that all three coupling matrix elements are valid only in the long-wavelength limit because they are derived on the basis of a continuum model for the phonons. However, even in the case of the smallest QDs the coupling only extends over a relatively small part of the Brillouin zone where the dispersion relations do not deviate much from the continuum case so that these matrix elements can still be considered to be good approximations (Krummheuer et al., 2002).

It is possible to derive closed-form analytical expressions for a number of linear or nonlinear δ -like signals. In order to do so, in this case we have to determine the complex polarization vector \mathbf{P} to linear order in the laser field. As \mathbf{P} is related to the off-diagonal element $Y = \langle dc \rangle$ of the electronic density matrix by

$$\mathbf{P} = \mathbf{M}_0 Y, \quad (2.8)$$

we have to calculate the linear response of Y . It is convenient to follow the generating functions approach outlined in Refs. (V. Axt et al., 1999; Steinbach et al., 1999) for a single mode system and in Ref. (V. M. Axt & Mukamel, 1997) for the multimode case. Specialized to the present model the generating function method involves the following steps: First one has to set up the Heisenberg equation of motion for the generating function (Krummheuer et al., 2002) as

$$Y(\{\alpha_{j,q}, \beta_{j,q}\}) = \left\langle d c e^{\sum_{j,q} \alpha_{j,q} b^\dagger} e^{\sum_{j,q} \beta_{j,q} b} \right\rangle. \quad (2.9)$$

Up to linear order in the laser field the resulting equation is closed. It is a first-order partial differential equation that can be easily solved (V. Axt et al., 1999; Steinbach et

al., 1999; V. M. Axt & Mukamel, 1997). The polarization is obtained from $\mathbf{P} = \mathbf{M}_0 Y = \mathbf{M}_0 Y (\{\alpha_{j,q}, \beta_{j,q} = 0\})$. As a result of this procedure it is found in agreement with previous results (Wehner et al., 1998) that the linear polarization induced by a δ -like laser pulse, i.e., $\mathbf{E}(t) = \mathbf{E}_0 \delta(t)$, which is polarized parallel to \mathbf{M}_0 is given by (Krummheuer et al., 2002)

$$\begin{aligned} P(t) &= \theta(t) \frac{i|\mathbf{M}_0|^2 \mathbf{E}_0}{\hbar} e^{-i\bar{\Omega}t} \exp \left[\sum_{j,q} |g_{j,q}|^2 \left(e^{-i\omega_j(q)t} - n_j(q) \left| e^{-i\omega_j(q)t} - 1 \right|^2 - 1 \right) \right] \\ &= \varepsilon_0 \chi(t) \mathbf{E}_0, \end{aligned} \quad (2.10)$$

where

$$n_j(q) = \frac{1}{e^{\hbar\omega_j(q)/k_B T} - 1} \quad (2.11)$$

stands for the equilibrium phonon occupation at temperature T , $g_{j,q} = \gamma_{j,q}^X / \omega_j(q)$ is a dimensionless coupling strength where $\gamma_{j,q}^X = \gamma_{j,q}^e - \gamma_{j,q}^h$ being the exciton coupling matrix element, the pulse area is $\theta(t) = 2\mathbf{M}_0 \cdot \mathbf{E}_0 / \hbar$ and

$$\bar{\Omega} = \Omega - \sum_{j,q} \omega_j(q) |g_{j,q}|^2 = \Omega - \sum_{j,q} \frac{(\gamma_{j,q}^X)^2}{\omega_j(q)} \quad (2.12)$$

represents the polaron shifted transition frequency. For optical phonons the quantity $S = \sum_q |g_{LO,q}|^2$ is usually called the Huang-Rhys parameter (Schmitt-Rink et al., 1987; Huang & Rhys, 1950). In the derivation of the linear polarization in Eq. 2.10 it has been assumed that before the laser excitation the system is in the electronic ground state and that the initial statistical operator for the phonon system corresponds to an equilibrium distribution at temperature T and is thus given by

$$\hat{\rho}_{ph} = \frac{\exp(-H_0^{ph}/k_B T)}{\text{Tr}(e^{-H_0^{ph}/k_B T})}, \quad (2.13)$$

where $H_0^{ph} = \hbar \sum_{j,q} \omega_j(q) b_{j,q}^\dagger b_{j,q}$. The linear susceptibility $\chi(t)$ defined in Eq. 2.10 contains contributions from all possible multiphonon processes. It is valid for arbitrary coupling strengths and temperatures. Using Eq. 2.10 it is easy to determine the linear absorption spectrum as the absorption coefficient at frequency ω is directly proportional to the imaginary part $Im[\chi(\omega)]$ where $\chi(\omega)$ is the Fourier transform of $\chi(t)$. As energy relaxation is not included in the model, the corresponding spectrum may contain unbroadened lines. The numerical results have been obtained by multiplying $\chi(t)$ by a factor e^{-t/t_0} and then performing the Fourier transformation. In order to seeing the effect of pure dephasing separately from other dephasing mechanisms the rather long time constant of $t_0 = 500$ ps has been chosen (Krummheuer et al., 2002).

It is usually not possible to obtain exact results for models with more complicated coupling schemes. In order to approximate the desired spectrum, perturbative approaches are mostly used in these cases. It is therefore instructive to compare the exact result in Eq. 2.10 with the outcome of commonly used approximations. A widely used approach for quantum kinetic studies of the carrier-phonon interaction is called the correlation expansion (Schilp, Kuhn, & Mahler, 1994; Kuhn, 1998). Within this approach one starts with the equation of motion for the off-diagonal element Y of the density matrix which reads

$$\frac{\partial}{\partial t} Y = -i\Omega Y + \frac{i}{\hbar} \mathbf{M}_0 \cdot \mathbf{E} - \mathbf{i} \sum_{j,q} \left[\gamma_{j,q}^X Y_{j,q}^{(-)} + \gamma_{j,q}^{X*} Y_{j,q}^{(+)} \right], \quad (2.14)$$

where the phonon-assisted density matrices $Y_{j,q}^{(-)}$ and $Y_{j,q}^{(+)}$ are defined as $Y_{j,q}^{(-)} = \langle dcb_{j,q} \rangle$ and $Y_{j,q}^{(+)} = \langle dcb_{j,q}^\dagger \rangle$. Unlike the equation of motion for the generating function $Y(\{\alpha_{j,q}, \beta_{j,q}\})$, Eq. 2.14 is not closed; instead it is the starting point for an infinite hierarchy of higher-order phonon-assisted density matrices. The correlation expansion approach is based on truncation of the phonon-assisted hierarchy by factorizing higher order phonon-assisted density matrices on a chosen level. Mostly the truncation is invoked after

the first step, i.e., one writes down equations of motion for the density matrices $Y_{j,q}^{(-)}$ and $Y_{j,q}^{(+)}$ and factorizes the density matrices with double phonon assistances, e.g., according to $\langle dcb_{j,q}^\dagger b_{j,q} \rangle \approx \langle dc \rangle \langle b_{j,q}^\dagger b_{j,q} \rangle$. This procedure results in the following equations for the phonon-assisted density matrices:

$$\begin{aligned}\frac{\partial}{\partial t} Y_{j,q}^{(-)} &= -i [\Omega + \omega_j(q)] Y_{j,q}^{(-)} - i \gamma_{j,q}^{X*} [1 + n_j(q)] Y, \\ \frac{\partial}{\partial t} Y_{j,q}^{(+)} &= -i [\Omega - \omega_j(q)] Y_{j,q}^{(+)} - i \gamma_{j,q}^X n_j(q) Y.\end{aligned}\quad (2.15)$$

The correlation expansion truncated at this level yields results that are correct up to second order in the phonon coupling. The solution of Eqs. 2.14 and 2.15 may be obtained by taking the Fourier transforms of these equations. From the relation between Y and the polarization one can then directly read off the linear susceptibility in frequency space:

$$\chi(\omega) = \frac{|\mathbf{M}_0|^2}{\hbar \epsilon_0} \left[\Omega - \omega - i\gamma_0 + \sum_{j,q} \frac{|\gamma_{j,q}^X|^2 [1 + n_j(q)]}{\omega + i\gamma_0 - \Omega - \omega_j(q)} + \sum_{j,q} \frac{|\gamma_{j,q}^X|^2 n_j(q)}{\omega + i\gamma_0 - \Omega + \omega_j(q)} \right]^{-1}.\quad (2.16)$$

Here, a finite minimal spectral width given by $\gamma_0 = 1/t_0$ has been introduced, which corresponds to the finite decay also used in the Fourier transform of the exact result (Krummheuer et al., 2002).

A spherical GaAs QD which is confined in the vertical (z) direction by infinite barriers while in the lateral (x, y) plane with a parabolic confinement potential is assumed. Taking the same potential shape for electrons and holes results in a lateral extension of the hole wave function which is by a factor of $(m_e/m_h)^{(1/4)} \approx 0.87$ smaller than the electron wave function. The vertical size of the QD is given by the well width while the lateral size is defined as the radius where the electron density is reduced to half its maximum value. In order to include the dispersion of the LO phonon branch, the shape of the dispersion relation obtained from a standard diatomic linear chain model adjusted

to the phonon dispersion relation given in the literature has been taken (Adachi, 1994). All phonon branches have been taken as isotropic. The resulted dispersion relations of the phonons are shown in figure 2.4 together with the angular integrated effective form factors (Krummheuer et al., 2002)

$$F^{eff}(|\mathbf{q}|) = \int_0^{2\pi} d\phi \int_0^\pi d\theta \sin(\theta) |F_q^e - F_q^h|^2 \quad (2.17)$$

corresponding to three different QD sizes $r = 3, 6,$ and 9 nm . In the case of the polar interaction mechanisms this effective form factor directly determines the phonon q space region to which the QD is effectively coupled. For deformation potential interaction due to different deformation potentials of electrons and holes a somewhat different quantity should appear in the integral, but also in this case Eq. 2.8 provides a good estimate of the range of relevant q values. Physically, the mathematical idealization of a δ -shaped laser pulse means that the pulse should be shorter than the characteristic time scales introduced by the interaction mechanisms. These time scales are 1-2 ps for the GaAs QD. Thus, the ultrafast limit will be satisfied in this QD for pulse durations of a few hundreds of femtoseconds (Krummheuer, Axt, & Kuhn, 2005).

It is seen in the figure that the form factors extend to higher q values with decreasing QD size. For large QDs the assumption of a constant LO phonon frequency, as it is usually applied in systems of higher dimensionality, is quite well satisfied while QDs below about 10 nm start to feel the dispersion. This means that the combined electron-LO-phonon system changes from a purely discrete system into one with a continuum part in the spectrum. In the case of AC phonons the relevant range of phonon frequencies increases with reduction of QD size leading to an effectively increasing width of the continuum in the spectrum. Figure 2.4 shows that the assumption of linear dispersion of both LA and TA phonons is well satisfied. Nevertheless, for the numerical evaluation of

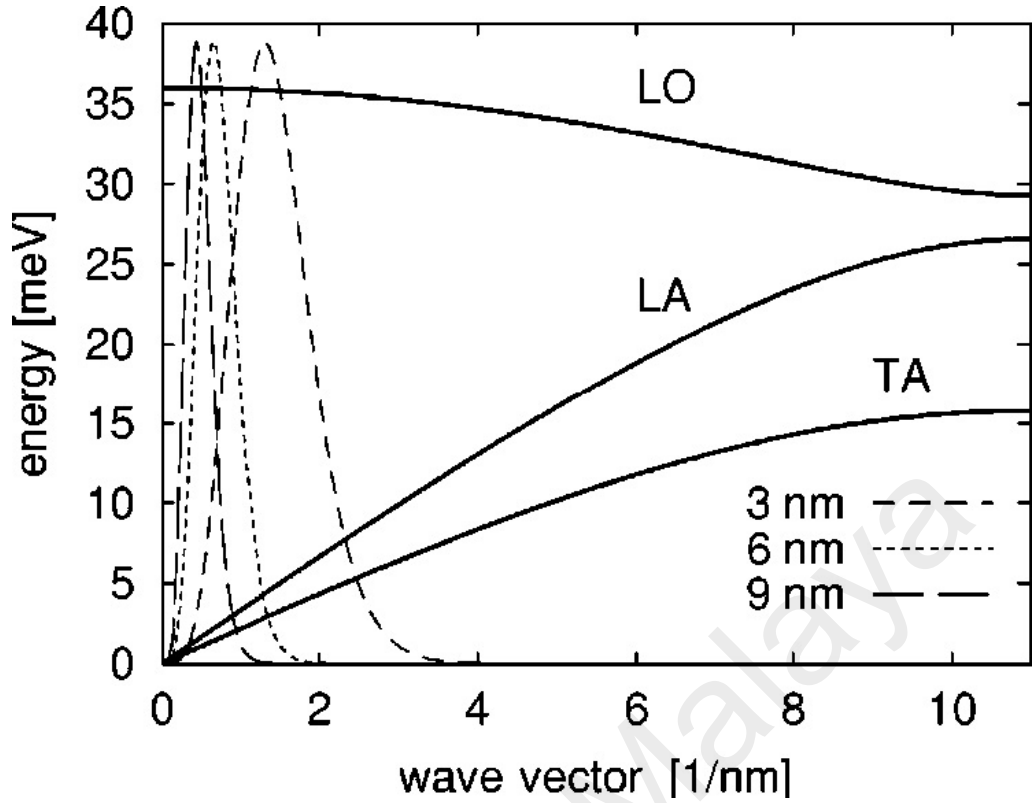


Figure 2.4: Dispersion relations of the LO, LA, and TA phonons taken in the calculations as well as normalized effective form factors [see Eq. 2.17] describing the coupling of QDs with three different sizes $r = 3, 6,$ and 9 nm to the various phonon modes (Krummheuer et al., 2002).

the formulas the full dispersion has always been taken.

Lattice anisotropy lifts the degeneracy inherent in the two branches of TA and TO. Structures with partly ionic binding are anisotropic. A more realistic picture of the dispersion in this case is shown in figure 2.5 (Klingshirn, 1995).

2.2.3 Dephasing due to Optical-Phonon Interaction

We first concentrate on the real time dynamics of the optically induced polarization in the electron-LO-phonon system. If the dispersion of the phonons is neglected it is clearly seen from Eq. 2.10 that the result is exactly the same as in the case of single phonon mode with the effective interaction matrix element $\gamma_{eff} = \sqrt{\sum_q |\gamma_q^e - \gamma_q^h|^2}$. This single mode model has been studied in detail in view of nonlinear optical signals as well, in particular the coherent control of phonon quantum beats in four-wave mixing signals, and the role of a stronger electron-phonon coupling in Refs. (V. Axt et al., 1999;

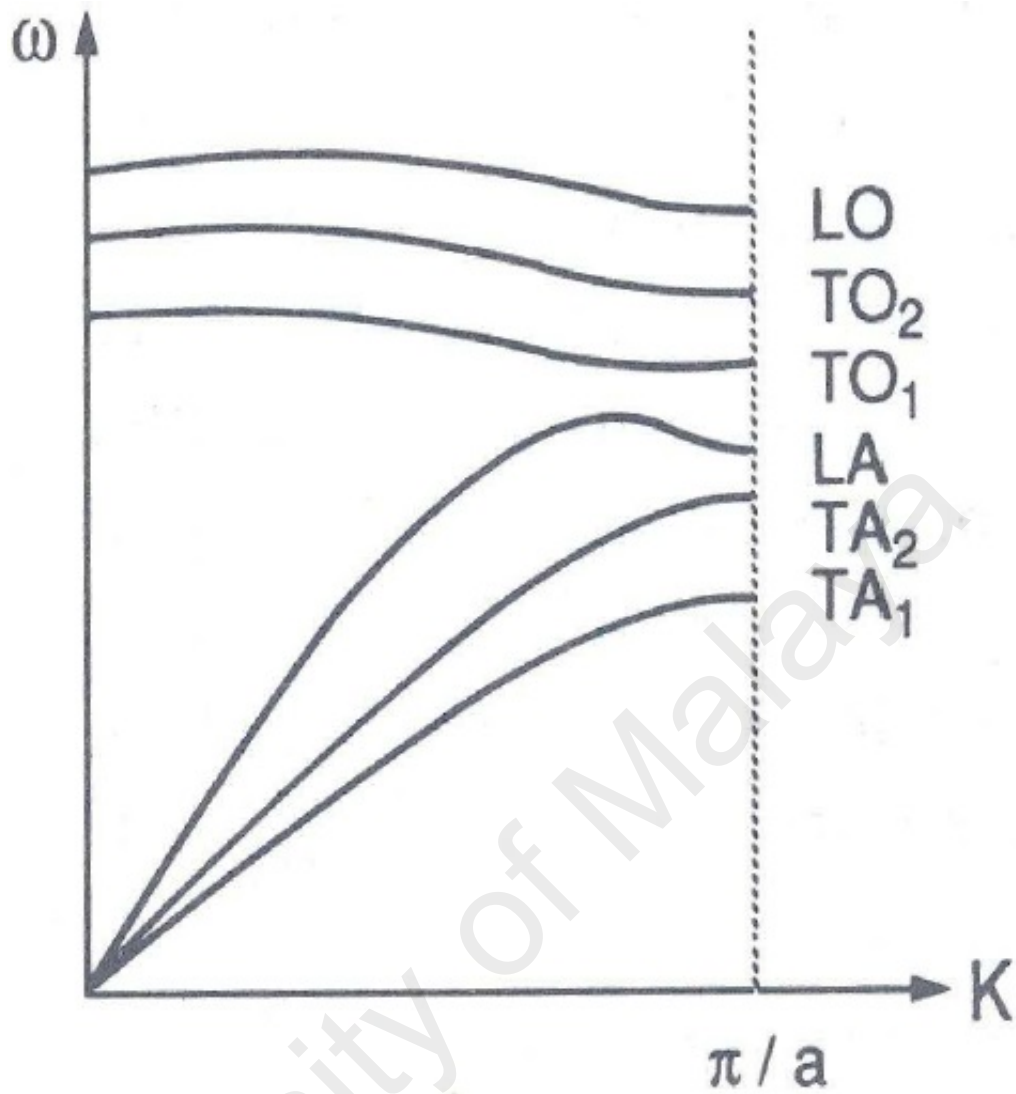


Figure 2.5: The degeneracy has been lifted in acoustic and optical dispersion curves by an anisotropic lattice. a represents the lattice constant (Klingshirn, 1995).

Steinbach et al., 1999; Castella & Zimmermann, 1999; Kuhn, Axt, Herbst, & Binder, 1999). The optical polarization resulting from the excitation with an optical pulse with a δ -function-like shape in time as well as the corresponding absorption spectrum are shown for the case of a 6-nm QD at temperature 300 K in figure 2.6(a) and (b). The optical polarization exhibits quantum beats with the phonon frequency; no decay is present. The spectrum consists of a series of δ -function peaks at the zero-phonon transition and at integer multiples of the phonon frequency above and, for nonzero temperature, below that transition. The weights of the various lines depend on temperature and, through the effective coupling constant (or the Huang-Rhys parameter), on the QD parameters. A closed-form

analytical expression in terms of Bessel functions is presented in Refs. (Schmitt-Rink et al., 1987; Huang & Rhys, 1950). Such phonon-assisted optical transitions in QDs have been observed in resonant Raman scattering (Scamarcio, Spagnolo, Ventruti, Lugará, & Righini, 1996) as well as in photoluminescence and photoluminescence-excitation spectroscopy (Heitz, Mukhametzhanov, Stier, Madhukar, & Bimberg, 1999; Heitz, Born, et al., 2000). The spectrum of the electron-phonon system is completely discrete without phonon dispersion. If the dispersion of the LO phonons is taken into account the system now has continuum parts and therefore decay processes are possible. The resulting optical polarization and the corresponding absorption spectra for the 6-nm QD are plotted in figures 2.6(c) and (d) under the same excitation condition as above, Figs. 2.5(e) and (f) display the results for a 3-nm QD. We clearly see that the phonon quantum beats in the optical polarization (Figs. 2.5(c) and (e)) are damped. The typical time scale for this damping is about 50 ps in the case of the 6-nm QD while it is about 10 ps for the 3-nm QD. This strong size dependence can be well understood from figure 2.4 which shows that the form factor of the small QD effectively probes a considerably broader range of frequencies leading to a faster decay due to destructive interference of the various q components in the polarization. The spectra now consist of the unbroadened (ZPL) as well as LO phonon sidebands which are broadened according to the frequency range of phonons which effectively couple to the exciton. For a better comparison in Figs. 2.6(d) and (f) the $|n|$ -phonon emission or absorption sideband have been shifted towards the ZPL by subtracting or adding $n\hbar\omega_{LO}(0)$ and they have been multiplied by the respective factors given in the caption. Here, $n > 0$ refers to emission and $n < 0$ to absorption sidebands. Since $\omega_{LO}(0)$ is the maximum frequency of the LO phonons the emission sidebands are now completely below the ZPL while the absorption sidebands are above this line. It is clearly seen that the $|n| = 2$ sidebands, corresponding to two-phonon transitions, exhibit a width which is twice the width of the $|n| = 1$ sidebands. Furthermore, the widths in the

case of the 3-nm QD are approximately a factor of 5 larger than those for the 6-nm QD corresponding to the enhanced damping of the quantum beats discussed above. The small but nonzero width of the ZPL is due to the additional phenomenological dephasing time $t_0 = 500$ ps which has been introduced to perform the Fourier transformation.

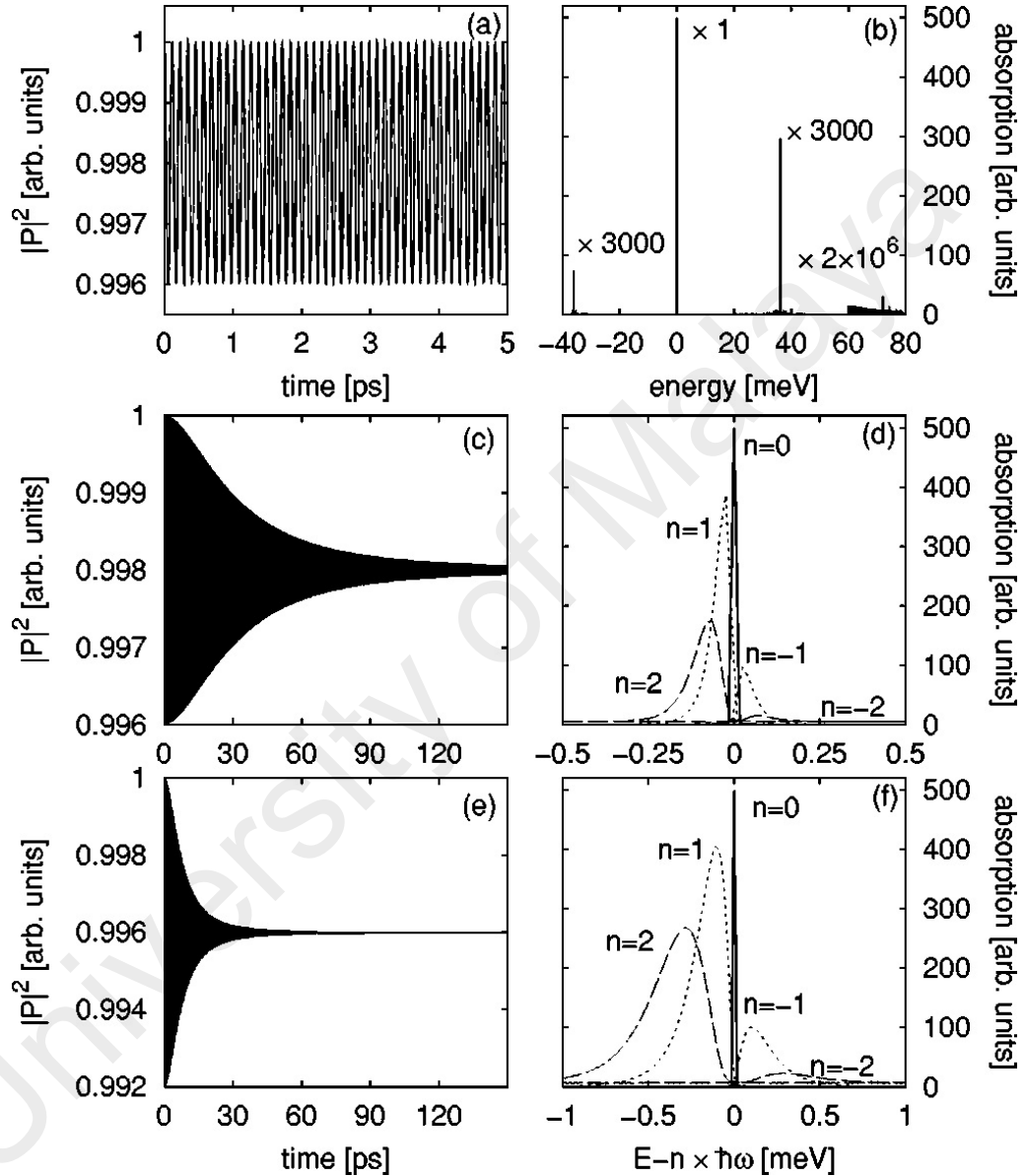


Figure 2.6: Optical polarizations induced by a δ -function-shaped optical pulse (left column) and absorption spectra (right column) for a QD interacting with optical phonons at a temperature of 300 K. The calculation results without phonon dispersion have been shown in the parts (a) and (b), in parts (c) and (d) [(e) and (f)] the results including dispersion are plotted for a 6-nm (3-nm) QD. The spectra of the n -phonon sidebands due to phonon emission ($n > 0$) or phonon absorption ($n < 0$) are shifted by $-n\hbar\omega_{LO}$ towards the ZPL. In part (d) they are multiplied by the factors 3×10^3 ($|n| = 1$) and 2×10^6 ($|n| = 2$); the corresponding factors in part (f) are 3×10^4 ($|n| = 1$) and 4×10^7 ($|n| = 2$) (Krummheuer et al., 2002).

2.2.4 Dephasing due to Acoustic-Phonon Interaction

AC phonons are characterized by a continuous spectrum starting at zero frequency. Therefore the phonon sidebands approach the ZPL and, under suitable conditions, may result in a broadened ZPL (Duke & Mahan, 1965). In figure 2.7 the optical polarization and the absorption spectrum are shown for a 3-nm QD at three different temperatures $T = 4, 77, \text{ and } 300 \text{ K}$, as obtained from calculations including piezoelectric (Figs. 2.7(a) and (b) and deformation potential (Figs. 2.6(c) and (d) coupling. Interestingly, it is found that in all cases the polarization remains at a finite value at long times corresponding to an unbroadened ZPL. This can be understood from the q dependence of the matrix element in the limit of small q values.

According to figure 2.4 it is found that for small q : $\omega_j(q) \rightarrow \omega_{LO}$ for the optical branch and $\omega_j(q) \rightarrow v_j q$ for the acoustic branches, where v_j are the respective sound velocities. Therefore, according to Eq. 2.6 the bulk coupling matrix elements of deformation couplings $\gamma_{j,q}^X = \gamma_{j,q}^e - \gamma_{j,q}^h$ scale as \sqrt{q} and the ones of piezoelectric coupling are proportional to $1/\sqrt{q}$. In general, the deformation potential for electrons and holes are different and the form factors of both carrier types approach unity for $q \rightarrow 0$, therefore the total coupling constant is proportional to q^2 . The bulk piezoelectric coupling constant, on the other hand, being a polar mechanism, has exactly the same value for electrons and holes. Then, the form factors of the electron and hole exactly cancel at $q = 0$. The lowest order in difference of the form factors is proportional to q^2 and thus the total coupling constant is proportional to $q^{3/2}$. A vanishing coupling constant for $q \rightarrow 0$ gives rise to an unbroadened ZPL (Krummheuer et al., 2002).

It can be seen in Figs 2.7(a) and (c) that the dynamics due to interactions with AC phonons exhibits a pronounced temperature dependence. At low temperatures the line is strongly asymmetric; there is only a contribution on the high-energy side of the ZPL

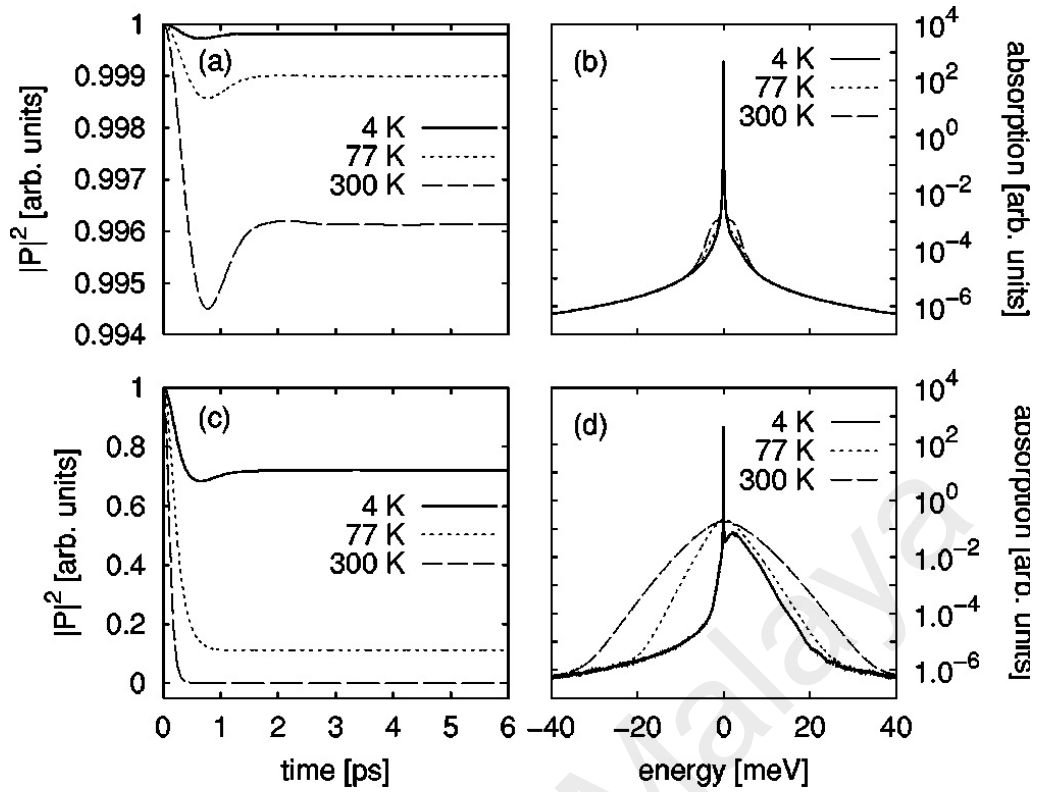


Figure 2.7: Optical polarizations induced by a δ -function-shaped optical pulse (left column) and absorption spectra (right column) for a 3-nm QD interacting with AC phonons at three different temperatures. Parts (a) and (b) refer to piezoelectric coupling, parts (c) and (d) to deformation potential coupling (Krummheuer et al., 2002).

due to phonon emission. With increasing temperature phonon absorption processes come into play and the line becomes more symmetric. Furthermore, the weight of the ZPL is reduced resulting in lower long time values of the polarization. By comparing the results for deformation potential and piezoelectric coupling it is found that the deformation potential contribution is clearly dominant, in agreement with Ref. (Takagahara, 1999). Even at 300 K piezoelectric coupling reduces the initial coherence by less than one percent. This is due to the large electron-hole overlap which strongly reduces all polar interaction mechanisms.

2.2.5 Dephasing due to Both Optical- and Acoustic-Phonon Interaction

In this section, the results of the previous sections are combined by taking into account all three types of interaction mechanisms simultaneously. Figure 2.8 shows the optical polarizations and the corresponding absorption spectra at three different tempera-

tures of $T = 4$, 77 , and 300 K for the case of a 6-nm QD (Krummheuer et al., 2002). The overall dynamics of the polarization is dominated by deformation potential interaction. There are superimposed quantum beats due to LO phonon coupling, which are visible only at the lowest temperature due to the different scales of the polarization axes. The lineshape around the ZPL is due to AC phonon interaction, as discussed in the previous section. This line is repeated with a decreasing strength, at multiples of the LO phonon frequency. Thus each LO phonon sideband acquires a background due to AC phonon interaction. Very similar spectra consisting of a narrow ZPL and a broad background have recently been observed in four-wave-mixing experiments on InGaAs QDs (Borri et al., 2001).

In figure 2.9 the polarization curves and absorption spectra at the same temperatures as above are plotted for a QD of 3 nm size (Krummheuer et al., 2002). The extension of the form factor to larger q values results in a pronounced increase in the widths of the AC phonon contribution in the spectra and a substantially faster initial decay of the polarization which now occurs on a time scale of 100 fs. In particular at 300 K the acoustic wings of the different LO phonon sidebands now merge and result in a smooth spectrum up to high energies.

2.2.6 Comparison with the Perturbative Approach

A particular feature of the IBM used here is the fact that it can be solved exactly. This feature is typically lost if the model is extended, e.g., by taking into account excited exciton states and phonon-induced transitions between these states or excitation by more realistic pulse shapes like Gaussian pulses. In such cases approximate techniques have to be used. The present model provides the opportunity to compare the exact results with results obtained from a correlation expansion as it is often applied in more complex and higher dimensional systems and therefore it allows us to clearly analyze the deviations

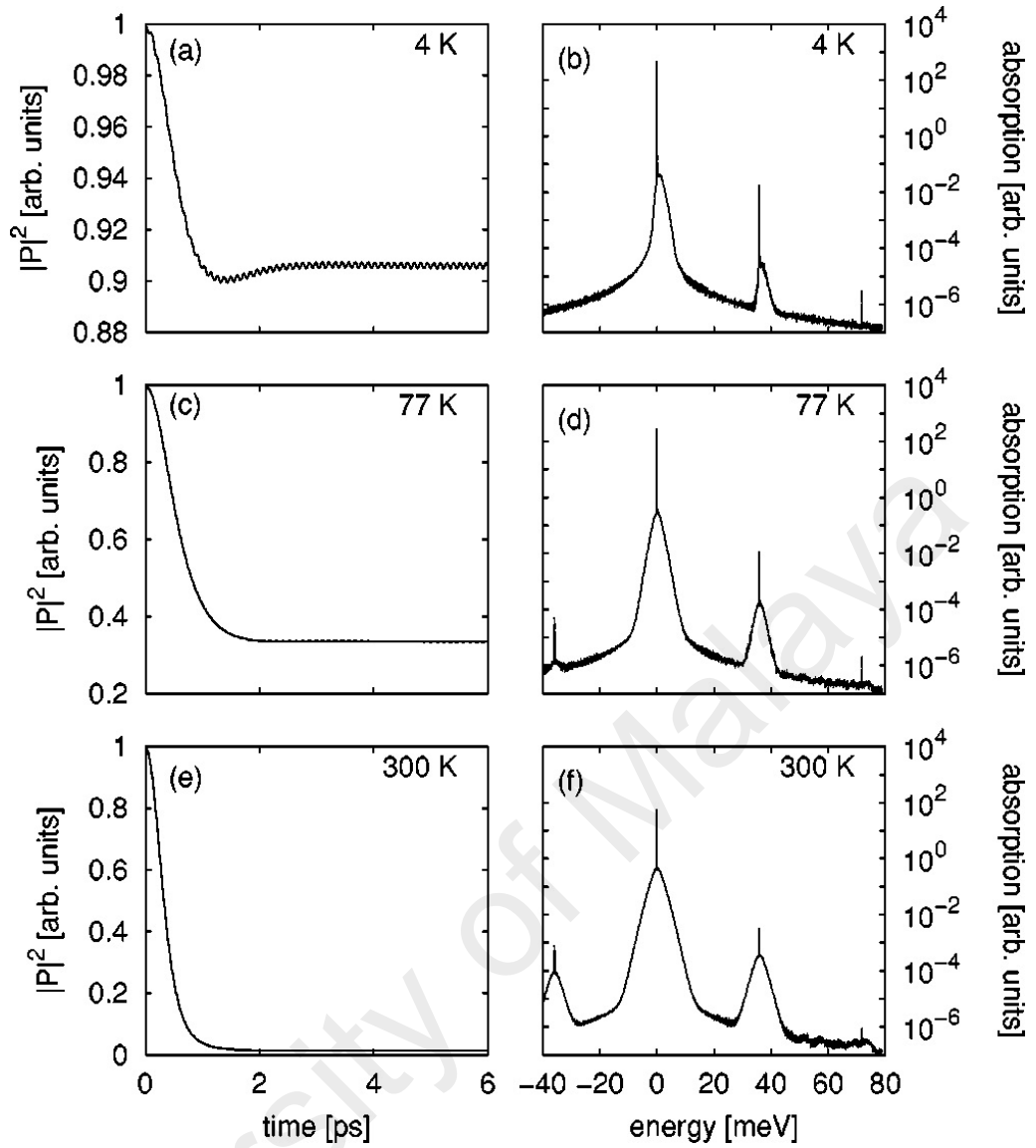


Figure 2.8: Optical polarizations induced by a δ -function-like optical pulse (left column) and absorption spectra (right column) for a 6-nm QD interacting with OP and AC phonons at three different temperatures $T = 4, 77, \text{ and } 300 \text{ K}$ (Krummheuer et al., 2002).

between exact and approximate solutions, which in most other cases is not possible. The absorption spectra of a 3-nm QD obtained from the exact solution (left column) with the spectra obtained from the correlation expansion up to second order in the interaction matrix element (Eq. 2.16) at temperature 4 K for the individual interaction mechanisms as well as for the complete model have been plotted in figure 2.10 (Krummheuer et al., 2002).

In the case of the polar optical interaction (Figs. 2.10(a) and (b)), there is a good agreement for the ZPL and for the first phonon sideband. Of course, the second side-

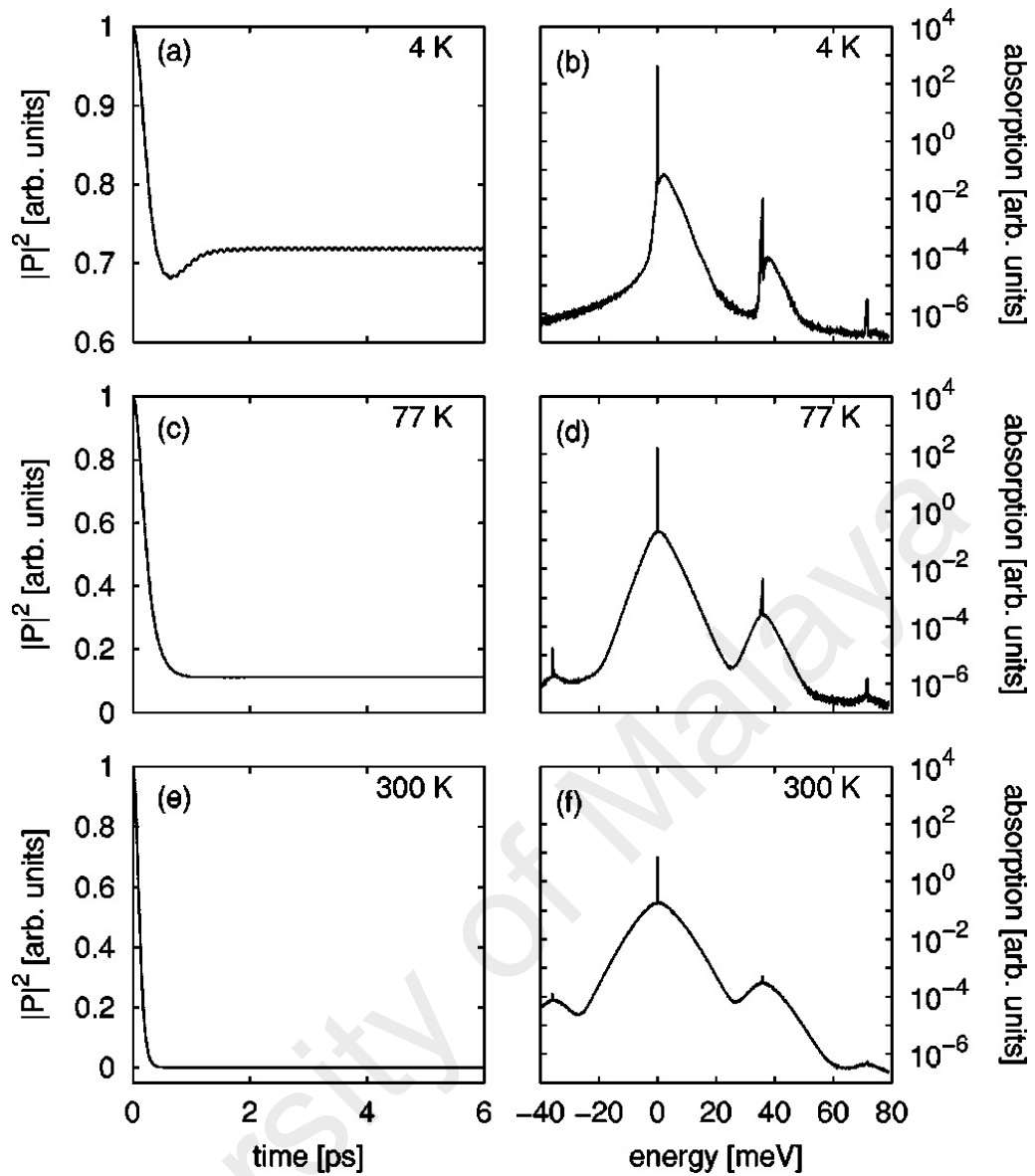


Figure 2.9: Same as figure 2.8 but for a 3-nm QD (Krummheuer et al., 2002).

band, involving a two-phonon transition, is absent in the perturbative result because multiphonon processes are neglected on this level. As has been shown in the previous sections the piezoelectric interaction is very weak. In particular at low temperatures it gives only a very small contribution to the spectrum. Therefore it is not surprising that multiphonon processes are negligible and exact and perturbative results are in good agreement (Figs. 2.10(c) and (d)). In the case of deformation potential coupling (Figs. 2.10(e) and (f)) it is found that both the height and the width of the spectrum corresponding to exact and approximate solutions are in quite good agreement. However, there are remarkable differences in the detailed shape. First, in the perturbative result the dip above the ZPL is much

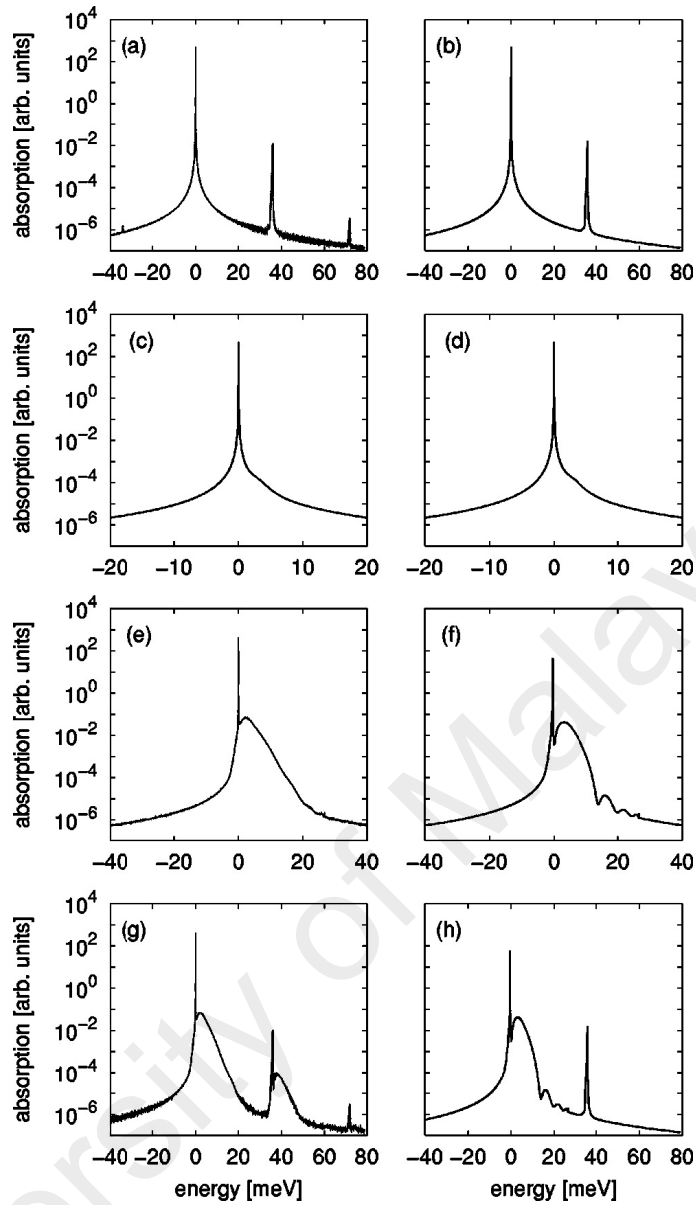


Figure 2.10: Comparison of the exact absorption spectra (left column) with those obtained from a correlation expansion up to the second order in the coupling matrix elements (right column) for (a) and (b) polar optical, (c) and (d) piezoelectric, and (e) and (f) deformation potential, as well as for (g) and (h) the combination of all mechanisms at a temperature of 4 K (Krummheuer et al., 2002).

more pronounced than in the exact result. This is due to the fact that one-phonon transitions with a small wave vector are strongly suppressed because, as already discussed above, in this range the matrix element is proportional to \sqrt{q} . Therefore positions in the immediate vicinity of the ZPL can only be reached by at least two-phonon processes which again are absent in the perturbative treatment. Second, the approximate absorption spectrum exhibits a series of dips above 10 meV which is absent in the exact result.

These dips originate from the form factor, in particular from the Fourier transform of the cosine wave function in the z direction. They are absent if in this direction a Gaussian wave function is also used. In the exact result these dips are obviously washed out due to multiphonon processes. Third, the approximate spectrum exhibits a sharp cutoff at an energy of 26 meV corresponding to the maximum energy of LA phonons (see figure 2.4) because higher energies are not accessible in a one-phonon process. Finally, in Figs. 2.10(g) and (h) the spectra of the full model are compared. Besides the features already discussed the most pronounced difference is the missing AC background of the one-LO phonon sideband. Of course, this background involves at least one OP and one AC phonon and therefore it is at least related to two-phonon processes and thus it is absent in the perturbative treatment which takes into account only one-phonon processes.

2.2.7 Comparison with Experiment

The coupling of a QD to its semiconductor matrix drastically influences the properties of the emitted photons. In particular, the excitonic recombination process is accompanied by a lattice distortion and the generation of polarons (Krummheuer et al., 2002; Förstner, Weber, Danckwerts, & Knorr, 2003). This scattering process between the exciton and the phonon leads to a dephasing that results in a reduction of the coherence length of the photons. However, most quantum optic experiments, such as those on indistinguishable photons or quantum cryptography systems using double Mach-Zehnder interferometers (Gisin, Ribordy, Tittel, & Zbinden, 2002), require long coherence length. Also, theory predicts that exciton-phonon scattering may be the limiting factor for generation of entangled photon pairs (Hohenester, Pfanner, & Seliger, 2007; Carmele, Milde, et al., 2010). On the other hand, luminescence broadening by phonon scattering is useful in experiments on the strong light-matter coupling: The phonon-assisted luminescence can be amplified by the cavity and can be observed even in micropillars containing only

a single QD (Reithmaier et al., 2004). Hence, to study the strong light-matter coupling theoretically (Laussy, del Valle, & Tejedor, 2008; Tarel & Savona, 2010), a complete luminescence spectrum, including phonon scattering, must be used.

Phonon scattering has been mostly studied until now on polar CdSe QDs, in which the phonon coupling is much stronger than, for example, in the non-polar InGaAs QD system. The latter one, however, was most successful for device applications in the past decade, such as for the generation of electrically driven single photons and entangled photon pairs (Shields, 2007; Bimberg et al., 2009; Salter et al., 2010). Photoluminescence measurements on ensembles of InGaAs QDs lead to the conclusion that coupling to optical phonons might be enhanced in QDs as compared to bulk material (Heitz et al., 1999). However, the line shape of a single LO phonon replica had never been studied experimentally before 2011. In this respect, electrically pumped single QDs allow us to study the exciton-phonon interaction on the fundamental level: A single electron-hole pair recombines under generation of a single photon and a phonon (Stock et al., 2011).

A number of theoretical approaches exist to describe, at least in part, exciton- and electron-LO phonon interaction. One of them suggested the importance of a second-order elastic interaction between QD charge carriers and LO phonons (Uskov, Jauho, Tromborg, Mørk, & Lang, 2000). The resulting Gaussian shape of the LO replica was, however, found to be an artifact (Muljarov & Zimmermann, 2006; Uskov, Jauho, Tromborg, Mørk, & Lang, 2006). Another strong coupling model suggested a coupling of LO phonons to excited electronic states in the QD or the wetting layer (Muljarov & Zimmermann, 2007, 2008), leading to a more triangular shape of the LO phonon replica. In 2010, the first exact solution of the electron-OP phonon interaction in the quantum optical regime was presented (Carmeletti, Richter, Chow, & Knorr, 2010). None of the models had been compared with experimental data on single QDs until 2011. A report on a comprehensive study of both exciton-AC and -OP phonon interaction in a highly efficient single-photon

source, based on an electrically driven single InGaAs/GaAs QD was presented in 2011 (Stock et al., 2011): By comparing experimental data with calculated spectra, it was demonstrated that phonon coupling strongly depends on a correct and not simplified description of the charge-carrier wave function, phonon dispersion, and the lifetime of the phonons. The devices consisted of InGaAs/GaAs QDs grown by molecular beam epitaxy with a density of $5 \times 10^8 \text{ cm}^{-2}$ embedded in a p-i-n diode structure. Electrical pumping of efficiently only one single QD was achieved by restricting the injected current through an AlO_x aperture. In order to increase the photon out-coupling efficiency, a microcavity consisting of 12 and 3 distributed Bragg mirror layers on the bottom and top of the device, respectively, was grown. The resulting cavity has a center energy at 1.292 eV with a quality factor $Q=140$. A detailed description of the device and single-photon emission at a pump repetition rate of up to 1 GHz can be found in Ref. (Lochmann et al., 2009). The electroluminescence (EL) of the device was measured in a microluminescence setup, consisting of a microscope objective [numerical aperture (NA)=0.8], a triple monochromator with a spectral resolution of $40 \mu\text{eV}$, and a liquid-nitrogen-cooled charged couple device detector. In order to obtain spectra with a sufficient large intensity dynamic range, a series of spectra with 10 s integration time each was summed up. The electroluminescence from only one QD could be studied in detail, due to the strong electrical current confinement in the devices.

At a bias of 1.41 V and a injected current of 5 nA, a series of 300 spectra of the exciton emission line for each given temperature were summed up. In a semi-logarithmic plot (figure 2.11), a clear broadening of the emission is visible. The features at -7 , -5 , and -3.5 meV from the dominating zero phonon line (ZPL) can be attributed to the recombination of other complexes in the QD or to weak luminescence from other QDs. These features vary from device to device and are therefore not related to phonon scattering. These features influence the phonon sidebands and mainly contribute to the difference

between theory and experimental data as shown in figure 2.11(b). The temperature dependence of the exciton peak position has been removed from figure 2.11(a) by plotting the spectra on a relative energy scale. In the experiment the linewidth of the ZPL is limited by the spectral resolution of the setup.

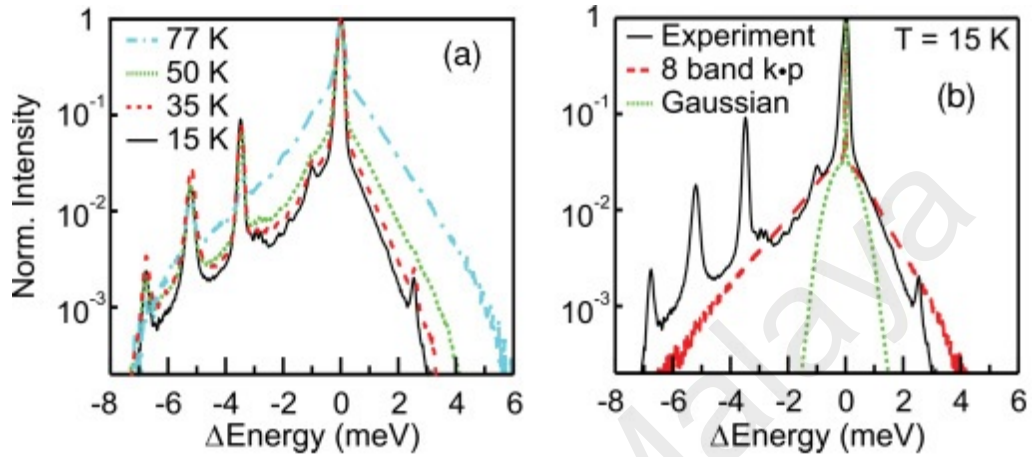


Figure 2.11: Semilogarithmic plot of the EL intensity of a single QD. (a) With increasing temperature the line broadening increases due to stronger AC phonon interaction. (b) Comparison of the measured line shape with two calculated spectra, using alternatively a simple Gaussian (red dashed curve) and a realistic eight-band k-p wave function (green dotted curve) (Stock et al., 2011).

At low temperatures (15 and 35 K), the broad sidebands of the ZPL are asymmetric due to spontaneous phonon emission, with larger intensity at the lower-energy side. For increasing temperatures (50 and 77 K) the broadening increases and becomes symmetric. Such properties of the sidebands are typical for AC phonon scattering: By emission or absorption of a phonon, the energy of the emitted photon will be reduced or increased, respectively, by the phonon energy. At lower temperatures, the phonon density n_{ph} is low and therefore, due to spontaneous processes, phonon emission [$\sim (n_{ph} + 1)$] of an (AC) phonon has a higher probability than the absorption ($\sim n_{ph}$). Hence, the resulting spectrum is asymmetric. With increasing temperature the phonon density increases ($n_{ph} \gg 1$) and the probabilities for emission and absorption become equal, resulting in a symmetric spectrum.

For the theoretical description of the luminescence spectrum, including AC phonon

scattering, the exactly solvable independent boson model was applied (Krummheuer et al., 2002; Förstner et al., 2003). This model describes the lowest optically active QD transition as a two-level system coupled to phonons by band diagonal interaction. For the numerical evaluation, the well-known GaAs bulk material parameters for the phonon dispersion and the deformation potential coupling were used (Krummheuer et al., 2002; Dachner et al., 2010). Therefore, the line shape of the calculated spectra depends only on the electron-phonon coupling matrix elements that are determined essentially by the wave functions of the electrons and holes in the QD. To gain insight into the microscopic interaction and its sensitivity to the character of the electronic wave functions, Gaussian wave functions (i.e., ground state of a harmonic oscillator)(Wojs, Hawrylak, Fafard, & Jacak, 1996) and wave functions calculated for a realistic QD using eight-band $k\cdot p$ theory (Schliwa, Winkelkemper, & Bimberg, 2007) were compared. Figure 2.11(b) shows the measured spectrum at 15 K in comparison to the theoretical line shape for both wave-function types. For a Gaussian wave function, often used in theoretical studies, the phonon scattering is strongly underestimated for any energy. In contrast to this, $k\cdot p$ wave functions reproduce the measured spectra very well. The main difference between the two wave-function models is their real space behavior, transferred to the decay of the coupling matrix elements in momentum space: In contrast to Gaussian functions, the more realistic eight-band $k\cdot p$ wave functions allow for an interaction at larger wave numbers. Therefore, larger phonon energies have more impact on the AC phonon sidebands. The large difference between the two calculated spectra clearly demonstrates the importance of realistic wave functions already for a qualitatively correct description of electron-phonon scattering. The measured spectra can be reproduced by using realistic eight-band $k\cdot p$ wave functions for temperatures up to 60 K. Another important result of the modeling of the measured spectra is that they are perfectly reproduced by using GaAs bulk phonon parameters only.

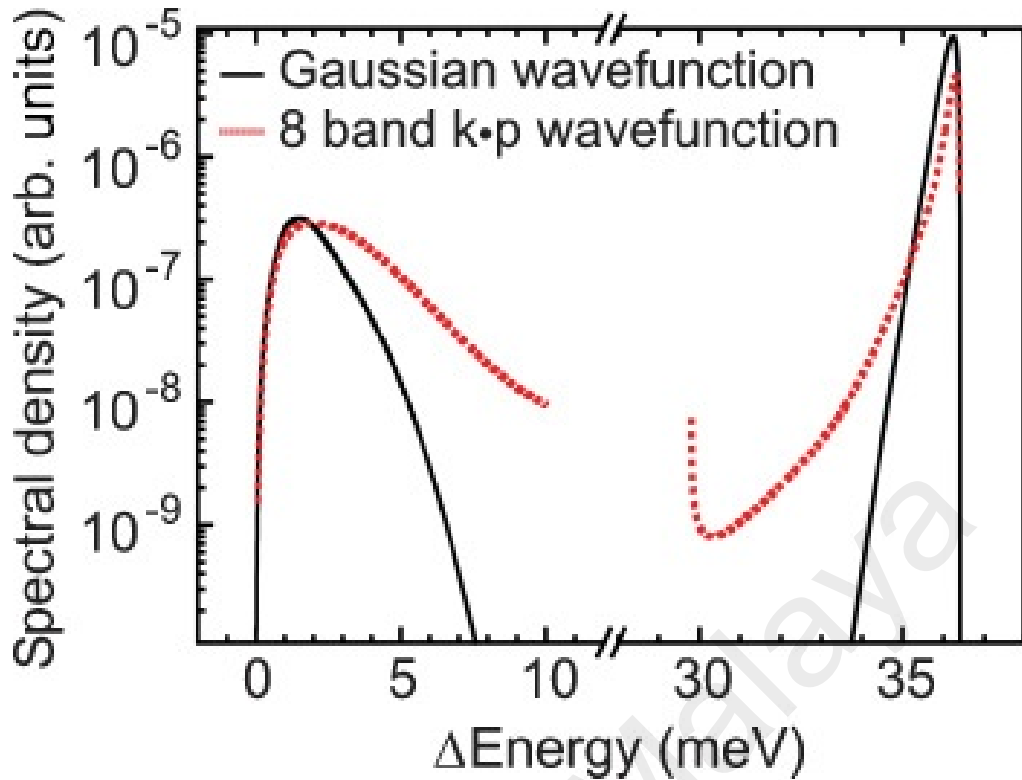


Figure 2.12: Comparison of the spectral phonon density for two different wave functions. For AC phonons (energy $< 10 \text{ meV}$) the Gaussian wave function (black curves) decreases too quickly, leading to an underestimation of the phonon scattering (Stock et al., 2011).

The influence of the wave function is also visible in figure 2.12, where we show the phonon spectral density (containing coupling strength, interaction matrix elements, and phonon dispersion) of the electron-phonon interaction for the two different wave functions. The spectral density at small energies ($< 10 \text{ meV}$) decays for a Gaussian wave function much faster than for the k·p wave function. This results in the energy space can be directly translated to momentum space via the linear dispersion. Even a change of the width of the Gaussian curve never reproduces the measured spectra as well as the eight-band k·p wave function.

In order to study scattering processes of optical (OP) phonons experimentally, a series of 1450 spectra of the LO-phonon replica, resulting in a five times longer integration time than for the AC phonon, was summed up. Figure 2.13(a) compares two spectra of the same QD under the same bias condition: The black dotted curve shows the exciton emission line around 1.3035 eV. For the second spectrum, the energy scale [on the top of

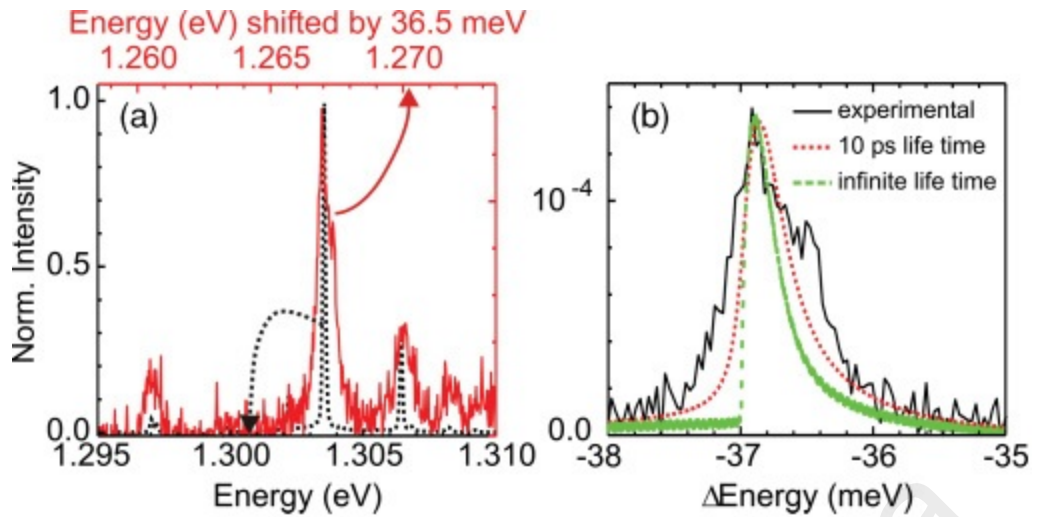


Figure 2.13: OP phonon replica of a single QD. (a) The black dotted curve shows three ZPL lines, each one having a replica, separated by 36.5 meV (red spectra, top energy scale). (b) Comparison of the LO line shape between experimentally measured (black) and calculated spectra with (red dotted curve) or without (green dashed curve) taking into account a finite lifetime of the phonon of 10 ps. A finite lifetime of the phonon provides a better description of the broad line shape of the LO phonon replica (Stock et al., 2011).

figure 2.13(a)] is shifted by 36.5 meV compared to the bottom scale. Three pronounced peaks are visible in this spectrum, and each of them has a “counterpart” in the black spectrum. For other QDs, we also found for almost every intense luminescence line a “counterpart” separated by around -36 meV.

These corresponding lines are attributed to the recombination of an exciton accompanied by the emission of an LO phonon. For different QDs, the phonon energy varies between -35.7 and -36.6 meV with no systematic trend, as compared to the ZPL energy. These energies are comparable to the LO phonon energy of strain-free GaAs bulk material of 36.59 meV. The variation of the phonon energy can be explained by differences in the strain of the GaAs material induced by size and composition of the actual QD (Heitz et al., 1996). At the energy of the InAs LO phonon replica (30.3 meV), within the intensity dynamic of five orders of magnitude, no luminescence is observed. This is in agreement with the results for AC scattering. Consequently, the electrons and holes in the QDs interact predominantly with phonons from the surrounding GaAs. The InAs phonon interaction is at least one order of magnitude less. No emission caused by local-

ized InAs-type phonons in the QD is observed.

We focus on the coupling strength of the exciton-LO phonon interaction. The coupling strength is usually described by the Huang-Rhys factor, given by the intensity ratio of the ZPL I_{ZPL} and the n th phonon replica I_n (at zero temperature) by $I_n/I_{ZPL} = S^n e^S / n!$ (Huang & Rhys, 1950; Landolt-Börnstein, 1987). In figure 2.13 the intensity is normalized with respect to the ZPL. Both the emission lines are located outside the cavity resonance in the stop band, so their intensities can be compared. The intensity of the LO phonon replica is about four orders of magnitude lower than the ZPL intensity, resulting in a Huang-Rhys factor of $S \approx 10^{-4}$. This value is one order of magnitude less than for GaAs bulk phonons, indicating a reduced phonon coupling in this electrically pumped single QD. The Huang-Rhys factor from the calculated spectral density (figure 2.12) has additionally been derived (Stock et al., 2011; May & Kuhn, 2000). The calculations yields factors of $S \approx 10^{-4}$, confirming the experimental result.

The line shape of the phonon replicas enables us to access the coupling mechanism between the exciton and the LO phonon: The recombination of an electron-hole pair in a QD has a discrete energy and the linewidth of the ZPL is only limited by the lifetime of the exciton to a few μeV (Borri et al., 2001). Therefore, any broadening of the luminescence upon generation of an LO phonon is due to the intrinsic phonon properties or coupling of the phonons to other modes. Figure 2.13(b) shows the LO phonon replica at larger spectral resolution. The resulting full width at half maximum of $700 \mu eV$ is well above the spectral resolution and about one hundred times larger than for the ZPL. Hence, LO phonons of varying energies are generated during the recombination processes in the same single QD. Also, the line shape is again slightly asymmetric, showing a faster decay on the low-energy side than on the high-energy side. This specific line shape is consistent with a broadening mechanism that results from a realistic wave-number-dependent LO phonon dispersion $\omega_{LO}(q)$ beyond the Einstein model $\omega_{LO} = const$: In such a dispersion

relation, a higher energy corresponds to a smaller momentum. Since the electron-phonon coupling favors low-momentum phonons, the generation of higher-energy phonons has a larger probability than that of lower-energy phonons, and thus yields an asymmetry of the line shape.

For a quantitative understanding of this coupling mechanism, we compare the experimental results with a model (figure 2.13), where LO phonon assisted luminescence spectra are calculated using the independent boson model and approximating the real optical-phonon dispersion by a cosine. This approximation agrees very well with the experimentally observed dispersion (Landolt-Börnstein, 1987). For the coupling matrix elements, Gaussian wave functions and eight-band k-p wave functions, respectively, again are compared. In contrast to the AC phonon coupling, the influence of different wave functions is less pronounced. In figure 2.12 it can be seen that the LO phonon part of the spectral density shows a much faster decay than the acoustic phonon part. Hence the LO phonon replicas for Gaussian and eight-band k-p wave functions differ only slightly. For a complete description of the LO phonon-scattering process, a finite lifetime of 10 ps ((Rudin, Reinecke, & Bayer, 2006) and (Bhatt, Kim, & Stroscio, 1994)) for the LO phonons has also been included. The resulting LO replica in figure 2.13(b) reproduces very well the measured line shape, whereas a line shape with neglected phonon lifetime is too narrow. A perfect fit to the experimental data results in a phonon lifetime of 5 ps. Additional phonon replica broadening, due to the influence of excited and wetting layer states, was predicted for the more enhanced electron-phonon coupling in CdSe systems (Muljarov & Zimmermann, 2007). A significant influence in the GaAs material system in the calculations could not be observed.

The AC and OP phonon scattering on the most fundamental level, at which a single photon and a phonon are generated by the recombination of a single exciton in a single electrically driven InGaAs/GaAs QD, were presented. By comparing experimental and

calculated spectra, we conclude that (i) GaAs bulk material phonon modes represent the dominant broadening mechanism; (ii) localized InAs-type phonons are not observed; (iii) a large LO replica broadening of $\approx 700 \mu eV$ is induced by interaction with large wave-number phonons, having a finite lifetime; (iv) k-p wave functions are essential for the description of the excitons; and (v) the independent boson model using these wave functions provides the proper wave-vector dependence for a quantitative understanding of the experimental results.

2.3 Quantum Dot-Cavity Quantum Electrodynamical Systems

Solid-state cavity quantum electrodynamic (cQED) systems, consist of a solid-state emitter like single semiconductor quantum dot (QD) coupled either resonantly or non-resonantly to single mode of an optical nano (micro) cavity, have promising properties for both fundamental and practical applications; A scalable QD-cQED platform, where the interaction between the single photon with the QD can be engineered and controlled to a high degree, can realize a perfect single photon source (Somaschi et al., 2016; He et al., 2013; Gazzano et al., 2013; Michler et al., 2000) which is a crucial requirement for quantum computation and information processing (Knill et al., 2001; O'Brien et al., 2009). It is also applicable for low-threshold and nano-scale lasers (Noda, 2006; Strauf & Jahnke, 2011; Michler, 2003) as well as tests of fundamental aspects of quantum mechanics (Haroche & Raimond, 2006). Since the QD is a solid structure, QD-cQED systems are inherently coupled to the environment (phonon bath) and the interactions of the QD carriers with phonons play an important role in the QD-cavity dynamics (Ates et al., 2009; Kaer, Gregersen, & Mork, 2013; Nysteen, Kaer, & Mork, 2013; Roy & Hughes, 2012). Resonating light in a cavity provides an efficient way of enhancing light-matter interaction since the coupling to one localized mode can be strongly enhanced compared to all other modes. It has been well understood that the light-matter (QD-cavity) coupling

efficiency can be improved by structuring the cavity, which is the essence of modern research in solid-state cQED (Lodahl et al., 2015). In photonic nanostructures the cavities can have very small mode volumes, which enhances the interaction strength. The two decisive cQED figures of merit are the quality factor Q and the effective mode volume V of the localized quasimode. In the following, various QD-cQED systems, including a nanophotonic cavity and single QD, with high- Q and small- V cavities are reviewed.

Micropillar cavities have been widely exploited as high- Q cavities. They can be fabricated by epitaxial growth of alternating layers of refractive indexes n_1 and n_2 (e.g., GaAs and AlGaAs) each of thickness $\lambda/4n_i$, $i = 1, 2$, and by subsequently etching a micropillar with a typical diameter of a few microns and a height of around $10 \mu\text{m}$ (Reithmaier et al., 2004). The alternating layers form a Bragg mirror with a reflectivity that is controlled by the number of layers. An extended spacer layer of length, e.g., $\lambda = n_1$ in between two such Bragg mirrors forms a highly localized cavity mode where QDs can be positioned; see figure 2.14(a). The two Bragg mirrors are often grown with different numbers of layers in order to make a one-sided cavity consisting of a highly reflecting mirror and an out-coupling mirror with an optimized transmission. The diameter of the micropillar is chosen to restrict the lateral extension of the guided mode confined in the high-index material, which leads to a small mode volume. Choosing the diameter below $1 - 2 \mu\text{m}$, however, is found to significantly reduce Q due to the sensitivity to sidewall roughness (Gazzano et al., 2013). Typical mode volumes accessible in micropillar cavities are at the level of $\sim 10 (\lambda/n)^3$ and tapered cavities have recently been proposed as a way of localizing light even better (Lermer et al., 2012). Highly localized cavity modes can be obtained by introducing defects in photonic-crystal membranes and a multitude of different design possibilities have been explored in the literature. This flexibility of being able to tailor a cavity mode by controlling the geometry of the photonic crystal and the defect area indeed provides a very important asset of the photonic crystal platform. One of the most success-

ful and important designs so far is the L3 cavity that is obtained from a 2D triangular lattice in a photonic-crystal membrane by leaving out three holes [cf. figure 2.14(b)], leading to a mode volume of less than $\sim (\lambda/n)^3$. It was realized that the Q factor can be significantly boosted by more than an order of magnitude by displacing the holes at each end of the cavity by just a fraction of a lattice constant, whereby leakage to radiation modes can be strongly suppressed (Akahane, Asano, Song, & Noda, 2003). This remarkable sensitivity to the detailed design reflects the large potential of photonic-crystal cavities. A cavity Q factor of 2×10^6 has been observed experimentally in modified L3 cavities in silicon at a wavelength of $1.55 \mu\text{m}$ (Lai et al., 2014). Lower Q factors are generally observed for GaAs cavities since they are matched to the shorter wavelength of InGaAs QDs of around 950 nm and therefore more sensitive to fabrication imperfections, residual scattering, and absorption due to the embedded QDs, as well as bulk and surface absorption, which is more pronounced at shorter wavelengths (Michael et al., 2007). A cavity Q factor of 3×10^4 has been reported in a GaAs L3 cavity containing a single QD (Hennessy et al., 2007). A number of different photonic-crystal cavity structures have been considered that potentially have higher Q factors including waveguide heterostructures (Song, Noda, Asano, & Akahane, 2005) for which a Q factor of 5.5×10^4 in a GaAs cavity with QDs has been reported (Ota, Iwamoto, Kumagai, & Arakawa, 2011), nanobeam cavities (Ohta et al., 2011), or even random Anderson-localized modes in photonic-crystal waveguides due to naturally occurring fabrication imperfections (Topolancik, Ilic, & Vollmer, 2007; Smolka et al., 2011). The nanobeam cavity displayed in figure 2.14(c) is a 1D photonic crystal consisting of etched holes in a narrow and thin membrane with a central defect area defining the cavity region (Ohta et al., 2011). Finally microdisk cavities [see figure 2.14(d)] constitute another class of resonators where the trapping of light is due to total internal reflection rather than Bragg scattering. In a microdisk cavity the light is confined to the rim of the disk in a whispering-gallery mode that can have a very high Q

(Srinivasan & Painter, 2007), generally, however, at the expense of larger mode volume compared to cavities employing Bragg scattering. Figure 2.14 summarizes the various cavity configurations including figures of merit in relation to their usage for cavity-QED experiments.

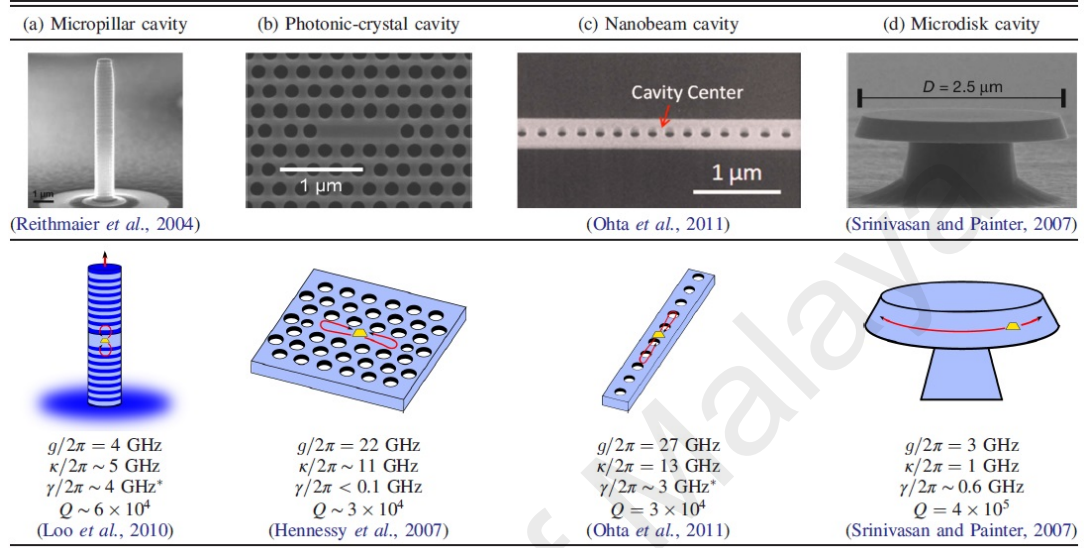


Figure 2.14: Overview of different QD-cQED systems including a nanophotonic cavity and single QD. Each panel displays a scanning electron micrograph of a real device along with a sketch illustrating the operational principle for a quantum emitter coupling to the structure. Furthermore, state-of-the-art experimental results are listed. (a) Micropillar cavity, the Bragg stack above and below the center of the pillar confines light to the central region as shown in the inset. (b) Modified photonic-crystal L3 cavity implemented in a membrane. The photonic band gap localizes light in the defect region and the schematic shows how a QD preferentially emits into the cavity mode. (c) A nanobeam cavity, the cavity mode is confined by 1D Bragg diffraction in the high-refractive-index material of the nanorod. (d) Microdisk cavity, the emitter couples to optical modes that travel circularly around the microdisk. The asterisk (*) indicates that in these cases γ was extracted from spectral rather than time-resolved data, i.e., it will be enlarged by dephasing processes.

One of the important quantities of QD-cQED systems, as shown in the figure, is QD-cavity coupling strength g which is obtained as

$$g = |\langle d \cdot E \rangle| = \left(\frac{1}{4\pi\epsilon_r\epsilon_0} \frac{\pi e^2 f}{mV} \right), \quad (2.18)$$

where d and E are dipole and electric field operator, respectively. m is the free electron mass. f/V is the oscillator strength per unit volume, ϵ_r and ϵ_0 are the relative and

vacuum permittivity (Gaussian units: $4\pi\epsilon_0 \rightarrow 1$), respectively. The oscillator strength is given as $f = 2m\omega_0 d^2 / e^2 \hbar$ where ω_0 is the cavity mode frequency and e is the electron charge. Other important parameters of QD-cavity systems include cavity decay rate, κ , QD recombination rate, γ_r , and cavity quality factor, Q , which is defined as $Q = \frac{\omega_0}{\kappa}$.

2.3.1 Theoretical Approaches to Investigate Quantum Dot-Cavity Quantum Electrodynamical Systems

Theoretical description of QD-cQED including carrier-phonon interactions has been discussed in the literature usually based on derivation of quantum master equation (ME) using the Liouville–von Neumann equation and the second-order Born approximation; One common approach is to use a standard weak-coupling theory, which only includes exciton-phonon interactions to second order and is known to break down at higher temperatures, strong exciton-phonon couplings (McCutcheon & Nazir, 2010), and in the presence of cavity coupling (Roy & Hughes, 2011). In another approach, exciton-cavity coupling is considered as a perturbation and time-convolutionless (TC) technique is applied (Hohenester et al., 2009). Applying the unitary polaron transformation to the model Hamiltonian, that encapsulates non-perturbative coupling effects beyond second-order Born approximation, and utilizing either the Nakajima-Zwanzig (NZ) (Wilson-Rae & Imamoglu, 2002; Kaer, Nielsen, Lodahl, Jauho, & Mørk, 2012) or TC (Kaer et al., 2012) projection operator techniques result in a polaron frame ME in NZ or TC form. A variationally optimized ME, through a combination of a variationally optimized unitary transformation and TC projection operator technique, for a coherently laser-driven QD has also been proposed (McCutcheon, Dattani, Gauger, Lovett, & Nazir, 2011). The variational ME gives reliable results over a wide range of parameters even in regimes in which previous ME approaches fail. However, these quantum MEs are obtained by applying second-order perturbation expansion and thus can only provide approximate results (Lee, Moix, & Cao, 2012). There are only a few non-perturbative techniques to attain the nu-

merically exact dynamics in all the regimes of parameters including strong coupling, high temperatures, and long-time dynamics. Those methods include the hierarchy master equation (Tanimura, 2006; Ishizaki & Tanimura, 2005), the multiconfiguration time-dependent Hartree approach (Meyer, Manthe, & Cederbaum, 1990; Beck, Jäckle, Worth, & Meyer, 2000; Thoss, Wang, & Miller, 2001), and the quasi-adiabatic propagator Feynman path-integral (QUAPI) (Makarov & Makri, 1994; Makri & Makarov, 1995b, 1995a) which usually is used as a "benchmark" to examine validity of standard approaches that utilize approximations (McCutcheon et al., 2011; Lee et al., 2012; Vagov, Croitoru, Axt, Machnikowski, & Kuhn, 2011). The main disadvantage of QUAPI or real-time path-integral (RTPI) compared to the approximate approaches is that it is computationally more expensive.

QUAPI or RTPI can be formulated in a closed form for models that the system is linearly coupled to harmonic-oscillator degrees of freedom (Sim, 2001) such as QD-cavity system coupled to environment phonons. An efficient method for calculation of the reduced density matrix (RDM) derived in QUAPI approach has been proposed (Makarov & Makri, 1994; Makri & Makarov, 1995b, 1995a), its subsequent improvement, making the method easier to implement, has been presented later (Sim, 2001). The main focus of these studies has been systems with ohmic or subohmic coupling types, for which physical problems, such as dynamic localization and the crossover between coherent and incoherent dynamics, have been studied (Vagov, Croitoru, Glässl, Axt, & Kuhn, 2011). When the effective environment spectral density $J(\omega)$ scales as $J(\omega) \sim \omega^\alpha$ in the low-frequency limit with $0 < \alpha < 1$, the system-environment coupling is called "subohmic". If $\alpha = 1$ it is called "ohmic" while the case $\alpha > 1$ is referred to as "superohmic". As we will show later and have also been discussed in the literature (McCutcheon et al., 2011; Vagov, Croitoru, Glässl, et al., 2011; Ramsay, Godden, et al., 2010; Ramsay, Gopal, et al., 2010; Machnikowski & Jacak, 2004; Vagov et al., 2004; Krummheuer et al., 2002; Vagov, Axt,

& Kuhn, 2002; Besombes, Kheng, Marsal, & Mariette, 2001; Borri et al., 2001; Stievater et al., 2001), the pure dephasing type carrier-phonon coupling in strongly confined semiconductor QDs represents an example for a system with superohmic coupling. The first implementation of the numerically accurate RTPI method that is able to deal with the superohmic couplings for a QD with few carrier states coupled to external Gaussian pulses and longitudinal acoustic (LA) phonons has been presented in Ref. (Vagov, Croitoru, Glässl, et al., 2011). Later, the authors extended their implementation to the case where the classical field is replaced by a single quantized cavity mode (Glässl et al., 2012), in this case, a QD without dissipation is coupled to LA phonon reservoir and a loss-less cavity. The published work does not include mathematical details of the extended method. To incorporate the losses, in Ref. (Vagov, Glässl, Croitoru, Axt, & Kuhn, 2014), the authors have obtained the evolution of the populations and coherences from a ME derived from the Liouville–von Neumann equation including the Jaynes-Cummings Hamiltonian and the standard Lindblad super-operators accounting for exciton-LA phonon interaction (phonon-induced pure dephasing rate), the QD, and cavity dissipations. This is the simplest way to account for cavity loss, radiative decay, and the QD coupling to LA phonons. Within this approach, the phonon-exciton interaction is not treated to all orders; In fact, it is also included phenomenologically like the losses. The Lindblad formalism does not account for the damping and frequency renormalizations of Rabi oscillations that are known to result from the dressing of the electronic states with LA phonons due to the pure dephasing coupling. As a phenomenological way to describe these renormalizations, the authors have introduced a modified QD-cavity coupling constant in their model. Then, they have extracted the values of LA phonon-induced pure dephasing rate and the modified coupling constant using a match of a phenomenological equation, reproducing the state population calculated by the RTPI approach, to the solution of the ME in the limited case of a loss-less QD-cavity system. Thus, their approach is basically an approximate

method with a number of phenomenological terms.

2.4 General Formulation of Path-Integral Approach

Many situations occur in quantum mechanics in which several systems are coupled together but one or more of them are not of primary interest. Problems in the theory of measurement and in statistical mechanics present good examples of such situations. For instance, suppose that the quantum behavior of a system is to be investigated when it is coupled to one or more measuring instruments. The instruments in themselves are not of primary interest. However, their effects are those of perturbing the characteristics of the system being observed. A more concrete example is the case of a QD in an excited state which interacts with the electromagnetic field in a lossy cavity resonator and a phonon bath. If, however, the QD were not coupled to any external disturbances, it would simply remain unperturbed in its original excited state. The phonon bath, although not of central interest to us, influences the behavior of the QD-cavity field system.

To make the discussion more definite, let us suppose there are two non-relativistic quantum systems whose coordinates are represented in a general way by Q and X coupled together through some interaction potential which is a function of the parameters of the two systems. It is desired to compare the expectation value of an observable which is a function of the Q variables only. As is well known, the complete problem can be analyzed by taking the Hamiltonian of the complete system, forming the wave equation, as follows:

$$\{H(Q) + H(X) + V(Q, X)\} \Psi(Q, X) = - \left(\frac{\hbar}{i} \right) \frac{\partial}{\partial t} \Psi(Q, X), \quad (2.19)$$

and then finding its solution. In general, this is an extremely difficult problem. In addition, when this approach is used, it is not easy to see how to eliminate the coordinates of X and include its effect in an equivalent way when making computations on Q . A satisfactory

method of formulating such problems like this in a general way was made available by the introduction of the Lagrangian formulation of quantum mechanics by Feynman. He applied the techniques afforded by this method extensively to studies in quantum electrodynamics. Thus, in a problem where several charged particles interact through the electromagnetic field, he found that it was possible to eliminate the coordinates of the field and recast the problem in terms of the coordinates of the particles alone. The effect of the field was included as a delayed interaction between the particles (R. P. Feynman, 1948, 1950).

The central goal of this section is to develop a general formalism for finding all of the quantum effects of an environmental system upon a system of interest, to investigate the properties of this formalism, and to draw conclusions about the quantum effects of environmental system on the system of interest.

In the next part, after a brief discussion of the Lagrangian formulation of quantum mechanics, a general formulation of the problem is made and certain functionals, called influence functionals, will be defined, which contain the effect of the environmental system on the system of interest in terms of the coordinates of the system of interest only.

It is to be emphasized that although we shall talk of general environmental system and system of interest, the Lagrangian formulation is restricted to cases involving momentum or coordinate operators. Therefore, strictly speaking, systems in which the spin is of importance are not covered by this analysis. However, this has no bearing on the results since their nature is such that their extension to the case where spins are important can be inferred (R. Feynman & Vernon, 1963, 2000).

An equivalent approach can be made to the problem using the Hamiltonian formulation of quantum mechanics by making use of the ordered operator calculus developed by Feynman (R. P. Feynman, 1951). This approach was used to some extent by Fano (Fano, 1957) and has been developed further by Makarov and Makri (Makarov & Makri,

1994; Makri & Makarov, 1995b, 1995a). Some advantages of this approach include many results may be obtained more simply than by the Lagrangian method and non-classical concepts such as spin enter the formalism naturally. However, the physical significance of the functions being dealt with are often clearer in the Lagrangian method.

2.4.1 Lagrangian Formulation of Quantum Mechanics

We begin the discussion with a brief introduction to the Lagrangian or space-time approach to quantum mechanics and the formal way in which one may set up problems of many variables. Let us suppose that we are considering a single system which has coordinates that are denoted by Q , and that for the time being it is not acted on by any other quantum system. It can be acted out by outside forces, however. The system may be very complicated, in which case Q represents all the coordinates in a very general way. If at a time t the variable Q is denoted by Q_t , then the amplitude for the system to go from position Q_τ at $t = \tau$ to Q_T at $t = T$ is given by

$$K(Q_T, T; Q_\tau, \tau) = \int_{\text{all } Q(t)} \exp[(i/\hbar)S(Q)] DQ(t), \quad (2.20)$$

in this integral which represents the sum over all possible paths $Q(t)$ in coordinate space from Q_τ to Q_T of the functional $\exp[(i/\hbar)S(Q)]$ where

$$S(Q) = \int_{\tau}^T L(\dot{Q}, Q, t) dt \quad (2.21)$$

is the action calculated classically from the Lagrangian for the trajectory $Q(t)$. For the case that Q is a single linear coordinate of position, this is represented in the diagram in figure 2.15. The magnitude of the amplitude for all paths is equal but the phase for each path is given by the classical action along that path in units of \hbar . Thus, amplitudes for neighboring paths which have large phases tend to cancel. The paths which contribute the

greatest amount are those whose amplitudes have stationary phases for small deviations around a certain path. This is the path for which the classical action is at an extremum and is, therefore, the classical path. Remarkably enough, for free particles and harmonic oscillators, the result, of the path integration is

$$K(Q_T, Q_\tau) = (\text{Smooth Function}) \exp[(i/\hbar) S_{Cl}], \quad (2.22)$$

where S_{Cl} is the action evaluated along the classical path between the two end points Q_τ and Q_T . However, for more complicated systems this simple relation does not hold.

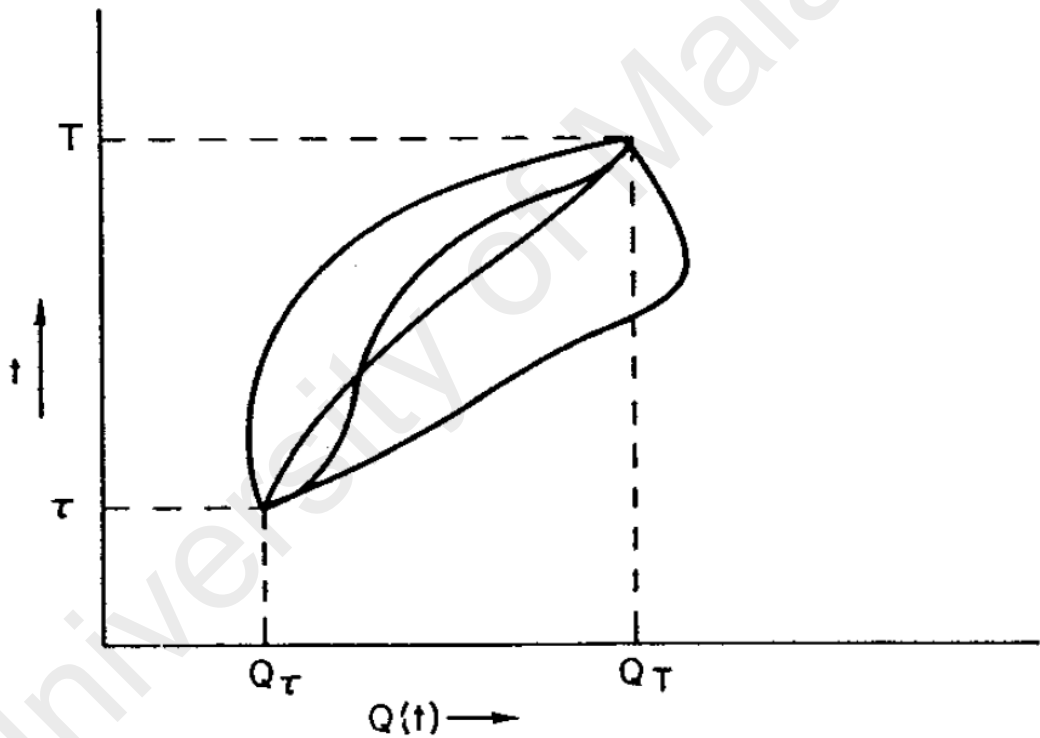


Figure 2.15: Space-time diagram showing possible paths for particle to proceed from Q_τ to Q_T .

Since $K(Q_T, Q_\tau)$ is the amplitude to go from coordinate Q_τ to Q_T , it follows that at $t = T$ the amplitude that the system is in a state designated by $\Phi_m(Q_T)$ when initially is

in a state $\Phi_n(Q_\tau)$ is given by

$$\begin{aligned} A_{mn} &= \int \Phi_m^*(Q_T) K(Q_T, Q_\tau) \Phi_n(Q_\tau) dQ_T dQ_\tau \\ &= \int \Phi_m^*(Q_T) \exp[(i/\hbar)S(Q)] \Phi_n(Q_\tau) DQ(t) dQ_T dQ_\tau. \end{aligned} \quad (2.23)$$

The probability of the transition from $n \rightarrow m$ is given by $|A_{mn}|^2$ and from Eq. 2.23 it can be written in the form of multiple integrals as follows:

$$\begin{aligned} P_{mn} &= \int \Phi_m^*(Q_T) \Phi_m(Q'_T) \exp(i/\hbar) [S(Q) - S(Q')] \\ &\quad \times \Phi_n(Q_\tau) \Phi_n^*(Q'_\tau) DQ(t) DQ'(t) dQ_T dQ'_T dQ_\tau dQ'_\tau. \end{aligned} \quad (2.24)$$

As an example of a more complicated case let us consider two systems whose coordinates are Q and X . The systems are coupled by a potential which can be designated as $V(Q, X)$ and incorporated in the total Lagrangian. We assume that when $V = 0$ the states of Q and X can be described by sets of wave functions $\Phi_k(Q)$ and $\chi_p(X)$ respectively. If, initially, Q is in a state $\Phi_n(Q_\tau)$ and X is in a state $\chi_i(X_\tau)$, then the amplitude that Q goes from state n to m while X goes from state i to f can be formed in a similar way to that of Eq. 2.23 as

$$\begin{aligned} A_{mf, ni} &= \int \Phi_m^*(Q_T) \chi_f^*(Q_T) \exp[(i/\hbar)S(Q, X)] \Phi_n(Q_\tau) \chi_i(X_\tau) \\ &\quad \times DQ(t) DX(t) dQ_T dX_T dQ_\tau dX_\tau, \end{aligned} \quad (2.25)$$

where $S(Q, X)$ represents the classical action of the entire system including both Q and X . The important property of separability afforded by writing the amplitude in this way is now apparent. For instance, if one wishes to know the effect that X has on Q when X undergoes a transition from state i to f , then all of the integrals on the X variables may be done first. What is left is an expression for A_{mn} for Q and in terms of Q variables

only but with the effect of X included. The extension of writing transition amplitudes for large numbers of systems is obvious. In principle the order in which the variables are eliminated is always arbitrary.

2.4.2 Definition of Influence Functional

A functional can now be defined which can be used to describe mathematically the effect of external quantum systems upon the behavior of a quantum system of interest.

The fundamental theorem may be stated as follows: For any system, Q , acted on by external classical forces and quantum mechanical systems as discussed above, the probability that it makes a transition from state $\Psi_n(Q_\tau)$ at $t = \tau$ to $\Psi_m(Q_T)$ at $t = T$ can be written as

$$P_{mn} = \int \Psi_m^*(Q_T) \Psi_m(Q'_T) \exp\left\{\frac{i}{\hbar} [S_0(Q) - S_0(Q')]\right\} F(Q, Q') \times \Psi_n^*(Q'_\tau) \Psi_n(Q_\tau) DQ(t) DQ'(t) dQ_\tau dQ'_\tau dQ_T dQ'_T, \quad (2.26)$$

where $F(Q, Q')$ contains all the effects of the external influences on Q and $S_0(Q) = \int_\tau^T L(\dot{Q}, Q, t) dt$ is the action of Q without external disturbance. The proof of this is straightforward. Let us examine two coupled systems characterized by coordinates Q and X . Q will represent the system of interest and X the quite general environmental system (excepting only the effects of spin) coupled by a general potential $V(Q, X, t)$ to Q . Assume Q to be initially ($t = \tau$) in state $\Psi_n(Q_\tau)$ and X to be in state $\chi_i(X_\tau)$, a product state. The probability that Q is found in state $\Psi_m(Q_T)$ while X is in state $\chi_f(X_T)$ at $t = T$

can be written in the manner discussed above and is

$$\begin{aligned}
P_{mf, ni} &= |A_{mf, ni}|^2 \\
&= \int \Psi_m^*(Q_T) \Psi_m(Q'_T) \chi_f^*(X_T) \chi_f(X'_T) \\
&\quad \times \exp \left\{ (i/\hbar) [S_0(Q) - S_0(Q') + S_0(X) - S_0(X') + S_I(Q, X) - S_I(Q', X')] \right\} \\
&\quad \times \Psi_n^*(Q'_\tau) \Psi_n(Q_\tau) \chi_i^*(X'_\tau) \chi_i(X_\tau) DQ(t) DX(t) DQ'(t) DX'(t) dQ_\tau dX_\tau \\
&\quad \times dQ'_\tau dX'_\tau dQ_T dX_T dQ'_T dX'_T, \tag{2.27}
\end{aligned}$$

The primed variables were introduced when the integrals for each $A_{mf, ni}$ were combined. Now if all the components of Eq. 2.27 which involves coordinates other than Q or Q' is separated out and designated as $F(Q, Q')$, then the following expression is obtained

$$\begin{aligned}
F(Q, Q') &= \int \chi_f^*(X_T) \chi_f(X'_T) \\
&\quad \times \exp \left\{ (i/\hbar) [S_0(X) - S_0(X') + S_I(Q, X) - S_I(Q', X')] \right\} \\
&\quad \times \chi_i^*(X'_\tau) \chi_i(X_\tau) DX(t) DX'(t) dX_\tau dX'_\tau dX_T dX'_T, \tag{2.28}
\end{aligned}$$

Incorporation of this expression into Eq. 2.27 yields the desired form as Eq. 2.26. If the path-integrals are written in terms of kernels, Eq. 2.28 becomes

$$\begin{aligned}
F(Q, Q') &= \int \chi_f^*(X_T) \chi_f(X'_T) K_Q(X_T, X_\tau) K_{Q'}^*(X'_T, X'_\tau) \\
&\quad \times \chi_i^*(X'_\tau) \chi_i(X_\tau) dX_\tau dX'_\tau dX_T dX'_T \tag{2.29}
\end{aligned}$$

where the subscript Q means that the kernel includes the effect of a potential $V(Q, X)$ acting on X during the interval $\tau < t < T$. As can be seen, F is a functional whose form depends upon the physical system X , the initial and final states of X , and the coupling between Q and X .

It is to be emphasized that the formulation of F is such that it includes all the effects of the environmental system in influencing the behavior of the system of interest. Thus, if there are two systems A and B which can act on Q , and if

$$F_{A \text{ on } Q} = F_{B \text{ on } Q} \quad (2.30)$$

then the effects of A on Q are the same as those of B on Q . It follows that if simplifying assumptions are necessary in finding $F_{A \text{ on } Q}$ and $F_{B \text{ on } Q}$ (due to the complicated nature of A and B) and if the resulting functions are equal, then within the approximations the effects of A and B on the system of interest are the same. In the situation where the environmental system is composed of a linear system or combinations of linear systems we shall see that the same form of F is always appropriate. To adapt this general form of F to a particular linear system it is only necessary to know such quantities as impedance and temperature which determine its classical behavior. In still other situations, very weak coupling between systems is involved. The approximate F which can be used in this case to represent the effect of the environmental systems has a form which is independent of the nature of the environmental system. This form is the same as for linear systems (R. Feynman & Vernon, 1963, 2000).

2.5 Temperature-Dependent Bandgap Variation

2.5.1 Photoluminescence Spectrum

In order to obtain photoluminescence (PL) spectrum of energy levels of a QD ensemble, the QD ensemble is excited at an energy well above those energy levels. This is so-called nonresonant excitation. The PL is inhomogeneously broadened because there is a contribution from every QD in the ensemble sample, which typically contains a variety of QD sizes.

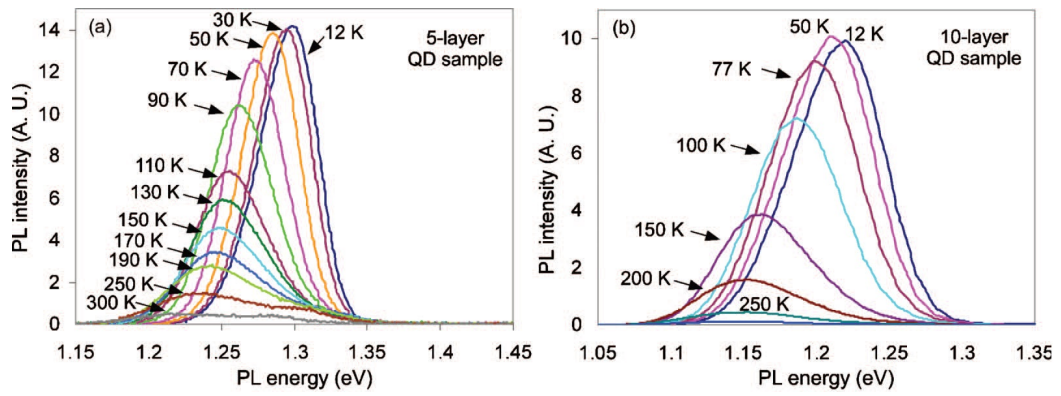


Figure 2.16: Temperature-dependent PL emission spectra of different QD samples (a) 5-layer and (b) 10-layer QD sample (Lu, Vaillancourt, Wen, 2010).

Figure 2.16 shows the temperature-dependent photoluminescence (PL) emission spectra of the 5-layer and 10-layer QD samples, respectively (Lu, Vaillancourt, & Wen, 2010). Assuming all photo-excited electron-hole pairs are effectively captured in the QDs and the lifetime of the photo-excited electron-hole pairs is 1 ns (Dawson et al., 2005), the laser excitation power density of 14 W/cm^2 gives an excitation density of $3.7 \times 10^{10}/\text{cm}^2$. Since the typical QD density is $2\text{-}3 \times 10^{10}/\text{cm}^2$ for each QD layer (Lu et al., 2007b, 2007a), the photo-excitation density is much lower than the QD densities for all the 5-layer and 10-layer QD samples. At this low excitation density, the photo-excited electron-hole pairs would occupy the ground state of the QDs at low temperature and PL emission is primarily from the ground states. It has been concluded that the PL emission in QDs is primarily due to the recombination of independent electron and holes rather than the relaxation of excitons (Dawson et al., 2005). Therefore, the exciton effect can be neglected and the PL emission spectra give the ground state energy (bandgap energy) of the QDs. The size variation in the QD ensemble gives the spectral width of the PL emission, which is also referred to as inhomogeneous broadening. At elevated temperatures, carriers (electrons and holes) can be thermally excited and redistributed into QDs with higher confinement energies (Sanguinetti et al., 1999). This causes a slight deviation from the standard Gaussian profile at the shape of the PL emission spectra. However, as one can see from figure

2.16, the whole PL spectrum shifts to lower energies as temperature increases. This indicates that the QD ensembles experience the same trend of temperature-dependent energy gap variations. For simplicity, the peak energy of the PL emission is used to represent the energy gap variations.

2.5.2 Semi-Empirical Models for Projecting Temperature-Dependent Bandgap Variation

Two mechanisms are responsible for temperature-dependent bandgap shift; the electron-phonon interaction and the thermal lattice expansion. For both mechanisms the contributions of the individual lattice oscillators with energies $\varepsilon = \hbar\omega$ are proportional to the average phonon occupation number $\bar{n} = [\exp(\varepsilon/k_B T) - 1]^{-1}$ (O'Donnell & Chen, 1991), temperature-dependent bandgap $E(T)$ can therefore be represented as

$$E(T) = E(0) - \frac{\alpha}{k_B} \int_0^\infty d\varepsilon \frac{\varepsilon w(\varepsilon)}{\exp(\varepsilon/k_B T) - 1}. \quad (2.31)$$

Here $\alpha = -dE(T)/dT|_{T \rightarrow \infty}$ is the slope of the linear T dependence in the high temperature limit, $E(0)$ is the band gap energy at 0 K and $w(\varepsilon) \geq 0$ is the normalized weighting function of the phonon oscillators, $\int d\varepsilon w(\varepsilon) = 1$. Different assumptions for $w(\varepsilon)$ lead to the several models such as power-function ansatz which is discussed in the following.

A convenient analytical treatment of $E(T)$ is obtained by a power-function (PF) ansatz (Pässler, 2003): $w(\varepsilon) = v(\varepsilon/\varepsilon_c)^{v-1}/\varepsilon_c$, $v > 0$ for ε up to the cutoff energy ε_c of the phonon spectrum, and $w(\varepsilon) = 0$ above. In this model, the $T \rightarrow 0$ asymptotes are given by power functions $[E(0) - E(T)] \propto T^p$, where the fractional exponent p usually ranges from 2 to 3 (Pässler, 1997, 1999). A detailed analysis shows that for the frequently observed regime of intermediate to large phonon dispersion $E(T)$ is given as

$$E(T) = E(0) - \frac{\alpha\theta}{2} \left\{ \left[1 + \sum_{n=1}^3 \alpha_n(v) \left(\frac{2T}{\theta} \right)^{n+v} + \left(\frac{2T}{\theta} \right)^{5+v} \right]^{1/(5+v)} - 1 \right\}, \quad (2.32)$$

where the expansion coefficients $\alpha_n(v)$ are

$$\alpha_1(v) = \frac{5+v}{6} \left(\frac{\pi}{2}\right)^{2+(v-1)^2/2},$$

$$\alpha_2(v) = \frac{1-v}{2},$$

$$\alpha_3(v) = \frac{(5+v)(1+v)^2}{3v(2+v)}.$$

The average phonon temperature $\theta = \langle \varepsilon \rangle / k_B = v \varepsilon_c / [k_B(1+v)]$ (Pässler, 2000), leading to a cutoff energy $\varepsilon_c = k_B \theta (1+v) / v$. The dispersion coefficient $\Delta = \sqrt{\langle \varepsilon^2 \rangle - \langle \varepsilon \rangle^2} / \langle \varepsilon \rangle$ is $1/\sqrt{v(2+v)}$ (Pässler, 2003). Besides the zero-temperature energy, this model contains three parameters for fitting the experimental data.

Another well-known model which originated from bulk semiconductors is the Varshni model (Y. Varshni, 1967; Y. P. Varshni, 1970). This model is empirically expressed as

$$E(T) = E(0) - \frac{\alpha T^2}{\beta + T}, \quad (2.33)$$

where α and β are the two Varshni coefficients to be determined by fitting the experimental data with Eq. 2.33. The Varshni equation was devised to fit the seemingly linear decrease in the high temperature region and the quadratic decrease in the low temperature region as observed in many semiconductor material systems.

We call the third semi-empirical model as Lu model, it describes as

$$E(T) = E(0) + \frac{\theta_1}{T - \theta_2}, \quad (2.34)$$

where θ_1 and θ_2 has temperature dimension, K , and together with $E(0)$ should be obtained from the fit of the experimental data (Lu et al., 2010). There are two additional methods called Fan or Vana and two-oscillator model which will be discussed in the next

chapter.

2.5.3 Temperature-Dependent Bandgap Variation in Quantum Dot Samples

It is appropriate to check whether models developed for bulk may be used for describing temperature-dependent bandgap in the QD structures. Figure 2.17 shows the temperature-dependent energy gap variation in the 5-layer QD sample at various temperatures from 12 to 300 K (Lu et al., 2010). A sigmoidal-shape temperature-dependent bandgap shrinkage was obtained. Similar observations have been reported ((Sanguinetti et al., 2002; Brusaferrri et al., 1996)). Also shown in figure 2.17 are the energy gap shrinking projected by using the Varshni's formula (Eq. 2.33) and the power function ansatz (Eq. 2.32), dashed green and red traces, respectively. The measured QD temperature-dependent energy gap variation shows significant deviation from the projections of these models. This indicates that QDs have different temperature-dependent bandgap energy properties than bulk semiconductors. The blue and pink traces are the calculated energy gaps by using Lu model (Eq. 2.34) in the low ($T < 100$ K) and high temperature ($T > 100$ K) regions.

According to figure 2.17, it seems that the Lu model can project the experimental data perfectly. However, a complete study of several works conducted for modeling of the temperature dependent shrinkage of In(Ga)As/GaAs SOQD bandgaps, one can infer that this basic property of QDs still cannot be described properly using the existing models; in the work performed by Wei et al. (Z. F. Wei et al., 2005) none of the aforementioned models were used, instead a model similar to the Varshni model could project the InGaAs QDs PL peak shrinkage data only up to 170 K. In the work done by Ortner et al. (Ortner et al., 2005), the four abovementioned models were used to project single-QD spectrum of In(Ga)As/GaAs QDs. The conclusion was that PF and two-oscillator models provide better fits than the Varshni and Fan (Vina) models. In the next work conducted by Lu et al.

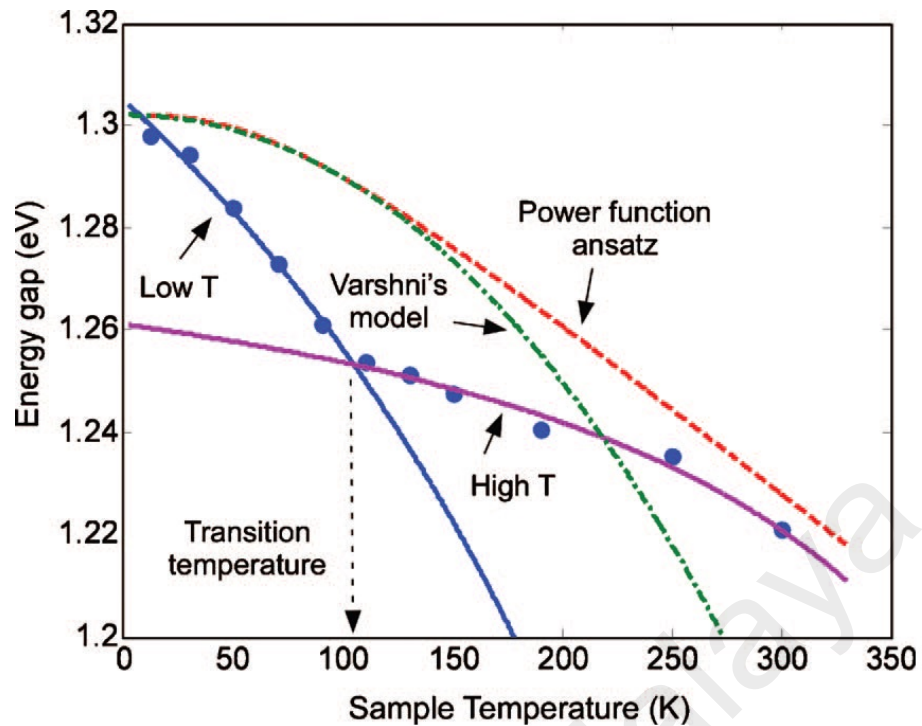


Figure 2.17: Temperature-dependent bandgap energy variation in the 5-QD sample at various temperatures from 12 to 300 K. The data were measured from the PL emission. Dashed green and red traces show the energy gap shrinking projected by using the Varshni's formula and the PF ansatz, respectively. Blue and pink traces show calculated bandgap energies by using Lu model at the low ($T < 100$ K) and high temperature ($T > 100$ K) regions, which show a good agreement with the experimental data (Lu, Vaillancourt, Wen, 2010).

(Lu et al., 2010), the conclusion was that the Lu model is able to project the InAs/GaAs QD data properly, using division of the whole temperature interval to two shorter parts for the Lu model (figure 2.17), compared to the Varshni and PF models. Finally, in the recent work performed by Yeo et al. (Yeo, Song, & Lee, 2011), applying the Varshni and Fan models to the sample A0 (figure 2.18), grown by conventional MBE, resulted in the conclusion that the Fan model fits the InAs QDs data better than the Varshni model, and the author stated that “Lu model completely fails to fit the whole data.” For the sample A0, the Fan model works generally well, but there are still three issues; first, the fit is not well for temperatures less than 60 K, second, there is a large discontinuity between 150 to 200 K as the temperature dependent behavior of the bandgap energy peak is not clear, and, finally, the Fan model itself offers phantom energy peaks for phonons if the

phonon dispersion is not zero. Therefore we come to the conclusion that the temperature-dependent PL peak evolutions of In(Ga)As/GaAs QDs still cannot be modeled properly for all the existing experimental data using those models.

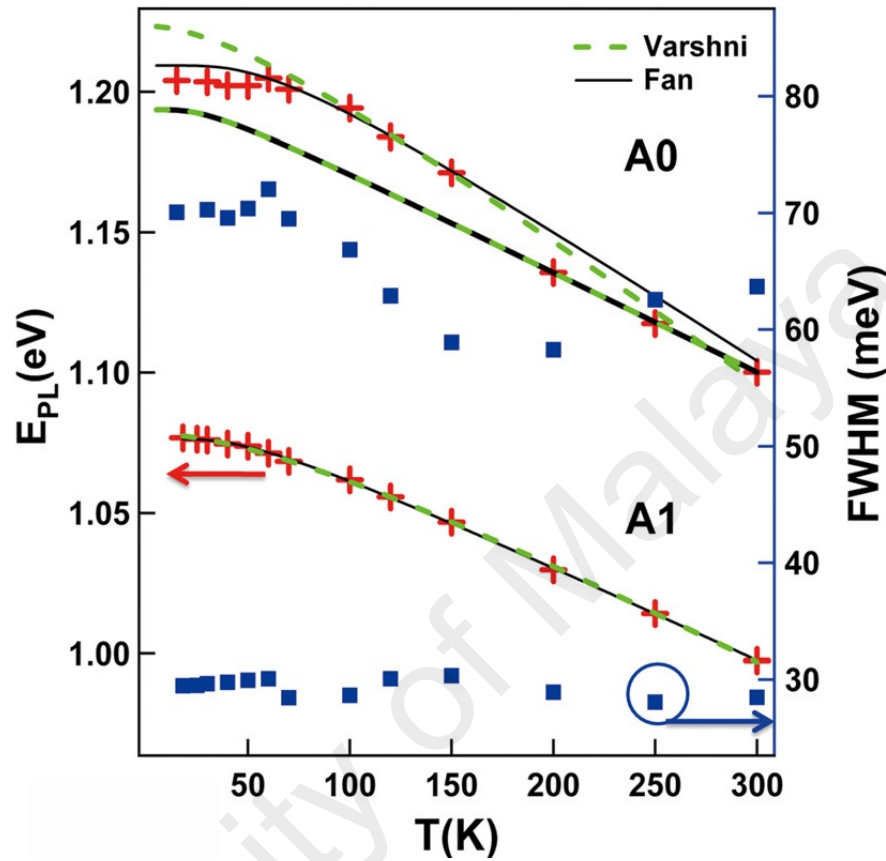


Figure 2.18: The temperature-dependent PL peak evolutions are presented at various temperatures (15–300 K) for the InAs QD sample grown in conventional MBE (A0) and migration-enhanced MBE (MEMBE) (A1). The red cross is the experimental PL peak energy at different temperatures. The blue rectangle indicates the experimental PL linewidth (FWHM). The green dashed lines and the black solid lines represent the projected energy gap variations by using Varshni and Fan models, respectively (Yeo, Song, Lee, 2011).

CHAPTER 3

MODELING AND SIMULATION METHODS

3.1 Introduction

In the first part of this chapter, the model describing a single QD inserted into a lossy nanophotonic cavity and coupled to a LA phonon bath is presented. To study the quantum dynamics of the open QD-cavity system modified real-time path-integral (RTPI) approach is discussed and an efficient algorithm to evaluate the derived density matrix is presented. Then, in the second part of the chapter, two oscillator model (TOM) is discussed, which will be used to model phonon-induced temperature-dependent shift of photoluminescence (PL) peak for experimental datasets of In(Ga)As/GaAs QDs with a different number of monolayers (MLs) and layers.

3.2 Dissipative Quantum Dot-Cavity System Coupled to a Superohmic Environment

We consider a semiconductor quantum dot (QD) in the strong confinement limit, i.e., the electronic single particle states are energetically well separated and the Coulomb interaction provides negligible mixing between them, linearly coupled to lattice vibrations (phonons). The QD is considered to have only two optically active electronic levels that are resonantly coupled to a single mode cavity. Assuming the lattice and dielectric properties of the confined QD do not differ notably from the environment, the phonon modes are approximated with the corresponding three-dimensional bulk modes, like in the bulk material. It has generally been approved that optical phonons do not contribute to exciton–phonon interactions at temperatures less than about 100 K (Borri et al., 2001; Muljarov & Zimmermann, 2004; Uskov et al., 2000; Takagahara, 1999; Ghodsi Nahri & Ooi, 2014), thus, restricting our simulations to those temperatures, we can safely neglect

the polar optical coupling to LO phonons. We also neglect the piezoelectric coupling to LA and TA phonons, which has been shown to have a small effect for (In,Ga)As QDs, and only account for the deformation potential coupling to LA phonons, which dominates the exciton-LA phonon interactions in (In,Ga)As QD (see Chap. 2).

Schematic representation of such a two level QD coupled to a single mode cavity and the LA phonon bath is illustrated in figure 3.1(a). A two-level QD, including a ground state (GS) represented by $|G\rangle$ and an excited state (ES) expressed by $|X\rangle$, is coupled to a single mode cavity, with two photon levels $|0\rangle$ and $|1\rangle$, through the coupling strength g . The phonon bath is represented by a continuum of LA phonon wave states $|q_1\rangle$ to $|q_M\rangle$, the matrix elements describing interaction of the QD with the phonon reservoir is expressed by γ_q . The radiative population decay of the excited QD is described by the rate γ_r . The cavity loss is represented by the rate κ . The QD-cavity system with these dissipation is called "dissipative QD-cavity system".

We first introduce the, possibly time dependent, total (model) Hamiltonian that describes the dissipative QD-cavity (DQC) system coupled to the phonon degrees of freedom as:

$$\begin{aligned} H(t) &= H_0^{QD} + H_0^C + H_I^{QD-C} + H_{\gamma_r}^{QD} + H_{\kappa}^C + H_0^{Ph} + H_I^{QD-Ph} \\ &= H_S + H_R + H_{SR}, \end{aligned} \quad (3.1)$$

where H_0^{QD} and H_0^C describe the uncoupled QD and cavity Hamiltonian, H_I^{QD-C} corresponds to the QD-cavity interaction Hamiltonian through which the QD state and the cavity mode become strongly coupled and new polariton modes, which have partial exciton and partial cavity character (Reithmaier et al., 2004; Hennessy et al., 2007), are formed. $H_{\gamma_r}^{QD}$ and H_{κ}^C represent QD and cavity dissipation Hamiltonian respectively. H_0^{Ph} is the Hamiltonian of free LA phonon bath and H_I^{QD-Ph} describes interaction of the QD with the

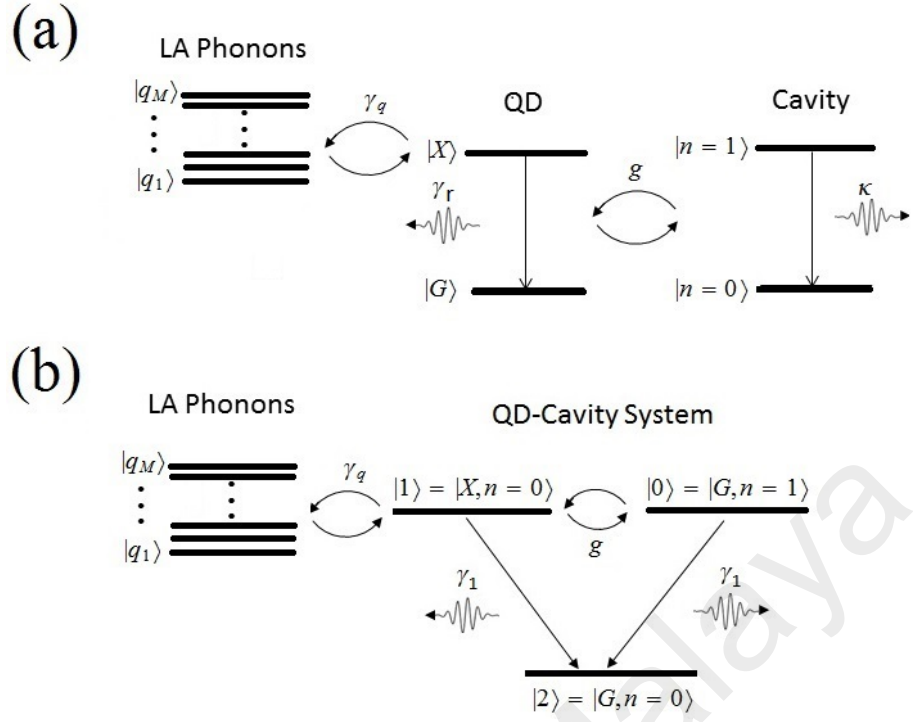


Figure 3.1: (a) A two-level QD, including a ground state $|G\rangle$ and an excited state $|X\rangle$, is coupled to a single mode cavity, with two photon levels $|0\rangle$ and $|1\rangle$, through the coupling strength g . The matrix elements γ_q describe interaction of the QD with the phonon reservoir which is represented by a continuum of LA phonon wave states. The radiative carrier recombination and the cavity loss rates are represented by γ_r and κ , respectively. (b) QD-cavity system represented in terms of the common basis states, with maximum one photon in the cavity or one exciton, interacting with the LA phonon bath and decaying with a g -dependent rate γ_1 .

phonon bath, which forms the polaronic quasiparticle that has partial exciton and partial LA phonon character and leads to renormalization of the exciton energy. We denote the Hamiltonian of the free QD and the cavity, the QD-cavity interaction, and the dissipation as system Hamiltonian, representing the dissipative Jaynes-Cummings Hamiltonian, and rewrite the total Hamiltonian in the system-reservoir formalism as the right-hand side of Eq. 3.1 where the reservoir Hamiltonian H_R represents the free LA phonon bath Hamiltonian and the system-reservoir Hamiltonian H_{SR} represents interaction Hamiltonian of the QD and the LA phonon bath. When the emitter energy and the cavity mode are near-resonant one can apply the rotating-wave approximation (RWA). The non-Hermitian dissipative QD-cavity system Hamiltonian, consisting of the closed QD-cavity system and

the dissipation, under the usual RWA and dipole approximation can be expressed as

$$\begin{aligned}
H_S = & \hbar\bar{\omega}_X |X\rangle\langle X| + \hbar\omega_C a^\dagger a + \hbar g \left(a^\dagger \sigma_- + \sigma_+ a \right) \\
& - i \frac{\hbar\gamma_r}{2} |X\rangle\langle X| - i \frac{\hbar\kappa}{2} a^\dagger a,
\end{aligned} \tag{3.2}$$

where the QD GS is taken as zero of the energy, $\bar{\omega}_X$ and ω_C are the polaron-shifted exciton and cavity photon angular frequency, $\bar{\omega}_X = \omega_X - \Omega_p$ where ω_X is the QD exciton energy and Ω_p is the polaronic shift. g is the QD-cavity coupling strength which describes the electromagnetic coupling between the exciton and the cavity mode and depends on the exciton dipole moment and the field distribution of the cavity mode (Andreani, Panzarini, & Gérard, 1999). a^\dagger (a) is the photon creation (annihilation) operator. The lowering and rising operators for the QD are defined as $\sigma_- = |G\rangle\langle X|$ and $\sigma_+ = |X\rangle\langle G|$ where $|G\rangle$ denotes GS of the QD (empty QD) and $|X\rangle$ represents the QD ES with a single exciton. The cavity leakage rate can be expressed in terms of the cavity quality factor Q and the QD transition frequency as $\kappa = \frac{\bar{\omega}_X}{Q}$. We concentrate on the case of a resonant QD-cavity system considering ω_C to be at resonance with the polaron-shifted exciton transition. The total Hamiltonian parts including the free phonon reservoir and the exciton-phonon coupling, described by the independent boson model (IBM) (G. Mahan, 1990; Hohenester, 2006), are represented as

$$\begin{aligned}
H_R = & \hbar \sum_q \omega_q b_q^\dagger b_q, \\
H_{SR} = & \hbar |X\rangle\langle X| \sum_q \left(\gamma_q^* b_q + \gamma_q b_q^\dagger \right),
\end{aligned} \tag{3.3}$$

where b_q^\dagger (b_q) creates (destroys) a LA phonon in a mode labeled by phonon wave vector \mathbf{q} , b_q^\dagger and b_q obey the usual equal-time commutation relations for bosons, ω_q is the corresponding phonon angular frequency. Pure dephasing interactions couple the carrier

occupations of the QD to phonon degrees of freedom, without introducing couplings between the carrier states, through the coupling constant γ_q which is the difference between electron-phonon and hole-phonon constants, $\gamma_q = \gamma_q^e - \gamma_q^h$. As the interaction part of the above dissipative QD-cavity system Hamiltonian is commuted with its free part including the non-Hermitian part and as we are only concerned with the dynamics of the system on the single-photon level we can define a common basis states, as shown in figure 3.1(b), for the system Hamiltonian as $\{|0\rangle = |G, n = 1\rangle, |1\rangle = |X, n = 0\rangle, |2\rangle = |G, n = 0\rangle\}$ where n refers to the number of photons in the cavity mode. The coupling between states $|0\rangle$ and $|1\rangle$ occurs due to the dipole interaction between them. The states $|0\rangle$ and $|1\rangle$ decay irreversibly to $|2\rangle$ with a g -dependent rate γ_1 which originates from both the cavity loss and the QD radiative recombination process, as a result of this coupling. Since both the decay channels result in an irreversible loss of population from the single excited states $|0\rangle$ and $|1\rangle$, which are the common basis states of the closed system, we can propagate the density matrix of these two basis states using the second-quantized Hamiltonian of Eq. 3.2. Projecting the Hamiltonian of Eq. 3.2 onto the lower-dimensional Hilbert subspace of the closed system changes the following parts of the total Hamiltonian as

$$\widehat{H}_S = \hbar \left(\omega_C - i\frac{\kappa}{2} \right) \widehat{s}_{00} + \hbar \left(\bar{\omega}_X - i\frac{\gamma_r}{2} \right) \widehat{s}_{11} + \hbar g (\widehat{s}_{01} + \widehat{s}_{10}), \quad (3.4)$$

$$\widehat{H}_{SR} = \hbar \widehat{s}_{11} \sum_q \left(\gamma_q^* b_q + \gamma_q b_q^\dagger \right) = \hbar \sum_q \left(\widehat{\gamma}_q^* b_q + \widehat{\gamma}_q b_q^\dagger \right), \quad (3.5)$$

where the hat sign stands for matrix operators acting in the common space of carrier-photon states and $s_{pq} = |p\rangle \langle q|$. The QD-phonon coupling can be expressed as a diagonal matrix $\widehat{\gamma}_q$ accounting for coupling of phonons to the different excitonic levels. For the case of a two level system, phonons only are coupled to ES of the QD. The effective phonon spectral density in terms of the QD-phonon coupling matrix element and the dispersion

relation, is given by (Vagov, Croitoru, Glässl, et al., 2011)

$$J(\omega) = \sum_q |\gamma_q|^2 \delta(\omega - \omega_q). \quad (3.6)$$

The QD-phonon coupling matrix element, accounting for the deformation potential coupling of electrons (holes) to LA phonons, is obtained as (Vagov et al., 2002)

$$\gamma_{\mathbf{q}}^{e(h)} = \frac{|\mathbf{q}| D_{e(h)}}{\sqrt{2V d \hbar \omega_{\mathbf{q}}}} \Psi^{e(h)}(\mathbf{q}), \quad (3.7)$$

where d is the density of the material, V is the phonon normalization volume, $D_{e(h)}$ denotes the deformation potential constant for electron (hole), and $\Psi^{e(h)}(\mathbf{q})$ is the form factor that can be calculated from the wave functions $\psi^{e(h)}(r)$ of the carriers confined in the QD as

$$\Psi^{e(h)}(\mathbf{q}) = \int_V |\psi^{e(h)}(\mathbf{r})|^2 e^{i\mathbf{q}\cdot\mathbf{r}} d^3r. \quad (3.8)$$

Assuming a spherical QD, the electron (hole) wave function, which is given by the ground-state solution of a harmonic oscillator, is expressed as (Vagov et al., 2002)

$$\psi^{e(h)}(\mathbf{r}) = \frac{1}{\pi^{3/4} \alpha_{e(h)}^{3/2}} \exp\left(-\frac{r^2}{2\alpha_{e(h)}^2}\right), \quad (3.9)$$

where α_e and α_h represent the electron and hole geometrical confinement lengths, respectively. The form factors resulted from these wave functions are obtained as

$$\Psi^{e(h)}(\mathbf{q}) = \exp\left(-\frac{q^2 \alpha_{e(h)}^2}{4}\right). \quad (3.10)$$

The bulk LA phonons with the linear dispersion relation, in the relevant energy range, $\omega_q = v_s |\mathbf{q}|$ is assumed (Krummheuer et al., 2002; Roszak, Grodecka, Machnikowski, &

Kuhn, 2005; Krügel, Axt, Kuhn, Machnikowski, & Vagov, 2005; Grosse & Zimmermann, 2007; Stock et al., 2011) with v_s being the sound velocity in the material. Inserting Eqs. 3.7 and 3.10 into Eq. 3.6 and replacing the summation over the wave vector \mathbf{q} with an integral, assuming an isotropic momentum space, the phonon spectral density is obtained as

$$J(\omega) = \frac{\omega^3}{4\pi^2 d \hbar v_s^5} \left[D_e \exp\left(-\frac{\omega^2 \alpha_e^2}{4v_s^2}\right) - D_h \exp\left(-\frac{\omega^2 \alpha_h^2}{4v_s^2}\right) \right]^2, \quad (3.11)$$

which scales, for small frequencies, as $J(\omega) \sim \omega^3$; therefore, it is indeed of the superohmic type. It tends to zero as a Gaussian function, faster than eight-band $\mathbf{k}\cdot\mathbf{p}$ wave functions (see figure 2.12), in the opposite limit of high frequencies. It is worth to note that other types of phonon modes, e.g., half-space or slab modes (Krummheuer, Axt, Kuhn, D'Amico, & Rossi, 2005), can be incorporated into the present approach as long as the modes form continua which lead to finite memory times. We take typical GaAs parameters: $d = 5370 \text{ kgm}^{-3}$, $v_s = 5110 \text{ ms}^{-1}$, $D_e = -14.6 \text{ eV}$, and $D_h = -4.8 \text{ eV}$ (Krummheuer et al., 2002) with $\alpha_e = 5 \text{ nm}$. We also consider a constant ratio $\alpha_h = 0.87\alpha_e$ for the electron and hole confinement lengths (Glässl et al., 2011).

3.3 Real-Time Path-Integral Approach for the Open Quantum Dot-Cavity System

3.3.1 Discretized Real-Time Path-Integral Formulation

Reduced open QD-cavity density matrix (RQCDM) is obtained by taking the partial trace over the density matrix of the total system, i.e. the open QD-cavity and the phonon bath, with respect to the phonon reservoir as

$$\hat{\rho}(t) = \text{Tr}_{ph}[\chi(t)], \quad (3.12)$$

also referred to as tracing out the degrees of freedom of the reservoir. To derive a discretized real-time path-integral (RTPI) representation for the RQCDM, we write the total

density matrix at time t , in Eq. 3.12, in terms of the initial total density matrix, $\chi(0)$, and the time evolution operator as

$$\hat{\rho}(t) = \text{Tr}_{ph}[U(t)\chi(0)U^\dagger(t)]. \quad (3.13)$$

We assume that the bath is initially at thermal equilibrium and that the system–bath interaction is switched on at $t = 0$, so that the total statistical operator initially can be factorized as product of carrier-photon and phonon operators

$$\chi(0) = \hat{\rho}(0) \otimes \frac{1}{Z} \exp \left[-\frac{\hbar}{k_B T} \sum_q \omega_q b_q^\dagger b_q \right], \quad (3.14)$$

where Z is the normalization constant of the phonon distribution at temperature T , and $\hat{\rho}(0)$ is the initial statistical operator for the carrier-photon system (initial RQCDM). The time evolution operator is given by

$$U(t) = T \exp \left(-\frac{i}{\hbar} \int_0^t H(t') dt' \right), \quad (3.15)$$

where T is the time ordering operator. As shown in the Appendix, Eq. 3.13 together with Eqs. 3.14 and 3.15 can be represented in the form of a path-integral, where the phonon variables are readily traced out. Time t is discretized into N time steps of the length $\varepsilon = t/N$ with the time grid points $t_n = n\varepsilon$ and $n = 0, \dots, N$. Any of the coupled basis states of the dissipative QD-cavity system, $|0\rangle$ or $|1\rangle$, at time t_n are represented by $|s_n^+\rangle$ for forward propagation in time and by $|s_n^-\rangle$ for backward propagation on a path that runs in the backward (decreasing) time direction. Here we write the final expression for

the RQCDM elements in the interaction picture as

$$\rho_{s_N^+ s_N^-}(t_N) = \lim_{N \rightarrow \infty} \prod_{n=1}^N \sum_{s_{n-1}^\pm} H_S^{s_n^+ s_{n-1}^+} H_S^{s_n^- s_{n-1}^-*} \prod_{n'=0}^n e^{f_{nn'}} \rho_{s_0^+ s_0^-}(0), \quad (3.16)$$

where the configuration summations are over all s_n^+ , s_n^- , which can be interpreted as "sum over all trajectories" of the open QD-cavity system that connect the RQCDM at time t_N to the initial one at time zero. For the present case of the three-level system with two coupled levels, involved in the dynamics, the indexes s_n^+ and s_n^- are assumed to take only the values 0 and 1. One approximates Eq. 3.16 with a finite N and ϵ in order to develop a numerical algorithm for practical calculations. $H_S^{s_n^+ s_{n-1}^+}$ and $H_S^{s_n^- s_{n-1}^-*}$ are one-dimensional short-time forward and backward bare system propagators which are defined as

$$H_S^{s_n^+ s_{n-1}^+} H_S^{s_n^- s_{n-1}^-*} = \langle s_n^+ | e^{-i\hat{H}_S \epsilon / \hbar} | s_{n-1}^+ \rangle \langle s_{n-1}^- | e^{i\hat{H}_S^\dagger \epsilon / \hbar} | s_n^- \rangle, \quad (3.17)$$

where the dissipative QD-cavity Hamiltonian, in the matrix form, for the present case of maximum one cavity photon is given by

$$\hat{H}_S = \hbar \begin{pmatrix} \omega_C - i\frac{\kappa}{2} & g \\ g & \bar{\omega}_X - i\frac{\gamma}{2} \end{pmatrix}.$$

In order to calculate matrix elements of the system short-time propagator and its Hermitian conjugate, between time steps n and $n-1$, presented in Eq. 3.17 \hat{H}_S should be diagonalized. The non-local bath functional $f_{nn'}$, accounting for effects of the phonon bath, in Eq. 3.16 is given by

$$f_{nn'} = - (s_n^+ - s_n^-) (\eta_{n-n'} s_{n'}^+ - \eta_{n-n'}^* s_{n'}^-), \quad (3.19)$$

where the short-time Feynman-Vernon-like influence functional is defined as $I_{nn'} = \exp(f_{nn'})$, the influence coefficient η_m , depending only on $m = n - n'$ time steps, is expressed as

$$\begin{aligned}\eta_{m \neq 0} &= \int_{m\varepsilon}^{(m+1)\varepsilon} d\tau \int_0^\varepsilon d\tau' K(\tau - \tau') \\ &= 4 \int_0^\infty d\omega \frac{J(\omega)}{\omega^2} \sin^2\left(\frac{\varepsilon\omega}{2}\right) \left\{ \coth\left(\frac{\hbar\omega}{2k_B T}\right) \cos(m\varepsilon\omega) - i \sin(m\varepsilon\omega) \right\},\end{aligned}\quad (3.20)$$

$$\begin{aligned}\eta_{m=0} &= \int_0^\varepsilon d\tau \int_0^\tau d\tau' K(\tau - \tau') \\ &= 2 \int_0^\infty d\omega \frac{J(\omega)}{\omega^2} \left\{ \sin^2\left(\frac{\varepsilon\omega}{2}\right) \coth\left(\frac{\hbar\omega}{2k_B T}\right) - i(\varepsilon\omega - \sin(\varepsilon\omega)) \right\},\end{aligned}\quad (3.21)$$

here the memory kernel (system-bath correlation function) $K(t)$, accounting for delayed influences by time t , is given by

$$K(t) = \int_0^\infty d\omega J(\omega) \left[\coth\left(\frac{\hbar\omega}{2k_B T}\right) \cos(\omega t) - i \sin(\omega t) \right]. \quad (3.22)$$

Note that while the influence functional introduces non-Markovian interactions between time points separated by several time steps m , the system propagator Eq. 3.17 only connects the nearest time point, which is a Markovian interaction. Eqs. 3.16-3.22 are core equations describing numerically exact RTPI approach, for the open QD-cavity system coupled to a continuum of LA phonon modes, enabling us to obtain the RQCDM elements at an arbitrary time (Ghods Nahri et al., 2016).

3.3.2 Memory Length Finiteness and Truncation of the Influence Coefficient

An efficient method for calculation of the reduced density matrix (RDM) in Eq. 3.16 is called “tensor multiplication scheme”, in which the RDM is evaluated by using a proper tensor propagator in each iteration, has been presented in Refs.(Makri & Makarov, 1995b, 1995a; Sim, 2001). It is based on the fact that for harmonic baths, described by smooth

spectral density functions, range of the nonlocal interactions in the influence functional is indeed finite for any temperature, including even zero temperature, such that the nonlocal kernel extends over only a few time steps if the path-integral is discretized by using accurate quasiadiabatic propagators (Makarov & Makri, 1994; Makri & Makarov, 1995b, 1995a). This is the case when the heat bath is characterized by a broad spectrum that extends to reasonably high frequencies, which is characteristic of condensed phase environments. This feature arises from destructive phase interference between modes located within the reservoir's broad spectral density, resulting in disruption of quantum coherence in the macroscopic bath which, in turn, leads to loss of memory of initial conditions after sufficiently long time periods. Although the evolution of the RDM is not Markovian in such cases the finite length of nonlocal interactions in the influence functional leads to Markovian dynamics for the tensor propagator, which implies that the long-time path-integral can be broken into a series of shorter time calculations, permitting iterative time evolution schemes. In fact, in cases where the memory length is not very long compared to the allowed time step, the tensor multiplication scheme provides a numerically exact means of calculating the quantum dynamics of (dissipative) systems coupled to dephasing (dissipating) reservoirs for arbitrarily long times, as it preserves the trace of the RDM, provided that the nonlocal interactions are not truncated too soon. The scheme also surpasses usual Monte Carlo methods as they are not feasible for long times due to the alternating signs in the discretized RTPIs (Makri & Makarov, 1995b, 1995a; Sim, 2001). We have plotted normalized real and imaginary parts of the memory kernel $K(t)$ in figure 3.2 in order to find the memory length (depth) at different temperatures. As it is clearly seen, at $T = 0 K$, real part of the memory kernel almost becomes zero after 5 ps, while at higher temperatures $T = 20 K$ and $T = 80 K$ the memory becomes shorter, taking the effective value about 4 ps. There is not noticeable change in the memory depth and amplitude for temperatures larger than $T = 20 K$. The memory amplitude is smallest

(not shown) and the memory depth is largest for low temperatures. The system-bath correlation function has a temperature independent imaginary part, in agreement with Ref. (Kaer et al., 2012), and it almost reaches zero at about 4.5 ps. Similarly the influence coefficient η_m has to be truncated at a cutoff time $t_c = \epsilon n_c$ as $\eta_{m>n_c}^c = 0$, where t_c is the memory length and n_c is the memory cutoff number (the number of time steps within the memory length).

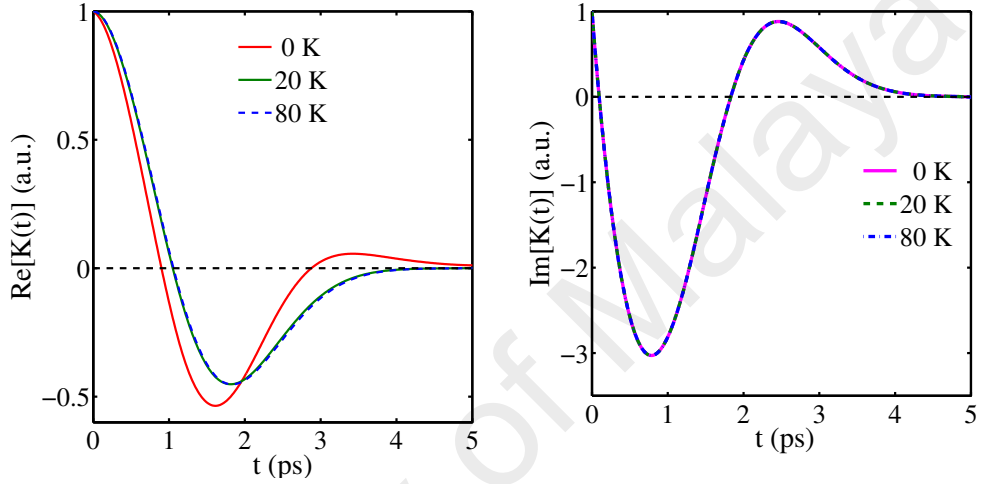


Figure 3.2: Time-dependence of normalized real (left panel) and imaginary (right panel) parts of the memory kernel $K(t)$ at different temperatures. It seems that the memory kernel with the length 4 ps, as $t_c = \epsilon n_c = 4$ ps, is appropriate for the spherical QD with radius 5 nm and the deformation potential coupling to LA phonons.

In order to obtain the required constraint for the truncated influence coefficient the important quantity $G(t)$ is defined as (Vagov, Croitoru, Glässl, et al., 2011)

$$G(t = N\epsilon) = \sum_{\mathbf{n}=1}^N \sum_{\mathbf{n}'=1}^n \eta_{\mathbf{n}-\mathbf{n}'}, \quad (3.23)$$

we can rewrite it as

$$G(N\epsilon) = N\eta_0 + \sum_{\mathbf{n}=1}^{N-1} (N-n) \eta_{\mathbf{n}}, \quad (3.24)$$

calculating $G((N+1)\epsilon) - G(N\epsilon)$ and substituting $\eta_{\mathbf{n}-\mathbf{n}'}$ from Eqs. 3.20 and 3.21, then, dividing the integral boundary 0 to ϵ by τ and using change of variables for τ and τ' ,

finally, we obtain

$$\begin{aligned}
G(t) &= \int_0^t d\tau \int_0^\tau d\tau' K(\tau - \tau') \\
&= \int_0^\infty d\omega \frac{J(\omega)}{\omega^2} \{ [1 - \cos(\omega t)] \coth\left(\frac{\hbar\omega}{2k_B T}\right) - i[\omega t - \sin(\omega t)] \}.
\end{aligned} \tag{3.25}$$

The long time asymptotics of Eq. 3.25, taking the coupling Eq. 3.11, evaluates to

$$\begin{aligned}
G(t \rightarrow \infty) &\rightarrow G_0 - i\Omega_p t \\
G_0 &= \int_0^\infty d\omega \frac{J(\omega)}{\omega^2} \coth\left(\frac{\hbar\omega}{2k_B T}\right) = \text{const.} \\
\Omega_p &= \int_0^\infty d\omega \frac{J(\omega)}{\omega} = \text{const.}
\end{aligned} \tag{3.26}$$

where $\lim_{t \rightarrow \infty} \cos(\omega t) = \lim_{t \rightarrow \infty} \sin(\omega t) = 0$ is considered. Here Ω_p is the standard polaronic shift, which effectively leads to a renormalization of the transition frequency, while $\exp[-G_0]$ defines the residual coherence, at temperature T , which remains in the closed QD-cavity system coupled to the bath in the long time limit. $\exp[-G_0/2]$ can be interpreted as a factor that renormalizes the Rabi frequency (Y.-J. Wei et al., 2014). It is appropriate to add the polaronic shift Ω_p to the exciton transition frequency, so that we have taken into account the renormalized exciton transition frequency $\bar{\omega}_X = \omega_X - \Omega_p$ in Eq. 3.2 and later on. G_0 increases with temperature, thereby reducing the residual coherence. In the present case of a dissipative QD-cavity system coupled to the phonon bath, the residual coherence is zero. For the case of the truncation approximation, i.e., $\eta_{m>n_c}^c = 0$, we divide $G(t)$ around the truncation point and obtain nonzero influence coefficients for

$m = n - n' \leq n_c$ as

$$\begin{aligned}
 G^c(t = N\varepsilon) &= \sum_{\mathbf{n}=1}^{n_c} \sum_{\mathbf{n}'=1}^n \eta_{n-n'}^c + \sum_{\mathbf{n}=\mathbf{n}_c+1}^N \sum_{\mathbf{n}'=1}^n \eta_{n-n'}^c \\
 &= \sum_{\mathbf{n}=1}^{n_c} \sum_{\mathbf{n}'=1}^n \eta_{n-n'}^c + \frac{t-t_c}{\varepsilon} \sum_{\mathbf{n}=0}^{n_c} \eta_n^c,
 \end{aligned} \tag{3.27}$$

the long time asymptotics of $G^c(t)$ in Eq. 3.27 is obtained as

$$\begin{aligned}
 G^c(t \rightarrow \infty) &\rightarrow G_0^c + G_I^c t \\
 G_0^c &= \sum_{\mathbf{n}=1}^{n_c} \sum_{\mathbf{n}'=1}^n \eta_{n-n'}^c, \quad G_I^c = \frac{1}{\varepsilon} \sum_{\mathbf{n}=0}^{n_c} \eta_n^c,
 \end{aligned} \tag{3.28}$$

since in this case of the truncation approximation, the asymptotic relations for the quantity $G(t)$ in Eq. 3.26 must also hold, therefore, comparing Eq. 3.28 with the exact asymptotic in Eq. 3.26 one obtains the following constraint for the truncated influence coefficient:

$$\sum_{\mathbf{n}=0}^{n_c} \eta_n^c = -i\varepsilon\Omega_p \tag{3.29}$$

which is consistent with the exact identity:

$$\sum_{\mathbf{n}=0}^{\infty} \eta_n = \int_0^{\infty} \varepsilon K(\tau) d\tau = -i\varepsilon \int_0^{\infty} d\omega \frac{J(\omega)}{\omega}. \tag{3.30}$$

In the truncation approximation, it is most important to enforce the constraint in Eq. 3.29 for the real part of the kernel, i. e.

$$\sum_{\mathbf{n}=0}^{n_c} \text{Re}[\eta_n^c] = 0. \tag{3.31}$$

It should be noted that the constraint Eq. 3.29 and the necessity of its enforcement is specific to the superohmic case (Vagov, Croitoru, Glässl, et al., 2011). To fulfill the

constraint in Eq. 3.29, we assume a possible complex nonzero value A for the following expression

$$\sum_{n=0}^{n_c} \eta_n^c + i\varepsilon\Omega_p = A. \quad (3.32)$$

Modifying the influence coefficient η_n^c according to

$$\bar{\eta}_n^c = \eta_n^c - \frac{1}{n_c + 1} \left(\sum_{n=0}^{n_c} \eta_n^c + i\varepsilon\Omega_p \right), \quad (3.33)$$

the constraint in Eq. 3.29 is fulfilled. It is mentioned in (Vagov, Croitoru, Glässl, et al., 2011) that in the case of superohmic coupling in QD systems, for which the truncation does not lead to qualitative changes of the system dynamics if Eq. 3.29 holds, possible quantitative errors due to the truncation can be well controlled by varying the time step ε and the memory cutoff length $t_c = \varepsilon n_c$. It should be noted, however, that as far as we have examined, for the present case of the QD-cavity system under investigation, if the constraint in Eq. 3.29 is not applied, a significant quantitative change occurs only in the real part of the off-diagonal RDM elements.

3.3.3 Implementation of the Numerical Algorithm

The truncated influence coefficient approximation, which is based on finiteness of range of the memory length, enormously decreases the numerical load for calculation of the RQCDM, Eq.3.16, especially when it is combined with the so-called tensor multiplication scheme. The original formulation of this scheme, presented in Refs. (Makarov & Makri, 1994; Makri & Makarov, 1995b, 1995a), was somewhat cumbersome and required multiple runs of the algorithm to obtain the complete time evolution. Its subsequent improvement allowing an “on-the-fly filtering” and “path re-indexing” has been proposed in Ref. (Sim, 2001). On-the-fly path selection or on-the-fly filtering process selects more probable paths in the course of the time propagation in a single run. The path re-indexing

process unifies all the similar paths into one with a weight obtained from summing up the weights of those trajectories for times larger than the memory length in the single run. Here, we present a brief summary of the method with few modifications, adapted for the dynamic calculation of the QD-cavity system coupled to the harmonic bath of LA phonon oscillators. We implement the algorithm through an iterative method containing a set of recurrence equations which briefly summarize the steps to evaluate Eq. 3.16. We start with rewriting Eq. 3.16, considering a finite N , at the present time t_q as

$$\rho_{s_q^+ s_q^-}(t_q) = \sum_{\{s_{q-1}^+, \dots, s_0^+\}} \sum_{\{s_{q-1}^-, \dots, s_0^-\}} \left[\prod_{n=1}^{q-1} H_S^{s_n^+ s_{n-1}^+} H_S^{s_n^- s_{n-1}^-*} \prod_{n'=0}^n e^{f_{nn'}} \rho_{s_i^+ s_i^-}(0) \right] \left[H_S^{s_q^+ s_{q-1}^+} H_S^{s_q^- s_{q-1}^-*} \prod_{n'=0}^q e^{f_{qn'}} \right], \quad (3.34)$$

where we have expressed the system propagator and the influence functional expressions as a product of the ‘‘history’’ and ‘‘memory’’ terms. For the RDM at the present time t_q , the history term includes only the interactions between the past grid-time points from $t_{n=0} = 0$ to $t_{n=q-1} = t_{n=q} - \varepsilon$ while the memory term corresponds to the interactions between the present grid-time point and the past time points. By identifying the history and the memory terms, the redundant calculations can be avoided. Following this separation idea and defining trajectories as sequences of s_n^+ and s_n^- , the discretized expression of the RQCDM in Eq. 3.34 can be rewritten as

$$\langle s_q^+ | \widehat{\rho}(t_q) | s_q^- \rangle = \sum_{j_{s_q^\pm}}^{L_{s_q^\pm}} T_{\bar{j}_{q-1}} M_{s_{j_q^\pm}}, \quad (3.35)$$

where \bar{j}_{q-1} represents the path segment from time $t_0 = 0$ to $t_{q-1} = (q-1)\varepsilon$ of j^{th} configuration, i.e., $\bar{j}_{q-1} = (s_{j_{q-1}}^+, \dots, s_{j_0}^+, s_{j_{q-1}}^-, \dots, s_{j_0}^-)$ where the subscript j_l correspond to the grid point at time $l\varepsilon$ on the j^{th} configuration. $L_{s_q^\pm}$ is the total number of possible configura-

rations ending at a certain pair (s_q^+, s_q^-) at time $q\epsilon$. In the two-level system each path is represented by a long sequence of 0s and 1s with the length $2(q+1)$. The history and the memory terms are then represented by

$$T_{\bar{j}_{q-1}} = \prod_{n=1}^{q-1} H_S^{s_{j_n}^+ s_{j_{n-1}}^+} H_S^{s_{j_n}^- s_{j_{n-1}}^-} \prod_{n'=0}^n e^{f_{j_{n'}}} \rho_{s_i^+ s_i^-}(0), \quad (3.36)$$

$$M_{s_{j_q}^\pm} = H_S^{s_{j_q}^+ s_{j_{q-1}}^+} H_S^{s_{j_q}^- s_{j_{q-1}}^-} \prod_{n'=0}^q e^{f_{j_{q'n'}}}, \quad (3.37)$$

where $M_{s_{j_q}^\pm}$ denotes the interactions of a certain pair $(s_{j_q}^+, s_{j_q}^-)$ at the present time t_q with the past time points on the j^{th} configuration. It can be seen that the history and memory terms can be reused as the next propagation history weight (term) without redundant calculations. However, as RDM propagates the number of configurations and corresponding weights to be stored increases exponentially as D^{2q} , where $D = 2$ is the number of system eigenstates and an initial state has been considered. Thus, we need to apply other mechanisms to decrease the storage array size; As the strength of nonlocal interactions drops off rapidly beyond a certain value of $t_c = \epsilon n_c$ due to coupling to the phonon bath, implying that only a finite memory length needs to be included, it is sufficient to include only $2^{2(n_c+1)}$ configurations for the times $t > t_c$ without losing numerical accuracy. Because of the finite memory length, by the time that RDM propagates up to $t_{n_c+p} = (n_c + p)\epsilon$, contributions from the first p time grid points are negligible and can thus be ignored without affecting the final results. For instance, if $p = 2$, the contributions of the initial point and the second grid point are neglected. Furthermore, some of the trajectories become identical allowing us to combine them as one effective path. This re-indexing of the trajectories leads to the reduction of the number of paths to be integrated and can be implemented when the propagator passes the bath memory time. Nevertheless, the number of configurations enhances exponentially to 2^{2n_c} as RDM propagates up to the bath memory time. To alleviate this, on-the-fly path filtering of the propagator functional is applied; it re-

moves the paths with weights less than a chosen cutoff from the path integration in each propagation step and may start from the first propagation step. The trajectory re-indexing technique, on the other hand, is applied for the propagation beyond the bath memory time. Accordingly, on-the-fly filtering and the trajectory re-indexing technique reduce the number of configurations to be integrated substantially. Figure 3.3 shows schematic representation of the configuration space including some trajectories (like the red path), started from an initial state, and the memory truncation for $n_c = 3$.

Considering the finite memory length, Eq. 3.34 can be rewritten for two different areas of time points n as

$$\rho_{s_n^+ s_n^-}(t_n) = \sum_{j_n^{\pm}}^{L_{s_n^{\pm}}} T_{\bar{j}_n}, \quad n \leq n_c \quad (3.38)$$

$$\rho_{s_n^+ s_n^-}(t_n) = \sum_{j_n^{\pm}}^{L_{s_n^{\pm}}^c} \bar{T}_{\bar{j}_n^c}, \quad n_c < n \quad (3.39)$$

where for $n \leq n_c$ each configuration is represented as $\bar{j}_n = (s_{j_n}^+, \dots, s_{j_0}^+, s_{j_n}^-, \dots, s_{j_0}^-)$ and $L_n = \sum_{s_n^{\pm}} L_{s_n^{\pm}}$ is the total number of possible paths ending at time $n\epsilon$. While for $n_c < n$ each trajectory segment is defined as $\bar{j}_n^c = (s_{j_n}^+, \dots, s_{j_{n-n_c}}^+, s_{j_n}^-, \dots, s_{j_{n-n_c}}^-)$ and $L_n^c = \sum_{s_n^{\pm}} L_{s_n^{\pm}}^c$.

The history weights are given by recurrence equations as

$$T_{\bar{j}_0} = \rho_{s_0^+ s_0^-}(t_0 = 0) = \rho_{s_i^+ s_i^-}, \quad n = 0 \quad (3.40)$$

$$T_{\bar{k}_n} = T_{\bar{k}_{n-1}} M_{k_n}, \quad 1 \leq n \leq n_c \quad (3.41)$$

$$\bar{T}_{k_n^c} = \bar{T}_{k_{n-1}^c} M_{k_n^c}, \quad n_c < n \quad (3.42)$$

where $T_{\bar{j}_0}$ is in fact the initial RQCDM elements and \bar{T}_{k_n} introduces summing up the weights of similar paths as a result of the trajectory re-indexing technique. The memory

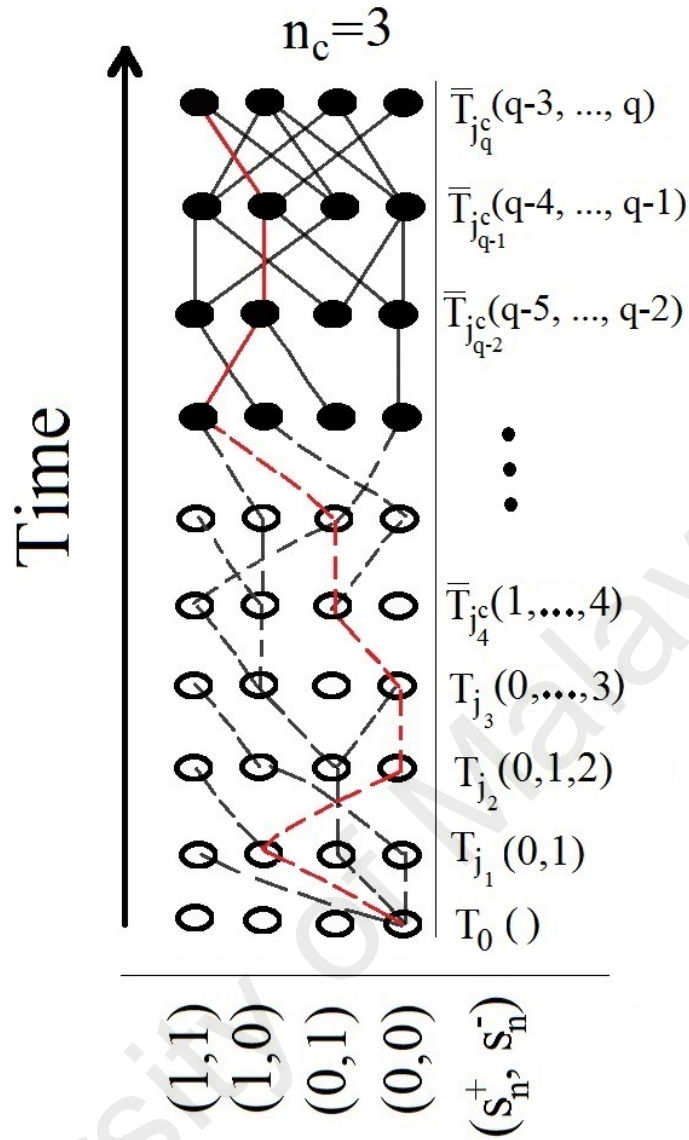


Figure 3.3: Schematic representation of the configuration space including some trajectories (like the red path), started from an initial state, and the memory truncation. The ovals indicate the time points t_n ; Solid ovals correspond to the points within the memory length with the memory cutoff number $n_c = 3$ for the time point t_q , while hollow ovals correspond to the time steps p , with $q - p > n_c$, which are not taken into account at the time t_q . The solid lines indicate the path segments included in $\bar{T}_{j_q}^c$, while the dashed lines indicate non-included path segments at the time t_q .

equations are given by

$$M_{k_1} = H_S^{s_{k_1}^+ s_{k_0}^+} H_S^{s_{k_1}^- s_{k_0}^- *} \exp \left(\sum_{\mathbf{n}=0}^1 \sum_{\mathbf{n}'=0}^n f_{k_{nn'}} \right), \quad n = 1 \quad (3.43)$$

$$M_{k_n} = H_S^{s_{k_n}^+ s_{k_{n-1}}^+} H_S^{s_{k_n}^- s_{k_{n-1}}^- *} \exp \left(\sum_{\mathbf{n}'=0}^n f_{k_{nn'}} \right), \quad 1 < n \leq n_c \quad (3.44)$$

$$M_{k_n}^c = H_S^{s_{k_n}^+ s_{k_{n-1}}^+} H_S^{s_{k_n}^- s_{k_{n-1}}^-} \exp \left(\sum_{n'=n-n_c}^n f_{k_{n'}} \right), \quad n_c < n \quad (3.45)$$

The algorithm, for evaluating equations 3.38 and 3.39, can be described in four steps:

Step 1. We begin with the propagation of RQCDM at time $t_1 = \varepsilon$ by constructing the product in equation 3.41 using equation 3.40 and the memory term given in equation 3.43. Defining the initial state (1, 1) the configurations number are $k_1 = 1, \dots, L_1 = 2^2$, and $L_{s_1^\pm} = 1$. The configurations number, at $t_0 = 0$, also are $j_0 = L_0 = 1$ and $f_{k_{00}} = 0$. The obtained weights are RQCDM elements at time $t_1 = \varepsilon$, according to equation 3.38.

Step 2. For $n \leq n_c$ ($n_c < n$), assuming at time point $n - 1$ we know all the paths \bar{j}_{n-1} (\bar{j}_{n-1}^c) of the length $2(n-1)$ ($2(n_c+1)$) with the form $(s_{j_{n-1}}^+, \dots, s_{j_1}^+, s_{j_{n-1}}^-, \dots, s_{j_1}^-)$ $((s_{j_{n-1}}^+, \dots, s_{j_{n-n_c-1}}^+, s_{j_{n-1}}^-, \dots, s_{j_{n-n_c-1}}^-))$, the configurations number $j_{n-1} = 1, \dots, L_{n-1}$ ($j_{n-1}^c = 1, \dots, L_{n-1}^c$), and with the complex weights $T_{\bar{j}_{n-1}}$ ($\bar{T}_{\bar{j}_{n-1}^c}$) whose norms are larger than a chosen cutoff (threshold) δ that sets the accuracy of the calculation. For $n_c < n$, we perform the trajectory re-indexing technique by removing the last element $s_{j_{n-n_c-1}}^\pm$ and summing up the weights of the resulted identical paths, therefore, a new number of unique trajectories \bar{k}_{n-1}^c with combined weights $\bar{T}_{\bar{k}_{n-1}^c}$ are obtained.

Step 3. The product in Eq. 3.41 (3.42) is constructed where the memory term is obtained according to Eq. 3.44 (3.45), the newly numbered configurations \bar{k}_n (\bar{k}_n^c) are obtained by adding all the possible new variables $s_n^+ = 0, 1$ and $s_n^- = 0, 1$ to the previous surviving paths \bar{j}_{n-1} (\bar{k}_{n-1}^c). “On-the-fly path selection” is implemented by comparing norms of all the newly numbered complex weights $T_{\bar{k}_n}$ ($\bar{T}_{\bar{k}_n^c}$) with δ to find all new noticeably contributing paths \bar{j}_n (\bar{j}_n^c) of the form $(s_{j_n}^+, s_{j_{n-1}}^+, \dots, s_{j_1}^+, s_{j_n}^-, s_{j_{n-1}}^-, \dots, s_{j_1}^-)$ $((s_{j_n}^+, s_{j_{n-1}}^+, \dots, s_{j_{n-n_c}}^+, s_{j_n}^-, s_{j_{n-1}}^-, \dots, s_{j_{n-n_c}}^-))$ with the weights $T_{\bar{j}_n}$ ($\bar{T}_{\bar{j}_n^c}$) whose norms are larger than δ . Only the configurations and weights of these new significantly contributing paths are stored. Total number of the paths \bar{j}_n (\bar{j}_n^c), i.e. L_n (L_n^c), is smaller than that of the paths

\bar{k}_n (\bar{k}_n^c) as a result of on the fly path filtering process which can be applied from the first propagation step.

Step 4. We obtain the augmented RDM (RQCDM) elements at the time step n , summing up over weights of the noticeably contributing configurations ending at a certain pair (s_n^+, s_n^-) as in Eq. 3.38 (3.39).

The procedure defined by steps 2–4 finds the most important contributing paths by an iterative construction, which is done “on-the-fly” and enables us to obtain the entire time evolution in a single run. The accuracy of the numerical results depends on three parameters that should be selected carefully; the time increment ε , the memory cutoff number n_c , and the threshold δ . The choice of εn_c is dictated by the effective temporal extension of the memory kernel (the memory length), which follows from the QD geometry and the coupling mechanism. As it is shown in figure 3.2, the choice of 4 ps length for the memory ($\varepsilon n_c = 4$ ps) is appropriate for the spherical QD with radius 5 nm and the deformation potential coupling to LA phonons. Therefore, we find that the memory length may also roughly be estimated by $2\tau_{ph} = 4a_e/v_s$, i.e., the time needed for a sound wave to cross the QD two times (3.91 ps). It turns out that the results converge for a time slice $\varepsilon = 0.4$ ps and the memory cutoff number $n_c = 10$. The threshold δ increases with the QD-cavity coupling strength g . The appropriate value for δ , in a given g , is obtained by comparing the results of few runs with different values δ until the results do not change notably with further decreasing δ . Parameters n_c and δ determine the total number of paths that need to be stored in the computer memory. The large number of paths that need to be memorized is the main limitation of the algorithm, especially for models with larger numbers of system states.

3.4 Two-Oscillator Model

A dispersion-related semi-empirical theory describing temperature dependence of the bandgap is based on the generally accepted interpretation that the temperature-dependent shrinkage of the exciton absorption and emission peak originates from the cumulative effect of mechanisms of electron–phonon interaction and thermal lattice expansion (Pässler, 2000). The real importance for a sufficiently general formulation of basic equations is the observation that, for both types of the qualitatively different gap shrinkage mechanisms, the contributions of the individual lattice oscillators with phonon energies $\varepsilon = \varepsilon_{jq} = \hbar\omega_{jq}$ [j branch, q wave vector] are proportional to the averages of Bose-Einstein phonon occupation number, $\bar{n}(\varepsilon; T) = [\exp(\varepsilon/k_B T) - 1]^{-1}$. Thus the temperature-dependent shift of PL peak can be generally represented by an integral of the form (Pässler, 2000, 2001)

$$E_g(T) = E_g(0) - \frac{\alpha}{k_B} \int_0^\infty d\varepsilon \frac{w(\varepsilon) \varepsilon}{\exp(\varepsilon/k_B T) - 1}, \quad (3.46)$$

where k_B is the Boltzmann constant, $E_g(0)$ is the bandgap at zero temperature [zero bandgap (ZBG)], and $w(\varepsilon)$ is a normalized weighting function as $\int d\varepsilon w(\varepsilon) = 1$, $\alpha = -dE_g(T)/dT|_{T \rightarrow \infty}$, which is temperature coefficient of the bandgap width in the high temperature limit. Different assumptions for $w(\varepsilon)$ lead to the several models. The weighting function may be expressed as a finite sequence of discrete peaks located at certain phonon energies $\varepsilon_i = \hbar\omega_i = k_B\theta_i$, $i = 1; 2; \dots; N$ (where θ_i are the associated phonon temperatures), i.e., (Pässler, 2000),

$$w(\varepsilon) = \sum_{i=1}^N W_i \delta(\varepsilon - \varepsilon_i), \quad (3.47)$$

where $\sum_{i=1}^N W_i = 1$. Inserting this discrete model function into Eq. 3.46, we obtain the T dependence expression of the form

$$E_g(T) = E_g(0) - \alpha \sum_{i=1}^N \frac{W_i \theta_i}{\exp(\theta_i/T) - 1}. \quad (3.48)$$

The simplest version is a single-oscillator model ($N = 1$) (Viña, Logothetidis, & Cardona, 1984; Pässler, 1997). This corresponds to the case of vanishing phonon dispersion, where the effective phonon temperature, $\theta = \varepsilon/k_B$, is the same with the phonon temperature, $\theta_1 = \varepsilon_1/k_B$, associated with the single oscillator in consideration. Thus the $E_g(T)$ dependence reduces to the Fan (Vina) model with the form (H. Y. Fan, 1951, 1967; Pässler, 1997, 2001, 2003)

$$E_g(T) = E_g(0) - \frac{\alpha \theta}{\exp(\theta/T) - 1} = E_g(0) - \frac{\alpha \theta}{2} \left[\coth\left(\frac{\theta}{2T}\right) - 1 \right], \quad (3.49)$$

where $\theta = \hbar\Omega/k_B$ is the temperature of the phonon oscillator with the angular frequency ω . Therefore, comparing with the Fan equation (H. Y. Fan, 1951, 1967; Yeo et al., 2011),

$$E_g(T) = E_g(0) - A(\langle n \rangle + const), \quad (3.50)$$

where $\langle n \rangle = 1/(e^{\hbar\omega/k_B T} - 1)$ is the Bose–Einstein statistics of phonons, the Fan parameter can be written as

$$A = \alpha \hbar \omega / k_B = \frac{e^2}{\sqrt{2} \hbar} \sqrt{m_0 \hbar \omega} \frac{1}{4\pi \varepsilon'} \left(\frac{1}{\varepsilon'_\infty} - \frac{1}{\varepsilon'_0} \right) \left(\sqrt{\frac{m_e}{m_0}} + \sqrt{\frac{m_h}{m_0}} \right), \quad (3.51)$$

where ε' is the dielectric constant, ε'_∞ and ε'_0 are the static and high frequency dielectric constants, respectively, m_0 is the free electron mass, and m_e and m_h are the effective electron and hole masses, respectively. The Fan (Vina) model gives a total of three fit param-

eters. For $N = 2$, the weighting function is given by $w(\varepsilon) = W_1 \delta(\varepsilon - \varepsilon_1) + W_2 \delta(\varepsilon - \varepsilon_2)$, where $\varepsilon_{1,2}$ are the energies of the oscillators with weights $W_{1,2}$. In the TOM $E_g(T)$ is then given by (Pässler, 2001; Ortner et al., 2005)

$$E_g(T) = E_g(0) - \alpha \left(\frac{W_1 \theta_1}{\exp(\theta_1/T) - 1} + \frac{(1 - W_1) \theta_2}{\exp(\theta_2/T) - 1} \right), \quad (3.52)$$

with the phonon temperatures and the average phonon temperature

$$\theta_{1,2} = \varepsilon_{1,2}/k_B, \quad \theta = W_1 \theta_1 + (1 - W_1) \theta_2. \quad (3.53)$$

The dispersion coefficient is expressed as

$$\Delta = \sqrt{(\theta_2 - \theta)(\theta - \theta_1)}/\theta. \quad (3.54)$$

The number of parameters that should be obtained using fit is 5. We set the high-energy oscillator, as it comprises TO and LO phonons, and the low-energy one, as it contains TA and LA phonons. We apply the TOM to fit the experimental data of the T-dependent shift of the bandgap peak of 15 available self-organised QD (SOQD) samples, with different MLs or number of layers, using the least squares technique. The TA phonon energy peaks for bulk InAs are 6.2 and 7.1 meV, and the LA ones are 18.5 and 20.5 meV (Madelung, 1982–89). Therefore we bound the low-energy oscillator to the energy interval 6.2–20.5 meV. The TO and LO phonon energy peaks for InAs QDs are 30.3 and 33.2 meV, respectively (Heitz, Makhmetzhanov, Stier, Madhukar, & Bimberg, 2000; Heitz et al., 1999, 1997). Thus we consider the interval 30.3-33.2 meV as the permitted energy interval for the high-energy oscillator. In the case of InGaAs/GaAs SOQDs, with 18 MLs (taken from (Z. F. Wei et al., 2005)), we guess AC phonon energy peaks as shown in Table 3.1. We also bound the OP phonon energy peaks to the energy interval 34.8-37.5

meV because TO and LO phonon energy peaks of InAs QDs are shifted by 3.5 ± 0.1 and 5.8 ± 1.7 meV, respectively, compared to bulk ones; therefore we apply these shifts to TO and LO phonon energy peaks of InGaAs bulk to derive the high-energy oscillator interval for InGaAs QDs. Table 3.1 shows the phonon energy peaks for bulk GaAs, InAs, and InGaAs (Madelung, 1982–89). We guess InGaAs data from InAs and GaAs ones.

Table 3.1: Phonon Energy Peaks for GaAs, InAs, and InGaAs Bulk

Bulk Material	TA Peak (meV)	LA Peak (meV)	TO Peak (meV)	LO Peak (meV)
InAs	6.2, 7.1	18.5, 20.5	26.7, 26.9	25.7, 29.1
GaAs	7.7, 9.8	25.8, 28.2	31.4, 33.3	29.7, 30, 35.5
InGaAs	7.1, 7.7	20.5, 25.8	26.9, 31.4	29.1, 29.7, 30

It has generally been approved that exciton–phonon interactions are through AC phonons at temperatures less than about 100 K (Muljarov & Zimmermann, 2004; Borri et al., 2001; Uskov et al., 2000; Takagahara, 1999; Schmitt-Rink et al., 1987). Therefore, in fitting a particular dataset using the least squares technique, we try to adjust the first fitted part just as a result of contribution of AC phonons. In addition, among several possible ways to fit the dataset, we try to find the way consisting of the least possible parts and with the minimum value of the mean squared 2-norm of the residual. The squared 2-norm of the residual (SNR) is sum of squared residuals, minimized by the least squares method. The two last above-mentioned conditions mathematically means

$$\begin{aligned}
 \min(SNR_{mean}, n) &= \min \left(\sum_{i=1}^{n_{\min}} SNR(i) \right) \\
 &= \min \left(\frac{\sum_{i=1}^{n_{\min}} \left(m_i \times \sum_{j=1}^{m_i} \left| E_{g_i}^{fit}(T_j) - E_{g_i}^{real}(T_j) \right|^2 \right)}{\sum_{i=1}^{n_{\min}} m_i + (n_{\min} - 1)} \right),
 \end{aligned} \tag{3.55}$$

where n_{\min} is the number of the least possible parts, and m_i is the number of the experimental points in i^{th} part. E_g^{fit} and E_g^{real} are the values of bandgap energy obtained using

fit and experiment, respectively. Under the aforementioned conditions, TOM can fit all the 15 samples datasets with good precision. For a certain sample, we define a total temperature interval, for each of AC (1) or OP (2) phonons, in which they contribute to the shift of PL energy peak according to the following formula

$$\Delta T_{tot}^{1(2)} = \sum_{l=1}^{n_{\min}} W_l^{1(2)} \Delta T_l^{trns}, \quad (3.56)$$

where $T_{tot}^{1(2)}$ is the total temperature interval and ΔT_l^{trns} are the lengths of the T-intervals, which are calculated as $\Delta T_l^{trns} = T_l^{trns} - T_{l-1}^{trns}$ where T_l^{trns} is the transition temperature from one part to the next one. We refer to these total temperature intervals as “total AC and OP phonon contributions.”

CHAPTER 4

RESULTS AND DISCUSSIONS

4.1 Introduction

In the first part of this chapter, we present the results obtained from numerically accurate RTPI simulation of the QD-cavity system dynamics initially prepared in the state $|1\rangle$, i.e. the QD is at ES with no photon within the cavity, and coupled to a LA phonon bath through deformation potential. The effects induced by impure dephasing of the dressed states (VRO damping), originated from exciton coupling to LA phonons and from dissipations including QD and cavity losses, on the quantum dynamics of the QD-cavity system are investigated. In the second part of the chapter, we present results of TOM projection of temperature-dependent shift of PL peak for In(Ga)As QDs with different number of monolayers and layers. We investigate the role and contributions of AC and OP phonons at the PL peak shift.

4.2 Quantum Dot-Cavity Quantum Electrodynamics: Impure Dephasing-Induced Effects

In terms of the decay dynamics, the emitter-cavity coupling efficiency can be divided into three different dynamical regimes; weak, intermediate, and coherent (Madsen et al., 2011). The coupling regimes are also divided into three regimes of weak, strong, and coherent in terms of appearance and resolution of so-called vacuum Rabi splitting (VRS) (Auffèves et al., 2010). A high degree controllable QD-cavity platform demands a comprehensive understanding of these different coupling regimes, especially, the strong coupling (SC) and coherent coupling (CC) regimes; The most striking feature of SC is the splitting of the spectral shape when the cavity and the QD are at resonance, in this case, the cavity and the QD lines do not superimpose but anticross with a splitting related to

the coupling strength (Laussy et al., 2008). This feature is called vacuum Rabi splitting (VRS) and has been observed several times (Reithmaier et al., 2004; Yoshie et al., 2004; Khitrova, Gibbs, Kira, Koch, & Scherer, 2006; Press et al., 2007; Peter et al., 2005; Hennessey et al., 2007). The most noticeable change of emission properties occurs clearly in the CC regime, where the usual irreversible spontaneous emission changes to a reversible exchange of energy between the QD and the cavity mode, resulting in so-called clear vacuum Rabi oscillation (VRO) which has been observed for laser-driven QDs (Stievater et al., 2001; Ramsay, Godden, et al., 2010; Ramsay, Gopal, et al., 2010).

Figure 4.1 shows the decay dynamics of the QD-cavity system for different coupling strengths at $T = 0$ K with the recombination rate $\gamma_r (= 0.001 ps^{-1}) = 0.0063 rad/ps = 4.135 \mu eV$ and the cavity decay rate $\kappa (= 0.0242 ps^{-1}) = 0.1519 rad/ps = 100 \mu eV$. At $g = 0 \mu eV$, where the QD and cavity are uncoupled. The QD ES decays exponentially with the rate γ_r . As g increases, the exponential decay is gradually transformed to a nonexponential one with an increasing rate. It can be seen that the population decay rate varies more rapidly for the intermediate QD-cavity coupling strengths compared to the small and large coupling strengths. Three distinct dynamical regimes of the coupling strength, in terms of the decay dynamics, can be identified in the figure as follows:

(a) Weak coupling (WC) regime or Markovian regime (corresponding to a bad cavity and a narrow linewidth emitter) where the state $|1\rangle$ decays exponentially in time with a Purcell enhanced rate (Madsen et al., 2011). In this regime, the QD-cavity system does not have time enough to couple coherently before the phonon-induced pure dephasing and irreversible decay into various radiative routes occur (Buckley, Rivoire, & Vuckovic, 2012). The WC regime, in this case, extends up to about $g = 15 \mu eV$ where the corresponding decay curve starts to deviate from an exponential decay significantly, as shown in figure 4.2. The condition $2g \ll (\kappa + \gamma_r)/2 + \gamma_{ph}$, offered in (Madsen et al., 2011), is fulfilled in this regime by extracting the value of phonon-induced pure dephasing rate,

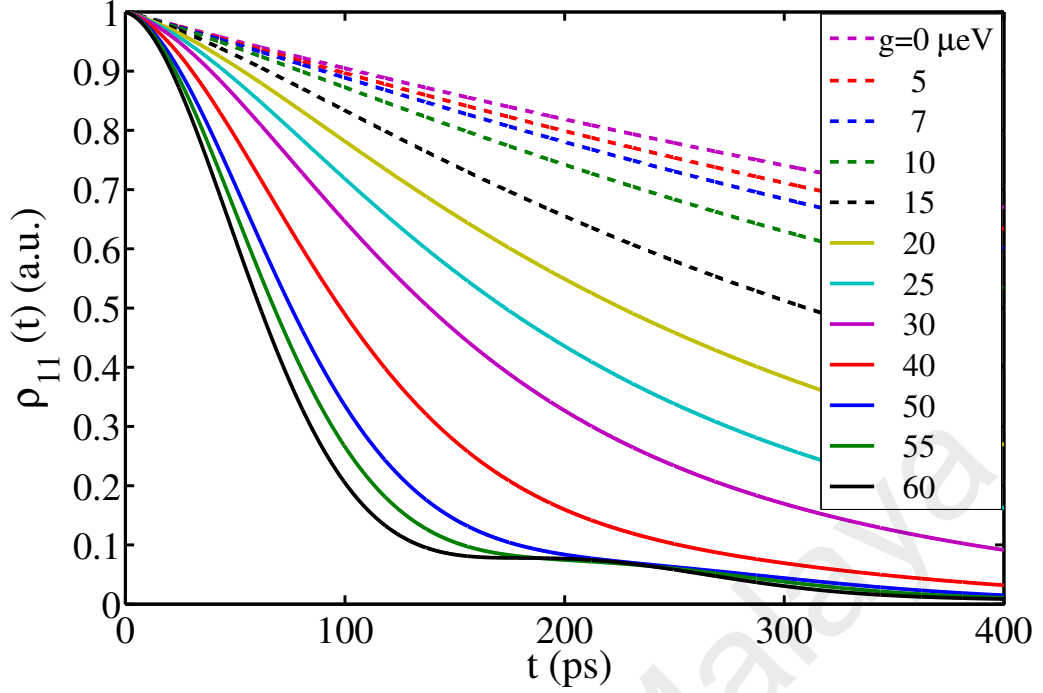


Figure 4.1: The decay dynamics of the QD-cavity system for different coupling strengths at $T = 0$ K with the recombination rate $\gamma_r (= 0.001 \text{ ps}^{-1}) = 0.0063 \text{ rad/ps} = 4.135 \text{ } \mu\text{eV}$ and the cavity decay rate $\kappa (= 0.0242 \text{ ps}^{-1}) = 0.1519 \text{ rad/ps} = 100 \text{ } \mu\text{eV}$. Three distinct dynamical regimes of weak, intermediate (strong), and coherent coupling can be determined in the figure.

γ_{ph} , from our microscopic RTPI calculation. However, this condition and the condition presented for the intermediate coupling (IC) regime, i.e. $2g \leq (\kappa + \gamma_r)/2 + \gamma_{ph}$, are not precise and do not provide a clear boundary between WC and IC regimes. Considering $g = 15 \text{ } \mu\text{eV}$ as the upper boundary of the WC regime, we may take the condition $2g \leq ((\kappa + \gamma_r)/2 + \gamma_{ph})/2$ into account, setting an upper boundary for the WC regime, for more accurate description of this regime. The nonzero value of phonon-induced pure dephasing rate $\gamma_{ph} = 0.0043 \text{ ps}^{-1} = 17.70 \text{ } \mu\text{eV}$, at $g = 15 \text{ } \mu\text{eV}$, is extracted from our microscopic RTPI calculation, as will be explained later.

(b) Intermediate coupling (IC) regime where the dynamics is non-Markovian leading to a nonexponential decay in time. In this regime, the state $|1\rangle$ decays irreversibly but non-exponentially due to the feedback from the cavity. The IC regime starts at about $g = 15 \text{ } \mu\text{eV}$ and continues up to about $g = 60 \text{ } \mu\text{eV}$. Therefore, it is inferred that the condition

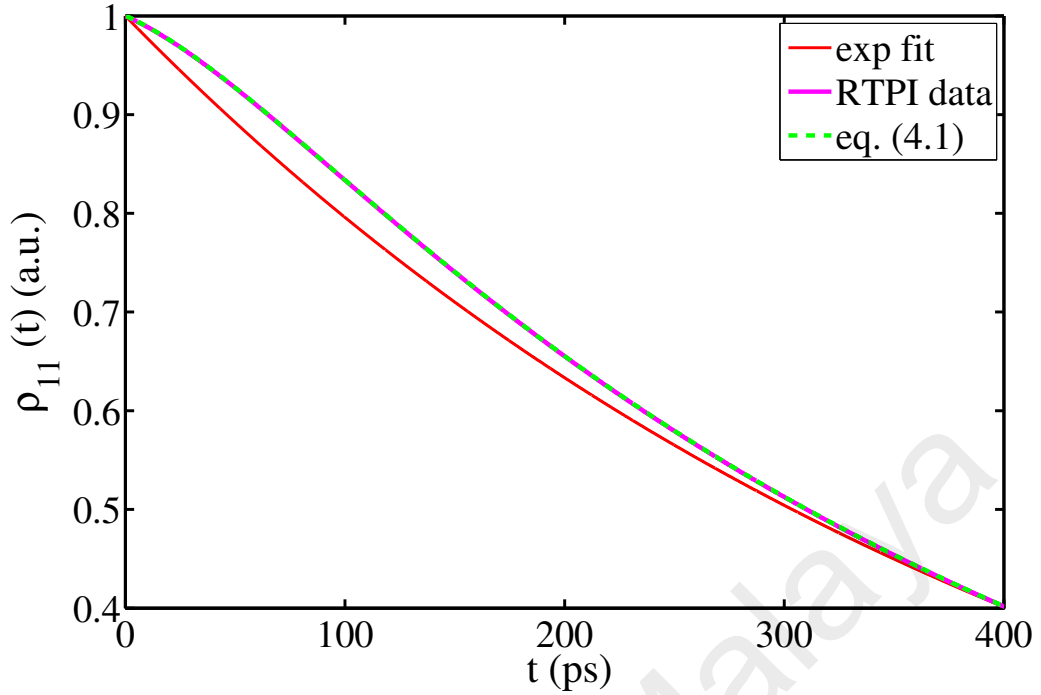


Figure 4.2: A comparison between the actual decay (pink), obtained using the numerical RTPI calculations, an exponential decay (red), obtained by fitting a single exponential to the actual decay, and a fit of the actual decay by using Eq. 4.1 (green) at $g = 15 \mu eV$ and $T = 0 K$.

$((\kappa + \gamma_r)/2 + \gamma_{ph})/2 \leq 2g \leq 2((\kappa + \gamma_r)/2 + \gamma_{ph})$ is satisfied for this regime. This condition modifies the condition given in Ref. (Madsen et al., 2011) setting a lower boundary and a higher upper boundary for the IC regime. It originates from the fact that our model is more accurate and elaborated compared to the model applied in Ref. (Madsen et al., 2011) which is an approximate model for moderate g (Madsen et al., 2011).

(c) The third regime is the coherent and non-Markovian regime where the time scale of forming coherent coupling between the QD and the cavity field is shorter than that of the pure dephasing and dissipations, which leads to re-excitation of the state in a reversible evolution. Consequently, clear vacuum Rabi oscillation (VRO) occurs. As it is seen in the figure, the coherent coupling (CC) regime starts at about $g = 60 \mu eV$, which means that the condition $(\kappa + \gamma_r)/2 + \gamma_{ph} \leq g$ should be satisfied in this regime. Our condition for the CC regime modifies the condition given in Ref. (Madsen et al., 2011) as well.

There is another classification of different operating regimes, in the literature, in

terms of appearance and resolution of so-called vacuum Rabi splitting (VRS). In this categorization, the regimes are called WC, SC, and CC. The SC is reached when the VRS occurs, i.e. spontaneous emission spectrum of the resonant QD-cavity system consists of two peaks with distinct frequencies and the equal width $(\kappa + \gamma_r + \gamma_{ph})/2$. The CC regime is obtained when the doublet is clearly resolved, which is the spectral counterpart of (clear) VRO (Auffèves et al., 2010). Our condition for the CC coupling regime means that clear VRO is reached when the doublet separation is larger than the sum of full width at half maximum (FWHM) of its peaks.

The nonexponential decay of the state $|1\rangle$, at the onset of the IC regime, can be explained by the existence of VRO with a very small frequency (see figure 4.10(b)), which we call unclear VRO originating from formation of the dressed states of the states $|0\rangle$ and $|1\rangle$. Therefore, the dynamical IC regime should match the SC regime; the onset of the IC regime, $g = 15 \mu eV$, almost matches with the bifurcation point (the onset of SC regime), considering the condition $|\kappa - \gamma_r - \gamma_{ph}|/2 \leq 2g$ for the SC regime (Auffèves et al., 2010; Reithmaier et al., 2004; Yoshie et al., 2004; Khitrova et al., 2006; Press et al., 2007; Peter et al., 2005; Hennessy et al., 2007; Vagov et al., 2014; Andreani et al., 1999; Rudin & Reinecke, 1999) with extracted values of γ_r from our microscopic RTPI calculation. Therefore, after this, we use SC instead of IC and call the three different dynamical regimes as WC, SC, and CC.

In order to distinguish between the role of population decay and impure dephasing (damping) induced by LA phonons, QD, and cavity dissipations on the quantum dynamics of the QD-cavity system, we have used the following phenomenological expression to reproduce the numerically exact RTPI results

$$\rho_{11}(t) = W_1 e^{-\gamma t} + W_2 e^{-\gamma_2 t} \cos(\omega_0 t + \theta) \quad (4.1)$$

where the first term, the decay part, corresponds to the population decay which is an exponential evolution while the second term, the damping (impure dephasing) part, is related to damping (impure dephasing) of VRO (of coherent coupling between the dressed states). W_1 and W_2 are the weighting coefficients, γ_1 is the effective population decay rate caused by the carrier recombination and cavity loss rates, γ_2 is the effective impure dephasing or VRO damping rate originated from the LA phonon-induced pure dephasing, the carrier recombination, and cavity dissipation rates. ω_0 is the VRO frequency (VRS) and θ is its initial phase. All the six parameters should be obtained by fitting equation 4.1 to the decay curves and depend on the QD-cavity coupling g , the temperature T , the loss mechanisms, and the QD parameters that enter into the carrier-phonon correlation function (Eq. 3.22). The proposed equation 4.1 projects perfectly the decay curves relating to different g and T , as shown in figure 4.3 for two cases. We also use this equation to reproduce the state population of the dissipation-less QD-cavity system, obtained from our microscopic RTPI calculation, in order to extract the phonon-induced pure dephasing rates at different g . Examples of fitting equation 4.1 to the exact state $|1\rangle$ population are shown in figure 4.4 for two cases. In this case, the state population reaches the superposition of the states $|0\rangle$ and $|1\rangle$ after complete damping of VRO. According to the extracted values of γ_{ph} and γ_2 , we propose the approximate equation $\gamma_2 \approx (\kappa + \gamma_r)/2 + \gamma_{ph}$. Therefore, the proposed conditions for determining different coupling regimes equally mean that for the SC regime the condition $\gamma_2/4 \leq g \leq \gamma_2$ is satisfied.

The corresponding spectra of the QD-cavity decay curves can be calculated by performing the Fourier transform of the equation 4.1 to obtain the real part of $\rho_{11}(t)$ in the spectral domain as

$$Re(\rho_{11}(\omega)) = \frac{W_1 \gamma_1}{\gamma_1^2 + \omega^2} + \frac{W_2}{2} \left[\frac{\gamma_2 \cos \theta + (\omega - \omega_0) \sin \theta}{\gamma_2^2 + (\omega - \omega_0)^2} + \frac{\gamma_2 \cos \theta - (\omega + \omega_0) \sin \theta}{\gamma_2^2 + (\omega + \omega_0)^2} \right], \quad (4.2)$$

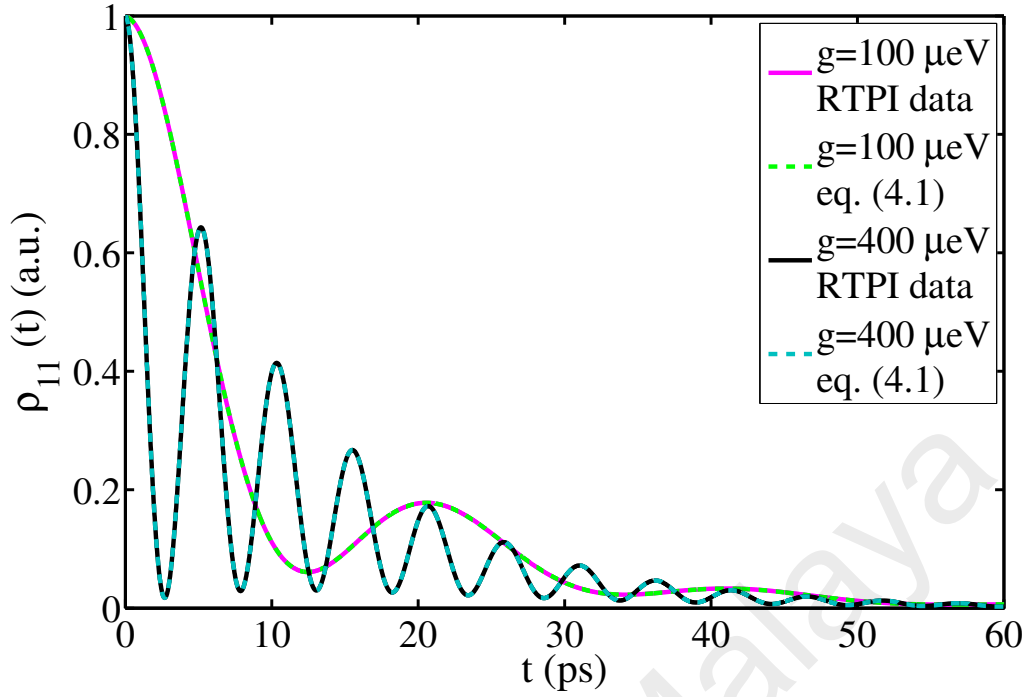


Figure 4.3: Comparison between the decay curves, obtained by RTPI approach, and a fit of the phenomenological expression 4.1 for two cases. The phenomenological expression fits the numerically exact results of the QD-cavity decay curves perfectly.

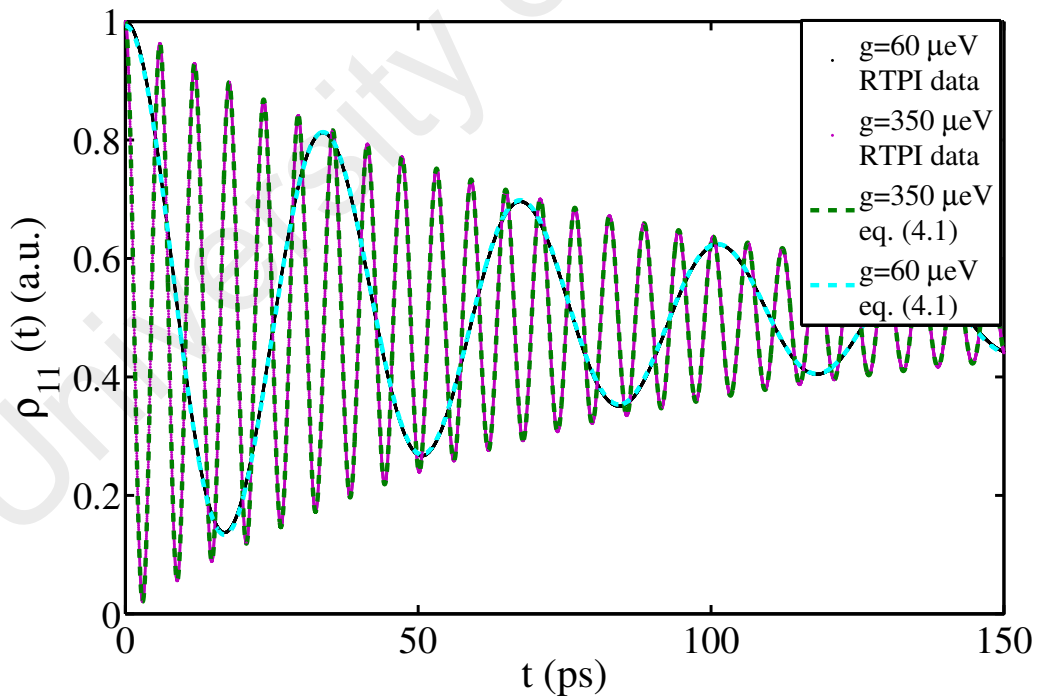


Figure 4.4: Two examples of fitting equation 4.1 to the exact state $|1\rangle$ population of the dissipation-less QD-cavity system, obtained from our microscopic RTPI calculation. The phenomenological expression projects the exact state population perfectly as well.

where the Fourier transform is defined as $\rho_{11}(\omega) = \int_0^\infty e^{-i\omega t} \rho_{11}(t) dt$. Figure 4.5 shows the corresponding normalized spectra of figure 4.1 calculated for different g at $T = 0 K$.

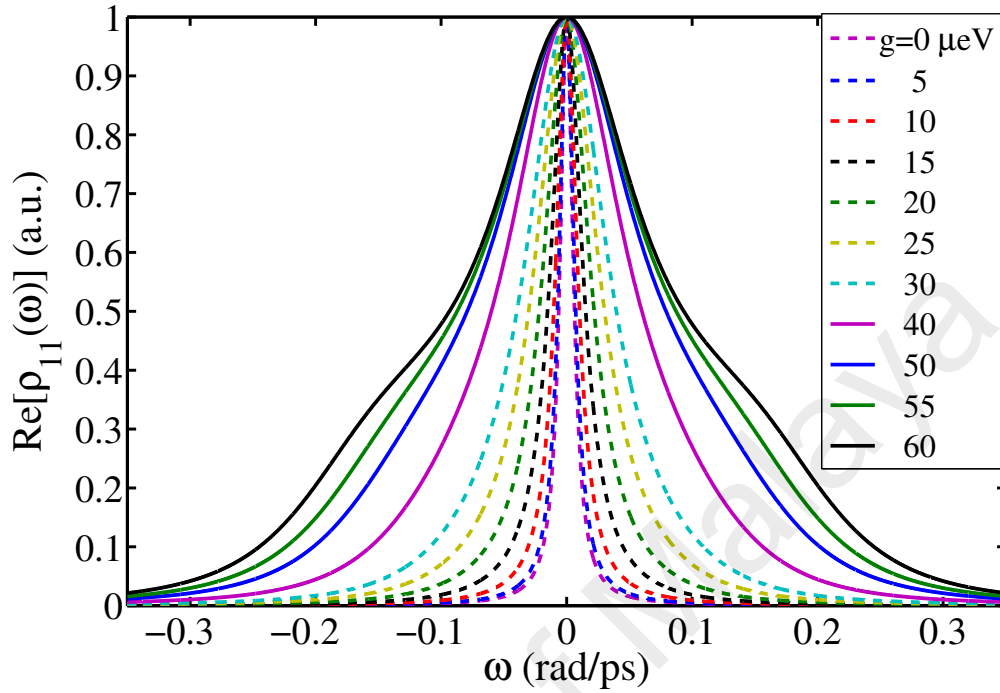


Figure 4.5: The corresponding normalized spectra, $Re(\rho_{11}(\omega))$, of the decay curves shown in figure 4.1, calculated for different values of the QD-cavity coupling g at $T = 0 K$ with $\gamma_r (= 0.001 ps^{-1}) = 0.0063 rad/ps = 4.135 \mu eV$ and $\kappa (= 0.0242 ps^{-1}) = 0.1519 rad/ps = 100 \mu eV$. The separated sideband peaks appear clearly at about $g = 60 \mu eV$, indicating the onset of the CC regime.

Equivalent of the decay part, in the spectral representation, is a Lorentzian function. A careful observation reveals that the second term (the pure dephasing part), at Eq. 4.2, begins to affect the Lorentzian spectrum notably at around $g = 15 \mu eV$ by decreasing its wings and FWHM (see Figs. 4.9 and 4.10), as a result of the existence of unclear VRO at the corresponding decay curve. This is the sign of system transfer from WC to SC regime in the spectral representation of the diagonal RQCDM element. As shown in the figure, separated sideband peaks appear obviously at about $g = 60 \mu eV$, as a result of the appearance of clear VRO, which indicate the crossover point between the SC and CC regimes. FWHM of the central peak of the spectra increases with g up to a certain value, then, a rollover occurs. We show this feature clearly in figure 4.7. Note that the spectra

presented in figure 4.5 are not the same as spontaneous emission spectra of the QD-cavity system. The spontaneous emission spectrum is a singlet spectrum in the weak coupling regime as the states $|0\rangle$ and $|1\rangle$ are at resonance. It splits into a doublet at the SC and CC regimes as a result of formation of the dressed states from the states $|0\rangle$ and $|1\rangle$. Figure 4.6 shows the normalized spectrum, Lorentzian part, and impure dephasing part, plotted for $g= 60 \mu eV$.

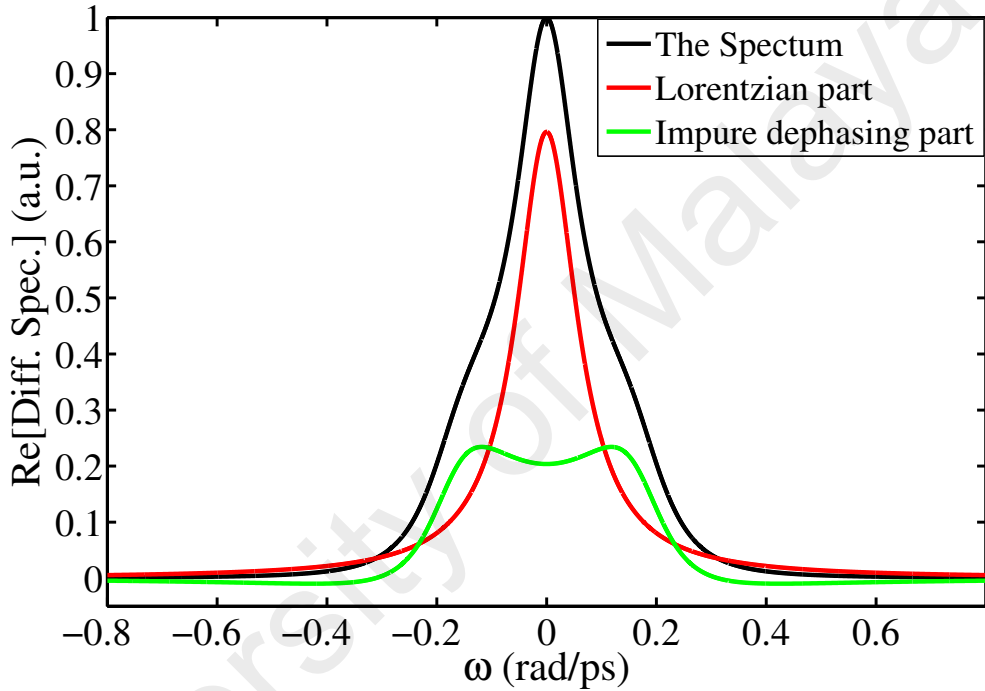


Figure 4.6: The normalized spectrum (black), Lorentzian part (red), and impure dephasing part (green), plotted for $g= 60 \mu eV$ and $T= 0 K$. The spectrum is obtained as a result of combination of the Lorentzian and impure dephasing part.

Shown in figure 4.7 is FWHM of the central peak of the spectra (CPFWM) for three different temperatures $T = 0, 20$ and $80 K$ as a function of g . The cubic spline data interpolation has been used to connect the many points (not shown) obtained from numerically exact RTPI calculations. According to figure 4.7, the CPFWM, at each T , starts from $2\gamma_r$ at $g = 0 eV$ and grows up to a maximum value with increase of g to a value which corresponds to the CC regime in that T , then, it decreases to an asymptotic line at $\kappa + \gamma_r (= 0.1582 rad/ps)$ with further enhancement of g . The maximum value of

CPFWM corresponds to $g = 71.25$; 108.03 ; and $264.02 \mu eV$ at $T = 0, 20$, and $80 K$, respectively. As can be seen in the figure, the width of the central band has a temperature-dependence for the coupling strengths smaller than about $g = 300 \mu eV$, its maximum also corresponds to a smaller g and is more obvious at a lower temperature.

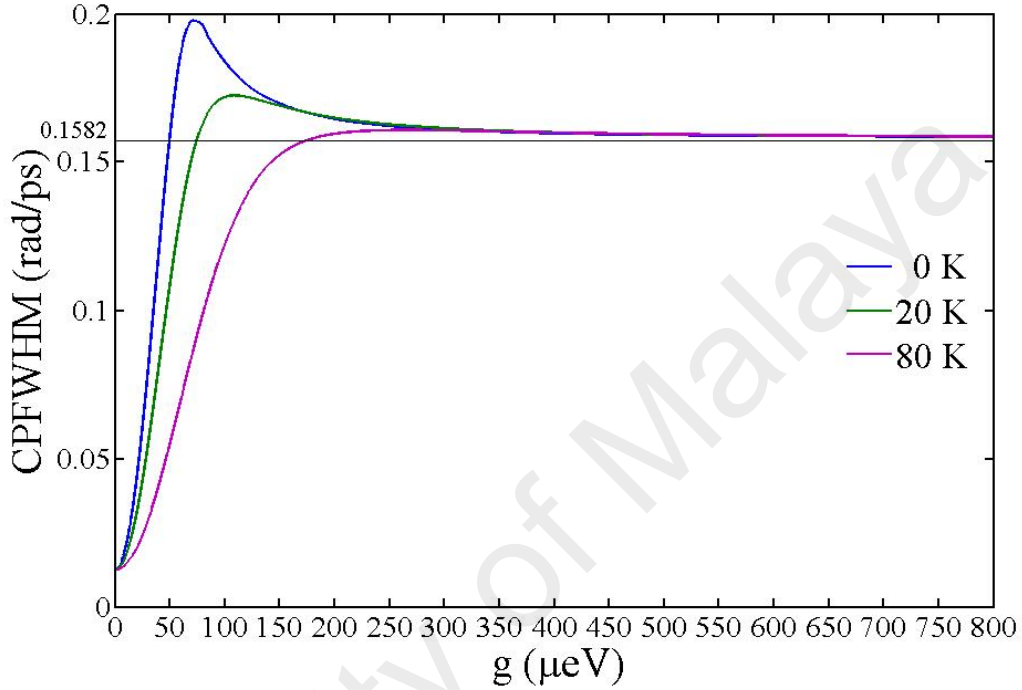


Figure 4.7: The central peak FWHM (CPFWM) extracted from the spectra for three different temperatures $T = 0, 20$ and $80 K$ as a function of g . $\gamma_r = 0.0063 \text{ rad/ps} = 4.135 \mu eV$ and $\kappa = 0.1519 \text{ rad/ps} = 100 \mu eV$. The cubic spline data interpolation has been used to connect the many points (not shown) calculated by numerically exact RTPI method.

We compare the behavior of FWHM of the effective population decay, $\Gamma_1 = 2\gamma_1$, with that of CPFWM for different g at $T = 0 K$ in figure 4.8. It can be seen that the effective population decay rate increases from the carrier recombination rate γ_r up to the upper limit $(\gamma_r + \kappa)/2$ with the coupling strength. It turns out that the highest achievable emission rate is $(\gamma_r + \kappa)/2$, which is in agreement with the previous finding (Buckley et al., 2012). The CPFWM and Γ_1 have almost the same values up to about $g = 27 \mu eV$, as shown in the inset of figure 4.8, which means the effective population decay rate is the most prominent contributor to the CPFWM. For larger intermediate QD-cavity coupling strengths, the impure dephasing (damping) part contributes to CPFWM notably, so that

it grows to larger values than Γ_1 . As g is enhanced further, contribution of the damping part to CPFWM decreases, as the sidebands appear in the spectra (see figure 4.10), which results in approaching CPFWM to the asymptotic line with the value $(\gamma_r + \kappa)$.

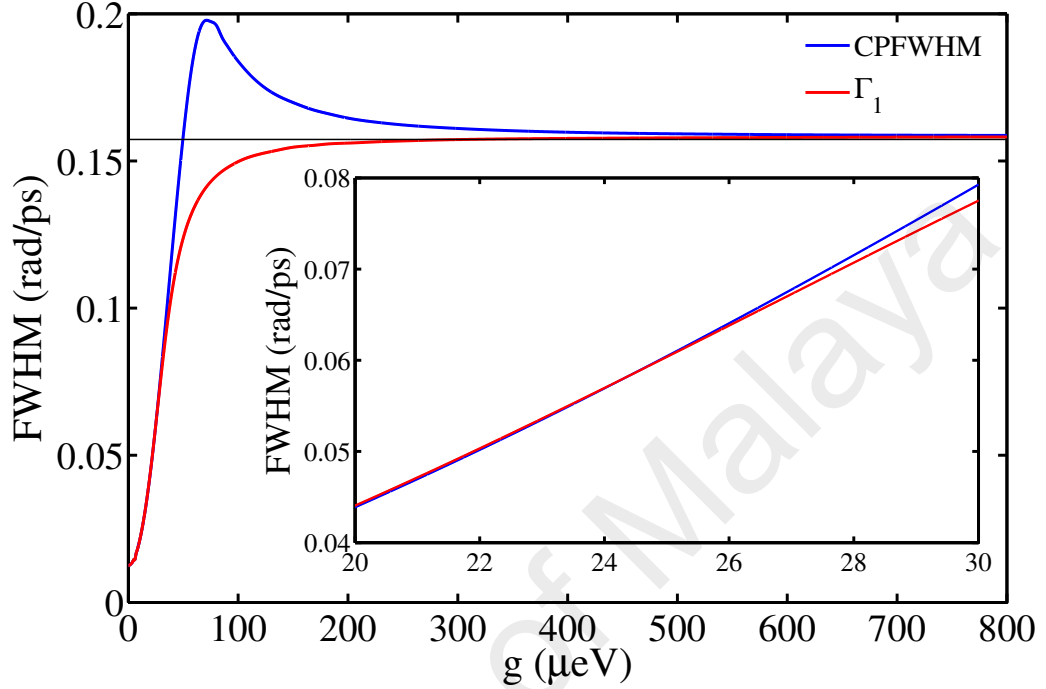


Figure 4.8: Γ_1 (FWHM of the effective population decay) and CPFWM versus g at $T = 0$ K. The inset shows Γ_1 and CPFWM at a short g interval. $\gamma_r = 0.0063$ rad/ps = 4.135 μ eV and $\kappa = 0.1519$ rad/ps = 100 μ eV. The cubic spline data interpolation has been used to connect the many points (not shown) calculated by numerically exact RTPPI method.

For more accurate investigation of the role of impure dephasing part in CPFWM, we introduce a new quantity $\delta_{FWHM} = CPFWM - \Gamma_1$ that can also be applied in determining the three different QD-cavity coupling regimes. Figure 4.9 shows the plot of δ_{FWHM} versus g at three different temperatures $T = 0, 20,$ and 80 K. As shown in the inset of figure 4.9, the introduced quantity δ_{FWHM} has considerable nonzero values above a critical value of g that can be considered as the crossover point from the WC to SC regime. This is because of the existence of unclear VRO, which leads to the significant contribution of the impure dephasing part to the decay dynamics and to central peaks of the spectra beyond that critical value of g (see figure 4.10(b)). Its contribution to the central peaks of the spectra (CPFWM) increases up to a maximum value with further

enhancement of g within the SC regime as a result of an increasing unclear VRO frequency (Figs. 4.9 and 4.10). This significant contribution leads to a decrease (except to $T = 80 K$) and then, an increase of CPFWHM compared to Γ_1 . The coupling strength g for which the contribution is maximum can be thought of as the onset of the CC regime as the sidebands (clear VRO) appear(s) clearly at about that g . For example, at $T = 0 K$, the maximum value of δ_{FWHM} corresponds to $g = 67.78 \mu eV$.

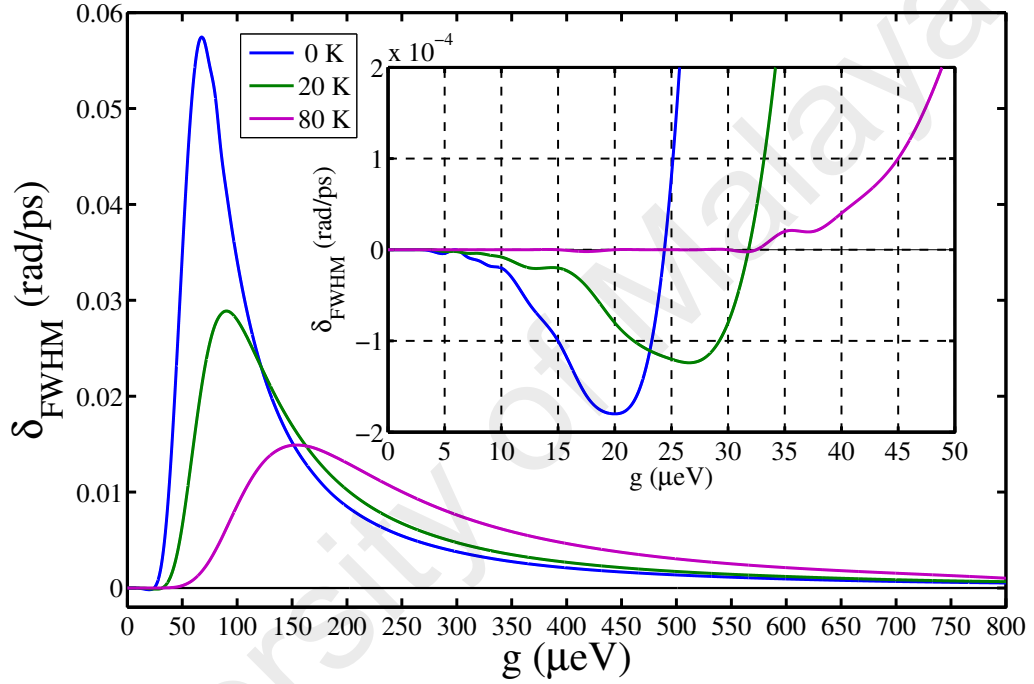


Figure 4.9: The introduced quantity δ_{FWHM} , which is difference of CPFWHM and Γ_1 , for different QD-cavity coupling strengths at three diverse temperatures $T = 0, 20$ and $80 K$. The inset of figure 4.9 shows the introduced quantity as the main figure at small g .

Figure 4.10(a) presents the normalized impure dephasing spectra (the second term at Eq. 4.2) for different coupling strengths at $T = 0 K$. Figure 4.10(b) shows the same spectra as figure 4.10(a) only for small g for a better view. We can clearly see in figure 4.10(b) that the impure dephasing spectra include a broadening and increasing central peak from about $g = 15 \mu eV$ up to $g = 50 \mu eV$. This phenomenon corresponds to the SC regime where the VRO is not clear and has very small frequencies. For larger g the impure dephasing spectra split as clear growing sidebands appear at about $g = 65 \mu eV$

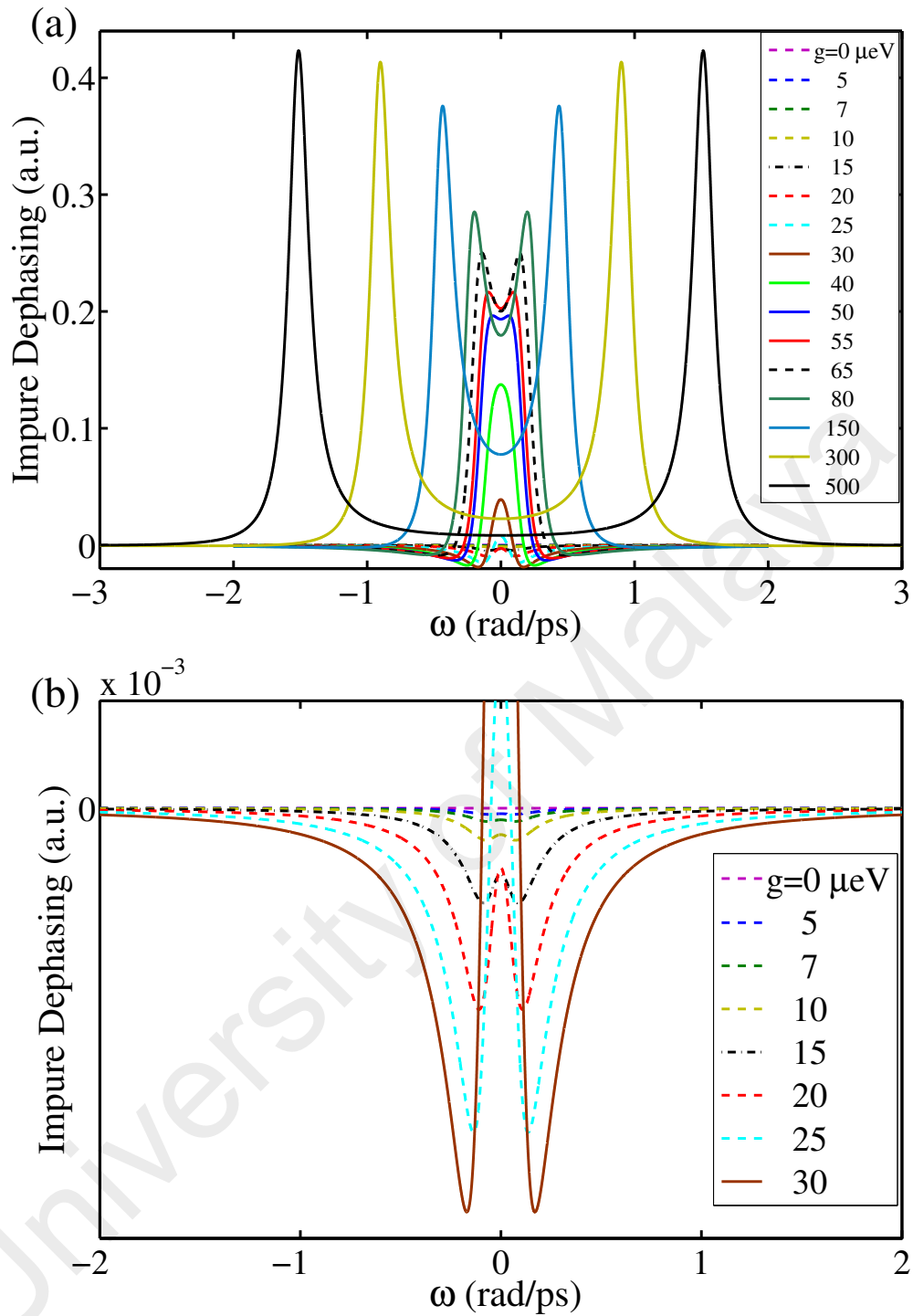


Figure 4.10: (a) The normalized impure dephasing spectra for different g at $T = 0 K$. As g increases within the CC regime, a rollover occurs and the contribution of (FWHM of) the impure dephasing spectra to (FWHM of) the central peak of the spectra, $Re(\rho_{11}(\omega))$, decreases to zero as a result of increasing clear VRO frequency which leads to growing separated sidebands. (b) The normalized impure dephasing spectra only for different small g at $T = 0 K$ for a better view. The parameters $\gamma_r = 0.001 ps^{-1} = 0.0063 rad/ps$ and $\kappa = 0.0242 ps^{-1} = 0.1519 rad/ps$ were used.

and beyond, as a result of increasing clear VRO frequency. In other word, VRO has a very small frequency (unclear VRO), as a result of formation of the dressed states of the

QD-cavity states, at the onset of the SC regime. Its frequency increases with the coupling strength within the SC regime, leading to the impure dephasing spectra with a broadening and growing single central peak. At the onset of the CC regime, with more increase of the VRO frequency, the clear VRO appears in the decay curve and the corresponding impure dephasing spectrum splits (the sidebands appear). With more enhancement of the coupling strength (more increase of clear VRO frequency), the sidebands grow and split further. Therefore, the contribution of the impure dephasing spectra to the central band of the spectra, $Re(\rho_{11}(\omega))$, grows with the coupling strength up to about $g \approx 65 \mu eV$. Above this value, a rollover occurs and the contribution of the impure dephasing term to the central peak of the spectra (CPFWM) gradually decreases to zero (Figs. 4.9 and 4.10). This means that, at the very large coupling constants, CPFWM once again originates only from the effective population decay rate and the effective VRO damping rate only contributes to FWHM of the sidebands of the triplet spectra.

According to figure 4.9, assuming $|\delta_{FWHM}| = 1 \times 10^{-4} \text{ rad/ps}$ is a considerable nonzero value, the SC regime begins at about $g = 15, 21.83$ and $45 \mu eV$ and the CC regime starts at about $g = 67.78, 90.34$ and $154.06 \mu eV$ at $T = 0, 20,$ and $80 K$, respectively.

As shown in figure 4.9, the onsets of SC and CC regime shift to higher values of g with enhancement of temperature, which confirm the previous finding that at a higher temperature a larger QD-cavity coupling is required to reach the SC regime (Vagov et al., 2014; Kaer, Nielsen, Lodahl, Jauho, & Mørk, 2010). In addition, the peak of δ_{FWHM} decreases with increase of temperature, which originates from an increase of the phonon-induced pure dephasing rate. For very large g , the variation rate and values of δ_{FWHM} are almost the same at all the considered temperatures, which mean that the decay and the damping part have completely independent contributions to the spectral triplet above almost the same g .

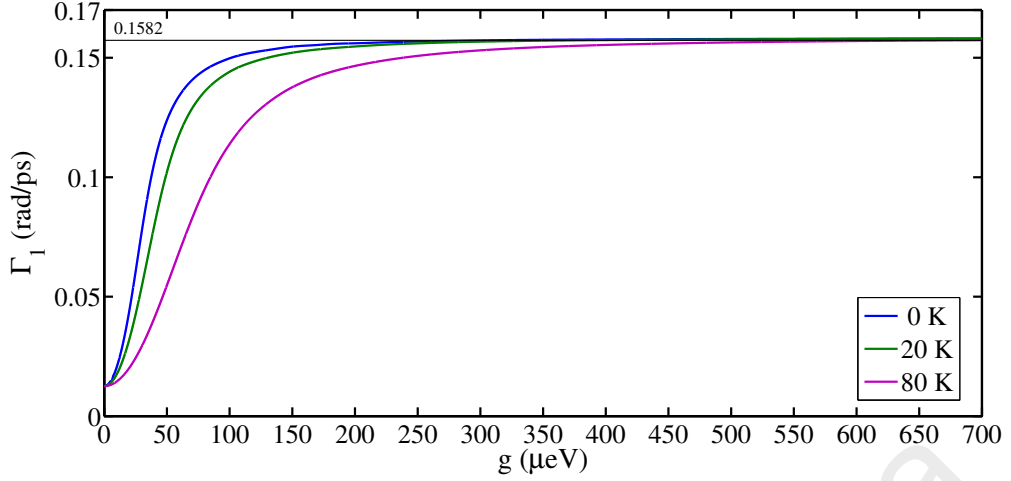


Figure 4.11: FWHM of the effective population decay, Γ_1 , versus g at three various temperatures $T = 0, 20,$ and $80 K$ with $\gamma_r = 0.0063 \text{ rad/ps} = 4.135 \mu\text{eV}$ and $\kappa = 0.1519 \text{ rad/ps} = 100 \mu\text{eV}$. The effective population decay rate is proportional to the inverse of temperature for the coupling strengths less than about $g = 500 \mu\text{eV}$.

To study the effect of temperature on the effective population decay rate we plot Γ_1 in terms of different QD-cavity coupling strengths g at three various temperatures $T = 0, 20,$ and $80 K$ in figure 4.11. As it is clearly seen in the figure, the effective population decay rate is proportional to the inverse of temperature for the coupling strengths less than about $g = 500 \mu\text{eV}$. As a result, at higher temperatures the maximum possible emission rate, $(\gamma_r + \kappa)/2$, can be obtained at larger QD-cavity coupling strengths. For the coupling constants larger than $g = 500 \mu\text{eV}$, the emission rate is insensitive to the temperature range under investigation ($T = 0 - 80 K$). This analysis reveals that the effective population decay rate is affected by at least four parameters; the cavity linewidth, the radiative recombination rate, the QD-cavity coupling strength, and temperature. In agreement with the previous result (Kaer et al., 2010), a temperature induced renormalization (reduction) of the light-matter coupling strength can be accounted for and extracted from the figure; the renormalized g of a bare g at any temperature is obtained by finding a g , at $T = 0 K$, which corresponds to the same value of Γ_1 as the bare g at that temperature. Therefore, the parameters affecting the effective population decay rate reduce to three; the cavity loss, the QD recombination rate, and a renormalized QD-cavity coupling strength.

Significant dependence of the renormalized coupling strength on temperature is observed as the lowering of the coupling strength at $T = 80 K$ is much more than that at $T = 20 K$. In addition, the difference between the renormalized and the bare coupling strength increases with the bare coupling constant as far as the maximum emission rate is reached. For instance, at $T = 80 K$, it is reached at about $g = 500 \mu eV$. For the coupling constants larger than $g = 500 \mu eV$, there is no temperature-induced renormalization (reduction) across the temperature range under investigation, which means that exciton-LA phonon interactions (polaron quasiparticle) can not affect formation of the polariton quasiparticle formed by dressing the QD with the cavity photon.

4.3 Temperature-dependent Shift of Photoluminescence Peak of In(Ga)As Quantum Dots: Role of Acoustic and Optical Phonons

Figure 4.12 shows the T-dependent shift of PL peak for SOQDs, grown by standard molecular beam epitaxy (MBE) technique, with different thicknesses (a) 1.8, (b) 2.4, and (c) 18 monolayers (MLs). The experimental data have been taken from (Sanguinetti et al., 1999; Z. F. Wei et al., 2005; Yeo et al., 2011). Table 4.1 shows the parameters obtained using fit (columns 2-6), Eqs. 3.53 and 3.54 (columns 7 and 8), the final column shows the obtained transition temperatures for SOQDs with 1.8, 2.4, and 18 MLs.

Table 4.1: Parameters Obtained Using Fit, Eqs. 3.53 and 3.54, the Final Column Shows the Obtained Transition Temperatures for SOQDs with 1.8, 2.4, and 18 MLs

MLs	$E_g(0)$ (eV)	$\alpha/10^{-4}$ (eV/K)	W_1	$\hbar\omega_1$ (meV)	$\hbar\omega_2$ (meV)	θ (K)	Δ	T^{trns} (K)
1.8	1.3231	12.20	1.00	12.2	33.2	141.50	0.00	103.38
	1.3164	7.30	1.00	6.2	33.2	71.83	0.00	159.37
	1.2374	3.00	0.00	6.2	33.2	384.64	0.00	201.00
2.4	1.2039	0.00	1.00	11.3	33.2	130.58	0.00	63.00
	1.2079	9.45	0.10	6.2	33.2	352.65	0.26	199.70
	1.1976	3.70	1.00	6.2	33.2	71.83	0.00	301.00
18	0.9461	2.00	1.00	9.8	37.5	113.86	0.00	72.65
	0.9450	5.30	1.00	20.6	37.5	238.96	0.00	180.64
	0.9009	0.46	0.00	7.1	37.5	434.46	0.00	201.00

In these cases, the dispersion of T-dependent shift of the bandgap peak from a mono-

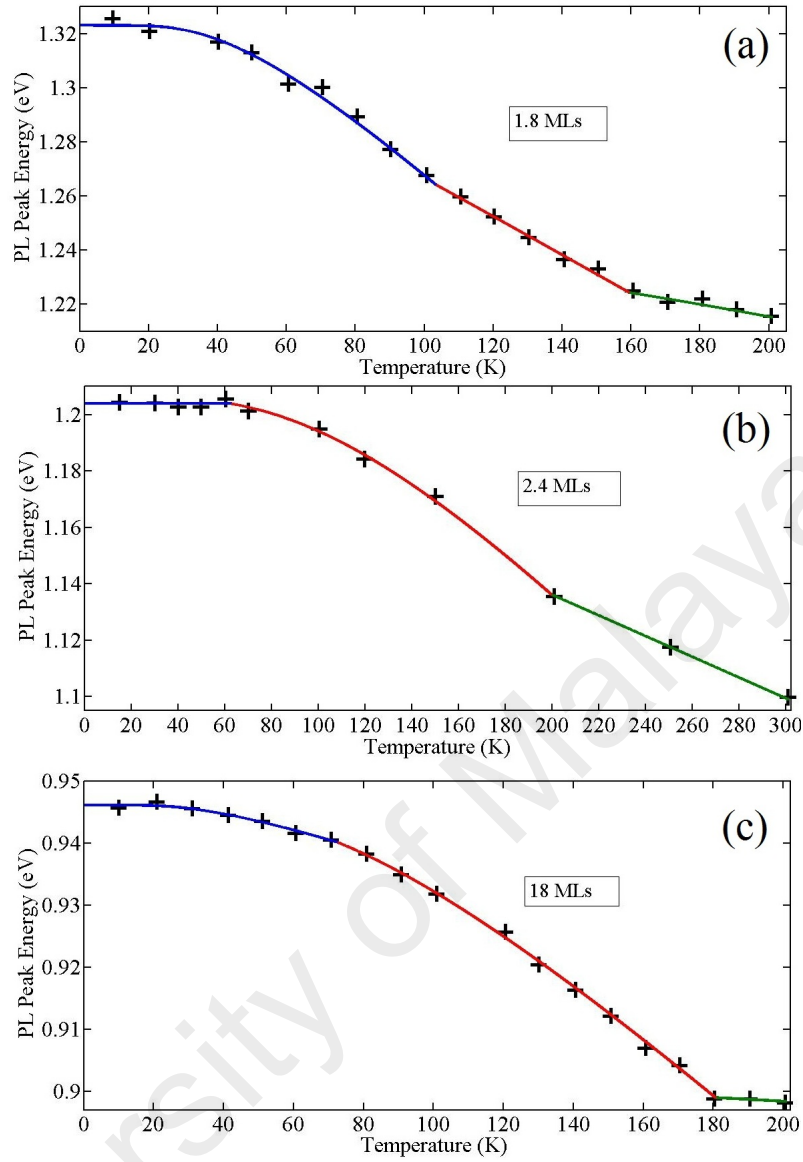


Figure 4.12: Fitted T-dependent shift of PL peak for SOQDs with different thicknesses (a) 1.8, (b) 2.4, and (c) 18 MLs. Dividing the whole T-interval to three shorter parts, shown by different colors, TOM projects the whole data successfully.

tonic behavior is high, which is called sigmoidal behavior; thus dividing the whole T-interval to three shorter parts, shown by different colors, TOM projects the whole data successfully. It is revealed that in each part only AC or OP phonons have the complete contributions (full weights) to the T-dependent shift, except to 2.4 MLs from 63 to 199.7 K, which means that excitons interact (inelastically) with AC or OP phonons separately in those parts.

According to the table 4.1, it is also shown that the phonon dispersion is zero, except

for 2.4 MLs for the interval of 63–199.7 K; thus TOM reduces to one-oscillator model (Fan or Vina model). In addition, here the transition temperature is the temperature in which the value of temperature coefficient of the bandgap width in the high temperature limit (α) and AC phonon energy or α and phonon contributions or all three of them change.

It should be noted that when the contribution of a certain kind of phonon is zero, we cannot determine the exact value of its energy. In this case, we just set it according to its energy in other parts with nonzero contributions. Thus AC phonon energy decreases or increases and then gets a rollover and decreases (for 18 MLs) at different T-intervals. In addition, comparing AC phonon energy of the first T-intervals, we find that decrease of zero bandgap (ZBG: the first value of $E_g(0)$ in each sample), which originates from enhancement of QD size, may lead to a decline of AC phonon energy (this result may not be true because the samples were grown by different groups) (Ghodsi Nahri & Ooi, 2014).

Figure 4.13 shows the fitted T-dependent shift of PL peak for SOQDs, fabricated by using conventional MBE, with different thicknesses: (a) 1, (b) 1.5, (c) 2, and (d) 2.5 MLs. The experimental data have been taken from Ref. (Xu et al., 1996). Table 4.2 shows the parameters obtained using fit, Eqs. 3.53 and 3.54, the obtained transition temperatures are also shown, similar to the previous figure.

In the case of 1.5 and 2.5 MLs, the AC and OP phonon contributions are separated from each other, and the phonon dispersion is zero. For 1 and 2 MLs, in addition to one and two parts with separated AC and OP phonon contributions, respectively, there is one part resulted from mixed AC and OP phonon contributions. Here the transition temperature is the temperature in which α , phonon contributions, and AC phonon energy or α and AC phonon energy change. It can be seen that AC phonon energy increases or increases and then gets a rollover and decreases (for 2 MLs) at the different T-intervals.

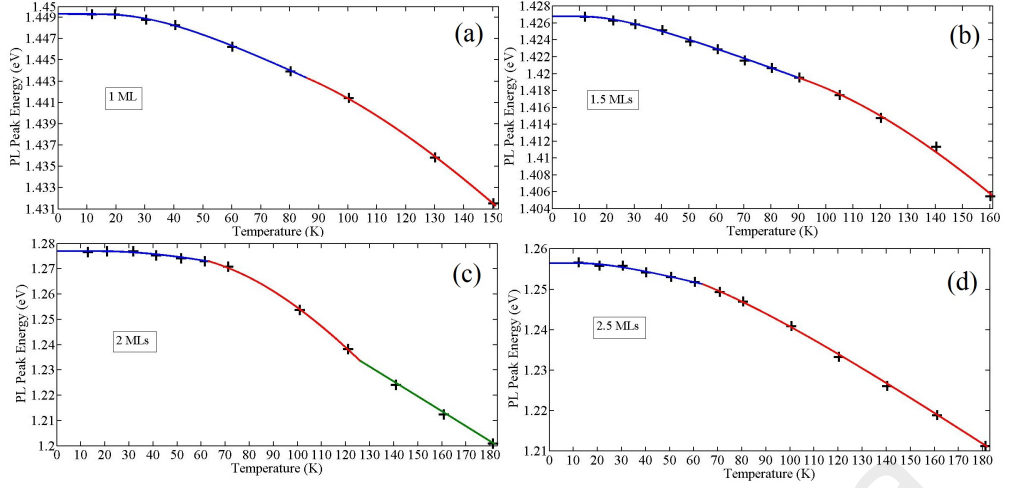


Figure 4.13: Fitted T-dependent shift of PL peak for SOQDs with different thicknesses: (a) 1, (b) 1.5, (c) 2, and (d) 2.5 MLs.

Table 4.2: Parameters Obtained Using Fit, Eqs. 3.53 and 3.54, and the Obtained Transition Temperatures for SOQDs with 1, 1.5, 2, and 2.5 MLs

MLs	$E_g(0)$ (eV)	$\alpha/10^{-4}$ (eV/K)	W_1	$\hbar\omega_1$ (meV)	$\hbar\omega_2$ (meV)	θ (K)	Δ	T^{trns} (K)
1	1.4493	1.42	1.00	9.5	30.3	109.65	0.00	85.78
	1.4461	3.40	0.22	20.5	30.3	325.24	0.14	151.00
1.5	1.4268	1.24	1.00	6.2	33.2	71.83	0.00	90.00
	1.4218	4.19	0.00	20.5	33.2	384.64	0.00	161.00
2	1.2770	2.00	1.00	10.8	30.3	124.70	0.00	62.90
	1.2769	15.00	0.29	20.5	30.3	317.26	0.16	126.02
	1.2897	6.00	1.00	6.2	30.3	71.83	0.00	182.00
2.5	1.2565	2.00	1.00	6.5	33.2	74.97	0.00	63.62
	1.2566	4.11	1.00	14.5	33.2	168.00	0.00	182.00

Comparing AC phonon energy of the first parts, we see that it gets two rollovers and decreases with increasing QD size (decreasing the ZBG).

It has been shown that an increase of exciton localization (i.e., increase of QD size and symmetry) results in enhancement of exciton–LO phonon interaction (Heitz et al., 1999). On the other hand, decreasing QDs size leads to enhancement of ZPL () weight, and thus AC phonon-exciton interaction (Borri et al., 2005; Besombes et al., 2001). Therefore we conclude that enhancement of QDs size, which leads to decrease of ZBG, and symmetry results in increasing exciton–OP phonon interactions and decreasing exciton–AC phonon interactions. We try to discuss this conclusion using our results;

Using Table 4.2 and Eq. 3.56, we find that when the value of MLs increases from 1 to

1.5 (ZBG decreases to 1.4268 eV), which results in enhancement of QDs size, total OP phonon contribution increases, while for further increase of QD thickness (size), total AC phonon contribution increases. Therefore we conclude that elevation of the number of MLs up to 1.5 (decline of ZBG down to 1.4268 eV) results in increase of QD symmetry, then a rollover happens and QD symmetry decreases for further increase of the number of MLs (decline of ZBG). Asymmetry in a QD, which originates from an elongation of the QD along one crystal axis and inbuilt strain in the crystal, results in asymmetric electron-hole exchange interaction in the QD and thus exciton fine-structure splitting (FSS) (Shields, 2007; Gammon, Snow, Shanabrook, Katzer, & Park, 1996). As shown in (Stevenson et al., 2006) and (Young et al., 2005), FSS decreases with increase of emission energy up to about 1.4 eV, then it is inverted and enhanced for QDs emitting at energies more than 1.4 eV. An emission energy, which is very near to 1.4 eV, corresponds to QDs with almost zero exciton FSS (Salter et al., 2010; Stevenson et al., 2006; Young et al., 2005). As we can see from Table 4.2, this emission energy is near to the PL peak emission energy of QDs with 1.5 MLs (1.4268 eV). According to our results, with increase of the ZBG (decrease of QD size) to 1.4268 eV (or more accurately, 1.4 eV), the QD symmetry increases, then a rollover happens and it decreases for further increase of the ZBG (decrease of QD size), thus we believe that change of the QD symmetry results in FSS change as the number of MLs decreases because only the QD symmetry can get a rollover like FSS with the ZBG variations. We also conclude that, for SOQDs grown using conventional MBE, the highest symmetry and the lowest FSS correspond to a certain ZBG about 1.42 eV (a certain number of MLs near to 1.5) or more accurately 1.4 eV (or more exactly, near to 1.6 ML (Stevenson et al., 2006).

Figures 4.14 and 4.15 show fitted T -dependent shrinkage of bandgap peak for SOQDs grown by common MBE and by other epitaxial techniques with different thicknesses; for Figs. 4.14(a) and 4.14(b) 1.6, for 4.14(c) and 4.14(d) 2.4, and for 4.15(a) and

4.15(b) 3 MLs. The experimental data have been taken from (Sanguinetti et al., 1999; Khmissi et al., 2011; Yeo et al., 2011; Sanguinetti et al., 2002). Figures 4.14(a) and 4.14(b) correspond to the SOQDs commonly assembled by using MBE and those which were grown by heterogeneous droplet epitaxy (HDE) method, respectively. There are no dislocations and wetting layer connecting the SOQDs in the second case. The PL of the second QDs sample does not show any of the typical temperature properties of Stranski–Krastanov QDs (SK-QDs), grown using SK (MBE) method, such as sigmoidal peak energy position as a result of lacking the thermally activated QD-QD coupling channel provided by the wetting layer; thus preventing the establishment of a common quasi-equilibrium in the whole QD ensemble (Sanguinetti et al., 2002). Figure 4.14(c) corresponds to InAs SOQDs built commonly using MBE, and figure 4.14(d) corresponds to the same SOQDs inserted in AlGaAs/GaAs modulation doped heterostructure (MDH) (Khmissi et al., 2011). Finally, Figs. 4.15(a) and 4.15(b) correspond to the PL peak shift of SOQDs grown using MBE and migration-enhanced molecular-beam epitaxy [abbreviated as MEE], respectively. The MEE method results in QDs with a thinner wetting layer, larger size, lower density, about 40% enhanced uniformity, two times larger aspect ratio, and a temperature insensitivity of the PL linewidth compared to QDs grown by conventional MBE (Yeo et al., 2011; Cho et al., 2006). Table 4.3 shows the obtained parameters for the abovementioned QDs.

As shown in Figs. 4.14 and 4.15, TOM fits the data very well by dividing the whole temperature interval up to three parts depending on the degree of dispersion of the PL peak from monotonic behavior. As we can see from Table 4.3, for the cases of 1.6 and 2.4 MLs, with increase of the ZBG (decrease of QDs size), total AC phonon contribution (AC phonon-exciton interactions) increases (total OP phonon contribution decreases), which suggests that HDE and MBE+MDH growth techniques most probably decrease QD symmetry (or preserve it) compared with the common MBE. Because, as concluded, both the

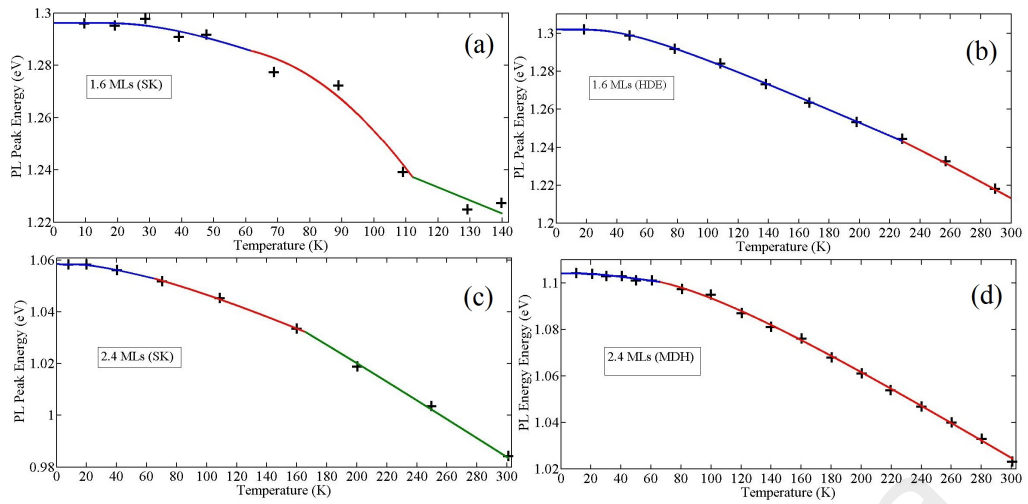


Figure 4.14: Fitted T-dependent shrinkage of bandgap peak for SOQDs grown by MBE, HDE, and MBE+MDH techniques with different thicknesses: (a) and (b) 1.6, (c) and (d) 2.4.

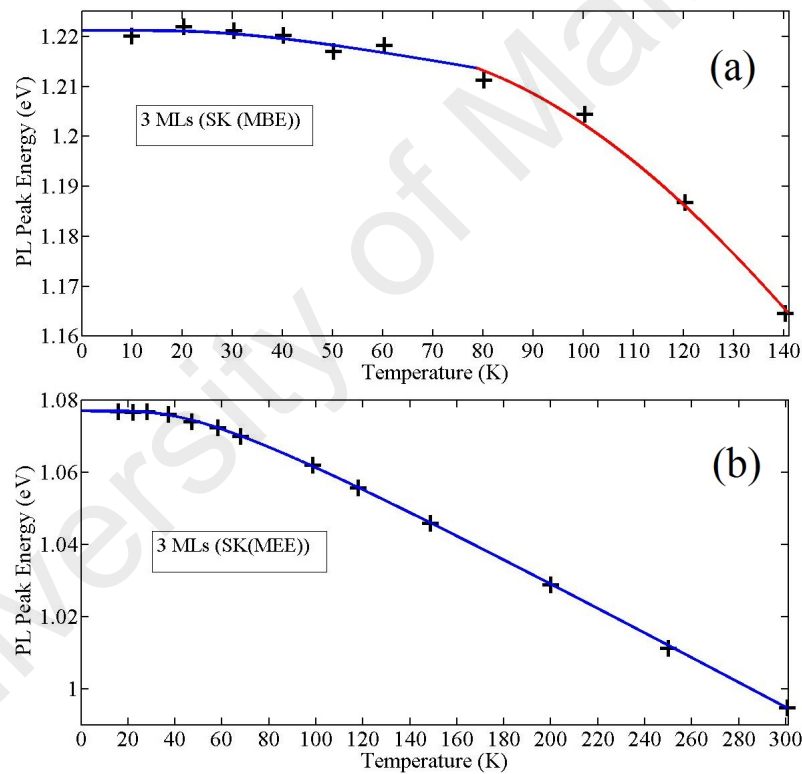


Figure 4.15: Fitted PL peak shift of QDs grown using (a) MBE and (b) migration enhanced MBE [abbreviated as MEE] for the same number of 3 MLs.

QD size and symmetry may affect AC phonon contribution, we also consider the possibility that the size decreases while the symmetry remains constant. In the case of 3 MLs (figure 4.15), on the contrary, with increase of QD size (decrease of ZBG) total AC phonon contribution increases, which suggests the MEE method certainly declines QD

Table 4.3: Parameters Obtained Using Fit, Eqs. 3.53 and 3.54, and the Obtained Transition Temperatures for SOQDs Grown Using MBE, HDE, MBE+MDH, and MEE Methods with 1.6, 2.4, and 3 MLs

1.6 MLs	$E_g(0)$ (eV)	$\alpha/10^{-4}$ (eV/K)	W_1	$\hbar\omega_1$ (meV)	$\hbar\omega_2$ (meV)	θ (K)	Δ	T^{trns} (K)
MBE	1.2962	5.20	1.00	10.1	33.2	116.70	0.00	61.57
	1.2885	40	0.00	20.5	33.2	384.64	0.00	111.95
	1.2770	5	1.00	6.2	33.2	71.83	0.00	140
HDE	1.3019	3.55	1.00	12.1	33.2	140.44	0.00	228.40
	1.2870	5	0.00	20.5	33.2	384.64	0.00	301
2.4 MLs	$E_g(0)$ (eV)	$\alpha/10^{-4}$ (eV/K)	W_1	$\hbar\omega_1$ (meV)	$\hbar\omega_2$ (meV)	θ (K)	Δ	T^{trns} (K)
MBE	1.0585	1.55	1.00	6.2	33.2	71.83	0.00	65.25
	1.0591	2.76	0.61	6.2	33.2	232.95	0.67	165.55
	1.0755	3.80	0.79	6.2	33.2	136.17	0.92	301
MBE MDH	1.1042	1	1.00	6.2	33.2	109.64	0.02	66.07
	1.0760	3.80	0.79	6.2	33.2	136.18	0.92	301
3 MLs	$E_g(0)$ (eV)	$\alpha/10^{-4}$ (eV/K)	W_1	$\hbar\omega_1$ (meV)	$\hbar\omega_2$ (meV)	θ (K)	Δ	T^{trns} (K)
MBE	1.2212	2	1.00	9.1	33.2	105.80	0.00	78.70
	1.2197	20.50	0.00	20.5	33.2	384.64	0.00	141
MEE	1.0769	3.51	1.00	12.4	33.2	144.11	0.00	301

symmetry compared with MBE.

It can be seen from figures 4.15(a) and 4.15(b) that the MEE method, which increases QDs uniformity, results in removing the dispersion (sigmoidal behavior). This result originates from the fact that a sample with more uniform QDs [QDs with a smaller inhomogeneous broadening (IHB)] has a smaller size (bandgap energy) distribution. It also has a smaller total PL peak shrinkage in the whole temperature interval. Since HDE and MBE+MDH methods also remove most of the dispersion, see figure 4.14, we infer that those growth methods increase the uniformity as well. In fact, HDE and MBE+MDH growth modes increase uniformity and decrease QD size and (most probably) symmetry, which result in removing the dispersion and increasing total AC phonon contribution and the maximum temperature which just AC phonons contribute to the PL peak redshift. While MEE increases QDs size and uniformity but decreases QD symmetry, which results in removal of the dispersion and enhancement of total AC phonon contribution (decline of total OP phonon-exciton interactions). It may be concluded that all three methods of

HDE, MBE+MDH, and MEE increase QDs uniformity; as a result of providing a thin (or no) wetting layer and accordingly, increase total AC phonon contribution and decrease the symmetry. This suggests a trade-off between QDs uniformity and symmetry as an enhancement in the uniformity (decrease of IHB) causes a decline in the symmetry and vice versa. It means that IHB, which is a characteristic of the whole sample, affects QD symmetry, which is a characteristic of the single QDs. This is similar to a result offered previously in (Ghodsi Nahri, 2012b), which states different IHBs cause to different homogeneous broadening (which is again a single QD characteristic) in a given temperature. Uniformity increases total AC phonon contribution and the symmetry increases total OP phonon contribution.

Comparing MBE data of Table 4.3 for 1.6 and 2.4 MLs, similarly, we find that decrease of ZBG, as a result of QDs size enhancement, results in decrease of QD symmetry, while comparing 2.4 and 3 MLs (MBE data), we find that increase of ZBG, as a result of decrease of QDs size, leads to enhancement of QD symmetry. We may attribute this phenomenon to change of ZBG backward and toward the critical value 1.4 eV which corresponds to the highest QD symmetry. Thus we infer that increase of ZBG up to a critical value about 1.4 eV, for QDs grown using MBE and MEE, results in enhancement of QD symmetry and total OP phonon contribution and decrease of QDs uniformity and total AC phonon contribution, while a rollover happens for further increase of ZBG. In order for this result always to be true, the growth details should still be the same. It is also nearly inferable from Table 4.1 that decrease of ZBG, as a result of QDs size enhancement, backward 1.4 eV leads to reduction of total OP phonon contribution and increase of total AC phonon contribution.

We can find the meaning of the transition temperature in Table 4.3 as follows: it is shown that α , phonon contributions, and AC phonon energy change in the different temperature parts in the cases of 1.6 and 3 MLs (MBE). While for 2.4 MLs, just α and

phonon contributions change, and the AC phonon energy remains constant.

AC phonon energy of the first parts alters with increase of the number of MLs. AC phonon energy mostly changes in different T-intervals of a certain sample. extracting a systematic behavior for AC phonon energy under variations of QDs size or in different T-intervals of a sample is not possible with the present data because only the SOQDs corresponding to figure 4.13 have the same growth details; even the related temperatures of those data are not up to 300 K.

Figure 4.16 shows fitted T-dependent shrinkage of bandgap energy peak for SOQDs, grown using MBE, with a different number of layers (a) 5 and (b) 10. The experimental data have been taken from (Lu et al., 2010). Table 4.4 shows the obtained parameters for the above mentioned QDs.

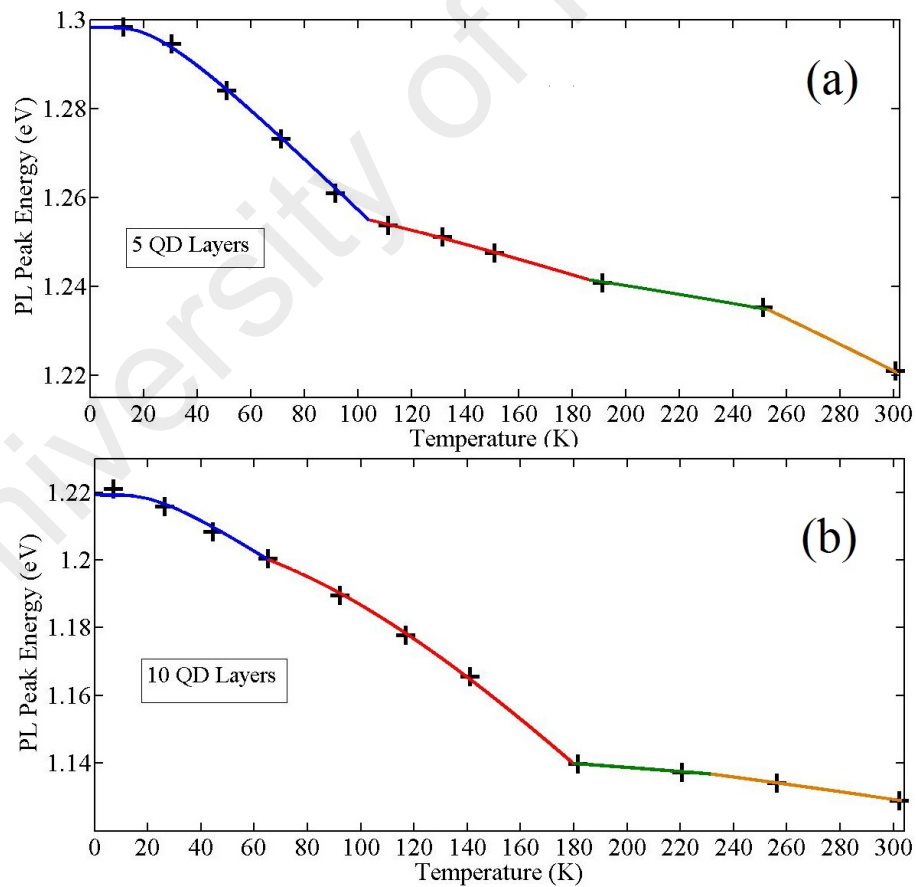


Figure 4.16: Fitted T-dependent shrinkage of bandgap energy peak for SOQDs with a different number of layers (a) 5 and (b) 10.

To fit the data using TOM, the whole T-interval is divided into four parts. Thus

Table 4.4: Parameters Obtained Using Fit, Eqs. 3.53 and 3.54, and the Obtained Transition Temperatures for SOQDs with Different Number of Layers 5 and 10

MLs	$E_g(0)$ (eV)	$\alpha/10^{-4}$ (eV/K)	W_1	$\hbar\omega_1$ (meV)	$\hbar\omega_2$ (meV)	θ (K)	Δ	T^{trns} (K)
5	1.2982	5.80	1.00	6.2	33.2	71.83	0.00	103.88
	1.2611	2.00	1.00	18.7	33.2	216.95	0.00	185.87
	1.2487	1.30	0.00	6.2	33.2	384.64	0.00	252.76
	1.2718	3.45	0.00	6.2	33.2	384.64	0.00	301
10	1.2192	5.35	1.00	6.2	33.2	71.83	0.00	65.03
	1.2108	8.60	0.32	6.2	33.2	282.03	0.52	179.78
	1.1440	0.80	0.00	6.2	33.2	384.64	0.00	231.33
	1.1485	1.30	0.00	6.2	33.2	384.64	0.00	303

TOM fit the data very well. Increase of the number of QD layers leads to decrease of ZBG (increase of QD size), since the total OP phonon contribution (OP phonon–exciton interactions) is enhanced; therefore we conclude that QD symmetry increases. In this case, and in the previous HDE and MBE+MDH cases, the critical value of ZBG may be different compared to previous MBE and MEE cases due to the effects of several QD layers, HDE, and MDH. Almost AC or OP phonons separately interact inelastically (impurely) with excitons. Thus a one-oscillator model can predict the phonon parameters correctly. Here, in the transition temperature, α and AC phonon energy or α and phonon contributions or all three of them or just α (for 5-QD layers at the transition temperature 252.76 and for 10-QD layers at 231.33 K) change. Besides, the AC phonon energy remains constant with enhancement of QDs size (decrease of the ZBG). Therefore we infer that each of a QDs size, the number of MLs or layers alone does not determine the AC phonon energy variations and other factors affect it.

The OP phonon energy, in different temperature parts of a certain sample, may be considered constant for whole samples, which show the discrete and dispersionless nature of the OP phonon energy compared to the continuous nature of AC phonon energy. Changing AC phonon energy in different T-intervals of a specific sample is reasonable because, as the PL peak shifts in the different energy intervals of that sample, strain and

quantum confinement (QDs size) alter, and it has been shown that strain and quantum confinement affect phonon energies (Heitz et al., 1996; Stock et al., 2011). So the AC phonon energy can be changed. Perhaps variations of strain and quantum confinement also are the causes of changes in phonon contributions in the different intervals of a QD sample.

University of Malaya

CHAPTER 5

CONCLUSIONS

In the first part of this work, an open QD-cQED system including a dissipative QD, initially prepared at ES, coupled to a LA phonon bath and a lossy cavity, with maximum one photon, has been studied using numerically accurate RTPI approach. Within this approach, we treated exciton-photon and exciton-phonon interactions on equal footing, exciton radiative decay and cavity loss were included phenomenologically through the non-Hermitian terms. Different coupling regimes of QD-cQED, called weak, intermediate, and coherent, defined in terms of the decay dynamics were discussed and stricter conditions identifying them were provided. It was found that these regimes match the coupling regimes defined in terms of appearance and resolution of VRS. Our results showed that to have the CC regime, VRS (the doublet separation) should be larger than the sum of the widths of the corresponding peaks. In order to discern between the role of population decay and impure dephasing (damping), induced by LA phonons and the dissipations, on the quantum dynamics of the QD-cavity system, we proposed a phenomenological expression which projects the QD-cavity decay curves perfectly, enabling us to calculate the corresponding spectra. The expression fits the decay curves very well. We found an approximate expression for the effective impure dephasing rate using a match of the state population for the dissipation-less QD-cavity system, calculated by our microscopic RTPI approach, to the phenomenological expression. It was found that the increase of light-matter coupling strength results in enhancing CPFWM from $2\gamma_r$ up to a maximum value within the CC regime then, decreasing it to an asymptotic line, the value of which is the sum of the QD and cavity dissipation rates. The width of the central peak of the spectra (CPFWM) is temperature dependent for not very large coupling strengths. The

effective population decay (emission) rate increases from the carrier recombination rate to a maximum value, which is mean of the QD and cavity dissipation rates, with the coupling strength. In order to study the role of the effective impure dephasing rate on CPFWHM we introduced a quantity that was used in determining the different coupling regimes as well. This quantity enabled us to define the onset of the SC regime as the point where the impure dephasing part begins to contribute to the central band of the spectra significantly, which originates from the existence of VRO with a very small frequency (unclear VRO), because the corresponding impure dephasing spectrum only includes a central peak. Its contribution to CPFWHM increases with the coupling strength up to the onset of the CC regime, then decreases as a result of the appearance of sidebands (splitting of the impure dephasing spectra), which originates from the appearance of clear VRO at the corresponding decay curves. CPFWHM arises solely from the effective population decay rate only at small and at very large coupling strengths. In other words, the effective population decay and impure dephasing rates contribute separately to the width of, respectively, the central and sideband peaks of the triplet spectra only beyond a very large coupling strength which is the same across the considered temperature range. Temperature-dependence of the effective population decay rate means that at a higher temperature a larger coupling strength is required to obtain the maximum achievable emission rate. There is no temperature induced renormalization (reduction) of the light–matter coupling strength at very large coupling constants.

In the second part, it was found that if whole temperature 0–300 K is divided into several parts (at most four parts), depending on the degree of dispersion from a monotonic behavior of T-dependent shift of PL peak and considering the first part as AC phonons have the total contribution, TOM is able to fit all the available data of In(Ga)As QDs very well. The meaning of transition temperature is the temperature in which the value of temperature coefficient of the bandgap width in the high temperature limit plus one or both of

phonon contributions and AC phonon energy change. Almost AC phonon energy varies in different T- (or energy) intervals of a certain sample, which may originate from a change in strain and quantum confinement. The numerical results suggest that excitons mostly interact (impurely) with AC or OP phonons separately, especially when T-dependent PL peak shift of a sample has a high dispersion from a monotonic behavior, which originates from a low QDs uniformity. Thus there is zero-phonon dispersion, and the TOM reduces to one-oscillator model (Fan or Vina model). Increasing QDs uniformity by using some growth techniques (HDE, MBE+MDH, and MEE) results in reducing or removing the dispersion (sigmoidal behavior), enhancing the total AC phonon contribution (exciton-AC phonon interaction) and the maximum temperature which AC phonons contribute to the T-dependent red shift of PL emission peak. We also proposed a tradeoff between QDs uniformity (IHB of the QDs sample) and QD symmetry. QDs uniformity directly changes (increases) total AC phonon contribution, and the symmetry directly affects (increases) total OP phonon contribution. Increasing ZBG, as a result of decrease of QDs size, up to a critical value about 1.4 eV, for In(Ga)As QDs grown using MBE and MEE, results in enhancement of QD symmetry and total OP phonon contribution and decrease of QDs uniformity and total AC phonon contribution, while a rollover happens for further enhancement of ZBG. Therefore we find that the highest QD symmetry and the lowest exciton FSS correspond to this critical value of ZBG. Enhancement of the number of QD layers (from 5 to 10) leads to increase of total OP phonon contribution and reduction of total AC phonon contribution. It seems that the critical value of ZBG, corresponding to QD samples containing several layers and those grown by HDE and MBE+MDH, is different than about 1.4 eV.

Appendices

University of Malaya

APPENDIX A

DERIVATION OF DISCRETIZED REAL-TIME PATH-INTEGRALS FOR DISSIPATIVE QUANTUM DOT-CAVITY SYSTEM COUPLED TO LONGITUDINAL ACOUSTIC PHONON BATH

In this appendix we present a discretized real-time path-integral representation of the dynamics for an open QD-cavity system coupled to a continuum of AC phonons, with smooth spectral density, by pure dephasing type interactions. A linear carrier-phonon coupling is assumed, which allows to eliminate the phonon degrees of freedom exactly and to construct a closed form of the influence functional integral for the system under investigation. Our model Hamiltonian including open QD-cavity (OQC) system coupled to the LA phonon reservoir, as described in Chap. 3, is

$$\begin{aligned}
 H(t) = \hat{H}_S + H_R + H_{SR} = & \hbar \left(\omega_C - i \frac{\kappa}{2} \right) \hat{s}_{00} + \hbar \left(\bar{\omega}_X - i \frac{\gamma_r}{2} \right) \hat{s}_{11} \\
 & + \hbar g (\hat{s}_{01} + \hat{s}_{10}) + \hbar \sum_q \omega_q b_q^\dagger b_q + \hbar \sum_q \left(\hat{\gamma}_q^* b_q + \hat{\gamma}_q b_q^\dagger \right), \quad (\text{A.1})
 \end{aligned}$$

where the hat sign stands for matrix operators acting in the subspace of the carrier-photon states. Here, the OQC system contains three levels denoted by $|0\rangle = |G, n=1\rangle$, $|1\rangle = |X, n=0\rangle$, and $|2\rangle = |G, n=0\rangle$ where n refers to the number of photons in the cavity mode. Only the states $|0\rangle$ and $|1\rangle$ are coupled due to the dipole interaction between them. The states $|0\rangle$ and $|1\rangle$ decay to the state $|2\rangle$ irreversibly with the variable rate γ_1 , as described in Chap. 3.

In order to derive a discretized RTPI representation for the RQCDM, we start by taking the partial trace over the total density matrix (total statistical operator), expressed in terms of the initial total density matrix, $\chi(0)$, and the time evolution operator, in the

interaction picture as

$$\hat{\rho}(t) = Tr_{ph}[U(t)\chi(0)U^\dagger(t)]. \quad (\text{A.2})$$

Identity operators, I_n , of the system-bath, i.e. the OQC system and its environment, is constructed as a direct product of identity operators in the space of carrier-photon states, $|s_n^+\rangle$, and the space of coherent phonon states, $|Z_n\rangle$, so that

$$\begin{aligned} I_n &= \hat{I}_n^{s^+} \otimes I_n^Z = \sum_{s_n^+} |s_n^+\rangle \langle s_n^+| \otimes \int_{-\infty}^{\infty} d\mu_n |Z_n\rangle \langle Z_n| \\ d\mu_n &= \prod_q e^{-\bar{Z}_{qn}Z_{qn}} \frac{d\bar{Z}_{qn}dZ_{qn}}{\pi}, \end{aligned} \quad (\text{A.3})$$

where the coherent phonon states are defined by $b_q|Z_n\rangle = Z_{qn}|Z_n\rangle$. The integrations are performed on the complex plane of the conjugate variables Z_{qn} and $\bar{Z}_{qn} = Z_{qn}^*$.

Performing the trace in Eq. A.2 over the phonon degrees of freedom, at time t , which, here, is equivalent to integrations over the phonon variables Z_{qf} we have

$$\begin{aligned} \rho_{s_f^+s_f^-}(t) &= \langle s_f^+ | Tr_{ph}[\chi(t)] | s_f^- \rangle \\ &= \int d\mu_f \langle s_f^+, Z_f | U(t)\chi(0)U^\dagger(t) | s_f^-, Z_f \rangle, \end{aligned} \quad (\text{A.4})$$

where $|s_f^+\rangle$ and $|s_f^-\rangle$ correspond to the system eigenbasis for forward and backward propagation in the final time t . Using the completeness relations of the system-bath at the initial time, with index i , for forward and backward propagation, we obtain

$$\begin{aligned} \rho_{s_f^+s_f^-}(t) &= \int d\mu_f \int d\mu_i \int d\mu_i' \sum_{s_i^+, s_i^-} \langle s_f^+, Z_f | U(t) | s_i^+, Z_i \rangle \\ &\quad \langle s_i^+, Z_i | \chi(0) | s_i^-, Z_i' \rangle \langle s_i^-, Z_i' | U^\dagger(t) | s_f^-, Z_f \rangle. \end{aligned} \quad (\text{A.5})$$

The time evolution operator, which correspond to the total Hamiltonian, is given by

$$U(t,0) = T \exp \left(-\frac{i}{\hbar} \int_0^t H(\tau) d\tau \right), \quad (\text{A.6})$$

where T is the time ordering operator. According to the Trotter discretization, we discretize the time interval $[0,t]$, of the integration over the total Hamiltonian, into N time steps of the length $\varepsilon = t_n - t_{n-1} = t/N$, yielding support points $t_n = n\varepsilon$ with $n = 1, \dots, N$, while we consider the limit $N \rightarrow \infty$ (or equivalently, $\varepsilon \rightarrow 0$), therefore

$$\int_0^t H(\tau) d\tau = \lim_{N \rightarrow \infty} \sum_{n=1}^N \int_{t_{n-1}}^{t_n} H(\tau) d\tau = \lim_{N \rightarrow \infty} \sum_{n=1}^N \varepsilon H(t_n), \quad (\text{A.7})$$

where we have approximated the time-varying Hamiltonian $H(\tau)$ by a piecewise constant Hamiltonian $H(t_n)$ in the small enough time intervals where the Hamiltonian is constant during each of the small time interval ε .

Factorizing the time-evolution operator with the discretized Hamiltonian, as a consequence of the Baker-Campbell-Hausdorff expansion for a sufficiently small time slice ε (Kleinert, 2006), and keeping the first-order accuracy of the discretization ($O(\varepsilon)$), omitting the higher orders of ε , we attain

$$U(t,0) \approx \lim_{N \rightarrow \infty} T \prod_{n=1}^N U(t_n, t_{n-1}) = \lim_{N \rightarrow \infty} T \prod_{n=1}^N e^{-i\varepsilon H(t_n)/\hbar}, \quad (\text{A.8})$$

where $t_0 = 0$, $t_N = t$ and the product is time ordered, with decreasing n from left to right. By inserting a complete set of states between each pair of the short-time evolution operators we have

$$U(t) \approx \lim_{N \rightarrow \infty} \left(e^{-i\varepsilon H(t_N)/\hbar} I_{N-1} \dots e^{-i\varepsilon H(t_2)/\hbar} I_1 e^{-i\varepsilon H(t_1)/\hbar} \right). \quad (\text{A.9})$$

Therefore, the first matrix element in Eq. A.5 is represented as

$$\begin{aligned} \langle s_N^+, Z_N | U(t) | s_0^+, Z_0 \rangle &= \lim_{N \rightarrow \infty} \sum_{s_{N-1}^+} \sum_{s_{N-2}^+} \dots \sum_{s_1^+} \int d\mu_{N-1} \int d\mu_{N-2} \dots \\ &\int d\mu_1 \prod_{n=1}^N A_n = \lim_{N \rightarrow \infty} T \prod_{n=1}^{N-1} \left[\sum_{s_n^+} \int d\mu_n \right] \prod_{n=1}^N A_n, \end{aligned} \quad (\text{A.10})$$

where initial and final states are denoted by indexes $n = 1$ and $n = N$ and short-time amplitude A_n is represented as

$$A_n = \langle s_n^+, Z_n | e^{-i\varepsilon H(t_n)/\hbar} | s_{n-1}^+, Z_{n-1} \rangle. \quad (\text{A.11})$$

Partitioning the total Hamiltonian into the one-dimensional free system Hamiltonian, $\hat{H}_S(t_n)$, and the influence Hamiltonian, $H_{Inf}(t_n) = H_R(t_n) + H_{SR}(t_n)$, and again factorizing the short time-evolution operator, keeping the first-order accuracy $O(\varepsilon)$, it can be written as

$$e^{-i\varepsilon H(t_n)/\hbar} \approx e^{-i\varepsilon \hat{H}_S(t_n)/\hbar} e^{-i\varepsilon H_{Inf}(t_n)/\hbar}. \quad (\text{A.12})$$

Using a complete set of system states and the fact that \hat{H}_S is diagonal in the phonon subspace and that H_{Inf} is diagonal in the subspace of carrier-photon states, the matrix element A_n is written as

$$A_n \approx \langle s_n^+ | e^{-i\varepsilon \hat{H}_S(t_n)/\hbar} | s_{n-1}^+ \rangle \langle s_{n-1}^+, Z_n | e^{-i\varepsilon H_{Inf}(t_n)/\hbar} | s_{n-1}^+, Z_{n-1} \rangle. \quad (\text{A.13})$$

Using a standard result for matrix elements of a normal ordered phonon operator function (Vagov, Croitoru, Glässl, et al., 2011),

$$\langle Z | F(b_q^\dagger, b_q) | Z' \rangle = e^{\sum_q \bar{Z}_q Z'_q} F(\bar{Z}_q, Z'_q), \quad (\text{A.14})$$

for the second matrix element in Eq. A.13, we obtain

$$\langle s_{n-1}^+, Z_n | e^{-i\varepsilon H_{Inf}(t_n)/\hbar} | s_{n-1}^+, Z_{n-1} \rangle = \langle s_{n-1}^+ | e^{\hat{S}_{0n}} | s_{n-1}^+ \rangle, \quad (\text{A.15})$$

where

$$\hat{S}_{0n} = \sum_q \bar{Z}_{qn} Z_{qn-1} - i\varepsilon \sum_q (\hat{\gamma}_{qn} \bar{Z}_{qn} + \hat{\gamma}_{qn}^* Z_{qn-1} + \omega_q \bar{Z}_{qn} Z_{qn-1}). \quad (\text{A.16})$$

The index n in the matrix $\hat{\gamma}_{qn}$ indicates that it acts on the carrier-photon states of the n^{th} time slice. Inserting Eq. A.15 into Eq. A.13 and substituting the result into A.10, the short-time amplitude and the matrix elements of the evolution operator are obtained as

$$\begin{aligned} A_n &\approx \langle s_n^+ | e^{\hat{S}_{0n} - i\varepsilon \hat{H}_S(t_n)/\hbar} | s_{n-1}^+ \rangle, \\ \langle s_N^+, Z_N | U(t) | s_0^+, Z_0 \rangle &= \langle s_N^+ | \lim_{N \rightarrow \infty} \hat{T} \prod_{n=1}^{N-1} \left[\int d\mu_n \right] e^{\hat{S}_0} | s_0^+ \rangle, \end{aligned} \quad (\text{A.17})$$

where \hat{T} is the time ordering operator for the operators in the carrier-photon state subspace and

$$\hat{S}_0 = \sum_{n=1}^N \left(\hat{S}_{0n} - i\varepsilon \hat{H}_S(t_n)/\hbar \right). \quad (\text{A.18})$$

Using the following identity:

$$\sum_{n=1}^N \bar{Z}_{qn} Z_{qn-1} = \bar{Z}_{qN} Z_{qN} + \sum_{n=1}^{N-1} \bar{Z}_{qn} Z_{qn} - \varepsilon \sum_{n=1}^N \bar{Z}_{qn} \frac{(Z_{qn} - Z_{qn-1})}{\varepsilon}. \quad (\text{A.19})$$

keeping the accuracy $O(\varepsilon)$ and using the conversion of summation to integral, as defined

in Eq. A.7, for the exponent in Eq. A.17 we gain

$$\begin{aligned}\widehat{S}_0 &= \sum_{n=1}^{N-1} \sum_q \bar{Z}_{qn} Z_{qn} + \sum_q \bar{Z}_q(t) Z_q(t) - \frac{i}{\hbar} \int_0^t d\tau \widehat{H}_S(\tau) \\ &\quad - \sum_q \int_0^t d\tau [\bar{Z}_q(\tau) \dot{Z}_q(\tau) + i\omega_q \bar{Z}_q(\tau) Z_q(\tau) + i\hat{\gamma}_q(\tau) \bar{Z}_q(\tau) + i\hat{\gamma}_q^*(\tau) Z_q(\tau)],\end{aligned}\tag{A.20}$$

where $\dot{Z}_{qn} = (Z_{qn} - Z_{qn-1})/\varepsilon$ and we used the boundary conditions $\bar{Z}_{qN} = \bar{Z}_q(t)$ and $Z_{qN} = Z_q(t)$.

As a result, the matrix elements of the evolution operator, defined in Eq. A.10 and A.11, become a path-integral over phonon variables, formally represented as

$$\langle s_f^+, Z_f | U(t) | s_i^+, Z_i \rangle = \langle s_f^+ | \int DZ e^{\widehat{S}(Z)} | s_i^+ \rangle,\tag{A.21}$$

where

$$\int DZ = \lim_{N \rightarrow \infty} \widehat{T} \prod_{n=1}^{N-1} \int \prod_q \frac{d\bar{Z}_{qn} dZ_{qn}}{\pi},\tag{A.22}$$

and the ‘‘action functional’’ \widehat{S} is given by

$$\begin{aligned}\widehat{S} &= \sum_q \bar{Z}_q(t) Z_q(t) - \frac{i}{\hbar} \int_0^t d\tau \widehat{H}_S(\tau) - \sum_q \int_0^t d\tau \\ &\quad [\bar{Z}_q(\tau) \dot{Z}_q(\tau) + i\omega_q \bar{Z}_q(\tau) Z_q(\tau) + i\hat{\gamma}_q(\tau) \bar{Z}_q(\tau) + i\hat{\gamma}_q^*(\tau) Z_q(\tau)].\end{aligned}\tag{A.23}$$

Since the action functional is quadratic in the phonon variables the corresponding path-integrals can be calculated exactly. The action is defined as $\widehat{S}(Z_q, \dot{Z}_q, \bar{Z}_q, t) = \sum_q \bar{Z}_q(t) Z_q(t) - \frac{i}{\hbar} \int_0^t d\tau \widehat{H}_S(\tau) - \sum_q \int_0^t L(Z_q, \dot{Z}_q, \tau) dt$ where $L(Z_q, \dot{Z}_q, \tau)$ is the Lagrangian. We expand the general path around the classical one as $Z_q(\tau) = Z_q^{Cl}(\tau) + \eta_q(\tau)$ where $\eta_q(\tau)$ denotes fluctuating paths about the classical one with the boundary conditions

$\eta_q(0) = \eta_q(t) = 0$. Classical trajectories are determined by the requirement that the action functional evaluated along them must be stationary, therefore,

$$\frac{\partial \widehat{S}_{Cl}(t)}{\partial Z_q^{Cl}} = 0, \quad \frac{\partial \widehat{S}_{Cl}(t)}{\partial \bar{Z}_q^{Cl}} = 0, \quad (\text{A.24})$$

where $\widehat{S}_{Cl}(t) = \widehat{S}(Z_q^{Cl}, \dot{Z}_q^{Cl}, \bar{Z}_q^{Cl}, t)$ is called extremal action. In order to satisfy Eq. A.24 the Lagrangian must obey the Euler-Lagrange equations (Khandekar, Lawande, & Bhagwat, 1998; Kakushadze, 2015), so that

$$\frac{d}{dt} \frac{\partial L}{\partial \dot{Z}_q^{Cl}} - \frac{\partial L}{\partial Z_q^{Cl}} = \dot{Z}_q^{Cl}(\tau) + i\omega_q Z_q^{Cl}(\tau) + i\widehat{\gamma}_q(\tau) = 0, \quad (\text{A.25})$$

and

$$\frac{d}{dt} \frac{\partial L}{\partial \dot{\bar{Z}}_q^{Cl}} - \frac{\partial L}{\partial \bar{Z}_q^{Cl}} = \dot{\bar{Z}}_q^{Cl}(\tau) - i\omega_q \bar{Z}_q^{Cl}(\tau) - i\widehat{\gamma}_q^*(\tau) = 0. \quad (\text{A.26})$$

Using the expansion about the classical path (fluctuation expansion), the equations of motion A.25 and A.26, and the boundary conditions for the fluctuating paths the action is obtained as $\widehat{S}(t) = \widehat{S}_{Cl} + \widehat{S}_\eta$ where $\widehat{S}_\eta = -\sum_q \int_0^t (\bar{\eta}_q(\tau) \dot{\eta}_q(\tau) + i\omega_q \bar{\eta}_q(\tau) \eta_q(\tau)) d\tau$. As the classical path, at each q , is stationary and the fluctuating paths are zero at the initial and final times, the path-integral for the evolution operator is obtained as

$$\langle s_f^+, Z_f | U(t) | s_i^+, Z_i \rangle = \left[\int D\eta e^{\widehat{S}_\eta} \right] \langle s_f^+ | e^{\widehat{S}_{Cl}} | s_i^+ \rangle. \quad (\text{A.27})$$

The general solutions of Eqs. A.25 and A.26 are obtained using the boundary conditions

$$Z_q^{Cl}(0) = Z_{qi}, \quad \bar{Z}_q^{Cl}(t) = Z_{qf}^*, \quad (\text{A.28})$$

as

$$Z_q^{Cl}(\tau) = Z_{qi} e^{-i\omega_q \tau} - i \int_0^\tau d\tau' e^{-i\omega_q(\tau-\tau')} \widehat{\gamma}_q(\tau'), \quad (\text{A.29})$$

$$\overline{Z}_q^{Cl}(\tau) = Z_{qf}^* e^{i\omega_q(\tau-t)} - i \int_\tau^t d\tau' e^{i\omega_q(\tau-\tau')} \widehat{\gamma}_q^*(\tau'). \quad (\text{A.30})$$

These classical paths are operators in the carrier-photon state subspace. It can be seen that now they are not complex conjugate which justifies the notation \overline{Z} .

To obtain the action evaluated along the classical path, we rewrite Eq. A.25 as

$$\dot{Z}_q(\tau) = -i\omega_q Z_q(\tau) - i\widehat{\gamma}_q(\tau), \quad (\text{A.31})$$

using Eq. A.29 the term $\overline{Z}_q(t) Z_q(t)$ can be written as

$$\overline{Z}_q(t) Z_q(t) = Z_{qf}^* Z_{qi} e^{-i\omega_q t} - i Z_{qf}^* \int_0^t d\tau' e^{-i\omega_q(t-\tau')} \widehat{\gamma}_q(\tau'), \quad (\text{A.32})$$

where we used the boundary condition in Eq. A.28. Substituting Eqs. A.29, A.31 and A.32 into Eq. A.23 we obtain the extremal action \widehat{S}_{Cl} for the path-integral of the evolution operator as

$$\begin{aligned} \widehat{S}_{Cl} = & -\frac{i}{\hbar} \int_0^t d\tau \widehat{H}_S(\tau) + \sum_q Z_{qf}^* Z_{qi} e^{-i\omega_q t} \\ & - \sum_q \int_0^t d\tau \int_0^\tau d\tau' e^{i\omega_q(\tau-\tau')} \widehat{\gamma}_q^*(\tau) \widehat{\gamma}_q(\tau') \\ & - i \sum_q Z_{qf}^* \int_0^t d\tau e^{i\omega_q(\tau-t)} \widehat{\gamma}_q(\tau) - i \sum_q Z_{qi} \int_0^t d\tau e^{-i\omega_q \tau} \widehat{\gamma}_q^*(\tau). \end{aligned} \quad (\text{A.33})$$

Now, we shall derive the extremal action $\widehat{S}_{Cl}^{\dagger}$ for path-integral of Hermitian conjugate (H.C.) of the evolution operator (time-reversal evolution operator) through the same steps

as for the evolution operator. Here, we mention some parts of the derivation; Discretized form of the time-reversal evolution operator U^\dagger similarly is written as

$$U^\dagger(t) \approx \lim_{N \rightarrow \infty} T' \prod_{n=1}^N U^\dagger(t_n, t_{n-1}) = \lim_{N \rightarrow \infty} T' \prod_{n=1}^N e^{i\varepsilon H'(t_n)/\hbar}, \quad (\text{A.34})$$

where T' is the time ordering operator increasing n from left to right. Substituting the completeness relation of the system-bath, $I'_n = \widehat{I}_n^{s_n^-} \otimes I_n^{Z'_n} = \sum_{s_n^-} |s_n^- \rangle \langle s_n^-| \otimes \int d\mu'_n |Z'_n \rangle \langle Z'_n|$, between each pair of the time-reversal evolution operator, the corresponding matrix elements in Eq. A.5 read as

$$\langle s_0^-, Z'_0 | U^\dagger(t) | s_N^-, Z_N \rangle = \lim_{N \rightarrow \infty} T' \prod_{n=1}^{N-1} \left[\sum_{s_n^-} \int d\mu'_n \right] \prod_{n=1}^N A_n^\dagger, \quad (\text{A.35})$$

where the short-time amplitude is represented by

$$A_n^\dagger = \langle s_{n-1}^-, Z'_{n-1} | e^{i\varepsilon H'(t_n)/\hbar} | s_n^-, Z'_n \rangle. \quad (\text{A.36})$$

Partitioning the total Hamiltonian into system and influence parts and factorizing the short time-reversal evolution operator with keeping $O(\varepsilon)$, then, using Eq. A.14 for the influence Hamiltonian and the identity in Eq. A.19 one finally obtains

$$\langle s_0^-, Z'_0 | U^\dagger(t) | s_N^-, Z_N \rangle = \langle s_0^- | \lim_{N \rightarrow \infty} \widehat{T}' \prod_{n=1}^{N-1} \left[\int d\mu'_n \right] e^{\widehat{S}_0} | s_N^- \rangle,$$

with

$$\begin{aligned} \widehat{S}_0 = & \sum_{n=1}^{N-1} \sum_q \overline{Z}'_{qn} Z'_{qn} + \sum_q \overline{Z}'_q(t) Z'_q(t) + \frac{i}{\hbar} \int_0^t d\tau \widehat{H}'_S(\tau) \\ & - \sum_q \int_0^t d\tau \left[Z'_q(\tau) \dot{\overline{Z}}'_q(\tau) - i\omega_q \overline{Z}'_q(\tau) Z'_q(\tau) - i\widehat{\gamma}'_q(\tau) \overline{Z}'_q(\tau) - i\widehat{\gamma}'_q{}^*(\tau) Z'_q(\tau) \right]. \end{aligned} \quad (\text{A.37})$$

Once again the summation to integral conversion and the boundary conditions $\bar{Z}'_{qN} = \bar{Z}'_q(t)$ and $Z'_{qN} = Z'_q(t)$ were used. The path-integral representation of the matrix elements of the time-reversal evolution operator is written as

$$\langle s_0^-, Z'_0 | U^\dagger(t) | s_N^-, Z_N \rangle = \langle s_i^- | \int DZ' e^{\hat{S}'(t)} | s_f^- \rangle, \quad (\text{A.38})$$

where

$$\int DZ' = \lim_{N \rightarrow \infty} \hat{T}' \prod_{n=1}^{N-1} \int \prod_q \frac{d\bar{Z}'_{qn} dZ'_{qn}}{\pi}, \quad (\text{A.39})$$

and the action functional \hat{S}' is given by

$$\begin{aligned} \hat{S}'(t) = & \sum_q \bar{Z}'_q(t) Z'_q(t) + \frac{i}{\hbar} \int_0^t d\tau \hat{H}'_S(\tau) - \sum_q \int_0^t d\tau \\ & \left[Z'_q(\tau) \dot{\bar{Z}}'_q(\tau) - i\omega_q \bar{Z}'_q(\tau) Z'_q(\tau) - i\hat{\gamma}'_q(\tau) \bar{Z}'_q(\tau) - i\hat{\gamma}'_q{}^*(\tau) Z'_q(\tau) \right]. \end{aligned} \quad (\text{A.40})$$

The classical paths are solutions of the Euler-Lagrange equations for the Lagrangian, so that

$$\frac{d}{dt} \frac{\partial L'}{\partial \dot{\bar{Z}}'_q{}^{Cl}} - \frac{\partial L'}{\partial \bar{Z}'_q{}^{Cl}} = \dot{Z}'_q{}^{Cl}(\tau) + i\omega_q Z'_q{}^{Cl}(\tau) + i\hat{\gamma}'_q(\tau) = 0, \quad (\text{A.41})$$

$$\frac{d}{dt} \frac{\partial L'}{\partial \dot{Z}'_q{}^{Cl}} - \frac{\partial L'}{\partial Z'_q{}^{Cl}} = \dot{\bar{Z}}'_q{}^{Cl}(\tau) - i\omega_q \bar{Z}'_q{}^{Cl}(\tau) - i\hat{\gamma}'_q{}^*(\tau) = 0. \quad (\text{A.42})$$

Employing the fluctuation expansion, the equations of motion A.41 and A.42, and the boundary conditions for the fluctuating paths the action is obtained as $\hat{S}'(t) = \hat{S}'_{Cl} + \hat{S}'_\eta$ where $\hat{S}'_\eta = -\sum_q \int_0^t (\eta'_q(\tau) \dot{\bar{\eta}}'_q(\tau) - i\omega_q \bar{\eta}'_q(\tau) \eta'_q(\tau)) d\tau$. Then, the path-integral for the time-reversal evolution operator is derived as

$$\langle s_i^-, Z'_i | U^\dagger(t) | s_f^-, Z_f \rangle = \left[\int D\eta' e^{\hat{S}'_\eta} \right] \langle s_i^- | e^{\hat{S}'_{Cl}} | s_f^- \rangle. \quad (\text{A.43})$$

Using the boundary conditions

$$Z_q^{Cl}(t) = Z_{qf}', \quad \bar{Z}_q^{Cl}(0) = Z_{qi}^*, \quad (\text{A.44})$$

the classical trajectories are obtained as

$$Z_q^{Cl}(\tau) = Z_{qf}' e^{-i\omega_q(\tau-t)} + i \int_{\tau}^t d\tau' e^{-i\omega_q(\tau-\tau')} \hat{\gamma}_q(\tau'), \quad (\text{A.45})$$

$$\bar{Z}_q^{Cl}(\tau) = Z_{qi}^* e^{i\omega_q\tau} + i \int_0^{\tau} d\tau' e^{i\omega_q(\tau-\tau')} \hat{\gamma}_q^*(\tau'), \quad (\text{A.46})$$

obtaining $\bar{Z}_q^{Cl}(t)$ using Eq. A.46 and $\dot{Z}_q^{Cl}(\tau)$ using Eq. A.42, substituting them together with Eq. A.46 into Eq. A.40 we derive the extremal action for the path-integral of the time-reversal evolution operator as

$$\begin{aligned} \hat{S}_{Cl} &= \frac{i}{\hbar} \int_0^t d\tau \hat{H}_S^t(\tau) + \sum_q Z_{qf}' Z_{qi}^* e^{i\omega_q t} \\ &\quad - \sum_q \int_0^t d\tau \int_0^{\tau} d\tau' e^{-i\omega_q(\tau'-\tau)} \hat{\gamma}_q(\tau) \hat{\gamma}_q^*(\tau') \\ &\quad + i \sum_q Z_{qf}' \int_0^t d\tau e^{-i\omega_q(\tau-t)} \hat{\gamma}_q^*(\tau) + i \sum_q Z_{qi}^* \int_0^t d\tau e^{i\omega_q\tau} \hat{\gamma}_q(\tau), \end{aligned} \quad (\text{A.47})$$

where the boundary condition in Eq. A.44 has been used. Both \hat{S}_{Cl} and \hat{S}_{Cl}^t , defined in Eqs. A.33 and A.47, are operators in the space of carrier-photon states which are denoted by indexes s^+ and s^- for \hat{S}_{Cl} and \hat{S}_{Cl}^t , respectively. s^+ and s^- propagate at the forward and backward time-direction, respectively.

Until now, we have eliminated the phonon degrees of freedom in the matrix elements of the time evolution operator and its H.C. and determined their path-integral representations along the classical trajectories by obtaining the corresponding extremal actions. Now, we should work on the third matrix element (matrix element of the initial total sta-

tistical operator) given in Eq. A.5; It is assumed that, in the carrier-photon and phonon coherent states representation, the initial total statistical operator $\chi(0)$, defined in Eq. 3.15, has the form

$$\chi(0) = \hat{\rho}(0) \otimes \frac{1}{Z} \exp \left[-\frac{\hbar}{k_B T} \sum_q \omega_q b_q^\dagger b_q \right], \quad (\text{A.48})$$

where Z is the normalization constant of the phonon distribution at temperature T (bare bath partition function at temperature T). Inserting it into the corresponding matrix element and using the identity operators, in the space of carrier-photon states, we have

$$\langle s_i^+, Z_i | \chi(0) | s_i^-, Z_i' \rangle = \sum_{s_i^+} \langle s_i^+, Z_i | \frac{1}{Z} e^{-\frac{\hbar}{k_B T} \sum_q \omega_q b_q^\dagger b_q} | s_i^+, Z_i' \rangle \langle s_i^+ | \hat{\rho}(0) | s_i^- \rangle, \quad (\text{A.49})$$

we can replace the phonon operators using Eq. A.14, so that

$$\langle s_i^+, Z_i | \chi(0) | s_i^-, Z_i' \rangle = \frac{1}{Z} \exp \left[\sum_q e^{-\frac{\hbar \omega_q}{k_B T}} Z_{qi}^* Z_{qi}' \right] \rho_{s_i^+ s_i^-}, \quad (\text{A.50})$$

where we have used the Taylor expansion and $\rho_{s_i^+ s_i^-}$ is the initial RQCDM element.

Inserting Eqs.A.27, A.43, and A.50 into Eq. A.5, for RQCDM we obtain

$$\begin{aligned} \rho_{s_f^+ s_f^-}(t) &= \frac{1}{\pi^3 Z} \left[\int D\eta D\eta' e^{(\hat{S}_\eta + \hat{S}'_\eta)} \right] \\ &\times \sum_{s_i^+, s_i^-} \int \prod_q \left[e^{-Z_{qf}^* Z_{qf} - Z_{qi}^* Z_{qi} - Z_{qi}'^* Z_{qi}'} dZ_{qf}^* dZ_{qf} dZ_{qi}^* dZ_{qi} dZ_{qi}'^* dZ_{qi}'} \right] \\ &\times \langle s_f^+, s_f^- | \exp \left(\hat{S}_{Cl} + \hat{S}'_{Cl} \right) | s_i^+, s_i^- \rangle \exp \left(\sum_q e^{-\frac{\hbar \omega_q}{k_B T}} Z_{qi}^* Z_{qi}' \right) \rho_{s_i^+ s_i^-}, \end{aligned} \quad (\text{A.51})$$

where the six-dimensional complex integral, over phonon eigenvalues and their complex conjugates at initial and final times, should be performed. To do so, we have used the

change of variables as $Z_{qk}^{(l)} = X + jY$ and $Z_{qk}^{(l)*} = X - jY$ with $dZ_{qk}^{(l)} dZ_{qk}^{(l)*} = dXdY$ where $k = f, i$ then, making use of the standard Gaussian integral (Gerry & Knight, 2005)

$$\int_{-\infty}^{\infty} e^{-\alpha s^2} e^{\pm\beta s} ds = \sqrt{\frac{\pi}{\alpha}} e^{\frac{\beta^2}{4\alpha}}, \quad (\text{A.52})$$

and after some calculation, finally, we arrive at

$$\rho_{s_f^+ s_f^-}(t) = \left[\int D\eta D\eta' e^{(\hat{S}_\eta + \hat{S}'_\eta)} \right] \sum_{s_i^+, s_i^-} \langle s_f^+, s_f^- | e^{\hat{F}_S + \hat{f}_B} | s_i^+, s_i^- \rangle \rho_{s_i^+ s_i^-}, \quad (\text{A.53})$$

where $Z = Tr(\exp \left[\sum_q e^{-\frac{\hbar\omega_q}{k_B T}} Z_{qi}^* Z_{qi} \right]) = \prod_q [1 - \exp(-\hbar\omega_q/k_B T)]^{-1}$ and the term $\left[\int D\eta D\eta' e^{(\hat{S}_\eta + \hat{S}'_\eta)} \right]$ is absorbed by a normalization when the final density matrix is calculated numerically. The system functional \hat{F}_S is represented as

$$\hat{F}_S = \frac{i}{\hbar} \int_0^t d\tau \left(\hat{H}'_S(\tau) - \hat{H}_S(\tau) \right), \quad (\text{A.54})$$

and the bath functional \hat{f}_B , accounting for effects of the environment, is given by

$$\begin{aligned} \hat{f}_B = & - \sum_q [n_q \int_0^t d\tau e^{-i\omega_q \tau} (\hat{\gamma}_q^*(\tau) - \hat{\gamma}_q(\tau)) \times \int_0^t d\tau' e^{i\omega_q \tau'} (\hat{\gamma}_q(\tau') - \hat{\gamma}_q^*(\tau')) \\ & - \int_0^t d\tau \int_0^t d\tau' e^{i\omega_q(\tau-\tau')} \hat{\gamma}_q(\tau) \hat{\gamma}_q^*(\tau') + \int_0^t d\tau \int_0^\tau d\tau' e^{-i\omega_q(\tau-\tau')} \hat{\gamma}_q^*(\tau) \hat{\gamma}_q(\tau') \\ & + \int_0^t d\tau \int_0^\tau d\tau' e^{i\omega_q(\tau-\tau')} \hat{\gamma}_q(\tau) \hat{\gamma}_q^*(\tau')]. \end{aligned} \quad (\text{A.55})$$

where $n_q = [\exp(\hbar\omega_q/k_B T) - 1]^{-1}$ is the Bose–Einstein distribution of phonons at temperature T . One can simplify \hat{f}_B if the excitonphonon coupling constants satisfy certain symmetry conditions, for example, they are purely real or imaginary, i.e. $\hat{\gamma}_q(\tau) = \hat{\gamma}_q^*(\tau)$

and $\widehat{\gamma}_q(\tau) = \widehat{\gamma}_q^*(\tau)$. Under these conditions, knowing that for any function,

$$\begin{aligned} \int_0^t d\tau \int_0^\tau d\tau' f(\tau, \tau') &= \int_0^t d\tau \int_0^\tau d\tau' f(\tau, \tau') + \int_0^t d\tau \int_\tau^t d\tau' f(\tau, \tau') \\ &= \int_0^t d\tau \int_0^\tau d\tau' [f(\tau, \tau') + f(\tau', \tau)], \end{aligned} \quad (\text{A.56})$$

and using the quantity

$$\begin{aligned} &(n_q + 1) e^{-i\omega_q(\tau - \tau')} + n_q e^{i\omega_q(\tau - \tau')} \\ &= \coth\left(\frac{\hbar\omega_q}{2k_B T}\right) \cos(\omega_q(\tau - \tau')) - i \sin(\omega_q(\tau - \tau')) \\ &= \mu_q(\tau - \tau'), \end{aligned} \quad (\text{A.57})$$

after some calculation finally, one obtains

$$\begin{aligned} \widehat{f}_B(t, t) &= -\sum_q \int_0^t d\tau \int_0^\tau d\tau' (\widehat{\gamma}_q^*(\tau) - \widehat{\gamma}_q^*(\tau')) \\ &\quad \times (\mu_q(\tau - \tau') \widehat{\gamma}_q(\tau') - \mu_q^*(\tau - \tau') \widehat{\gamma}_q(\tau')) \\ &= \int_0^t d\tau \int_0^\tau d\tau' \widehat{\phi}_B(\tau, \tau'). \end{aligned} \quad (\text{A.58})$$

The system functional \widehat{F}_S contains nondiagonal operators in the carrier-photon state space while the bath functional \widehat{f}_B includes diagonal phonon coupling matrices.

Equations A.53-A.55 and A.57-A.58 define the evaluated path-integral, over phonon variables for the forward and backward time propagation, expressed using continuous time-ordered products of operators in the space of carrier-photon states. Now, we shall construct a new path-integral over eigenstates of the closed QD-cavity system, propagating forward and backward at time, by returning to a suitable discretized representation. Since the main steps are analogous to the previous cases of construction of the path-integral with phonon variables, we briefly present the derivation steps; We discretize the

integral in Eq. A.54 as in Eq. A.7 and the two-dimensional integral in Eq. A.58 making use of the Trotter discretization as (Dattani, Pollock, & Wilkins, 2012)

$$\begin{aligned}\widehat{f}_B(t, t) &= \sum_{n=1}^N \int_{t_{n-1}}^{t_n} d\tau \left(\sum_{n'=1}^{n-1} \int_{t_{n'-1}}^{t_{n'}} d\tau' + \int_{t_{n-1}}^{\tau} d\tau' \right) \widehat{\phi}_B(\tau, \tau') \\ &= \sum_{n=1}^N \widehat{f}_B(t_n, t_{n'}).\end{aligned}\quad (\text{A.59})$$

In order to calculate matrix elements of the exponential operator $e^{\widehat{F}_S + \widehat{f}_B}$, in Eq. A.53, between the system states at time slices n and $n - 1$ we factorize it, keeping the accuracy $O(\epsilon)$, as in Eq. A.8. As the system is now described by two sets of carrier-photon states $|s_n^+\rangle$ and $|s_n^-\rangle$, for the forward and backward time propagation, respectively, the system identity operators are built by direct products of those sets' identity operators as, $\widehat{I}_n = \widehat{I}_n^{s^+} \otimes \widehat{I}_n^{s^-} = \sum_{s_n^+} \sum_{s_n^-} |s_n^+\rangle \langle s_n^+| \otimes |s_n^-\rangle \langle s_n^-|$. Inserting a complete set of system states between each pair of the short-time exponential operators, we rewrite Eq. A.53 in the discretized form as

$$\rho_{s_N^+ s_N^-}(t) = \lim_{N \rightarrow \infty} \widehat{T} \sum_{\{s_{N-1}^+, \dots, s_0^+\}} \sum_{\{s_{N-1}^-, \dots, s_0^-\}} \prod_{n=1}^N \lambda_n \rho_{s_0^+ s_0^-}, \quad (\text{A.60})$$

where the short-time amplitude is given by

$$\lambda_n = \langle s_n^+, s_n^- | e^{\widehat{F}_S(t_n) + \widehat{f}_B(t_n, t_{n'})} | s_{n-1}^+, s_{n-1}^- \rangle, \quad (\text{A.61})$$

and the short-time system and bath functional are represented as

$$\begin{aligned}\widehat{F}_S(t_n) &= \frac{i}{\hbar} \int_{t_{n-1}}^{t_n} d\tau \left(\widehat{H}'_S(\tau) - \widehat{H}_S(\tau) \right) \\ \widehat{f}_B(t_n, t_{n'}) &= - \sum_q \int_{t_{n-1}}^{t_n} d\tau \left(\sum_{n'=1}^{n-1} \int_{t_{n'-1}}^{t_{n'}} d\tau' + \int_{t_{n-1}}^{\tau} d\tau' \right) \{ \mu_q(\tau - \tau') \widehat{\gamma}_{qn}^* \widehat{\gamma}_{qn'} \\ &\quad - \mu_q^*(\tau - \tau') \widehat{\gamma}_{qn}^* \widehat{\gamma}_{qn'} - \mu_q(\tau - \tau') \widehat{\gamma}_{qn}^* \widehat{\gamma}_{qn'} + \mu_q^*(\tau - \tau') \widehat{\gamma}_{qn}^* \widehat{\gamma}_{qn'} \}.\end{aligned}\quad (\text{A.62})$$

where $\widehat{\gamma}_q(\tau) = \widehat{\gamma}_{qn}$, $\widehat{\gamma}_q(\tau') = \widehat{\gamma}_{qn'}$.

Factorizing the exponential operator in Eq. A.61, while it is substituted by Eq. A.62 and A.63, similar to Eqs. A.8 and then, separating the corresponding matrix elements we arrive at

$$\rho_{s_N^+ s_N^-}(t) = \lim_{N \rightarrow \infty} \prod_{n=0}^{N-1} \left[\sum_{s_n^+} \sum_{s_n^-} \right] \prod_{n=1}^N H_S^{s_n^+ s_{n-1}^+} H_S^{s_n^- s_{n-1}^- *} \prod_{n'=1}^n e^{f_{nn'}} \rho_{s_0^+ s_0^-}, \quad (\text{A.64})$$

where the configuration summations are over all s_n^+ and s_n^- with $n = 0, \dots, N-1$, which can be interpreted as "sum over all trajectories" of the open QD-cavity system that connect the RQCDM at time t to the initial one at time zero. We can rewrite Eq. A.64 as

$$\rho_{s_N^+ s_N^-}(t) = \lim_{N \rightarrow \infty} \prod_{n=1}^N \sum_{s_{n-1}^\pm} H_S^{s_n^+ s_{n-1}^+} H_S^{s_n^- s_{n-1}^- *} \prod_{n'=1}^n e^{f_{nn'}} \rho_{s_0^+ s_0^-}. \quad (\text{A.65})$$

For the present case of the three-level system with two coupled levels, involving in the dynamics, the indexes s_n^+ and s_n^- are assumed to take only the values 0 and 1. $H_S^{s_n^+ s_{n-1}^+}$ and $H_S^{s_n^- s_{n-1}^- *}$ are one-dimensional short-time forward and backward bare system propagators which are derived as

$$H_S^{s_n^+ s_{n-1}^+} H_S^{s_n^- s_{n-1}^- *} = \langle s_n^+ | e^{-i\widehat{H}_S \varepsilon / \hbar} | s_{n-1}^+ \rangle \langle s_{n-1}^- | e^{i\widehat{H}_S^\dagger \varepsilon / \hbar} | s_n^- \rangle, \quad (\text{A.66})$$

where the time-independent open QD-cavity system Hamiltonian

$$\widehat{H}_S = \hbar \left(\omega_C - i\frac{\kappa}{2} \right) \widehat{s}_{00} + \hbar \left(\bar{\omega}_X - i\frac{\gamma_r}{2} \right) \widehat{s}_{11} + \hbar g (\widehat{s}_{01} + \widehat{s}_{10}) \quad (\text{A.67})$$

in the matrix form, for the present case of maximum one cavity photon, is represented by

$$\widehat{H}_S = \hbar \begin{pmatrix} \omega_C - i\frac{\kappa}{2} & g \\ g & \bar{\omega}_X - i\frac{\gamma}{2} \end{pmatrix}.$$

In order to calculate the short-time forward and backward system propagators, \widehat{H}_S should be diagonalized. The non-local discretized bath functional $f_{nn'}$ in Eq. A.65 is given by

$$f_{nn'} = -\eta_{s_n^+ s_{n'}^+} - \eta_{s_{n'}^- s_n^-} + \eta_{s_{n'}^- s_n^+} + \eta_{s_n^- s_{n'}^+}, \quad (\text{A.69})$$

where the influence coefficients $\eta_{\alpha\beta}$ (α and β denote arbitrary combinations of the indexes of s^+ and s^-) are obtained as

$$\eta_{\alpha_n \beta_{n'}} = \int_{t_{n-1}}^{t_n} d\tau \int_{t_{n'-1}}^{t_{n'}} d\tau' K_{\alpha_n \beta_{n'}}(\tau - \tau'), \quad n' < n \quad (\text{A.70})$$

$$\eta_{\alpha_n \beta_n} = \int_{t_{n-1}}^{t_n} d\tau \int_{t_{n-1}}^{\tau} d\tau' K_{\alpha_n \beta_n}(\tau - \tau'), \quad n' = n \quad (\text{A.71})$$

where the discretized system-bath correlation function (memory kernel) is given by

$$K_{\alpha_n \beta_{n'}}(\tau - \tau') = \sum_q \mu_q (\tau - \tau') \gamma_{q\alpha_n}^* \gamma_{q\beta_{n'}}, \quad n' \leq n \quad (\text{A.72})$$

the memory kernel $K_{\alpha_n \beta_{n'}}$ accounts for retarded influences by $m = n - n'$ time steps. $\gamma_{q\alpha}$ are the diagonal elements of the system-bath coupling matrix. Equations A.65 - A.72 define the discretized RTPI representation of time-evolution of the RQCDM corresponding to the three level system having two coupled level with purely real or imaginary exciton-phonon coupling constants. The exciton-phonon coupling is absent in the absence of excitons, i.e., $\gamma_{q0} = 0$, and $\gamma_{q1} = \gamma_q$, and since s_n^+ and s_n^- , in the present case, only take the values 0 and 1 therefore, we rewrite the bath functional as

$$f_{nn'} = - (s_n^+ - s_n^-) (\eta_{n-n' s_{n'}^+} - \eta_{n-n' s_{n'}^-}). \quad (\text{A.73})$$

The short-time Feynman-Vernon-like influence functional is defined as $I_{nn'} = \exp(f_{nn'})$. Replacing the summation over the wave vector \mathbf{q} with an integral, assuming an isotropic momentum space, and using the effective phonon spectral density, presented in Eq. 3.6,

$$J(\omega) = \sum_q |\gamma_q|^2 \delta(\omega - \omega_q), \quad (\text{A.74})$$

the system-bath correlation function is obtained as

$$\begin{aligned} K(\tau - \tau') &= \int_0^\infty d\omega J(\omega) \mu(\tau - \tau') \\ &= \int_0^\infty d\omega J(\omega) \left\{ \coth\left(\frac{\hbar\omega}{2k_B T}\right) \cos(\omega(\tau - \tau')) - i \sin(\omega(\tau - \tau')) \right\}, \end{aligned} \quad (\text{A.75})$$

where $J(\omega)$ is given in Eq. 3.11 and we have substituted $\mu(\tau - \tau')$ from Eq. A.57. Deducting $t_{n'-1}$ and t_{n-1} from the 2D integral boundaries in Eqs. A.70 and A.71 respectively and inserting Eq. A.74 into them we arrive at

$$\begin{aligned} \eta_{m \neq 0} &= \int_{m\varepsilon}^{(m+1)\varepsilon} d\tau \int_0^\varepsilon d\tau' K(\tau - \tau') \\ &= 4 \int_0^\infty d\omega \frac{J(\omega)}{\omega^2} \sin^2\left(\frac{\varepsilon\omega}{2}\right) \left\{ \coth\left(\frac{\hbar\omega}{2k_B T}\right) \cos(m\varepsilon\omega) - i \sin(m\varepsilon\omega) \right\}, \end{aligned} \quad (\text{A.76})$$

$$\begin{aligned} \eta_{m=0} &= \int_0^\varepsilon d\tau \int_0^\tau d\tau' K(\tau - \tau') \\ &= 2 \int_0^\infty d\omega \frac{J(\omega)}{\omega^2} \left\{ \sin^2\left(\frac{\varepsilon\omega}{2}\right) \coth\left(\frac{\hbar\omega}{2k_B T}\right) - i(\varepsilon\omega - \sin(\varepsilon\omega)) \right\}, \end{aligned} \quad (\text{A.77})$$

which are the influence coefficients presented in Eqs. 3.20 and 3.21 of Chap 3. After performing the time integrations to account for interactions of the initial time point with

other time points we add n , $n' = 0$ to the influence functional term and rewrite Eq. A.65 as

$$\rho_{s_N^+ s_N^-}(t) = \lim_{N \rightarrow \infty} \prod_{n=1}^N \sum_{s_{n-1}^\pm} H_S^{s_n^+ s_{n-1}^+} H_S^{s_n^- s_{n-1}^-} \prod_{n'=0}^n e^{f_{nn'}} \rho_{s_0^+ s_0^-}, \quad (\text{A.78})$$

where we have used the fact that according to Eq. A.73, defining the initial state $(s_n^+, s_n^-) = (0, 0)$ or $(1, 1)$, $f_{00} = 0$. Equation A.78 is the final expression for the RQCDM elements in the interaction picture, given in equation 3.16 of Chap. 3. One approximates Eq. A.78 with a finite N and ε in order to develop a numerical algorithm for practical calculations.

University of Malaya

REFERENCES

- Adachi, S. (1994). *GaAs and related materials*. World Scientific.
- Akahane, Y., Asano, T., Song, B.-S., & Noda, S. (2003). High-q photonic nanocavity in a two-dimensional photonic crystal. *Nature (London)*, *425*, 944.
- Andreani, L. C., Panzarini, G., & Gérard, J.-M. (1999, Nov). Strong-coupling regime for quantum boxes in pillar microcavities: Theory. *Physical Review B*, *60*, 13276-13279.
- Ates, S., Ulrich, S. M., Ulhaq, A., Reitzenstein, S., Löffler, A., Hofling, S., & Michler, P. (2009). Non-resonant dot-cavity coupling and its potential for resonant single-quantum-dot spectroscopy. *Nature Photonics*, *3*, 724.
- Auffèves, A., Gerace, D., Gérard, J.-M., Santos, M., Andreani, L. C., & Poizat, J.-P. (2010, Jun). Controlling the dynamics of a coupled atom-cavity system by pure dephasing. *Physical Review B*, *81*, 245419.
- Axt, V., Herbst, M., & Kuhn, T. (1999). Coherent control of phonon quantum beats. *Superlattices and Microstructures*, *26*(2), 117 - 128.
- Axt, V. M., & Mukamel, S. (1997). *In nonlinear optical materials. IMA volumes in mathematics and its applications* (Vol. 101). Springer.
- Barenco, A., Deutsch, D., Ekert, A., & Jozsa, R. (1995, May). Conditional quantum dynamics and logic gates. *Physical Review Letters*, *74*, 4083-4086.
- Barve, A., Rotter, T., Sharma, Y., Lee, S., Noh, S., & Krishna, S. (2010). Systematic study of different transitions in high operating temperature quantum dots in a well photodetectors. *Applied Physics Letters*, *97*, 061105.
- Basu, P. K. (1997). *Theory of optical processes in semiconductors: bulk and microstructures*. Clarendon Press, Oxford University Press.
- Beck, M., Jäckle, A., Worth, G., & Meyer, H.-D. (2000). The multiconfiguration time-dependent hartree (MCTDH) method: a highly efficient algorithm for propagating wavepackets. *Physics Reports*, *324*(1), 1 - 105.
- Benisty, H. (1995, May). Reduced electron-phonon relaxation rates in quantum-box systems: Theoretical analysis. *Physical Review B*, *51*, 13281-13293.
- Benson, O., Santori, C., Pelton, M., & Yamamoto, Y. (2000, Mar). Regulated and entangled photons from a single quantum dot. *Physical Review Letters*, *84*, 2513-2516.
- Besombes, L., Kheng, K., Marsal, L., & Mariette, H. (2001, Mar). Acoustic phonon broadening mechanism in single quantum dot emission. *Physical Review B*, *63*, 155307.

- Bhatt, A. R., Kim, K. W., & Strosio, M. A. (1994). Theoretical calculation of longitudinal-optical-phonon lifetime in GaAs. *Journal of Applied Physics*, 76(6), 3905-3907.
- Biasiol, G., & Heun, S. (2011). Compositional mapping of semiconductor quantum dots and rings. *Physics Reports*, 500(4–5), 117 - 173.
- Bimberg, D., Stock, E., Lochmann, A., Schliwa, A., Tofflinger, J. A., Unrau, W., & Kalagin, A. K. (2009). Quantum dots for single- and entangled-photon emitters. *IEEE Photonics Journal*, 1(1).
- Biolatti, E., Iotti, R. C., Zanardi, P., & Rossi, F. (2000, Dec). Quantum information processing with semiconductor macroatoms. *Physical Review Letters*, 85, 5647–5650.
- Bockelmann, U., & Bastard, G. (1990, Nov). Phonon scattering and energy relaxation in two-, one-, and zero-dimensional electron gases. *Physical Review B*, 42, 8947–8951.
- Bonadeo, N. H., Chen, G., Gammon, D., Katzer, D. S., Park, D., & Steel, D. G. (1998, Sep). Nonlinear nano-optics: Probing one exciton at a time. *Physical Review Letters*, 81, 2759–2762.
- Borri, P., Langbein, W., Mørk, J., Hvam, J. M., Heinrichsdorff, F., Mao, M.-H., & Bimberg, D. (1999, Sep). Dephasing in InAs/GaAs quantum dots. *Physical Review B*, 60, 7784–7787.
- Borri, P., Langbein, W., Schneider, S., Woggon, U., Sellin, R. L., Ouyang, D., & Bimberg, D. (2001, Sep). Ultralong dephasing time in InGaAs quantum dots. *Physical Review Letters*, 87, 157401.
- Borri, P., Langbein, W., Woggon, U., Stavarache, V., Reuter, D., & Wieck, A. D. (2005, Mar). Exciton dephasing via phonon interactions in InAs quantum dots: Dependence on quantum confinement. *Physical Review B*, 71, 115328.
- Brown, K. R., Lidar, D. A., & Whaley, K. B. (2001, Dec). Quantum computing with quantum dots on quantum linear supports. *Physical Review A*, 65, 012307.
- Brun, T. A., & Wang, H. (2000, Feb). Coupling nanocrystals to a high- q silica microsphere: Entanglement in quantum dots via photon exchange. *Physical Review A*, 61, 032307.
- Brus, L. E. (1984). Electron–electron and electron-hole interactions in small semiconductor crystallites: The size dependence of the lowest excited electronic state. *Journal of Chemical Physics*, 80(9), 4403.
- Brusaferri, L., Sanguinetti, S., Grilli, E., Guzzi, M., Bignazzi, A., Bogani, F., & Franchi, S. (1996). Thermally activated carrier transfer and luminescence line shape in self-organized InAs quantum dots. *Applied Physics Letters*, 69, 3354.
- Buckley, S., Rivoire, K., & Vuckovic, J. (2012). Engineered quantum dot single-photon sources. *Reports on Progress in Physics*, 75, 126503.

- Burkard, G., Loss, D., & DiVincenzo, D. P. (1999, Jan). Coupled quantum dots as quantum gates. *Physical Review B*, *59*, 2070–2078.
- Carmelet, A., Milde, F., Dachner, M.-R., Harouni, M. B., Roknizadeh, R., Richter, M., & Knorr, A. (2010, May). Formation dynamics of an entangled photon pair: A temperature-dependent analysis. *Physical Review B*, *81*, 195319.
- Carmelet, A., Richter, M., Chow, W. W., & Knorr, A. (2010, Apr). Antibunching of thermal radiation by a room-temperature phonon bath: A numerically solvable model for a strongly interacting light-matter-reservoir system. *Physical Review Letters*, *104*, 156801.
- Castella, H., & Zimmermann, R. (1999, Mar). Coherent control for a two-level system coupled to phonons. *Physical Review B*, *59*, R7801–R7804.
- Chamarro, M., Gourdon, C., Lavallard, P., & Ekimov, A. I. (1995). Enhancement of exciton exchange interaction by quantum confinement in cdse nanocrystals. *Japanese Journal of Applied Physics*, *34*(S1), 12-14.
- Chen, P., Piermarocchi, C., & Sham, L. J. (2001, Jul). Control of exciton dynamics in nanodots for quantum operations. *Physical Review Letters*, *87*, 067401.
- Cheng, X., Lowe, S. B., Reece, P. J., & Gooding, J. J. (2014). Colloidal silicon quantum dots: from preparation to the modification of self-assembled monolayers (sams) for bio-applications. *Chemical Society Reviews*, *43*(2680), 2680–2700.
- Cho, N. K., Ryu, S. P., Song, J. D., Choi, W. J., Lee, J. I., & H., J. (2006). Comparison of structural and optical properties of InAs quantum dots grown by migration-enhanced molecular-beam epitaxy and conventional molecular-beam epitaxy. *Applied Physics Letters*, *88*, 133104.
- Claudon, J., Bleuse, J., Malik, N., Bazin, M., Jaffrennou, P., Gregersen, N., & Gerard, J. (2010). A highly efficient single-photon source based on a quantum dot in a photonic nanowire. *Nature Photonics*, *4*, 174-177.
- Dachner, M.-R., Malic, E., Richter, M., Carmele, A., Kabuss, J., Wilms, A., & Knorr, A. (2010). Theory of carrier and photon dynamics in quantum dot light emitters. *physica status solidi (b)*, *247*(4), 809–828.
- Dattani, N. S., Pollock, F. A., & Wilkins, D. M. (2012). Analytic influence functionals for numerical feynman integrals in most open quantum systems. *Quant. Phys. Lett.*, *1*(1), 35-45.
- Dawson, P., Rubel, O., Baranovskii, S. D., Pierz, K., Thomas, P., & Göbel, E. O. (2005, Dec). Temperature-dependent optical properties of InAs/GaAs quantum dots: Independent carrier versus exciton relaxation. *Physical Review B*, *72*, 235301.
- Duke, C. B., & Mahan, G. D. (1965, Sep). Phonon-broadened impurity spectra. i. density of states. *Physical Review*, *139*, A1965–A1982.
- Eliseev, P. G., Li, H., Stintz, A., Liu, G. T., Newell, T. C., Malloy, K. J., & Lester, L. F.

- (2000). Transition dipole moment of InAs/InGaAs quantum dots from experiments on ultralow-threshold laser diodes. *Applied Physics Letters.*, 77(2), 262.
- Fan, H. Y. (1951, Jun). Temperature dependence of the energy gap in semiconductors. *Physical Review*, 82, 900–905.
- Fan, H. Y. (1967). *Photon-electron interaction, crystals without fields* (Vol. p. 134). Springer.
- Fan, X., Takagahara, T., Cunningham, J., & Wang, H. (1998). Pure dephasing induced by exciton–phonon interactions in narrow GaAs quantum wells. *Solid State Communications*, 108(11), 857 - 861.
- Fano, U. (1957, Jan). Description of states in quantum mechanics by density matrix and operator techniques. *Review of Modern Physics*, 29, 74-93.
- Feynman, R., & Vernon, F. (1963). The theory of a general quantum system interacting with a linear dissipative system. *Annals of Physics*, 24, 118 - 173.
- Feynman, R., & Vernon, F. (2000). The theory of a general quantum system interacting with a linear dissipative system. *Annals of Physics*, 281(1), 547 - 607.
- Feynman, R. P. (1948, Apr). Space-time approach to non-relativistic quantum mechanics. *Review of Modern Physics*, 20, 367–387.
- Feynman, R. P. (1950, Nov). Mathematical formulation of the quantum theory of electromagnetic interaction. *Physical Review*, 80, 440–457.
- Feynman, R. P. (1951, Oct). An operator calculus having applications in quantum electrodynamics. *Physical Review*, 84, 108–128.
- Förstner, J., Weber, C., Danckwerts, J., & Knorr, A. (2003, Sep). Phonon-assisted damping of Rabi oscillations in semiconductor quantum dots. *Physical Review Letters*, 91, 127401.
- Gammon, D., Snow, E. S., Shanabrook, B. V., Katzer, D. S., & Park, D. (1996, Apr). Fine structure splitting in the optical spectra of single GaAs quantum dots. *Physical Review Letters*, 76, 3005–3008.
- Gammon, D., Snow, E. S., Shanbrook, B. V., Katzer, D. S., & Park, D. (1996). Homogeneous linewidths in the optical spectrum of a single gallium arsenide quantum dot. *Science*, 273, 87.
- Gazzano, O., de Vasconcellos, S. M., Arnold, C., Nowak, A., Galopin, E., Sagnes, I., & Senellart, P. (2013). Bright solid-state sources of indistinguishable single photons. *Nature Communication*, 4, 1425.
- Gerry, C., & Knight, P. (2005). *Introductory quantum optics*. Cambridge University Press.
- Ghods Nahri, D. (2012a). Analysis of dynamic, modulation, and output power properties

of self-assembled quantum dot lasers. *Laser Physics Letters*, 9, 682–690.

- Ghods Nahri, D. (2012b, Jul). Investigation of the effects of nonlinear optical gain and thermal carrier excitation on characteristics of self-assembled quantum-dot lasers. *Optics Express*, 20(14), 14754–14768.
- Ghods Nahri, D. (2012c). Simulation of output power and optical gain characteristics of self-assembled quantum-dot lasers: Effects of homogeneous and inhomogeneous broadening, quantum dot coverage and phonon bottleneck. *Optics Laser Technology*, 44(8), 2436 - 2442.
- Ghods Nahri, D., Mathkoo, F. H. A., & Ooi, C. H. R. (2016, Dec.). Real-time path-integral approach for dissipative quantum dot-cavity quantum electrodynamics: Impure dephasing-induced effects. *Journal of Physics: Condensed Matter*, 29, 055701.
- Ghods Nahri, D., & Ooi, C. H. R. (2014, May). Modeling temperature-dependent shift of photoluminescence peak of In(Ga)As quantum dots with acoustic and optical phonons as two oscillators. *Journal of the Optical Society of America B*, 31(5), 1182–1191.
- Gisin, N., Ribordy, G., Tittel, W., & Zbinden, H. (2002, Mar). Quantum cryptography. *Review of Modern Physics*, 74, 145–195.
- Glässl, M., Sörgel, L., Vagov, A., Croitoru, M. D., Kuhn, T., & Axt, V. M. (2012, Jul). Interaction of a quantum-dot cavity system with acoustic phonons: Stronger light-matter coupling can reduce the visibility of strong coupling effects. *Physical Review B*, 86, 035319.
- Glässl, M., Vagov, A., Lüker, S., Reiter, D. E., Croitoru, M. D., Machnikowski, P., & Kuhn, T. (2011, Nov). Long-time dynamics and stationary nonequilibrium of an optically driven strongly confined quantum dot coupled to phonons. *Physical Review B*, 84, 195311.
- Grahn, H. T. (1999). In semiconductor physics. World Scientific.
- Grosse, F., & Zimmermann, R. (2007, Jun). Electron-phonon interaction in embedded semiconductor nanostructures. *Physical Review B*, 75, 235320.
- Haroche, S., & Raimond, J. (2006). *Exploring the quantum*. Oxford University Press.
- Harrison, P. (2005). *Quantum wells, wires and dots: Theoretical and computational physics of semiconductor nanostructures*. John Wiley Sons Ltd.
- He, Y.-M., He, Y., Wei, Y.-J., Wu, D., Atatüre, M., Schneider, C., & Pan, J.-W. (2013). On-demand semiconductor single-photon source with near-unity indistinguishability. *Nature Nanotechnology*, 8, 213.
- Heitz, R., Born, H., Hoffmann, A., Bimberg, D., Mukhametzhanov, I., & A., M. (2000). Resonant raman scattering in self-organized InAs/GaAs quantum dots. *Applied Physics Letters*, 77, 3746–3748.

- Heitz, R., Grundmann, M., Ledentsov, N. N., Eckey, L., Veit, M., Bimberg, D., & Alferov, Z. I. (1996). Multiphonon relaxation processes in self-organized InAs/GaAs quantum dots. *Applied Physics Letters*, *68*, 361–363.
- Heitz, R., Makhmetzhanov, I., Stier, O., Madhukar, A., & Bimberg, D. (2000). Phonon-assisted polar exciton–transitions in self-organized InAs/GaAs quantum dots. *Physica E*, *7*, 398.
- Heitz, R., Mukhametzhanov, I., Stier, O., Madhukar, A., & Bimberg, D. (1999, Nov). Enhanced polar exciton-LO-phonon interaction in quantum dots. *Physical Review Letters*, *83*, 4654–4657.
- Heitz, R., Veit, M., Ledentsov, N. N., Hoffmann, A., Bimberg, D., Ustinov, V. M., & Alferov, Z. I. (1997, Oct). Energy relaxation by multiphonon processes in InAs/GaAs quantum dots. *Physical Review B*, *56*, 10435–10445.
- Hennessy, K., Badolato, A., Winger, M., Gerace, D., Atatüre, M., Gulde, S., & Imamoglu, A. (2007). Quantum nature of a strongly coupled single quantum dot–cavity system. *Nature (London)*, *445*, 896.
- Hohenester, U. (2006). *Handbook of theoretical and computational nanotechnology*. American Scientific.
- Hohenester, U., Laucht, A., Kaniber, M., Hauke, N., Neumann, A., Mohtashami, A., & Finley, J. J. (2009, Nov). Phonon-assisted transitions from quantum dot excitons to cavity photons. *Physical Review B*, *80*, 201311.
- Hohenester, U., Pfanner, G., & Seliger, M. (2007, Jul). Phonon-assisted decoherence in the production of polarization-entangled photons in a single semiconductor quantum dot. *Physical Review Letters*, *99*, 047402.
- Huang, K., & Rhys, A. (1950). Theory of light absorption and non-radiative transitions in f-centres. *Proceedings of the Royal Society of London A: Mathematical, Physical and Engineering Sciences*, *204*(1078), 406–423.
- Ishizaki, A., & Tanimura, Y. (2005). Quantum dynamics of system strongly coupled to low-temperature colored noise bath: Reduced hierarchy equations approach. *Journal of the Physical Society of Japan*, *74*(12), 3131-3134.
- Kaer, P., Gregersen, N., & Mørk, J. (2013). The role of phonon scattering in the indistinguishability of photons emitted from semiconductor cavity QED systems. *New Journal of Physics*, *15*(3), 035027.
- Kaer, P., Nielsen, T. R., Lodahl, P., Jauho, A.-P., & Mørk, J. (2010, Apr). Non-markovian model of photon-assisted dephasing by electron-phonon interactions in a coupled quantum-dot–cavity system. *Physical Review Letters*, *104*, 157401.
- Kaer, P., Nielsen, T. R., Lodahl, P., Jauho, A.-P., & Mørk, J. (2012, Aug). Microscopic theory of phonon-induced effects on semiconductor quantum dot decay dynamics in cavity QED. *Physical Review B*, *86*, 085302.

- Kakushadze, Z. (2015). Path integral and asset pricing. *Path integral and asset pricing, Quantitative Finance*, 15:11, 1759-1771, 15:11, 1759-1771.
- Kelly, M. J. (1995). *Low-dimensional semiconductors: materials, physics, technology, and devices*. Clarendon Press, Oxford University Press.
- Khandekar, D., Lawande, S. W., & Bhagwat, K. V. (1998). *Path-integral methods and their applications*. World Scientific.
- Khitrova, G., Gibbs, H. M., Kira, M., Koch, S. W., & Scherer, A. (2006). A vacuum rabi splitting in semiconductors. *Nature Physics*, 2, 81-90.
- Khmissi, H., Baira, M., Sfaxi, L., Bouzaïene, L., Saidi, F., Bru-Chevallier, C., & Maaref, H. (2011). Optical investigation of InAs quantum dots inserted in AlGaAs/GaAs modulation doped heterostructure. *Journal of Applied Physics*, 109, 054316.
- Kleinert, H. (2006). *Path integrals in quantum mechanics, statistics, polymer physics, and financial markets, 4th ed.* World Scientific.
- Klingshirn, C. F. (1995). *Semiconductor optics*. Springer.
- Knill, E., Laflamme, R., & Milburn, G. J. (2001). A scheme for efficient quantum computation with linear optics. *Nature (London)*, 409, 46.
- Krügel, A., Vagov, A., Axt, V. M., & Kuhn, T. (2007, Nov). Monitoring the buildup of the quantum dot polaron: Pump-probe and four-wave mixing spectra from excitons and biexcitons in semiconductor quantum dots. *Physical Review B*, 76, 195302.
- Krummheuer, B., Axt, V. M., & Kuhn, T. (2002, May). Theory of pure dephasing and the resulting absorption line shape in semiconductor quantum dots. *Physical Review B*, 65, 195313.
- Krummheuer, B., Axt, V. M., & Kuhn, T. (2005, Dec). Coupled polarization and acoustic-phonon dynamics after optical excitation of quantum dots near surfaces. *Physical Review B*, 72, 245336.
- Krummheuer, B., Axt, V. M., Kuhn, T., D'Amico, I., & Rossi, F. (2005, Jun). Pure dephasing and phonon dynamics in GaAs- and GaN-based quantum dot structures: Interplay between material parameters and geometry. *Physical Review B*, 71, 235329.
- Krügel, A., Axt, V. M., Kuhn, T., Machnikowski, P., & Vagov, A. (2005). The role of acoustic phonons for Rabi oscillations in semiconductor quantum dots. *Applied Physics B*, 81,, 897.
- Ku, P., Sedgwick, F., Chang-Hasnain, C. J., Palinginis, P., Li, T., Wang, H., & Chuang, S. (2004, Oct). Slow light in semiconductor quantum wells. *Optics Letters*, 29(19), 2291–2293.
- Kuhn, T. (1998). Theory of transport properties of semiconductor nanostructures. In (p. 173). Chapman and Hall.

- Kuhn, T., Axt, V. M., Herbst, M., & Binder, E. (1999). Coherent control in atoms, molecules, and semiconductors. In (p. 113). Kluwer Academic.
- Ladd, T. D., Jelezko, F., Laflamme, R., Nakamura, Y., Monroe, C., & O'Brien, J. L. (2010). Quantum computers. *Nature*, *464*, 45-53.
- Lai, Y., Pirotta, S., Urbinati, G., Gerace, D., Minkov, M., Savona, V., & Galli, M. (2014). Genetically designed L3 photonic crystal nanocavities with measured quality factor exceeding one million. *Applied Physics Letters*, *104*, 241101.
- Landolt-Börnstein. (1987). *Semiconductors: Intrinsic properties of group IV elements and II-V, II-VI and I-VII compounds* (Vol. III/22a). Springer, Berlin.
- Laussy, F. P., del Valle, E., & Tejedor, C. (2008, Aug). Strong coupling of quantum dots in microcavities. *Physical Review Letters*, *101*, 083601.
- Lee, C. K., Moix, J., & Cao, J. (2012). Accuracy of second order perturbation theory in the polaron and variational polaron frames. *Journal of Chemical Physics*, *136*, 204120.
- Lerner, M., Gregersen, N., Dunzer, F., Reitzenstein, S., Höfling, S., Mørk, J., & Forchel, A. (2012, Jan). Bloch-wave engineering of quantum dot micropillars for cavity quantum electrodynamics experiments. *Physical Review Letters*, *108*, 057402.
- Lochmann, A., Stock, E., Tofflinger, J. A., Unrau, W., Toropov, A., Bakarov, A., & Bimberg, D. (2009). Electrically pumped, micro-cavity based single photon source driven at 1 GHz. *Electronics Letters*, *45*(11), 566-567.
- Lodahl, P., Mahmoodian, S., & Stobbe, S. (2015, May). Interfacing single photons and single quantum dots with photonic nanostructures. *Review of Modern Physics*, *87*, 347-400.
- Loss, D., & DiVincenzo, D. P. (1998, Jan). Quantum computation with quantum dots. *Physical Review A*, *57*, 120-126.
- Lu, X., Vaillancourt, J., & Meisner, M. J. (2007a). A modulation-doped longwave infrared quantum dot photodetector with high photoresponsivity. *Semiconductor Science and Technology*, *22*, 993.
- Lu, X., Vaillancourt, J., & Meisner, M. J. (2007b). Temperature dependent photoresponsivity and high-temperature (190 k) operation of a quantum dot infrared photodetector. *Applied Physics Letters*, *91*, 051115.
- Lu, X., Vaillancourt, J., & Wen, H. (2010). Temperature-dependent energy gap variation in InAs/GaAs quantum dots. *Applied Physics Letters*, *96*, 173105.
- Machnikowski, P., & Jacak, L. (2004, May). Resonant nature of phonon-induced damping of rabi oscillations in quantum dots. *Physical Review B*, *69*, 193302.
- Madelung, H. T. O. (1982-89). *Landolt-bornstein: Numerical data and functional relationships in science and technology* (Vol. 17a/b and 22a). New Series, Group III,

Springer.

- Madsen, K. H., Ates, S., Lund-Hansen, T., Löffler, A., Reitzenstein, S., Forchel, A., & Lodahl, P. (2011, Jun). Observation of non-markovian dynamics of a single quantum dot in a micropillar cavity. *Physical Review Letters*, *106*, 233601.
- Mahan, G. (1990). *Many-particle physics*. Plenum Publishers.
- Mahan, G. D. (1972). Polarons in ionic crystals and polar semiconductors. In (p. 533). Amsterdam.
- Makarov, D. E., & Makri, N. (1994). Path integrals for dissipative systems by tensor multiplication. Condensed phase quantum dynamics for arbitrarily long time. *Chemical Physics Letters*, *221*(5), 482 - 491.
- Makri, N., & Makarov, D. (1995a). Tensor propagator for iterative quantum time evolution of reduced density matrices. ii. numerical methodology. *Journal of Chemical Physics*, *102*, 4611.
- Makri, N., & Makarov, D. (1995b). Tensor propagator for iterative quantum time evolution of reduced density matrices. i. theory. *Journal of Chemical Physics*, *102*, 4600.
- May, V., & Kuhn, O. (2000). *Charge and energy transfer dynamics in molecular systems*. Wiley-VCH Verlag, Berlin.
- McCutcheon, D. P. S., Dattani, N. S., Gauger, E. M., Lovett, B. W., & Nazir, A. (2011, Aug). A general approach to quantum dynamics using a variational master equation: Application to phonon-damped rabi rotations in quantum dots. *Physical Review B*, *84*, 081305.
- McCutcheon, D. P. S., & Nazir, A. (2010). Quantum dot rabi rotations beyond the weak exciton-phonon coupling regime. *New Journal of Physics*, *12*, 113042.
- Meyer, H.-D., Manthe, U., & Cederbaum, L. (1990). The multi-configurational time-dependent hartree approach. *Chemical Physics Letters*, *165*(1), 73 - 78.
- Michael, C. P., Srinivasan, K., Johnson, T. J., Painter, O., Lee, K. H., Hennessy, K., & Hu, E. (2007). Wavelength- and material-dependent absorption in GaAs and AlGaAs microcavities. *Applied Physics Letters*, *90*, 051108.
- Michler, P. (2003). *Single quantum dots, topics of applied physics*. Springer-Verlag.
- Michler, P., Kiraz, A., Becher, C., Schoenfeld, W. V., Petroff, P. M., Zhang, L., & Imamoglu, A. (2000). A quantum dot single-photon turnstile device. *Science*, *290*(5500), 2282–2285.
- Mukamel, S. (1995). *Principles of nonlinear optical spectroscopy*. Oxford University Press.
- Muljarov, E. A., Takagahara, T., & Zimmermann, R. (2005, Oct). Phonon-induced exciton dephasing in quantum dot molecules. *Physical Review Letters*, *95*, 177405.

- Muljarov, E. A., & Zimmermann, R. (2004, Nov). Dephasing in quantum dots: Quadratic coupling to acoustic phonons. *Physical Review Letters*, *93*, 237401.
- Muljarov, E. A., & Zimmermann, R. (2006, Jan). Comment on "dephasing times in quantum dots due to elastic LO phonon-carrier collisions". *Physical Review Letters*, *96*, 019703.
- Muljarov, E. A., & Zimmermann, R. (2007, May). Exciton dephasing in quantum dots due to LO-phonon coupling: An exactly solvable model. *Physical Review Letters*, *98*, 187401.
- Muljarov, E. A., & Zimmermann, R. (2008). Exciton dephasing in quantum dots: Coupling to LO phonons via excited states. *Physics Status Solidi b*, *245*, 1106.
- Muller, M., Bounouar, S., Jons, K. D., Glassl, M., & Michler, P. (2014, March). On-demand generation of indistinguishable polarization-entangled photon pairs. *Nature Photonics*, *8*(3), 224–228.
- Nilsson, J., Stevenson, R. M., Chan, K. H. A., Skiba-Szymanska, J., Lucamarini, M., Ward, M. B., & Shields, A. J. (2013). Quantum teleportation using a light-emitting diode. *Nature Photonics*, *7*, 311–315.
- Noda, S. (2006). Seeking the ultimate nanolaser. *Science*, *314*(5797), 260–261.
- Nysteen, A., Kaer, P., & Mork, J. (2013, Feb). Proposed quenching of phonon-induced processes in photoexcited quantum dots due to electron-hole asymmetries. *Physical Review Letters*, *110*, 087401.
- O'Brien, J., Furusawa, A., & Vuckovic, J. (2009). Photonic quantum technologies. *Nature Photon.*, *3*, 687.
- O'Donnell, K. P., & Chen, X. (1991). Temperature dependence of semiconductor band gaps. *Applied Physics Letters.*, *58*, 2924.
- Ohta, R., Ota, Y., Nomura, M., Kumagai, N., Ishida, S., Iwamoto, S., & Y., A. (2011). Strong coupling between a photonic crystal nanobeam cavity and a single quantum dot. *Applied Physics Letters.*, *98*, 173104.
- Ortner, G., Schwab, M., Bayer, M., Pässler, R., Fafard, S., Wasilewski, Z., & Forchel, A. (2005, Aug). Temperature dependence of the excitonic band gap in $\text{In}_x\text{Ga}_{1-x}\text{As}/\text{GaAs}$ self-assembled quantum dots. *Physical Review B*, *72*, 085328.
- Ota, Y., Iwamoto, S., Kumagai, N., & Arakawa, Y. (2011, Nov). Spontaneous two-photon emission from a single quantum dot. *Physical Review Letters*, *107*, 233602.
- Palinginis, P., & Wang, H. (2001). High-resolution spectral hole burning in CdSe/ZnS core/shell nanocrystals. *Applied Physics Letters.*, *78*, 1541.
- Park, Y.-S., Guo, S., Makarov, N. S., & Klimov, V. I. (2015, Aug). Room temperature single-photon emission from individual perovskite quantum dots. *ACS Nano*, *9*(10), 10386–10393.

- Peaker, A. R., & Grimmeiss, H. G. (1991). *Low-dimensional structures in semiconductors: from basic physics to applications*. Plenum Press.
- Pelton, M., & Yamamoto, Y. (1999, Mar). Ultralow threshold laser using a single quantum dot and a microsphere cavity. *Physical Review A*, *59*, 2418–2421.
- Peter, E., Senellart, P., Martrou, D., Lemaître, A., Hours, J., Gérard, J. M., & Bloch, J. (2005, Aug). Exciton-photon strong-coupling regime for a single quantum dot embedded in a microcavity. *Physical Review Letters*, *95*, 067401.
- Phillips, M., & Wang, H. (2002, Oct). Spin coherence and electromagnetically induced transparency via exciton correlations. *Physical Review Letters*, *89*, 186401.
- Press, D., Götzinger, S., Reitzenstein, S., Hofmann, C., Löffler, A., Kamp, M., & Yamamoto, Y. (2007, Mar). Photon antibunching from a single quantum-dot-microcavity system in the strong coupling regime. *Physical Review Letters*, *98*, 117402.
- Pässler, R. (1997). Basic model relations for temperature dependencies of fundamental energy gaps in semiconductors. *Physics Status Solidi B*, *200*, 155.
- Pässler, R. (1999). Parameter sets due to fittings of the temperature dependencies of fundamental bandgaps in semiconductors. *Physics Status Solidi B*, *216*, 975.
- Pässler, R. (2000). Moderate phonon dispersion shown by the temperature dependence of fundamental band gaps of various elemental and binary semiconductors including wide-band gap materials. *Journal of Applied Physics*, *88*, 2570.
- Pässler, R. (2001). Temperature dependence of fundamental band gaps in group IV, III – V, and II – VI materials via a two-oscillator model. *Journal of Applied Physics*, *89*, 6235–6240.
- Pässler, R. (2003). Semi-empirical descriptions of temperature dependences of band gaps in semiconductors. *Physics Status Solidi B*, *236*, 710.
- Rafailov, E., McRobbie, A. D., Cataluna, M. A., O’Faolain, L., Sibbett, W., & Livshits, D. A. (2006). Investigation of transition dynamics in a quantum-dot laser optically pumped by femtosecond pulses. *Applied Physics Letters*, *88*, 041101.
- Ramsay, A. J., Godden, T. M., Boyle, S. J., Gauger, E. M., Nazir, A., Lovett, B. W., & Skolnick, M. S. (2010, Oct). Phonon-induced Rabi-frequency renormalization of optically driven single InGaAs/GaAs quantum dots. *Physical Review Letters*, *105*, 177402.
- Ramsay, A. J., Gopal, A. V., Gauger, E. M., Nazir, A., Lovett, B. W., Fox, A. M., & Skolnick, M. S. (2010, Jan). Damping of exciton Rabi rotations by acoustic phonons in optically excited InGaAs/GaAs quantum dots. *Physical Review Letters*, *104*, 017402.
- Reithmaier, J. P., Şek, G., Löffler, A., Hofmann, C., Kuhn, S., Reitzenstein, S., & Forchel, A. (2004). Strong coupling in a single quantum dot–semiconductor microcavity

system. *Nature (London)*, 432, 197-200.

Roszak, K., Grodecka, A., Machnikowski, P., & Kuhn, T. (2005, May). Phonon-induced decoherence for a quantum-dot spin qubit operated by raman passage. *Physical Review B*, 71, 195333.

Roy, C., & Hughes, S. (2011, Jun). Phonon-dressed mollow triplet in the regime of cavity quantum electrodynamics: Excitation-induced dephasing and nonperturbative cavity feeding effects. *Physical Review Letters*, 106, 247403.

Roy, C., & Hughes, S. (2012, Mar). Polaron master equation theory of the quantum-dot mollow triplet in a semiconductor cavity-QED system. *Physical Review B*, 85, 115309.

Rudin, S., & Reinecke, T. L. (1999, Apr). Oscillator model for vacuum Rabi splitting in microcavities. *Physical Review B*, 59, 10227–10233.

Rudin, S., Reinecke, T. L., & Bayer, M. (2006, Oct). Temperature dependence of optical linewidth in single InAs quantum dots. *Physical Review B*, 74, 161305.

Salter, C. L., Stevenson, R. M., Farrer, I., Nicoll, C. A., Ritchie, D. A., & Shields, A. J. (2010). An entangled-light-emitting diode. *Nature*, 465, 594–597.

Sanguinetti, S., Henini, M., Grassi Alessi, M., Capizzi, M., Frigeri, P., & Franchi, S. (1999, Sep). Carrier thermal escape and retrapping in self-assembled quantum dots. *Physical Review B*, 60, 8276–8283.

Sanguinetti, S., Mano, T., Oshima, M., Tateno, T., Wakaki, M., & Koguchi, N. (2002). Temperature dependence of the photoluminescence of InGaAs/GaAs quantum dot structures without wetting layer. *Applied Physics Letters*, 81, 3067.

Scamarcio, G., Spagnolo, V., Ventruti, G., Lugará, M., & Righini, G. C. (1996, Apr). Size dependence of electron—LO-phonon coupling in semiconductor nanocrystals. *Physical Review B*, 53, R10489–R10492.

Schilp, J., Kuhn, T., & Mahler, G. (1994, Aug). Electron-phonon quantum kinetics in pulse-excited semiconductors: Memory and renormalization effects. *Physical Review B*, 50, 5435–5447.

Schliwa, A., Winkelkemper, M., & Bimberg, D. (2007, Nov). Impact of size, shape, and composition on piezoelectric effects and electronic properties of In(Ga)AsGaAs quantum dots. *Physical Review B*, 76, 205324.

Schmitt-Rink, S., Miller, D. A. B., & Chemla, D. S. (1987, May). Theory of the linear and nonlinear optical properties of semiconductor microcrystallites. *Physical Review B*, 35, 8113–8125.

Schrier, J., & Whaley, K. B. (2005, Aug). Atomistic theory of coherent spin transfer between molecularly bridged quantum dots. *Physical Review B*, 72, 085320.

Shchukin, V. A., & Bimberg, D. (1999, Jul). Spontaneous ordering of nanostructures on

- crystal surfaces. *Review of Modern Physics*, *71*, 1125–1171.
- Sherwin, M. S., Imamoglu, A., & Montroy, T. (1999, Nov). Quantum computation with quantum dots and terahertz cavity quantum electrodynamics. *Physical Review A*, *60*, 3508–3514.
- Shields, A. J. (2007). Semiconductor quantum light sources. *Nature Photonics*, *1*, 215–223.
- Sim, E. (2001). Quantum dynamics for a system coupled to slow baths: On-the-fly filtered propagator method. *Journal of Chemical Physics*, *115*, 4450.
- Smolka, S., Thyrestrup, H., Sapienza, L., Lehmann, T. B., Rix, K. R., Froufe-Pérez, L. S., & Lodahl, P. (2011). Probing the statistical properties of anderson localization with quantum emitters. *New Journal of Physics*, *13*(6), 063044.
- Somaschi, N., Giesz, V., Santis, L. D., Loredò, J. C., Almeida, M. P., Hornecker, G., & Senellart, P. (2016). Near-optimal single-photon sources in the solid state. *Nature Photonics*, *10*, 340-345.
- Song, B.-S., Noda, S., Asano, T., & Akahane, Y. (2005). Ultra-high-Q photonic double-heterostructure nanocavity. *Nature Materials*, *4*, 207.
- Srinivasan, K., & Painter, O. (2007). Linear and nonlinear optical spectroscopy of a strongly coupled microdisk–quantum dot system. *Nature (London)*, *450*, 862.
- Stangl, J., Holý, V., & Bauer, G. (2004, Sep). Structural properties of self-organized semiconductor nanostructures. *Review of Modern Physics*, *76*, 725–783.
- Steinbach, D., Kocherscheidt, G., Wehner, M. U., Kalt, H., Wegener, M., Ohkawa, K., & Axt, V. M. (1999, Nov). Electron-phonon quantum kinetics in the strong-coupling regime. *Physical Review B*, *60*, 12079–12090.
- Stevenson, R. M., Salter, C. L., Nilsson, J., Bennett, A. J., Ward, M. B., Farrer, I., & Shields, A. J. (2012, Jan). Indistinguishable entangled photons generated by a light-emitting diode. *Physical Review Letters*, *108*, 040503.
- Stevenson, R. M., Young, R. J., Atkinson, P., Cooper, K., Ritchie, D. A., & Shields, A. (2006). A semiconductor source of triggered entangled photon pairs. *Nature (London)*, *439*, 179–182.
- Stievater, T. H., Li, X., Steel, D. G., Gammon, D., Katzer, D. S., Park, D., & Sham, L. J. (2001, Sep). Rabi oscillations of excitons in single quantum dots. *Physical Review Letters*, *87*, 133603.
- Stock, E., Dachner, M.-R., Warming, T., Schliwa, A., Lochmann, A., Hoffmann, A., & Bimberg, D. (2011, Jan). Acoustic and optical phonon scattering in a single In(Ga)As quantum dot. *Physical Review B*, *83*, 041304.
- Strauf, S., & Jahnke, F. (2011). Single quantum dot nanolaser. *Laser Photonics Reviews*, *5*(5), 607–633.

- Takagahara, T. (1999, Jul). Theory of exciton dephasing in semiconductor quantum dots. *Physical Review B*, *60*, 2638–2652.
- Tanamoto, T. (2000, Jan). Quantum gates by coupled asymmetric quantum dots and controlled-NOT-gate operation. *Physical Review A*, *61*, 022305.
- Tanimura, Y. (2006). Stochastic Liouville, Langevin, Fokker–Planck, and master equation approaches to quantum dissipative systems. *Journal of the Physical Society of Japan*, *75*(8), 082001.
- Tarel, G., & Savona, V. (2010, Feb). Linear spectrum of a quantum dot coupled to a nanocavity. *Physical Review B*, *81*, 075305.
- Thoss, M., Wang, H., & Miller, W. H. (2001). Self-consistent hybrid approach for complex systems: Application to the spin-boson model with debye spectral density. *Journal of Chemical Physics*, *115*, 2991.
- Topolancik, J., Ilic, B., & Vollmer, F. (2007, Dec). Experimental observation of strong photon localization in disordered photonic crystal waveguides. *Physical Review Letters*, *99*, 253901.
- Uskov, A. V., Jauho, A.-P., Tromborg, B., Mørk, J., & Lang, R. (2000, Aug). Dephasing times in quantum dots due to elastic LO phonon-carrier collisions. *Physical Review Letters*, *85*, 1516–1519.
- Uskov, A. V., Jauho, A. P., Tromborg, B., Mørk, J., & Lang, R. (2006, Jan). Uskov *et al.* reply:. *Physical Review Letters*, *96*, 019704.
- Vagov, A., Axt, V. M., & Kuhn, T. (2002, Oct). Electron-phonon dynamics in optically excited quantum dots: Exact solution for multiple ultrashort laser pulses. *Physical Review B*, *66*, 165312.
- Vagov, A., Axt, V. M., Kuhn, T., Langbein, W., Borri, P., & Woggon, U. (2004, Nov). Nonmonotonous temperature dependence of the initial decoherence in quantum dots. *Physical Review B*, *70*, 201305.
- Vagov, A., Croitoru, M. D., Axt, V. M., Machnikowski, P., & Kuhn, T. (2011). Dynamics of quantum dots with strong electron phonon coupling: Correlation expansion vs. path integrals. *physica status solidi (b)*, *248*(4).
- Vagov, A., Croitoru, M. D., Glässl, M., Axt, V. M., & Kuhn, T. (2011, Mar). Real-time path integrals for quantum dots: Quantum dissipative dynamics with superohmic environment coupling. *Physical Review B*, *83*, 094303.
- Vagov, A., Glässl, M., Croitoru, M. D., Axt, V. M., & Kuhn, T. (2014, Aug). Competition between pure dephasing and photon losses in the dynamics of a dot-cavity system. *Physical Review B*, *90*, 075309.
- Varshni, Y. (1967). Temperature dependence of the energy gap in semiconductors. *Physica*, *34*(1), 149 - 154.

- Varshni, Y. P. (1970, Nov). Temperature dependence of the elastic constants. *Physical Review B*, 2, 3952–3958.
- Vasileiadis, M., Alexandropoulos, D., Adams, M. J., Simos, H., & Syvridis, D. (2008). Potential of InGaAs/GaAs quantum dots for applications in vertical cavity semiconductor optical amplifiers. *IEEE Journal of Selected Topics in Quantum Electronics*, 14(4), 1180-1187.
- Viña, L., Logothetidis, S., & Cardona, M. (1984, Aug). Temperature dependence of the dielectric function of germanium. *Physical Review B*, 30, 1979–1991.
- Wehner, M. U., Ulm, M. H., Chemla, D. S., & Wegener, M. (1998, Mar). Coherent control of electron-LO-phonon scattering in bulk GaAs. *Physical Review Letters*, 80, 1992–1995.
- Wei, Y.-J., He, Y., He, Y.-M., Lu, C.-Y., Pan, J.-W., Schneider, C., & Nazir, A. (2014, Aug). Temperature-dependent mollow triplet spectra from a single quantum dot: Rabi frequency renormalization and sideband linewidth insensitivity. *Physical Review Letters*, 113, 097401.
- Wei, Z. F., Xu, S. J., Duan, R. F., Li, Q., Wang, J., Zeng, Y. P., & Liu, H. C. (2005). Thermal quenching of luminescence from buried and surface InGaAs self-assembled quantum dots with high sheet density. *Journal of Applied Physics*, 98, 084305.
- Wilson-Rae, I., & Imamoglu, A. (2002, May). Quantum dot cavity-QED in the presence of strong electron-phonon interactions. *Physical Review B*, 65, 235311.
- Wojs, A., Hawrylak, P., Fafard, S., & Jacak, L. (1996, Aug). Electronic structure and magneto-optics of self-assembled quantum dots. *Physical Review B*, 54, 5604–5608.
- Xu, Z. Y., Lu, Z. D., Yang, X. P., Yuan, Z. L., Zheng, B. Z., Xu, J. Z., & Chang, L. L. (1996, Oct). Carrier relaxation and thermal activation of localized excitons in self-organized InAs multilayers grown on GaAs substrates. *Physical Review B*, 54, 11528–11531.
- Yeo, I., Song, J. D., & Lee, J. (2011). Temperature-dependent energy band gap variation in self-organized InAs quantum dots. *Applied Physics Letters*, 99, 151909.
- Yoshie, T., Scherer, A., Hendrickson, J., Khitrova, G., Gibbs, H. M., Rupper, G., & Deppe, D. G. (2004). Vacuum rabi splitting with a single quantum dot in a photonic crystal nanocavity. *Nature*, 432, 200-203.
- Young, R. J., Stevenson, R. M., Shields, A. J., Atkinson, P., Cooper, K., Ritchie, D. A., & Skolnick, M. S. (2005, Sep). Inversion of exciton level splitting in quantum dots. *Physical Review B*, 72, 113305.
- Zanardi, P., & Rossi, F. (1998, Nov). Quantum information in semiconductors: Noiseless encoding in a quantum-dot array. *Physical Review Letters*, 81, 4752–4755.
- Zrenner, A. (2000). A close look on single quantum dots. *Journal of Chemical Physics*, 112, 7790.